TEAM tAO

2004 VISUALIZATION CHALLENGE PAGE 1903

24 September 2004

Science

Vol. 305 No. 5692
Pages 1857–2036 $10

AAAS

Science

COVER Economically important fishes of the southeastern United States include amberjack, red snapper, vermilion snapper, black seabass, red grouper, black grouper, goliath grouper, and gag. All of these species are considered overfished or experiencing overfishing in the Gulf of Mexico, the South Atlantic, or both. See page 1958. [Drawings: Diane Rome Peebles]

Volume 305
24 September 2004
Number 5692

DEPARTMENTS

NEWS OF THE WEEK

1890

NEWS FOCUS

1914

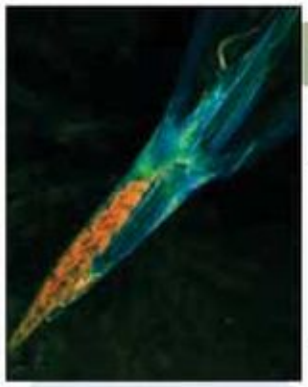

LETTERS

BOOKS *ET AL.*

POLICY FORUM

PERSPECTIVES

REVIEW

Contents continued

SCIENCE EXPRESS www.sciencexpress.org

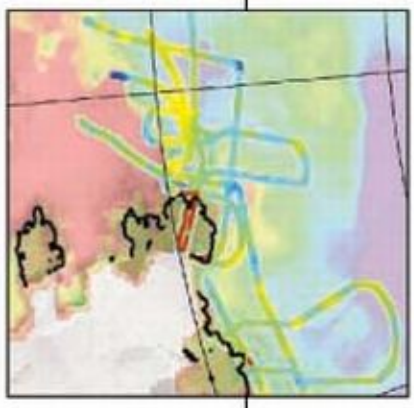

TECHNICAL COMMENT ABSTRACTS

BREVIA

RESEARCH ARTICLES

1933

REPORTS

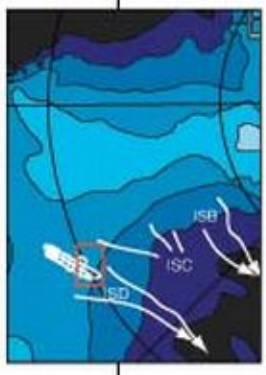

1948

Contents continued

REPORTS CONTINUED

1922 &1960

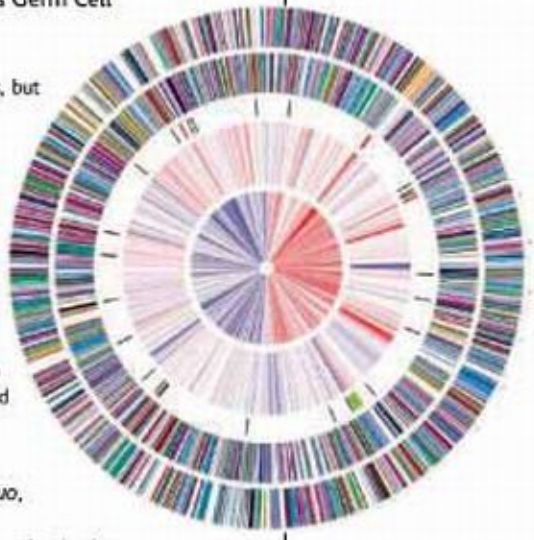

1966

AAAS
ADVANCING SCIENCE, SERVING SOCIETY

SCIENCE (ISSN 0036-8075) is published weekly on Friday, except the last week in December, by the American Association for the Advancement of Science, 1200 New York Avenue, NW, Washington, DC 20005. Periodicals Mail postage (publication No. 484460) paid at Washington, DC, and additional mailing offices. Copyright © 2004 by the American Association for the Advancement of Science. The title SCIENCE is a registered trademark of the AAAS. Domestic individual membership and subscription (51 issues): $130 ($74 allocated to subscription). Domestic institutional subscription (51 issues): $500. Foreign postage extra: Mexico, Caribbean (surface mail) $55; other countries (air assist delivery) $85. First class, airmail, student, and emeritus rates on request. Canadian rates with GST available upon request, GST #1254 88122. Publications Mail Agreement Number 1069624. Printed in the U.S.A.

Change of address: allow 4 weeks, giving old and new addresses and 8-digit account number. Postmaster: Send change of address to Science, P.O. Box 1811, Danbury, CT 06813–1811. Single copy sales: $10.00 per issue prepaid includes surface postage; bulk rates on request. Authorization to photocopy material for internal or personal use under circumstances not falling within the fair use provisions of the Copyright Act is granted by AAAS to libraries and other users registered with the Copyright Clearance Center (CCC) Transactional Reporting Service, provided that $15.00 per article is paid directly to CCC, 222 Rosewood Drive, Danvers, MA 01923. The identification code for Science is 0036-8075/85 $15.00. Science is indexed in the *Reader's Guide to Periodical Literature* and in several specialized indexes.

Contents continued

sciencenow www.sciencenow.org Daily News Coverage

Terrorism Causes Spike in Traffic Deaths
Attacks may have widespread effects on health and behavior.

Microbes Implicated in Crohn's Disease
Study adds to evidence that bacteria in milk could be behind the gut disease.

Methane in the Mantle?
Lab experiments suggest not all fossil fuels come from fossils.

Bioinformatics thrives in the Netherlands.

science's next wave www.nextwave.org Career Resources for Young Scientists

Global/Netherlands: Bioinformatics in the Netherlands—Thriving and Exciting *T. Hulsen*
Learn about the job, funding, and training opportunities in bioinformatics in the Netherlands.

Global/US: Grid Computing—Crossing the Chasm *S. Reddy*
Grid computing enables greater computing power in a collaborative environment at lower cost.

Global/US: Information Assurance Careers *M. E. Kabay*
Demand for information security professionals is exceeding the supply of credentialed graduates.

Global/US: Careers in Computer Science Research *J. Austin*
Career opportunities in computer science remain strong.

US: Educated Woman, Chapter 31—Year 4 Commences *M. P. DeWhyse*
A fourth-year graduate student can't believe she's made it this far.

MiSciNet: The Battle Is at the Top *S. Clemmons*
Everything goes well until a worker reaches the upper ranks.

science's sage ke www.sageke.org Science of Aging Knowledge Environment

Experimental Rodent Strain: Brown Norway Rat *D. J. Holmes*
This strain is used extensively in studies involving autoimmune diseases.

News Focus: Acid Trip *R. J. Davenport*
Blocking pH-sensitive calcium channels prevents stroke damage.

News Focus: Yin and Yang *M. Leslie*
Inflammatory molecules fight and foster atherosclerosis.

Keeping blood vessels in balance.

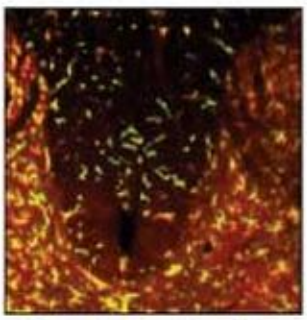

Pain markers in microglia.

science's stke www.stke.org Signal Transduction Knowledge Environment

Review: Cell Signaling and the Genesis of Neuropathic Pain *R.-R. Ji and G. Strichartz*
Central and peripheral signaling pathways contribute to the initiation and maintenance of pain after nerve injury.

Connections Maps: Pheromone Signaling Pathways in Yeast *H. G. Dohlman*
G proteins activate a MAPK cascade when yeast detect cells of the opposite mating type.

Connections Maps: Filamentous Growth Pathway in Yeast *D. M. Truckses, L. S. Garrenton, J. Thorner*
Three signaling cascades control invasive growth.

Connections Maps: High Osmolarity Glycerol (HOG) Pathway in Yeast *P. J. Westfall, D. R. Ballon, J. Thorner*
A MAPK cascade is at the center of this cell stress pathway.

Separate individual or institutional subscriptions to these products may be required for full-text access.

Science and the Bush Administration

In various ways, the scientific community in the United States—and in other nations as well—has expressed concern about the way in which decisions about scientific issues have been subjected to political tests by the Bush administration. For example, the Union of Concerned Scientists (UCS), in a statement that I signed along with many others, said in pertinent part: "When scientific knowledge has been found to be in conflict with its political goals, the administration has often manipulated the process through which science enters into its decisions." The UCS and John H. Marburger III, President Bush's science advisor, have continued to trade charge and countercharge. Now a committee of the National Academies is examining some of the issues at stake, including the important matter of criteria for appointing scientists to government posts and advisory committees.

I leave this unfinished debate in those capable hands. But as we approach the election, it is important to examine the most critical issues at the interface of science and politics in the determination of public policy. And on several of these issues, a new pattern of behavior by the administration is becoming clear. The sequence is as follows: A government position is taken on a matter of scientific importance; policy directions are announced and scientific justifications for those policies are offered; strong objections from scientists follow; the scientific rationale is then abandoned or changed, but the policies based on that science remain, stuck in the same place.

U.S. policy with respect to HIV/AIDS is a case in point. The virus is spreading at an alarming rate, devastating Africa and now making horrifying inroads into the teeming continent of Asia. Stopping the spread, especially among the youngest and most productive members of society, should be the highest international priority. With a vaccine far in the future, stemming the tide requires that we educate people to protect themselves; and although abstinence and fidelity prevent exposure to HIV, under most circumstances the only safe and effective protection is condoms.

Many policies based on incorrect science remain.

Initially, the Bush administration gave scant recognition to the protective value of condom use. The Centers for Disease Control Web site (which was once changed to suggest, incorrectly, a possible relation between abortion history and breast cancer) contains a confusing mixture: some emphasis on condom failure rates and a plug for abstinence. Complaints apparently led to the addition of a positive statement about condom effectiveness. The U.S. Agency for International Development now promotes condom use. But the emphasis is on use in selected target populations, although the value of much more widespread use has been demonstrated repeatedly in scientific studies.

Climate change has had a similar history. Repeated administration statements questioned the science behind the position of the Intergovernmental Panel on Climate Change (IPCC) that the global warming seen in the past 100 years is associated with human activity. Now, at last, comes a statement from an interagency administration committee, signed by cabinet secretaries, confirming the IPCC position. In the policy domain, however, we still have a long-range research program aimed toward a "hydrogen economy," but no commitment to current mitigation of this growing crisis.

As for stem cells, the arbitrary decision to restrict federally supported research to the few cell lines available before the president's statement in 2001 still holds. After sustained criticism from the scientific community, the administration has conceded that the research is valuable. It has made funding available for research but nevertheless maintains the cell line restriction. And it supports legislation that would criminalize research involving nuclear transfer from somatic donor cells—work focused on making stem cell research more valuable, both therapeutically and experimentally.

In these cases, either religious conservatism or economically based political caution has played a determining role in administration policy. However, it looks as though the criticism from individual scientists and from the UCS has been influential in causing the administration to be more honest about the underlying science. We should welcome this new posture. Nevertheless, although the realities of the science may be better accepted, the policy implications are still being ignored. Our goal now should be to have the policies track the science.

David Baltimore

David Baltimore is president of the California Institute of Technology in Pasadena, CA.

Published by AAAS

This Week

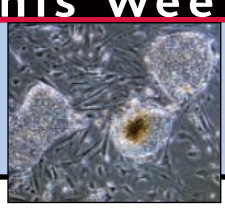

PAGE 1887
Stem cell patents turned down

1889
Survival in the Pacific

SPACE SCIENCE

Rising Cost of Shuttle and Hubble Could Break NASA Budget

Science may have to pay a steep price for putting the space shuttle back in business. Last week, NASA science chief Al Diaz ordered his managers to find at least $400 million in cuts to space and earth science efforts so that the space shuttle could resume flying in 2005, according to NASA officials. Billions of dollars in unexpected shuttle costs also threaten aeronautics and the nascent exploration effort.

The crunch comes only 7 months after President George W. Bush proposed an ambitious new trajectory for the space agency that officials said would not strain NASA's budget. Finishing the space station and closing down the shuttle program early in the next decade would free up money for lunar and martian robotic and human missions, they explained. Under that plan, spending on science would grow from $4 billion in 2004 to $5.6 billion in 2009, while shuttle spending would drop from $4 billion to $3 billion.

But the expected cost of fixing the shuttle fleet, grounded since the loss of Columbia over Texas on 1 February 2003, has soared to at least $2.2 billion. At the same time, NASA is also scrambling to find a similar amount for a robotic mission to the ailing Hubble Space Telescope. Worst of all, neither the White House nor Congress seems willing or able to rescue the agency.

The White House rebuffed a recent plea by NASA Administrator Sean O'Keefe for additional funding to cope with the agency's fiscal crisis, Administration sources say. And the president's 2005 request has received a rocky reception from a Congress faced with a massive budget deficit and the war in Iraq. "There isn't the money to mount an aggressive exploration program," says Malcolm Peterson, former NASA comptroller. "And if there isn't budgetary relief, I don't know where else you go [for funding] except science."

To fly the shuttle safely again, NASA will need as much as $760 million for next year alone, says Steven Isakowitz, NASA's current comptroller. Privately, agency managers expect the figure to rise to $1 billion for the 2005 fiscal year that begins next week and remain at that level for the next few years. To cope, NASA managers are being told that science must pony up approximately half of that shortfall, with the rest coming from aeronautics and exploration. Diaz, who assumed the job in August as part of an agency reorganization, declined to be interviewed. Agency spokesperson Donald Savage said Diaz was "uncomfortable" discussing budget matters.

The agency already wants $866 million more to start the exploration program in the coming year. That effort includes work on a lunar orbiter, a sophisticated nuclear electric system for interplanetary trips, and a large launcher to replace the shuttle. The Senate funding panel that oversees NASA this week approved $15.6 billion for the agency in 2005, only $200 million more than this year's figure and far short of the Administration's request of $16.2 billion. Still, that tops the House level of $15.2 billion, and some senators were hoping to add another $800 million when the bill reached the Senate floor this week.

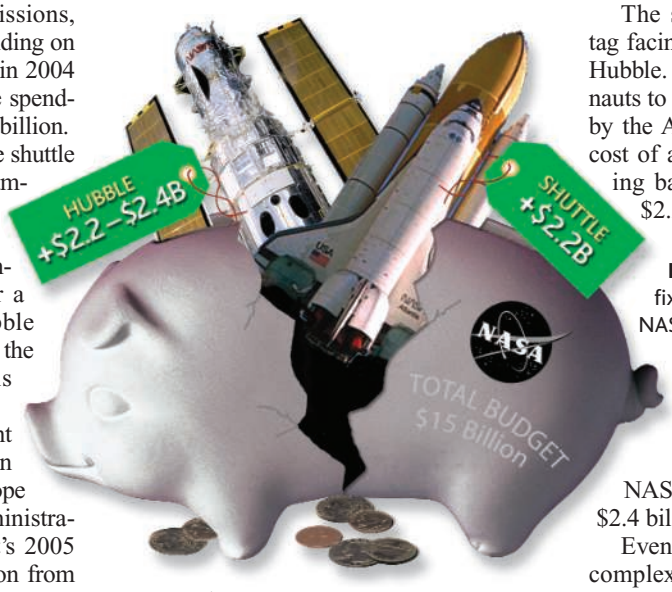

Bad break. Unexpectedly high costs to fix the shuttle and Hubble have thrown NASA into a serious fiscal crisis.

"There is no doubt whatsoever that whatever we choose, we'll have to make difficult decisions," says Isakowitz. "And that includes science, aeronautics, and exploration" programs. Anything short of the president's request, he says, would have a "negative" impact on science.

But even if Congress obliges, NASA will remain in a deep budget hole. O'Keefe was clear at an 8 September Senate hearing that science and exploration for now must take a back seat to human space flight. "Agenda number one is return to flight and complete the station," he said.

Many lawmakers are impatient with the ballooning shuttle costs. Senator Sam Brownback (R–KS), who chairs the Senate panel that oversees NASA's programs, insists that the answer is to phase out the shuttle as soon as possible. He told *Science* that "the Administration has just got to walk away from the shuttle more quickly." Proposals to do that include using cheaper, expendable launchers or reducing the number of solar panels and reorienting the station's current position in orbit. Those options would not sit well with NASA's international partners, however, and O'Keefe told the Senate committee that "I don't see a really significant diminution of the flight rate."

The second huge and unplanned price tag facing NASA is for robotic servicing of Hubble. O'Keefe has rejected sending astronauts to conduct the mission. A recent study by the Aerospace Corp. for NASA put the cost of a "Cadillac" mission to replace dying batteries and critical instruments at $2.2 billion. That figure is far higher than an earlier estimate by NASA's Goddard Space Flight Center in Greenbelt, Maryland, which put the price tag at $1.3 billion. Other NASA officials say privately that at least $2.4 billion is needed.

Even with ensured funding, however, a complex robotic mission is a race against time. The Aerospace Corp. study predicts that the Cadillac effort would take 5.4 years, and NASA engineers fear that Hubble could shut down as early as 2009. Goddard managers believe they could launch such a mission by December 2007, but an internal NASA study found that date too optimistic by 2 years. A shuttle mission could be ready in 2.5 years, says Michael Moore, a Hubble program executive. But that, NASA insists, would cost $200 million more than the Cadillac robotic mission.

Cheaper options include a simpler ef- ▶

CREDIT: L. CREVELING/*SCIENCE*; IMAGE SOURCES: ARTVILLE; NASA

Published by AAAS

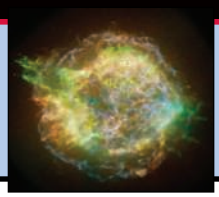

fort to deorbit the giant telescope safely, which NASA estimates would cost as little as $400 million. Some researchers and engineers want NASA to build a "Hubble-lite" that would incorporate the new instruments already waiting to fly. Despite their claim that the new mission would cost less than $1 billion, NASA is not seriously considering this option.

Given the tough budget environment, Administration and congressional sources say some programs inevitably will face the ax in 2005. One likely target is the multibillion-dollar Prometheus program to build a new nuclear electric power system (*Science*, 30 January, p. 614). The scrapping of the Prometheus program would be a big blow to planetary scientists, who are depending on that system to power the Jupiter Icy Moons Orbiter in the next decade. "I don't think we're facing cancellation," says Craig Steidle, chief of NASA's new exploration effort. But he acknowledges that reductions could force changes to Prometheus. There are no plans to cut work in the biological and physical sciences, says Steidle, who also oversees those programs.

Scientists inside and outside the agency will be watching closely to see whether O'Keefe can convince Bush and Congress to provide relief or whether research must be sacrificed for the shuttle and Hubble. "It's all very difficult and confusing," says one NASA manager. "How the heck is the agency going to fix this?"

–ANDREW LAWLER

NATIONAL SCIENCE FOUNDATION

President Reverses Course, Taps Bement as Director

For most scientists, agreeing to become the next director of the $5.5 billion U.S. National Science Foundation (NSF) would mean accepting a heavier workload. However, for Ardent Bement, last week's nomination by President George W. Bush could eventually mean a shorter workday.

For the past 7 months, Bement, a materials engineer with a track record in both academic and industrial research, has headed two agencies. He has been director of the National Institute of Standards and Technology (NIST) since December 2001 and assumed the additional title of acting NSF director in February, when microbiologist Rita Colwell left abruptly before her term was due to end in August (*Science*, 20 February, p. 1116). When he agreed to take on responsibility for NSF, Bement and the president's science adviser, John Marburger, agreed that it would only be a temporary gig.

But the NSF job, which comes with a 6-year term, proved harder to fill than expected. Uncertainty over the outcome of the November election, combined with a gloomy federal budget outlook, scared some away. Last month, "after a few other candidates had dropped out," Bement says that White House officials surprised him by asking if he would be interested. "At some point we realized that his credentials were as strong or stronger than [those of] the other people on our list," says Marburger.

Bement, meanwhile, was piling up plaudits from members of Congress and the scientific community as well as his overseers at the National Science Board. "It would be hard to think of a better person for the job," says Representative Sherwood Boehlert (R–NY), chair of the House Science Committee. "I was taking it one day at a time," says the unassuming Bement, and it was a long day: getting to NIST at sunrise, putting in 10 hours at NSF, and returning to NIST in the evening. Bement plans to remain NIST director until confirmed for the NSF job.

Familiar face. President Bush congratulates acting NSF Director Arden Bement on his nomination.

CREDIT: PAUL MORSE/WHITE HOUSE PHOTO

At 72, Bement insists that he's got "plenty of juice" left in him, and science board chair Warren Washington agrees that "doing two jobs doesn't seem to be a problem for [Bement]." But physicist Neal Lane, who held the NSF post during the Clinton Administration, thinks that the twin assignments are a bad idea, even if they may be about to end. "It's too much for one person," says Lane, now a university professor at Rice University in Houston, Texas.

Bement says he can wear two hats because of "outstanding backup" at NIST, in particular, acting director Hratch Semerjian. And he says that, although he'll miss running an agency that performs research (NIST operates labs but NSF does not), his interim assignment at NSF has whetted his appetite. In addition to the chance to follow NSF's 2006 budget request, which he prepared and shipped to the White House this month, Bement says he's hoping to fill three vacancies for assistant NSF directors—overseeing the education, biology, and social and behavioral sciences directorates—by the end of the year. "I like the challenge," he says about running an agency whose reputation for excellence won it a 2001 promise from Congress of a doubled budget but whose low profile hinders its ability to turn that promise into hard cash. "I also feel a strong duty to serve the community."

Bement's legion of supporters hopes that he'll win quick confirmation from the Senate, which could take up his nomination as early as this week. But if the Senate fails to act before it adjourns next month, Bement's status will enter a complex bureaucratic limbo.

Although NSF officials had erroneously concluded that a 1998 law on filling federal vacancies prohibited Bement from being offered the top job, the same law does set boundaries on his tenure as acting director. Bement came within 3 days of reaching a 210-day limit for an acting director when the president nominated him, and that clock would restart if the Senate doesn't act. But it would stop again if the president renominates him next year, meaning there's a chance Bement could continue to hold both agency jobs for quite a while.

–JEFFREY MERVIS

Published by AAAS

PALEOANTHROPOLOGY

Oldest Human Femur Wades Into Controversy

PARIS—Tempers flared last week in a sweltering salon at the French Academy of Sciences here* as scientists hotly debated the attributes of anthropology's most famous thighbone, the 6-million-year-old femur of an ancient Kenyan hominid called *Orrorin tugenensis*.

More than 100 scholars packed the academy's opulent, wood-paneled *Grande Salle* to witness the first face-to-face gathering of the discoverers of the three oldest putative hominids. In talks and a panel discussion, the researchers discussed whether *Orrorin* and other contenders for the title of earliest human ancestor walked upright and in what manner. Bipedalism is a traditional hallmark of membership in the human family rather than being an ancestor of chimpanzees, gorillas, or quadrupedal apes.

Walking the walk? Researchers argued over the evidence for the gait used by the owner of this ancient thighbone.

The speakers were particularly interested in learning more about *Orrorin*'s legs. Paleontologist Brigitte Senut of the National Museum of Natural History in Paris presented recently published computed tomography (CT) scans of *Orrorin*'s thighbone (*Science*, 3 September, p. 1450). According to Senut, the scans show that the bone is thicker on the bottom of the subhorizontal neck of the femur, indicating that weight was put on the top of the bone. Other features also suggest that the hips were stabilized in a manner similar to those of modern humans. In fact, Senut proposed that *Orrorin*'s gait was more humanlike than that of the 2- to 4-million-year-old australopithecines. If so, australopithecines would be bumped off the direct line to humans—a dramatic revision of our prehistory.

But paleoanthropologist Tim White of the University of California, Berkeley, immediately attacked this view of *Orrorin*. He said that the resolution of the CT scans was so poor that it was impossible to be certain of the pattern of bone thickness. CT scan expert James Ohman of Liverpool John Moores University in the U.K., who was not at the meeting, agreed that the published scans were taken at the wrong angle.

White further grilled Senut about the fossil analysis, asking if her team had directly measured the internal structure of the bone at a preexisting break, a more reliable means of gathering the data than CT scanning. Senut responded that colleagues had suggested doing the scans to make her case stronger and added in an interview that the bone was broken in a zigzag pattern that made it difficult to photograph. In her view, other features on the bone make it clear that *Orrorin* had walked upright—so there was no need to unglue the bone and measure it.

White accepts that *Orrorin* walked upright and so is one of the first members of the hominid family. But he says Senut has offered little evidence as to *Orrorin*'s gait. "Was it human, an *Australopithecus* pattern, or something different?" he asked. Even standard x-rays would help answer that question. As the discussion grew more heated, White called Senut's displacement of australopithecines "*une position créationniste*," because it suggests that *Orrorin*'s femur was quite modern 6 million years ago, rather than evolving in stages.

Senut declared indignantly that she is not a creationist—and then asked White to provide his own evidence about the mysterious *Ardipithecus ramidus*. A partial skeleton of that 4.4-million-year-old species was discovered by White's team, the Middle Awash Research Project, in Ethiopia from 1994 to 1996, but the bones remain unpublished.

White responded by projecting images of the *Ardipithecus* skull for the first time in public. The CT scans were startling: The skull was so crushed that the top of the vault was smashed almost to the base, forming a slab of hundreds of chalky pieces. White described it as "road kill." The reconstruction uses micro–CT scans to reassemble the specimen. "This is the most fragile hominid skeleton ever found," says White. "We are very sorry it's taken us this long to do, but I think you want the right answer instead of the quick answer." **–ANN GIBBONS**

* Prehistoric Climates, Cultures, and Societies, Paris, France, 13–16 September.

CREDIT: MARC DEVILLE/GAMMA

ScienceScope

Senate Gives NIH 4% Boost

A Senate appropriations committee last week approved a bill giving the National Institutes of Health (NIH) a 2005 budget of $28.9 billion, a 4%, $1.1 billion boost over 2004's. Although modest, the raise surpasses the meager 2.6% increase approved by the House last July, in line with President Bush's request. "We're obviously pleased," says David Moore, head of governmental relations for the Association of American Medical Colleges.

The Senate committee was silent, however, on several controversial moves taken by the House, which had voted to ban future funding for two NIH psychology studies and put a 50-person limit on the number of Department of Health and Human Services staff members sent to foreign meetings. It also recommended that NIH post copies of grantees' research articles in a public archive within 6 months of publication by a journal (*Science*, 10 September, p. 1548). Any further action on these issues, and NIH's ultimate budget number, won't be settled until the two bodies negotiate a final spending bill, which could take months. **–JOCELYN KAISER**

A Cancer Genome Project?

An expert panel offering biotechnology advice to National Cancer Institute (NCI) Director Andrew von Eschenbach expects to propose an ambitious new project that would identify all major cancer genes.

The task force, led by Eric Lander of the Broad Institute in Cambridge, Massachusetts, and Lee Hartwell of the Fred Hutchinson Cancer Research Center in Seattle, Washington, gathered advice from about 50 scientists who met in focus groups from March to June. Last week, Lander told the National Cancer Advisory Board (NCAB) that the group's draft plan includes a "Human Cancer Genome Project" that would analyze tissue samples to compile a database of all genes that are mutated in at least 5% of major cancers. "It is a finite problem," he said.

A second project would pose specific challenges in detection, such as using nipple fluid to detect breast cancer. The panel also wants NCI to set up a permanent technology panel that would produce "actionable" items with timelines and budgets, Lander said. He expects to present the full report at NCAB's December meeting.

Finding money for new initiatives could be difficult. But NCAB Chair John Niederhuber, an oncologist at the University of Wisconsin, Madison, says that by presenting Congress with a "business plan," NCI "might be able to tell a very powerful story." **–JOCELYN KAISER**

Published by AAAS

MICROBIOLOGY

Scientist Pleads Guilty of Receiving Illegally Imported Avian Flu Virus

A plea for help from a U.S. veterinary scientist working overseas has led to criminal charges against two researchers and five biotech company officials. The case is seen as the latest warning from the U.S. government about the serious repercussions of importing pathogens without proper permits.

Fowl shipment. Prosecutors claimed John Rosenberger's actions threatened U.S. poultry flocks.

On 8 September, John Rosenberger, a microbiologist at the University of Delaware, Newark, agreed to a fine of up to $250,000 and 6 months of home detention after pleading guilty to receiving and concealing a poultry virus smuggled into the country from Saudi Arabia. In the preceding months, five former officials of Maine Biological Laboratories (MBL) in Winslow, which also received the smuggled virus and developed a vaccine for it, pleaded guilty to committing mail fraud, lying to federal agencies, and concealing samples of the pathogen. And on 9 September, Mark Dekich, an employee of a Saudi poultry company who is charged with sending the virus, was indicted on charges of smuggling and making false statements to federal agencies. The case is before U.S. District Court in Bangor, Maine.

According to court documents, Dekich asked for Rosenberger's help in 1998 in identifying the subtype of avian influenza afflicting his company's chicken flocks. After receiving the sample, Rosenberger asked one of his lab employees to ship it to a U.S. Department of Agriculture lab in Ames, Iowa, labeling it as an isolate obtained from Delaware. The federal lab identified the virus as subtype H9N2—a strain not known to be fatal to humans. After doing work on its sample, MBL shipped two batches of the vaccine to the Saudi company for $850,000, falsely labeling them as a vaccine for Newcastle disease.

The microbiologist's offense "was serious in that it knowingly introduced a pathogen into the country that could endanger commercial flocks," says George Dilworth, assistant U.S. attorney for Maine. "Anybody in a similar position should know they risk serious repercussions if they engage in such conduct."

Rosenberger's prosecution is yet another warning that researchers must pay closer attention to regulations governing the handling of microbial samples, says Janet Shoemaker, director of public affairs at the American Society for Microbiology. "There is good reason for the government to be concerned about such violations from the public health point of view," she says.

The University of Delaware says it wasn't aware of the case before Rosenberger pleaded guilty but that it has since begun an audit of laboratory procedures. Rosenberger is currently on leave and is due to retire in January after 23 years at the university.

–YUDHIJIT BHATTACHARJEE

DOE LABS

Firing Draws Protest at Los Alamos

A senior scientist fired this week by Los Alamos National Laboratory (LANL) as part of a response to long-standing safety and security problems says he will contest his dismissal. The scientist is one of a dozen workers punished in what Director G. Peter Nanos called a move to restore public "trust and confidence" in the lab and "exercise control over our own destiny."

"We will challenge the [firing] … and try to get it reversed or reduced," says David Cremers, an award-winning laser researcher and 24-year lab veteran who was involved in a laser accident earlier this year that injured an intern. The incident was one of several safety and security lapses that in July prompted Nanos to suspend 23 employees and shut down all work at the 12,000-employee lab in New Mexico (*Science*, 23 July, p. 462). The controversial decision, which has cost LANL millions of dollars per day, came just as the University of California was gearing up to defend its contract to manage the lab for the U.S. government.

Last week, in an e-mail to lab staff, Nanos announced that he was firing four workers, punishing seven others, and awaiting one resignation. One worker was still under investigation, he wrote, and 10 others had been cleared of any wrongdoing. Lab officials would not identify the punished workers but told reporters that three were involved in a July incident in which officials concluded that computer disks holding classified data were missing from a safe in the lab's Weapons Physics Directorate. Politicians briefed on the case say it now appears that the missing disks never existed and were the product of sloppy record-keeping.

Science has learned the names of those involved in the laser accident, however. In addition to firing Cremers, LANL is negotiating the resignation of chemist Thomas J. Meyer, the lab's associate director for strategic research and a member of the National Academy of Sciences. Meyer declined comment.

According to a lab investigation report, the 14 July accident occurred as Cremers was demonstrating to a female undergraduate student a dual-laser technique for vaporizing and analyzing soil samples. With the intern out of the room, Cremers fired one laser to suspend soil particles in a target chamber. Then, with the laser on a nonlasing setting, he invited her back into the room to view the particles. The laser burned a nearly half-millimeter hole in the intern's retina as she bent over the target, damaging her vision. The report concluded that the researchers were not wearing the required eye protection and had ignored other safety rules.

Light lesson. Lab issued safety alert after laser incident.

"I will have responses to some of the committee's findings," Cremers says. Both sides seem to agree that there is no obvious explanation for how the laser fired.

Nanos, meanwhile, says the punishments mark a new era, and officials say the entire lab should be back to work by next month. "We are not the old Los Alamos anymore," he said at a 17 September all-hands meeting. But one LANL researcher says the turmoil has put morale "near rock bottom. Some of us are looking for the exits."

–DAVID MALAKOFF AND CHARLES SEIFE

CREDITS: (TOP TO BOTTOM) KATHY FLICKINGER; LANL

Published by AAAS

EUROPEAN PATENTS

Stem Cell Claims Face Legal Hurdles

Researchers hoping to sew up rights to discoveries involving human embryonic stem (ES) cells in Europe are facing an uphill battle. In recent months, the European Patent Office (EPO) has rejected two applications involving human ES cells and limited a third, arguing each time that the patents would violate the European Patent Convention, which prohibits the industrial or commercial use of human embryos. The decisions are subject to appeal, but the initial rulings signal a wide gap between policies at EPO, which issues patents valid in its 28 member countries, and those of the U.S. Patent and Trademark Office (USPTO), which has granted dozens of patents involving cells derived from human embryos.

The recent cases include one of the fundamental patents in the field, filed by James Thomson of the University of Wisconsin, Madison, and granted in 1998 by USPTO. It covers the techniques used to derive primate ES cells—including those from humans. On 13 July, EPO rejected the application; the patent's owner, the Wisconsin Alumni Research Foundation (WARF), filed an appeal earlier this month.

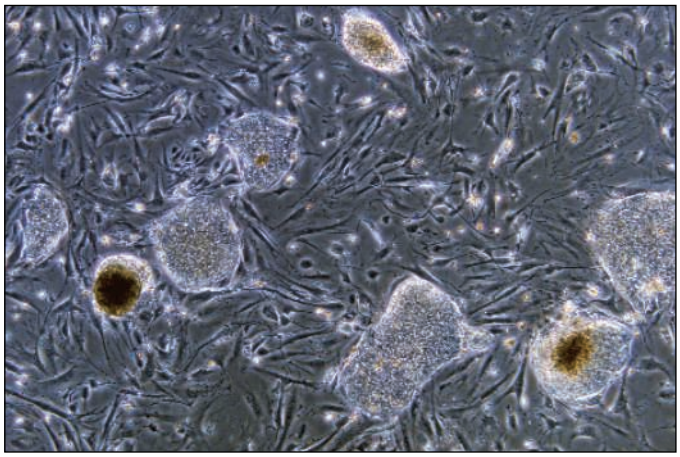

Not patentable? EPO has rejected a University of Wisconsin patent application on methods to derive human ES cells, shown above.

CREDIT: UNIVERSITY OF WISCONSIN, MADISON

The first clue to the office's reluctance came in 2002, when an EPO review panel ruled on a controversial patent involving genetic markers used to identify stem cells. The panel decided that any claims involving human ES cells violated the European Patent Convention (*Science*, 2 August 2002, p. 754). At the hearing, the patent holders, the University of Edinburgh, U.K., and Stem Cell Sciences of Melbourne, Australia, agreed to strike all references to human ES cells, but they have since decided to appeal. George Schlich, a patent attorney handling the case, says that although the remaining claims are useful, the owners thought it was worth asking EPO to reconsider. "It's a big enough point to merit being considered at a higher level," he says. "Lots of people would have been disappointed if it were left there."

In the meantime, before the appeal is heard, EPO patent examiners are taking the review panel's decision as a precedent. Citing the Edinburgh decision, examiners have rejected the WARF patent as well as an application from David J. Anderson of the California Institute of Technology (Caltech) describing a method to isolate neural stem cells from embryonic tissue. The university appealed the decision in March. A third application from Oliver Brüstle of the University of Bonn on a method to differentiate neural cells from mammalian ES cells is still under review, but examiners at hearings in August expressed doubts about claims involving human ES cells.

"It appears the Edinburgh decision is being applied uniformly by the examiners," says Julian Crump of the law firm Mintz Levin in London, who represents Caltech in the Anderson case. Siobhán Yeats, director of examination in biotechnology for EPO, says that although the recent decisions are consistent, final policy "is still in flux" and will be decided by the EPO boards of appeal. She said a decision on the Edinburgh appeal is unlikely before late next year.

The recent decisions probably will not slow the pace of basic research, Crump says, but they will have a chilling effect on any European biotech companies that might have considered investing in embryo-related cell technologies. Biotech companies in general depend strongly on patent protection for their initial worth, he notes, adding, "so to be asked to put it all on ice for a year or two or three, it's extremely difficult."

Determined applicants could still turn to individual countries to guard their intellectual property. Several EPO member countries, including the U.K. and Germany, have more lenient policies. The British patent office has specifically said that methods involving already existing embryo cells are patentable, and the German patent office granted Brüstle a patent in 1999. **–GRETCHEN VOGEL**

ScienceScope

Blair Turns Up Heat on Climate Change

LONDON—U.K. Prime Minister Tony Blair has pledged to make climate change "a top priority" during Britain's presidency of the Group of Eight (G8) leading industrialized nations next year. Current global commitments to reducing carbon dioxide emissions are "insufficient," Blair said in a speech last week, warning that shifts in climate threaten "catastrophic changes for our world."

Blair's G8 strategy aims to build consensus on basic climate science and on ways of accelerating the research and technology needed to meet the threat. As a first step, the U.K.'s Hadley Centre in Exeter will host an international conference next February to consider how much greenhouse gas is too much. But scientists can only identify the likely consequences of warming, warns climate researcher Michael Hulme, director of the Tyndall Centre for Climate Change Research in Norwich. Society and policymakers, he says, must decide what level of climate change is "dangerous."

–FIONA PROFFITT

UCSF Faces Animal Charges

As the fourth-largest recipient of NIH funds and landlord for thousands of research animals, the University of California, San Francisco (UCSF), has long been a target of animal activists. Now, it is a target of charges by the U.S. Department of Agriculture (USDA). Last week, UCSF officials opened the *San Francisco Chronicle* and discovered that USDA is charging the university with 60 violations of the Animal Welfare Act, including operating on a lamb without anesthesia and depriving monkeys of water. "The gravity of [UCSF's] violations is great," USDA alleges, detailing problems with animal housing and veterinary care over a 2-year period between 2001 and 2003. The paper received the complaint from In Defense of Animals, an animal-rights group.

UCSF says it still hasn't received the complaint, which a USDA official says was sent by certified mail on 3 September. But in a statement, the university promised an "in-depth" review of the charges. It said that it had already addressed all of the problems and denied that UCSF researchers had operated on a lamb without anesthesia. The university has just received fresh accreditation for its lab animal facilities, they add. UCSF has 20 days to respond to USDA's charges.

–CONSTANCE HOLDEN

Published by AAAS

SETTLEMENT OF THE PACIFIC

Heaven or Hellhole? Islands' Destinies Were Shaped by Geography

When Polynesians spread across the Pacific, some flourished in what became island paradises. Others deforested the islands they colonized and, as on Easter Island, sank into warfare and cannibalism. Archaeologists have long wondered what went wrong. Now a unique, Pacific-wide analysis teases out the environmental factors that stacked the deck against some colonists.

"It's a nice step forward," says archaeologist Patrick Kirch of the University of California (UC), Berkeley. "They are hitting on some key factors." Archaeologists had studied many of those factors—including rainfall, size of landmass, and degree of isolation—for a few islands, says ecologist Peter Vitousek of Stanford University. But none had taken such a broad, quantitative look. "It's an original and valuable approach," he says.

The work, by archaeologist Barry Rolett of the University of Hawaii, Honolulu, and geographer Jared Diamond of UC Los Angeles, began after Diamond asked Rolett why the Marquesas, unlike Easter Island, had kept their forests. Rolett has worked in French Polynesia for 20 years, examining Polynesians' environmental impact, with a focus on the Marquesas, 1200 kilometers east of Tahiti. But Diamond's question inspired him to cast a wider net.

To answer it, the pair examined 69 islands across the Pacific. Rolett combed through the journals of early explorers such as James Cook to estimate how well forested the islands were at the time of European contact. For each island, they also quantified a range of environmental variables that might make forests fragile or resilient. After crunching the numbers, the two discovered what mattered most: Warmer, wetter islands were more likely to have resisted deforestation, as were big islands, islands whose high, rugged terrain made it hard to grow crops, and those dusted regularly with soil-enriching volcanic ash.

Breadbasket. Islanders retained tree cover on the Marquesas by planting coconut and breadfruit; rugged mountains preserved native forest.

CREDIT: BARRY ROLETT

The model, described this week in *Nature*, suggests that the troubles of Easter Island's colonists weren't entirely their fault. "They were in one of the most challenging situations, on one of the most environmentally fragile islands," Rolett says. (The only islands more fragile were deforested and abandoned before European contact.) Easter Island's isolation was also a factor, the researchers concluded, by making it less likely that domesticated plants could have survived the voyage. None of the most important food trees, such as breadfruit, made it to Easter Island, for example, forcing the colonists to rely on less sustainable slash-and-burn agriculture to grow bananas, sweet potatoes, and sugar cane. In addition, fires used to clear land could easily spread from fields to forests on a small, dry island like Easter.

In contrast, the equally small and dry Marquesas had retained their forests better than the model predicted because the Polynesians there cultivated breadfruit trees, Rolett says. (An island saying goes: "Plant a breadfruit tree when a child is born and no one will ever starve.") With forests providing the main source of food, Marquesas islanders had no need to turn to slash-and-burn agriculture to sustain a growing population. Even today, the Marquesas retain more than half of their pre-contact forest cover.

–ERIK STOKSTAD

RUSSIAN SCIENCE

Academicians React Angrily to Draft Reform Plan

Moscow—After obtaining a leaked document last week, members of the Russian Academy of Sciences (RAS) erupted in an angry discussion about what many viewed as a government plan to slash the research establishment. At a meeting of the RAS presidium here on 14 September, president Yuri Osipov chaired a session on plans—in the works for more than a decade—to trim Russia's network of science institutions. Some argued that the new proposal would eliminate all but 200 of Russia's scientific institutions, including most of RAS's 454 affiliates.

Osipov at first suggested that the group avoid discussing the unofficial document. But RAS vice president Nikolay Plate criticized the reform effort, saying it was designed to take the academy's property. However, a spokesperson said RAS has no plan to send comments on the document to the ministry of science and education.

Andrey Svinarenko, Russia's deputy minister of science and education, confirmed that the paper reflected a presentation he made to the ministry's council. But he argued that it was a reasonable plan, noting that the number of research organizations in Russia has doubled since the 1990s to at least 5000. Svinarenko said that many of these are small, with three to 15 staff members, making them ineffective and costly to maintain.

The draft plan would set a new standard: To receive government research funds, an organization would have to devote at least 35% of its output or services to research or technology development. Any that fail would have to find private money and integrate with universities, be sold, or close down.

Former science minister Vladimir Fortov, now chief of an RAS division, says the reform agenda reflects "an old idea" held by some officials that "there is too much science in Russia." He claims that some "want to eliminate most of our scientific institutions," with a goal of spending money on innovation centers. "The goal is good," Fortov says, but should not be pursued at the expense of basic science. "Innovations must be funded by those who are interested in them, not the government." The best reform would be to support those who continue to do basic research, despite poor funding, low salaries, and lack of equipment.

Svinarenko insists that reform would not damage RAS. But he argues that the government needs to create a nucleus of modern and well-equipped organizations—and that it must concentrate its resources.

–ANDREY ALLAKHVERDOV AND VLADIMIR POKROVSKY

Andrey Allakhverdov and Vladimir Pokrovsky are writers in Moscow.

Published by AAAS

Two new vaccines against a major cause of deadly childhood diarrhea are nearing the market. Will the entire effort crash and burn as spectacularly as it did 5 years ago?

Rotavirus Vaccines' Second Chance

In 1998, the world was poised to launch a major assault on one of humanity's deadliest childhood scourges. After years of development work, Wyeth-Lederle Vaccines and Pediatrics introduced into the United States a long-awaited vaccine to prevent the most common cause of severe, dehydrating diarrhea: rotavirus infection. It quickly became part of the routine immunization package. Within the first 9 months, more than 600,000 infants received drops of the live vaccine, and the company was eyeing potential U.S. sales of more than $300 million a year. Public health agencies around the world were equally ebullient: If they could get the vaccine into the poorest countries, where roughly 85% of deaths from rotavirus gastroenteritis occur, they could save perhaps a half-million lives a year.

Then came a devastating setback. In summer 1999, the U.S. Centers for Disease Control and Prevention (CDC) reported a rare but alarming association between the vaccine and a potentially fatal bowel obstruction, called intussusception. Wyeth immediately pulled the vaccine, RotaShield, from the market, amid consensus that the risk, then pegged at 1 in 2500 children immunized, was far too great in the United States, where diarrheal deaths are exceedingly rare.

The move dashed hopes of using the vaccine in developing countries—even though, with 1 in 200 children there dying of rotavirus diarrhea each year, the benefits would have greatly overwhelmed the risks. "A rare event in the United States meant the world would not get the benefit," said Roger Glass, a longtime rotavirus researcher and head of the viral gastroenteritis section at CDC, at a recent meeting in Mexico City.* "It challenged our vision of equity."

Now the global medical and scientific community has a second chance to get it right. Two new rotavirus vaccines are in the final stages of clinical trials, and evidence so far suggests they are safe and effective. The manufacturers, GlaxoSmithKline Biologicals (GSK) in Belgium and Merck & Co. in Whitehouse Station, New Jersey, are bullish; GSK plans to introduce the vaccine first in Mexico in 2005. The Global Alliance for Vaccines and Immunizations (GAVI)—created to strengthen immunization in developing countries—is throwing its money and clout behind the vaccines, and various public health agencies are subsidizing clinical trials. This private-public venture is being heralded as a model for how to accelerate the introduction of other, badly needed vaccines to the poorest countries of the world.

Yet, despite all this heart, muscle, and money, success is far from ensured. First, both companies want to recoup their substantial investments—$500 million for GSK and perhaps $800 million to $1 billion for Merck. How can they do that and offer the vaccine at an affordable price in poor countries? The RotaShield debacle has also left a legacy of doubt and uncertainty that will require additional testing, and time, to dispel. Complicating matters, the disease itself—rotavirus gastroenteritis—is hardly a household word, and health ministers may not be willing to spend scarce dollars to fight something they have never heard of.

Then there are nagging doubts about whether a live oral vaccine based on one attenuated strain (the GSK product), or several (Merck's), can protect against the bewildering array of rotavirus serotypes, or varieties, some of which have just recently been detected. Both manufacturers insist they can. Finally, although the vaccines have done well in trials in Europe and Latin America, their effectiveness where they are needed most—in the poor-est parts of Asia and Africa—has yet to be demonstrated.

The world may have a second chance, but the stakes are high, and a second failure would be a crushing blow.

Grim picture. Deaths from rotavirus gastroenteritis are clustered in the developing world. Until recently, the toll was pegged at 440,000 deaths a year (above); new estimates put it at 608,000.

CREDITS (TOP TO BOTTOM): CDC; SOURCE: R. GLASS/CDC

Ubiquitous and deadly

Highly contagious, rotavirus hits hard and fast. Within 18 to 24 hours of exposure, children develop fever, violent vomiting, and diarrhea that, if left untreated, can quickly lead to death. In severe cases, the only recourse is intravenous fluids.

The virus is also ubiquitous; all children everywhere are infected in the first few years of life. But its toll varies enormously. In the United States, rotavirus gastroenteritis causes an estimated 70,000 or more hospitalizations a year, a half-million doctor and clinic visits, and 20 to 40 deaths. In poor countries, however, where children may be

* 6th International Rotavirus Symposium, 7–9 July 2004.

Published by AAAS

Young victims. Severe rotavirus infections occur mostly in children under age 1 or 2. Here, an infant hospitalized with rotavirus last February sleeps in San Rafael hospital about 10 kilometers west of San Salvador, El Salvador.

undernourished, suffer from multiple gastrointestinal infections, and lack ready access to a hospital, the virus is far more deadly. Exactly how dangerous is tricky to pin down, though, as physicians rarely test for it.

Until recently, the estimate was that rotavirus infection causes about 22% of all severe cases of diarrhea, accounting for about 440,000 of the 1.56 million deaths from diarrhea each year. But new surveillance data from an international effort to gauge the disease burden suggest that's a gross underestimate. As CDC epidemiologist Umesh Parashar reported at the Mexico City meeting, rotavirus was detected in 60% of stool samples from children hospitalized with severe diarrhea in Vietnam; 41% in China; 56% in Myanmar; and 29% in Hong Kong.

Based on those and other data, Parashar and colleagues now estimate that rotavirus accounts for 39% of all cases of severe diarrhea, which translates into 608,000 deaths worldwide each year, mostly in children under age 1 or 2. After studying the disease for decades, Glass had expected few surprises from the surveillance data, but "the results blew us away," he says. In the United States as well, asserts Paul Offit, chief of infectious diseases at Children's Hospital of Philadelphia, Pennsylvania, and one of the developers of the Merck vaccine, prevalence is vastly underestimated. "It's the second most common reason kids come to the hospital in the winter in Philadelphia," he says. "The disease is a big deal in the United States."

Abrupt demise, long recovery

Because very few children die of rotavirus gastroenteritis in the United States, some people were skeptical that RotaShield would be profitable. Yet despite the steep cost ($38 for each of three doses), the vaccine had a huge—and brief—success.

Its downfall began on 16 July 1999, when CDC reported 15 cases of intussusception—a rare defect that makes the bowel fold like a telescope—associated with the vaccine. If recognized early, the obstruction can be surgically treated, but it can be fatal. The risk, originally pegged at 1 in 2500 children immunized, or 1600 excess cases of intussusception a year, was deemed unacceptable in the United States, where only 1 in 100,000 children die of rotavirus infection. CDC withdrew its recommendation, and Wyeth pulled the vaccine in October 1999.

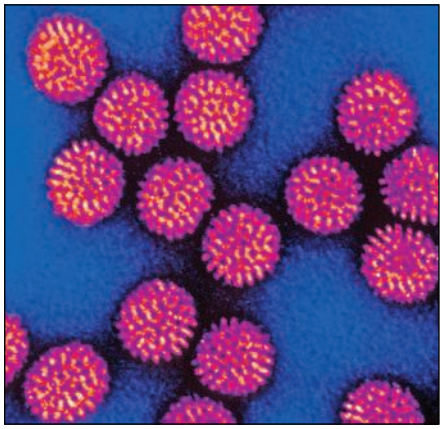

Quick-change artist. Rotavirus comes in many serotypes, some just recently detected, posing challenges to vaccine design.

The decision sparked an outcry among international health experts, who felt deprived of a potent weapon. Albert Z. Kapikian, one of the developers of RotaShield at the U.S. National Institute of Allergy and Infectious Diseases (NIAID), argued for a permissive recommendation that would enable U.S. physicians to use the vaccine at their discretion. That would have sent a powerful message to developing nations, he says, and perhaps spurred its adoption there. "But it fell on deaf ears," says Kapikian. When the World Health Organization (WHO) held a pivotal meeting in 2000 to assess whether and how developing countries might introduce RotaShield, health ministers gave it thumbs-down. "They said they didn't want their population to be seen as second-class citizens. If it was not good enough for U.S. kids, it was not good enough for their infants either," recalls Kapikian.

RotaShield's demise prompted some soul-searching at Merck and GSK, both of which had already invested millions in their rotavirus vaccines. In the end—with some encouragement from WHO, CDC, and other public health agencies—both decided to proceed, gambling that their vaccines would be safe and profitable and taking very different paths both scientifically and commercially.

Both efforts got a boost in 2002 when GAVI declared rotavirus vaccines one of two priorities and gave the new Rotavirus Vaccine Program (RVP) in Seattle, Washington, $30 million over several years to speed their introduction to the poorest countries of the world. Tore Godal, GAVI's executive secretary, argues that the world can no longer accept the status quo, when a lifesaving vaccine is introduced first in the United States but doesn't make it into developing countries for 20 years

CREDITS (TOP TO BOTTOM): CDC; LUIS ROMERO/AP; CDC/PETER ARNOLD

Published by AAAS

or more: "We've really got to reduce that gap."

For GSK and Merck, the first order of business has been to show that their vaccines do not trigger intussusception—a task that turned out to be hugely complicated. No one knows why RotaShield caused intussusception, although the link is real, concedes Lone Simonsen, an epidemiologist at NIAID. The oral live vaccine was made by combining three human rotavirus serotypes and one rhesus serotype. In retrospect, some suspect that the simian virus was the problem. Whatever the cause, since the vaccine was withdrawn, several studies have suggested that its risk was far lower, around 1 in 10,000. In Mexico, Simonsen reported unpublished data suggesting the risk would be as low as 1 in 40,000 if the vaccine were administered in the first 2 months of life, before intussusception from natural causes begins to rise.

But that good news presents a quandary: Trying to prove the absence of a very small risk has forced the companies to conduct some of the most massive and expensive clinical trials ever undertaken. Merck's phase III trial involves 68,000 subjects and counting, mostly in the United States and Finland, with smaller numbers in nine other countries; GSK's phase III trial has enrolled more than 63,000 in 11 Latin American countries and Finland. Both are being watched closely by independent safety panels that would halt the trials if they saw an increased risk of intussusception.

To John Wecker, who runs RVP from the Program for Appropriate Technology in Health (PATH) in Seattle, the ongoing trials bode well: "The companies are moving forward. I assume they have judged the risks acceptable."

Offit is encouraged that neither of the new vaccines seems to cause the mild side effects associated with RotaShield, such as fever and vomiting, much less intussusception. "It is unlikely they will," he adds, because the new vaccines are "so biologically different" from RotaShield. (Merck's is a human-bovine reassortant, and GSK's is a monovalent human vaccine.) Even so, he adds, "we won't be convinced until we give it to several million kids."

Both Merck's Penny Heaton and GSK's Beatrice de Vos agree they can't rule out a risk conclusively until the vaccines are approved and tracked in large postmarketing studies. And should the two new vaccines be found to pose a small risk, most experts would still recommend their widespread adoption in developing countries. "It is imperative that we rethink the risk-benefit equation," said Offit at the meeting.

Huge trials. GSK's Rotarix and Merck's RotaTeq are being tested in some of the largest and most expensive clinical trials ever. At top, the first Nicaraguan baby to receive Rotarix.

But will they work?

Data so far indicate that both the GSK and Merck vaccines offer strong protection against severe disease in the United States, Europe, and Latin America. But it is unclear whether those results hold in other parts of the world. There are two issues.

One is cross-protection. Ideally, a vaccine should protect against the well-known and emerging strains of rotavirus. Glass is particularly concerned about serotype G9, which ongoing surveillance efforts show is becoming increasingly important across Asia, and G8, gaining prevalence across Africa. "We didn't even know G9 existed when these two vaccines were designed," he says. Both companies express confidence that their products will be broadly effective, although they are banking on very different scientific strategies.

GSK went with a monovalent human vaccine, explains de Vos, director of clinical development, because it mimics the natural immune response that follows initial rotavirus infection. Infants are repeatedly exposed to a variety of strains of rotavirus, but only the first one or two episodes develop into life-threatening disease. GSK's vaccine, Rotarix, is based on an attenuated version of the prevalent G1 serotype. At the meeting, de Vos reported that Rotarix has shown significant protection against G1 and non-G1 types, including G9. "There is clear cross-protection," agrees Glass, who has seen GSK's preliminary data. "But its efficacy against a full range of strains, especially G2, remains to be demonstrated."

The same is true for Merck's human-bovine vaccine, RotaTeq, which contains the five serotypes that account for some 75% of the global burden: G1, G2, G3, G4, and P1. Again, says Glass, there is good evidence that RotaTeq protects against these serotypes, but no evidence that it protects against G9.

The second and perhaps overriding concern is that there are simply no data to show that either vaccine works in the poorest countries of Asia and Africa, where one child dies each minute from rotavirus infection. "We need to make testing in Africa and Asia a global priority," says Glass. But even then, he cautions, "we won't have these studies for several years."

Experience with other live oral vaccines in poor countries provides reason for concern, says Glass. "We know when we put a live oral vaccine into the mouths of babes in poor countries, it is not processed the same way as in kids in Finland. We saw that with oral polio vaccine and cholera vaccine," both of which require many more doses in, say, India or Africa, to induce the same immune response. And some earlier candidate rotavirus vaccines "were unsuccessful in African kids and less successful in Latin American kids."

This is where Wecker's RVP and other global health agencies are struggling to make a difference. Even before RVP was created with GAVI funding, a consortium of agencies, including CDC, the U.S. National Institutes of Health, WHO, the U.S. Agency for International Development, and the Children's Vaccine Fund, had been helping implement efficacy trials for Africa and Asia. "They won't do it on their own," says Godal of GAVI. In 2005, with support from RVP and others, GSK will conduct two trials in South Africa and Bangladesh. Merck is also exploring developing country trials with RVP, GAVI, the Pan American Health Organization (PAHO), and others agencies.

Paying customers first

Sometime next year, results from the large clinical trials should be released. Then comes the tough challenge of getting the vaccines approved and, eventually, to the countries that need them most. Both GSK and Merck plan to recoup their investments by charging more for the vaccine in wealthy countries while negotiating a guaranteed supply and lower price for government purchase in poorer countries. Just how low is key, says Jon Andrus of PAHO, who notes that Latin American coun-

CREDITS (TOP TO BOTTOM): FRANCIS J. VAN BRUSTEGHEM; GLAXOSMITHKLINE

tries now struggle to pay $3.86 a dose for a combination childhood vaccine.

GSK has decided not to gamble on the U.S. market—at least for now. Instead, it is taking the unusual route of launching the vaccine first in Mexico—which has approved the vaccine even before clinical trials are complete—and then across Latin America. "We are doing the reverse of what's been done in the past," said Jean Stephenne, president and general manager of GSK Biologicals, at a press conference in Mexico. "We are going where the need is greatest. … In Latin America we can save thousands of lives; in the United States we won't."

GSK is also starting in a middle-income country with a substantial private market to support a two-tiered price for the vaccine. So far, Stephenne is mum on the price, saying only that it will be "not unreachable" and will be based on country income.

This new model is not problem-free, however. For one, Mexico's decision to license GSK's drug based on preliminary data has raised eyebrows among vaccine experts. "It sets a bad precedent," says one. Although GSK hopes Mexico's example will speed approval across Latin America, Wecker questions whether Mexico's decision will carry the same weight as a formal blessing from the U.S. Food and Drug Administration (FDA).

Stephenne isn't ruling out the U.S. market, but, he concedes, liability is a key factor. "If by unluck there is one case of intussusception, we will have to prove it is not linked to the vaccine—that is a risk we didn't want to take." In 2005, GSK will apply for approval in Europe, he said. And then, after discussions with FDA, the company will decide whether to apply in the United States, perhaps in 2010.

Merck, by contrast, is taking a more traditional route, testing extensively in the United States and Europe and seeking approval there in the second half of 2005. As Heaton explained, because the risk of intussusception was unknown, the company wanted to test the vaccine first in countries with high standards of medical care, should a problem arise. An added benefit, she says, is that FDA approval speeds acceptance globally. Heaton and others at Merck say the company is committed to introducing the vaccine into developing countries as soon as possible.

Both companies are counting on partnerships with GAVI and other public health agencies to pull it off. PAHO, for instance, will play a key role in introducing the vaccines into Latin American countries that can't afford to pay the same price as private patients in Mexico. Once all the safety data are in, an independent advisory board to PAHO will evaluate both vaccines. If the organization recommends that countries include rotavirus vaccine as part of routine immunization, it will then negotiate a uniform and affordable price for public health programs across the continent, says Andrus.

Similarly, once the vaccines have been approved, in perhaps 5 to 7 years, then WHO could make a global recommendation in favor of rotavirus vaccines. GAVI would then support the vaccine's introduction "in all the poorest countries where it makes epidemiological sense," says Godal. GAVI is already working with both GSK and Merck to set a price for the 75 poorest countries of the world. What's an acceptable price? "All I can say is $10 for a set of immunizations is too much," says Godal. "No price is affordable in Africa," adds Wecker.

If the companies and donors can find a way to make this new model work for rotavirus vaccines, which have the benefit of being relatively well understood and tested, then perhaps it can also speed the delivery of vaccines against tuberculosis, malaria, and AIDS. If the model doesn't pan out for rotavirus, however, poor countries may be waiting a long time before those newer vaccines arrive.

–LESLIE ROBERTS

Paleontology

China Clamps Down on Mining To Preserve Cambrian Site

Strip-mining for phosphate imperils Chengjiang, a vast and remarkably rich site of early Cambrian fossils

The Chengjiang region of China's southwestern Yunnan Province has been a boon for scientists trying to understand the Cambrian explosion of life forms of some 500 million years ago. One key finding, a 3-centimeter-long fish, pushed back the first appearance of vertebrates by an astounding 55 million years. Another prized trophy, an invertebrate named Yunnanozoon, may be the oldest example of a chordate, the group that gave rise to vertebrates, although other scientists argue that Yunnanozoon could be part of an even more primitive group.

Unfortunately for scientists, however, the discovery of this vast bed of well-preserved, soft-bodied fossils coincided with the discovery of valuable phosphate laced throughout the site. The resulting strip-mining has been a boon for the economy of one of China's poorest provinces. And it has created tension between two groups wanting to dig for different resources in the same area.

Scientists scored a decisive victory recently when the Yunnan provincial government ordered the last of a number of major strip-mining operations around the Mount Maotian fossil site to cease operations by 1 October. Unfortunately, the closures come too late to prevent the Mount Maotian site from being left as an island of preservation amid a sea of environmental destruction—an important criterion when seeking the type of designation from international preservation organizations that China covets to attract tourists. And it does nothing to control mining around other fossil sites within the vast Chengjiang formation in other jurisdictions.

"It makes my heart bleed," says Hou Xianguang, a paleontologist at Yunnan University in Kunming, who is credited with finding the first Chengjiang fossils at Mount Maotian in 1984. Hou and his colleagues hope that protection will be extended to other sites, allowing scientists to continue to pursue hot topics such as the origin of vertebrates and the evolutionary relationships of marine animals.

The Cambrian explosion began some 540 million years ago, when a multitude of new life forms bearing the body plans of

CREDIT: QIN QING

Urgent plea. Paleontologist Hou Xianguang hopes to keep mines away from fossil sites.

Published by AAAS

Unwelcome neighbors. Phosphate strip mines in the Mount Maotian region abut the Chengjiang field station in Yunnan Province in southwestern China.

CREDIT: QIN QING

most modern animals first arose. Some 10 million years later, what is now the Chengjiang formation was the bed of a vast shallow sea, and the bodies of these diverse new marine creatures were entombed in the sediment. Subsequent geologic movements pushed the formation above sea level and formed an arid, sparsely vegetated region of rolling hills while also forming pockets of phosphate ore.

Ironically, these two treasures were discovered at about the same time. "When I was there in 1984 they had just begun surveying the potential [phosphate] reserves," Hou recalls, and digging for both fossils and phosphate has accelerated ever since.

The Chengjiang formation stretches over some 10,000 square kilometers. Hou says three groups are currently working three sites separated by up to 50 kilometers, and several more fossil-laden sites are yet to be explored. The fossils turning up are "fantastically interesting and important," says Simon Conway Morris, a paleontologist at Cambridge University in the United Kingdom. And the Chengjiang formation is older than any other Cambrian-era fossil site yet discovered, giving insights into the earliest appearances of these new life forms. "In terms of the scientific problems of the Cambrian explosion, [the Chengjiang fossils] are extraordinarily interesting," Conway Morris says.

In 1999, Conway Morris and colleague Shu Degan of Northwest University in Xi'an reported the oldest vertebrate yet found, a 3-cm fish some 530 million years old. And Conway Morris believes more exciting finds are on the way. "People are really just scratching the surface at the moment," he says.

Mining operations have grown at a similar pace, and phosphate mining and processing provide roughly two-thirds of the annual tax revenues of Chengjiang County, which includes the Mount Maotian site. Dozens of enterprises have licenses to strip-mine specific tracts. And although the Chengjiang formation is vast and the mining is limited to certain regions, scientists worry that companies are encroaching on known fossil beds and disrupting others yet to be found.

The problem is acute in the Mount Maotian area, where Chen Junyuan, a paleontologist who heads the Chengjiang work station of the Nanjing Institute of Geology and Paleontology (NIGP), says, "the digging is now just tens of meters away" from the spot where the first Chengjiang fossils were found. Officials of the De'an Phosphate Chemical Co., the mining operator, declined interview requests.

Government officials have made some progress in protecting the Chengjiang fossils. An 18-square-kilometer tract around the Mount Maotian site and NIGP's nearby field station was one of the first 11 National Geological Parks designated by the Ministry of Land and Resources in 2001. But protection only extends to the park border. Li Minglu, an official in charge of environmental protection at the Ministry of Land and Resources, says the ministry can't intervene unless the mining crosses into the park itself.

That stance doesn't satisfy Hou. "What sort of a park is it if it is surrounded and nibbled at by mining explosions, garbage, and smoking factories?" he asks. He would like to see mining controlled and kept away from known fossil sites.

NIGP's Chen says the local government was at first reluctant to do anything about the mining because of its importance to the local economy. But local authorities had a change of heart when they decided to promote tourism by raising international recognition of the importance of Mount Maotian. One part of the plan to protect it would be a listing as a United Nations Educational, Scientific, and Cultural Organization (UNESCO) World Heritage Site. Chen Jiayou, manager of the county's Administration of the Chengjiang Fossils, says the province, Yuxi City, and the county are cooperating and have already spent about $2.5 million preparing their bid.

The next step is to gain the support of national officials, because applications to UNESCO must come from national governments. Meanwhile, Chen says they recognize that success will ultimately depend not only on the significance and protection of the site itself but also on having a well-preserved natural buffer zone around it. That would require an end to strip-mining.

Guo Yongming, an official working with the mining administration section of Yuxi City, says some of the operators had valid licenses to mine that were issued before the importance of the fossils was recognized. Before any mines could be closed, Guo says, "we had to agree on compensation." Some 25 mines were closed over the last several years, including two in the vicinity of Mount Maotian. The government has spent $7.5 million on legal expenses and compensation for mine operators with valid licenses. The one remaining mine in the Mount Maotian area had been scheduled to cease operations by the end of October, but the provincial government has moved up the date to 1 October.

Hou welcomes the move but wishes it had come sooner. Recognizing that time was running out, the mine operators have been trying to maximize output. "The mining has been very aggressive over the last 3 years," Hou says.

Meanwhile, mining activities continue as usual in other parts of the region, including near the Haikou area where Hou's team and a group from Northwest University are currently digging. Hou doubts that the local Kunming city government will move to control the mining anytime soon. "They are not trying to boost tourism," he says. Even so, he hopes local officials will eventually curtail mining operations before the shovels come too close to his precious fossils.

–DENNIS NORMILE AND XIONG LEI

Xiong Lei writes for *China Features* in Beijing.

Biology and the Inkjets

Tissue engineers and other biologists experiment with cheap inkjet printers

Don't throw away that out-of-date inkjet printer. Older model inkjets, although lacking in the newest bells and whistles, are finding second lives as inexpensive robots that can dependably dispense minuscule amounts of growth factors and other proteins and even whole cells, in any pattern, gradient, or grid that can be drawn. Whether it's enabling a few thousand crystallization experiments, depositing gradients of attractants and repellants to study how growing nerve cells respond, or creating a grid of mammalian cells for high-throughput screening, that printer gathering dust could be just the tool for the creative biologist.

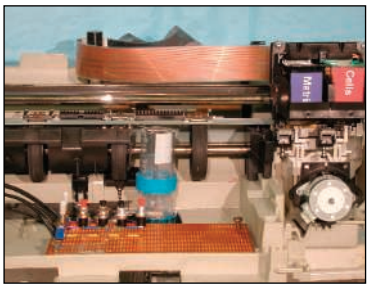

Ready-made robot. Printers of the 1990s are being reconfigured to lay down biomaterials.

Inkjets can print repeatedly over a given area, offering the ability to create three-dimensional constructs simply and reproducibly. Older versions from the mid-1990s, which tend to have wider nozzles than newer ones, are particularly good at spitting out molecules and cells. For example, tissue engineers interested in studying cell interactions or creating artificial skin, blood vessels, and whole organs, are using inkjets to deposit precisely ordered layers of different cell types, complete with growth factors and extracellular matrices. In a prototype experiment published recently in the January 2005 issue of *Biomaterials*, bioengineer Thomas Boland of Clemson University in South Carolina and his colleagues have used a modified Hewlett-Packard (HP) inkjet to apply viable mammalian cells to a variety of "papers," including collagen gel. The Clemson team has also printed sheets of skin cells that could be used in skin grafting.

Although inkjet technology has already found widespread use in a variety of nonpublishing applications, such as microelectronics manufacturing, its potential in cell and molecular biology research is only now coming into focus. "This is a very cool use of inexpensive technology," says Jeffrey Esko, a molecular biologist at the University of California, San Diego.

Esko, who in the mid-1970s invented the widely adopted replica-plating technique for making copies of mammalian cells growing in petri dishes, says that inkjet printing could have an equally huge impact on biology. "Using any one of a number of cell lines, you could screen an entire genome for mutations on a single piece of paper or study how different growth signals affect the possible differentiation pathways of stem cells," he explains. "Inkjet printing really opens up the possibility of doing some amazingly complex experiments that have been out of our reach until now."

Inkjet technology has entered the biology lab because of its ability to generate, under surprisingly benign conditions, tiny droplets of reproducible size and deposit them at a spot with positional accuracy of 100 micrometers or better. Each printer comes with its own software program, known as a printer driver, that translates computer-generated graphical information into a specific pattern of droplets.

Depending on the brand, inkjets use one of two technologies. HP printers heat the material in the ink cartridges to create a meniscus, which pinches off to form a droplet. Although many biologists initially assumed that the heat needed to generate the droplet would damage proteins and cells, Boland found that the internal temperature of a droplet rises a mere 10°C. "Proteins and cells come through just fine," he says. Epson and Canon printers use acoustic energy, rather than heat, to generate the meniscus. An advantage of this approach is that it is possible to create much smaller drops—of a picoliter or less—by proper tuning of the acoustic frequency.

To study how muscle cells respond to multiple cues, Ryoichi Matsuda and colleagues at the University of Tokyo have employed a Canon inkjet to create arrays of various growth factors. In one recent study, the researchers deposited 16 different combinations of two growth factors onto a polystyrene sheet and documented the growth of muscle cells placed at each site. Although the data, published last year in *Zoological Research*, revealed no surprises, the experiment did demonstrate how easy it is to design and analyze a cell's response to multiple, simultaneous signals, Esko says.

To lay down mammalian cells, along with growth factors and immobilizing matrices, in layers, a step toward what Boland calls "organ printing," he and his colleagues are using a basic HP printer modified so that the printing substrate can pass straight through the printer without curling around a roller. They also rewrote the printer driver to adjust for the fact that the viscosity of biological materials, which affects droplet size, is not uniform. "We want to try printing multiple cell types in a three-dimensional matrix to see if we can mimic the structure of a tissue and to see if the cells will grow in the right orientation to one another," Boland explains. His group is attempting to deposit nerve and muscle cells next to one another to see if they form functional neuromuscular junctions.

Other investigators are making more significant modifications to their printer. Raul Cachau, a chemist at the National Cancer Institute in Frederick, Maryland, and Eduardo Howard of Argentina's Instituto de Fisica de Liquidos y Sistemas Biologicos have tuned the acoustic energy generator on an Epson printer to create picoliter-size droplets for crystallographic studies. "When you have a few micrograms of some novel compound, it's hard to determine the optimal conditions for growing crystals," he says. "But with the inkjet printer you can conduct hundreds of experiments ... with minuscule amounts of compound."

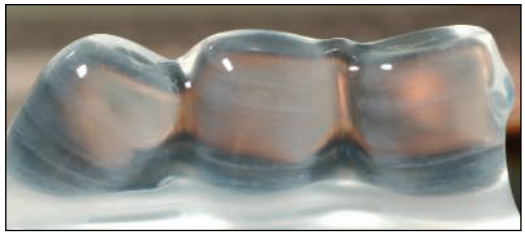

Constructed tissue. These three tubes of endothelial cells were put down in layers by a modified desktop printer.

Cachau's goal is to develop the technology so that labs, particularly those in less developed countries, can build their own instrument for a few hundred dollars. Of course, as anyone who owns an inkjet printer can attest, the printer is cheap. It's the ink that's expensive.

–JOE ALPER

Joe Alper is a writer in Louisville, Colorado.

CREDIT: T. BOLAND/CLEMSON UNIVERSITY

Published by AAAS

A Bit of Icy Antarctica Is Sliding Toward the Sea

The latest gauging of West Antarctic glaciers confirms that when the ocean eats at one end of a glacier, it can draw far-distant ice toward the sea, with potentially dangerous consequences

As the global climate warms up, glaciologists' big worry is polar ice, especially the ice sheet of West Antarctica, the muscular arm that juts from the huge mound of ice in East Antarctica. They aren't concerned about warmer air per se; even the thinner West Antarctic Ice Sheet (WAIS) would hold out against its effects for millennia. But researchers have long wondered whether warming could somehow get at the WAIS indirectly, destabilize it, and send its ice into the sea to melt, raising sea level up to a disastrous 5 meters in a few centuries. With the publication online (www.sciencemag.org/cgi/content/abstract/1099650) of the latest survey of glaciers flowing into West Antarctica's Amundsen Sea, most glaciologists now allow that there probably is a way for warming to accelerate the movement of at least some of the WAIS ice toward the sea.

Glaciologist Robert Thomas of NASA contractor EG&G at the Wallops Island facility in Virginia and colleagues confirm that the half-dozen glaciers flowing into the Amundsen Sea have been getting thinner and thinner the past 15 years, and that one of them—the Pine Island Glacier—has been flowing faster and faster for more than 100 kilometers inland. "It's not necessarily a sign of [WAIS] collapse," says glaciologist Richard Alley of Pennsylvania State University, University Park, "but it could lead to a collapse."

However, no one can say whether the recent glacial acceleration will continue, whether it could reach more distant ice if it does continue, or whether other, more voluminous parts of the WAIS could suffer similar effects. "We're not running for the hills," says Alley, but "this is the wake-up call for the scientific community to get serious about it all."

Since the start of the 1990s, glaciologists have been closely monitoring the flow of ice from the Pine Island Glacier and nearby glaciers using motion-sensing radar, ice-penetrating radar, and laser and radar altimeters mounted on satellites and aircraft. By the end of the decade, the ice in at least some glacial channels nearing the sea seemed to be thinning and accelerating.

To learn more, Thomas and his colleagues, in cooperation with Centro de Estudios Científicos in Valdivia, Chile, rode an instrument-laden Chilean Navy P-3 aircraft 2700 kilometers to the remote Amundsen Sea coast. The onboard ice-penetrating radar found that the ice is far thicker than thought, on average 400 meters deeper than previously estimated near the coast. Combined with satellite radar velocity estimates from the late 1990s, those greater thicknesses implied that the glaciers are hauling away about 253 cubic kilometers of ice per year. That's about 90 cubic kilometers more than accumulates each year from snowfall.

By analyzing recent satellite radar data, Thomas and colleagues confirm that ice withdrawals have been accelerating, at least through the Pine Island Glacier, the largest of the group. They calculate that it sped up by 3.5% between April 2001 and early 2003, making for a 25% increase since the mid-1970s. And the drawdown is not limited to areas near the coast. The P-3 data show a thinning, presumably induced by the faster flow, that extends along the main trunk of the Pine Island Glacier and averages about 1.2 meters per year between 100 and 300 kilometers inland.

Ice parade. Some West Antarctic glaciers are flowing faster to the sea, breaking into more icebergs, and raising sea level faster.

These latest results from West Antarctica confirm an unsettling view of glacier behavior. For 30 years, glaciologists have debated whether one part of a glacier can "feel" what's happening in a distant part of the same glacier. At the coastal end of the Pine Island Glacier, for example, warmer water seems to be melting the underside of the glacier's floating ice shelf (*Science*, 24 July 1998, pp. 499 and 549), pushing landward the point at which the advancing glacier floats off the sea floor.

If an ice shelf pinned against an embayment's shore and floor helps slow a glacier's flow—as was hypothesized in the 1970s—and if changes at the coast could make themselves felt far up the glacier, then the Pine Island Glacier's so-called grounding line retreat would accelerate glacier flow well upstream. The researchers think that's what they're seeing. "I'm convinced the glacier feels what is happening a long way away," says Thomas. Similar accelerations struck after two other floating ice tongues recently broke up in West Antarctica and Greenland (*Science*, 30 August 2002, p. 1494).

"It's a very impressive piece of work," says Alley. "Too many different lines of evidence are agreeing now" for them to be wrong about the thinning or the speedup of the past 10 to 15 years. "Ice shelves may well play a role in the dynamics of glaciers," agrees geoscientist Michael Oppenheimer of Princeton University in New Jersey. But the next problem is that "we don't know why things are melting away at Pine Island Glacier." Oceanographers can't say whether the ocean warming that seems responsible is part of a cycle that will reverse itself or a long-term trend driven by greenhouse warming. And they can't say whether the WAIS's two largest ice shelves—the Texas-size Ronne and Ross ice shelves—could be melted as well.

Even if glaciologists knew what the ocean was going to do, their models for predicting glacier behavior are still so rudimentary that they can't say whether more distant, slower moving ice feeding the main ice streams will respond too. So plenty of uncertainties remain, notes Oppenheimer, but he adds, "I'm starting to get worried."

–RICHARD A. KERR

CREDIT: CECS/NASA ANTARCTIC PROJECT

Published by AAAS

Reconstructing a Star's Demise, Bit by Exploded Bit

NEW ORLEANS, LOUISIANA—The energetic universe jazzed 440 scientists here from 7 to 11 September at the American Astronomical Society's High Energy Astrophysics Division meeting.

The death of a giant star is both glorious and messy. A supernova sprays freshly forged elements into space in an inside-out radioactive jumble, while shock waves reverberate through the expanding storm of matter. The entire hot cloud glows in radio waves, optical light, and x-rays. Now, the most exquisite x-ray view yet of a supernova's remains has fired up astrophysicists who yearn to retrace the explosion—a process still shrouded in mystery.

The debris forms a well-known object just 10,000 light-years away called Cassiopeia A, first spotted in the late 17th century. As the youngest and brightest supernova remnant, "Cas A" is a natural target for x-ray satellites. Earlier this year, NASA's Chandra X-ray Observatory stared at Cas A for 11.5 days. The detailed maps thrilled astrophysicists at the meeting. "We won't have another image with this resolution for some time," says Una Hwang of NASA's Goddard Space Flight Center (GSFC) in Greenbelt, Maryland.

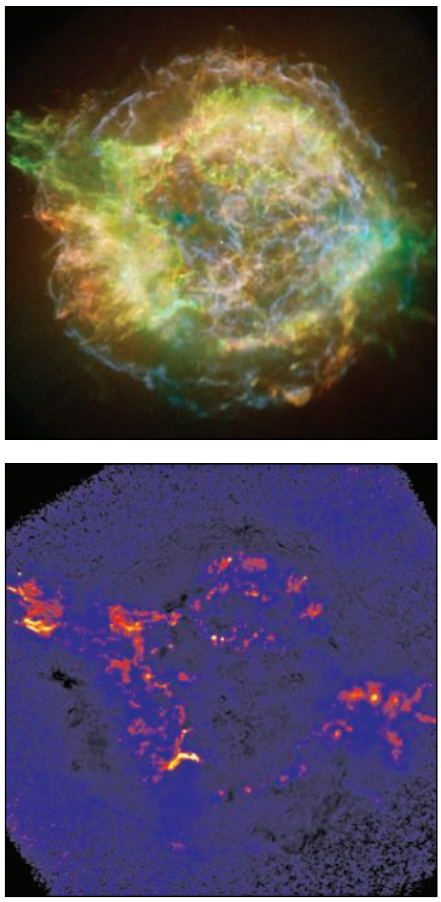

It's a blast. X-rays from Cassiopeia A reveal shocked elements (*top*) and two jets.

Chandra's sharp vision exposed the outermost blobs of expelled matter, still racing at nearly 10,000 kilometers per second. On opposite sides of the remnant, the silicon-rich blobs form two prominent jets, one of which was barely seen in previous images. Such double-sided jets—junior versions of the ones thought to blast outward from gamma ray bursts—may arise more commonly than expected in ordinary supernovas, Hwang says.

In some supernova models, outflows of matter escape into nearby cavities of mostly empty space. But faint knots at the tip of one jet in Cas A are so hot that they clearly are blasting through denser material around the original star, says astrophysicist J. Martin Laming of the Naval Research Laboratory in Washington, D.C. "This really clinches the observation of a reverse shock wave [from the pressure of the surrounding medium] heating the jets," he notes. That more violent physical picture will lead to a firmer calculation of how much energy the star channeled along those directions.

Chandra's image of a bright dot within Cas A—presumably a neutron star formed when the star's core collapsed—shows that the object is darting away from the remnant's center at 330 kilometers per second. Although the speed isn't unusual, the direction is strange. "We'd expect the kick to be aligned with the jets, but it's perpendicular to them," Hwang says. "It's a bit of a puzzle." This and other aspects of the explosion's dynamics will open "a window on neutron star birth," comments astrophysicist David Helfand of Columbia University in New York City.

Fully re-creating the star's immolation from the Chandra data—and images at other wavelengths—will take years. But it's a worthy goal, researchers say, because the elements of our world came from such explosions long ago. "This is a tremendously exciting data set," says astrophysicist Michael Stage of the Massachusetts Institute of Technology (MIT) in Cambridge, noting that x-ray spectral patterns reveal the elemental mixture of each burning knot of gas. "For the first time, we have enough x-ray counts to get really good spectra in regions where substantially different physics is going on."

X-ray Flares Size Up a Neutron Star

The densest stuff in the universe—matter just shy of vanishing into a black hole—inhabits the weird interiors of neutron stars. Created at the hearts of supernovas, these objects crush more than a sun's worth of mass into balls just 20 kilometers wide or so. But that "or so" vexes scientists. Knowing the exact size of a neutron star is critical to determining whether its core consists merely of neutrons crammed together or something more exotic, such as hypothesized "strange quark matter."

New results announced at the meeting narrow the possible diameters for one neutron star halfway across the Milky Way: 19 to 30 kilometers, with a most likely value of 23 kilometers. That range doesn't yet allow theorists to eliminate any models for ultradense matter, but it shows that earlier, disputed measurements were probably on track. "There are uncertainties, but this one piece of information is terribly useful," says astrophysicist Madappa Prakash of Stony Brook University in New York.

To derive their estimate, graduate student Adam Villarreal of the University of Arizona, Tucson, and NASA GSFC astrophysicist Tod Strohmayer examined light from a neutron star that sucks gas from a companion. Hydrogen and helium pile into a thickening blanket on the spinning star. Every few hours, the layer's pressure and temperature soar high enough to ignite a fierce thermonuclear burst.

NASA's Rossi X-ray Timing Explorer satellite detected 38 such bursts from the binary during sporadic observations over 7 years. When Villarreal and Strohmayer combined all burst records into a single statistical analysis, they concluded that x-rays from the flares flicker 45 times every second. The neutron star must spin at that rate, they deduced—a surprise, because other neutron stars in similar binaries spin at least four times as fast.

CREDITS (TOP TO BOTTOM): J. DAVIS *ET AL.*/MIT/CXC/NASA; U. HWANG *ET AL.*/GSFC/CXC/NASA

Published by AAAS

The slow spin vindicates a 2002 study of the strength of gravity on the same body, says astrophysicist Deepto Chakrabarty of MIT. That research—which led to a wider range of plausible masses and sizes—came under fire, because skeptics claimed a rapid spin would skew the results. With the slower rotation pointing to a reliable gravity figure, Strohmayer and Villarreal factored the spin rate into a model of how the star radiates in x-rays. The best fit was a diameter of 23 kilometers and a mass about 1.75 times as massive as our sun, they reported—a slightly heftier mass than that measured for most other neutron stars.

Theorists praise the technique, but they caution that interpreting the results is fraught with potential errors. "This inference stems from much of the [burst] activity taking place exactly on the surface, but it could happen at various levels of depth," says Prakash. His colleague at Stony Brook, astrophysicist James Lattimer, adds that observers must identify the unmistakable fingerprints of a broader suite of elements in the x-ray flares to tighten gravity calculations.

"We need to know the radius within a kilometer to exclude models [of neutron star matter]," Lattimer says. For now, a strange stew of squeezed quarks—which would produce a smaller neutron star, in most cases—remains viable.

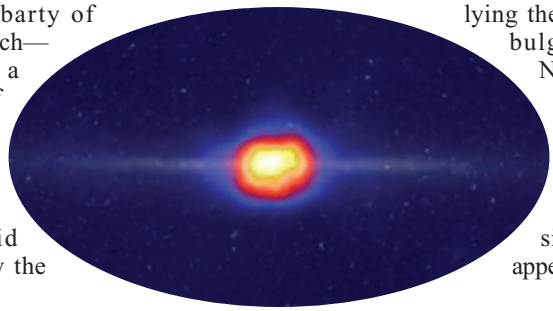

Antiglow. Gamma rays trace antimatter only in our galaxy's central bulge of old stars, not in its disk.

CREDITS: (TOP TO BOTTOM) J. KNÖDLSEDER *ET AL.*/CESR/ESA; D. BERRY/NASA

A Positron Map of the Sky

Astronomers have produced a startling new sky survey, based not on matter that shines but on antimatter that annihilates. The sources of the particles aren't yet known, but a European-led team reported that the antimatter clusters around the home of the Milky Way's most ancient stars.

For 30 years, astronomers have known that our galaxy creates a steady flow of positrons, the antimatter counterparts of electrons. When a positron and an electron collide in space, they destroy each other and spit out two gamma rays. The European Space Agency's INTEGRAL satellite, launched in October 2002, records those sparks far more sensitively than previous missions had done (*Science*, 19 December 2003, p. 2051).

The satellite's first all-sky map of the emission, released at the meeting, shows a bright patch of gamma rays overlying the galaxy's central bulge of old stars. None of the energy that was detected streams from the flat disk, where younger stars like our sun reside. "Young stars appear ruled out," says astrophysicist Georg Weidenspointner of the Centre d'Etude Spatiale des Rayonnements in Toulouse, France. "We did not expect [the central concentration] to this extent."

That leaves two classes of sources, Weidenspointner says. Old stars in binary tangos with white dwarfs, neutron stars, or black holes can flare up in various explosions including type 1a supernovas—the same objects used to trace the accelerating growth of the universe. Such supernovas spawn huge amounts of unstable nickel-56, which emits positrons during its decay chain. That's an ongoing bounty, says NASA GSFC astrophysicist Bonnard Teegarden: "You get one of these every few hundred years, producing a bunch of positrons, and it takes them 100,000 years to 1,000,000 years to annihilate."

Eager theorists are pursuing a more speculative source: lightweight particles of dark matter that may decay within a cocoon around the galaxy's core. As INTEGRAL watches the sky, it might be able to distinguish between a diffuse antimatter glow from widespread dark matter and more pointlike sources from old stars. However, a new study led by astrophysicist John Beacom of Ohio State University in Columbus argues that dark matter is a long shot. The patterns of extra radiation expected from such events don't match the energies seen by earlier gamma ray satellites, Beacom's team claims (arxiv.org/abs/astro-ph/0409403).

INTEGRAL's detections will increase sixfold as the mission goes on, so the fuzzy positron map will only get sharper. As astrophysicist Dieter Hartmann of Clemson University in South Carolina says, "They are really well on their way to conducting positron astrophysics."

–ROBERT IRION

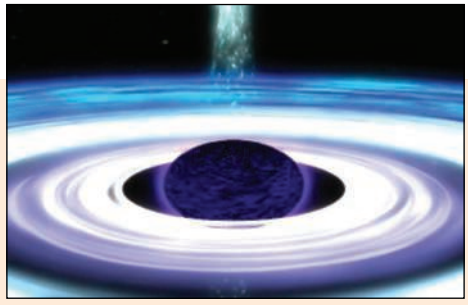

Hot plate. A black hole's accretion disk blazes in x-rays as gas spirals inward.

Snapshots From the Meeting

Orbits of doom. Astronomers may have caught their first glimpse of a blob of matter spiraling toward a giant black hole. X-rays from the core of a galaxy cycled in a repetitive pattern nearly four times during a daylong view by Europe's XMM-Newton satellite. A team led by Kazushi Iwasawa of the University of Cambridge, U.K., concluded that a hot spot within an accretion disk—a flattened torus of gas that envelops the black hole—orbited at one-fifth the speed of light, at about the same distance from the hole as Earth's distance from the sun. Colleagues were tantalized, but some warned that the signals aren't statistically compelling.

Cold search. Neutrino sensors embedded in the Antarctic ice have not yet traced any of the zippy particles to a specific source. Analysis of 3369 neutrinos detected by the AMANDA experiment through 2003 showed that they came from random directions, reported astrophysicist Steven Barwick of the University of California, Irvine. The new study—three times as sensitive as the one reported in the team's most recent publication—included attempts to pinpoint neutrinos from 119 gamma ray bursts. "AMANDA is just too small," Barwick said. A gigantic successor, called IceCube, will spot far more neutrinos starting next year.

Pulsar power. Hundreds of radio pulsars—the spinning remnants of massive stars that explode—probably swarm around the black hole at our Milky Way's core. Radio telescopes should find several pulsars with orbits lasting less than a century, predicted astrophysicist Eric Pfahl of the University of Virginia, Charlottesville. Pfahl reported that subtle variations in the clockwork blips from such pulsars would effectively map the black hole's turbulent environment. Searches are under way at the Green Bank Telescope in West Virginia and elsewhere.

–R.I.

Published by AAAS

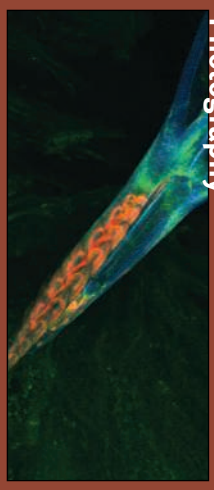

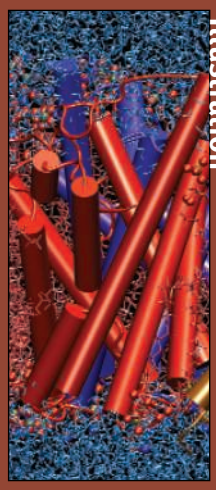

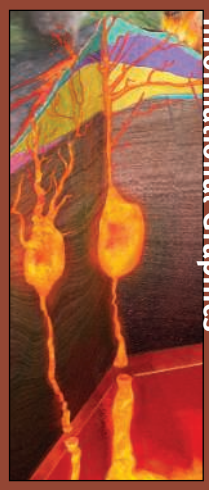

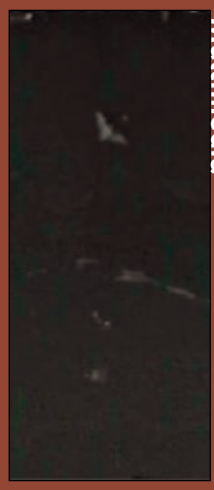

2004 Visualization Challenge

A multicolored deer tick latched onto the ear of a hamster … water molecules shuttling across a cell membrane … a bat's sonar locking onto its prey … the cauldron of Mount Etna getting ready to rumble. The following pages bring to life intricate interactions, from the workings of cells to the geological processes that threaten cities. These stunning visualizations won top honors in the second Science and Engineering Visualization Challenge, cosponsored by *Science* and the National Science Foundation (NSF).

We launched this annual international competition last year to showcase and encourage an increasingly important aspect of science: the ability to convey the essence and excitement of research in digitized images, color diagrams, and even multimedia presentations. Investigators at the outermost frontiers of science and engineering frequently study phenomena that are extremely difficult even for most scientists to visualize—and downright formidable for the general public that ultimately supports the global research enterprise. When that research is depicted vividly and comprehensibly in pictures, everybody benefits.

For this year's challenge, we invited submissions in five categories: photography, illustration, informational graphics, and two kinds of multimedia: interactive and noninteractive. Entries were screened by a committee from NSF and *Science*. Then an independent panel of experts in scientific visualization reviewed the 50 finalists and selected the best, which appear in these pages. (This year, the judges decided not to name an overall winner in interactive graphics in part because they felt that no single entry combined excellent graphics with full interactivity.) We congratulate the winners and all the other entrants.

Susan Mason of NSF organized this year's challenge; David Grimm of *Science*'s News staff wrote the text that accompanies the winning images. Stewart Wills of *Science* has put together a special Web presentation, including audiovisual clips, at www.sciencemag.org/sciext/vis2004. Winning submissions will also be featured at the AAAS annual meeting in February.

Entries for 2005 are being solicited now through announcements in *Science* and on the NSF Web site. We urge all researchers and science communicators to participate in this unique and inspiring competition.

Curt Suplee, Director, Office of Legislative and Public Affairs, NSF
Monica Bradford, Executive Editor, *Science*

Panel of Judges

Donna J. Cox
Professor, School of Art and Design, University of Illinois, Urbana-Champaign
Specialist in three-dimensional computer animation

Felice Frankel
Research Scientist, Massachusetts Institute of Technology, Cambridge
Science photographer and director, Envisioning Science Project

Gary Lees
Chair and Director, Department of Art as Applied to Medicine, Johns Hopkins University, Baltimore, Maryland
Specialist in medical illustration

Thomas Lucas
Thomas Lucas Productions, New York City
Producer of science documentaries

Boyce Rensberger
Director, Knight Science Journalism Fellowships, MIT
Science journalist formerly at The Washington Post *and* The New York Times

Published by AAAS

PHOTOGRAPHY

Autofluorescence of Tick Nymph on a Mammalian Host

Marna E. Ericson, University of Minnesota, Dermatology

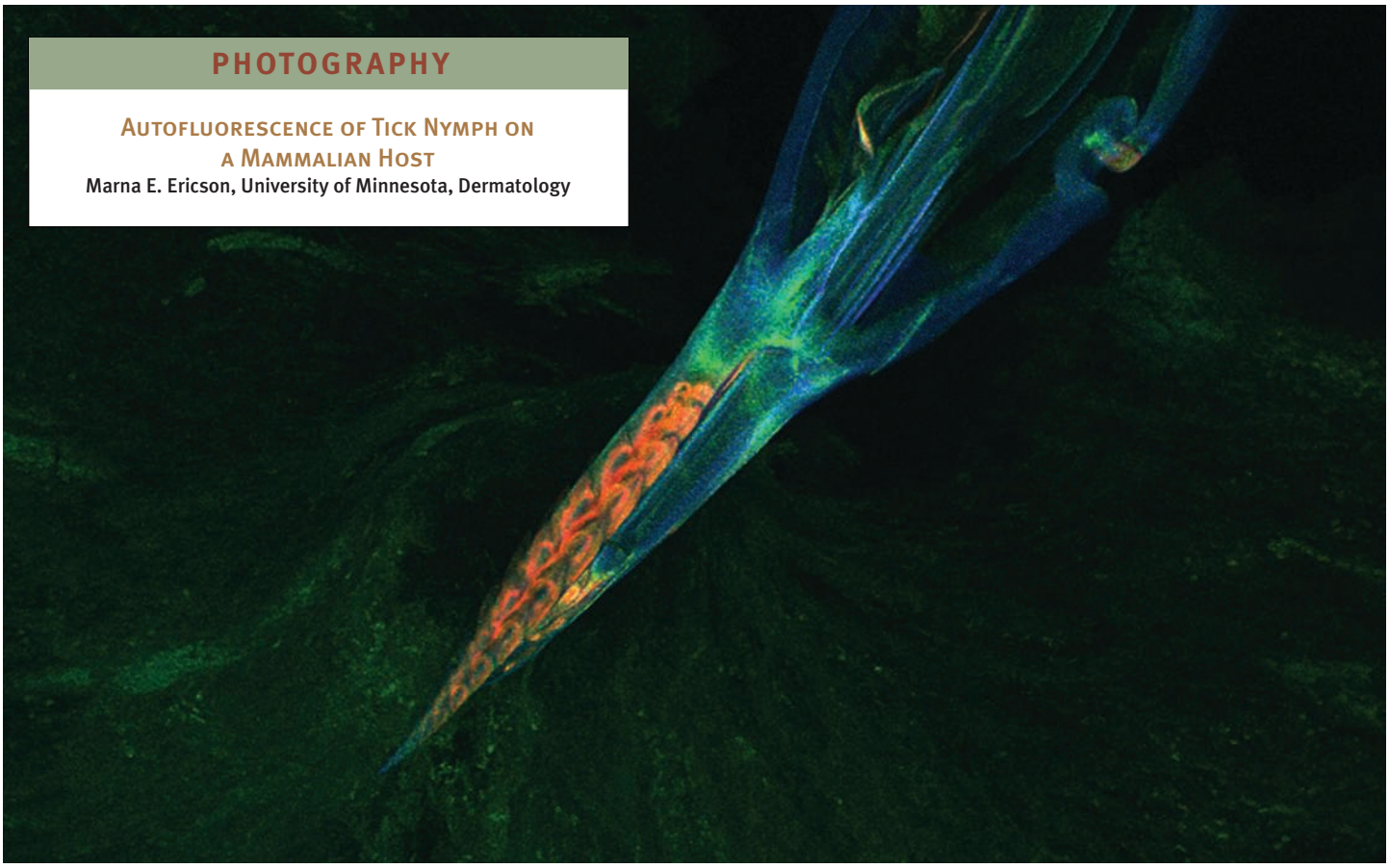

A blood-sucking tick has never looked so stunning. The makeover is thanks to Marna Ericson of the University of Minnesota, Minneapolis, who used laser scanning confocal microscopy to capture the autofluorescence of a common deer tick as it feasted on the ear of a golden hamster.

When ticks feed, they transmit bacteria to their hosts that can cause a variety of illnesses in humans, including Lyme disease. Ericson's group wanted to understand how this transmission takes place by engineering fluorescent versions of the tick-associated bacteria. But first the researchers needed to make sure that the color they selected for the bacteria would be distinguishable from the natural autofluorescence of the tick and hamster.

Judging by the rainbow of hues in Ericson's photograph, this could be a challenge. The colors of the tick's mouth range from the emerald green and brilliant violet of its outer shell to the volcanic red and salmon-orange of its flesh-piercing structures. Even the tissue of the hamster's ear fluoresces; that's the faint olive glow of the background. Ericson says the photograph highlights the "importance of good [autoflourescence] controls."

"I found this picture incredibly striking," says panel of judges member Felice Frankel. Frankel believes the picture won because of its "clarity of representation and the way it captures a real-time moment."

HONORABLE MENTION

Antarctic Diatom Chain

Unicellular plants form a conga line, while their antisocial relatives stick to themselves, in Dee Breger's photomicrograph. Breger, of Drexel University in Philadelphia, Pennsylvania, captured the moment by colorizing a scanning electron micrograph of a microplankton sample pulled from the depths of the Antarctic Sea. Oceanographers collected the sample during a 2002 expedition that investigated the role of marine iron in diatom growth and atmospheric levels of carbon dioxide.

Pasture of Instabilities

Plastic can produce spectacular imagery under the right circumstances. To create this image, polymer science and engineering graduate student Ting Xu of the University of Massachusetts, Amherst, applied an electric field to a thin film of polystyrene. The field amplifies irregularities on the surface of the film, which appear as colorful patterns under optical microscopy. The image is part of VISUAL, an NSF-supported outreach program designed to educate the public about science.

Published by AAAS

ILLUSTRATION

WATER PERMEATION THROUGH AQUAPORINS

Emad Tajkhorshid and Klaus Schulten,
Theoretical and Computational Biophysics Group,
University of Illinois, Urbana-Champaign

If you look closely at the image below, you can see water molecules doing the twist. The dance is the highlight of a revealing look at the complex machinery a cell uses to exchange water with its environment.

Aquaporin channels provide a conduit for water to cross the cell membrane, but they somehow prevent smaller particles, like protons, from getting through. To understand this selectivity, computational biophysicists Emad Tajkhorshid and Klaus Schulten of the University of Illinois, Urbana-Champaign, constructed one of the largest atomic simulations ever attempted. The group assembled four membrane-bound aquaporin channels from more than 55,000 digital atoms and then added virtual water.

The winning illustration is a snapshot of the simulation in progress. Boomerang-shaped water molecules flip as they march single file through the narrow pore of the gold aquaporin, while the red balls and fibers that make up the cell's membrane keep the outside water (top) from mixing with the cellular pool (bottom). The display allowed the researchers to crack the mystery of aquaporin's discriminating tastes. "The flipping of the water molecules prevents protons from hopping through the pore," says Tajkhorshid, who notes that this novel mechanism of selectivity could not have been determined using traditional experimental methods.

"This is an almost-perfect use of existing [protein-modeling] software," says panel of judges member Felice Frankel. "It intelligently combines many of the methods used to represent proteins while successfully expressing a larger scientific idea." Plus, she says, "it's also very beautiful."

HONORABLE MENTION

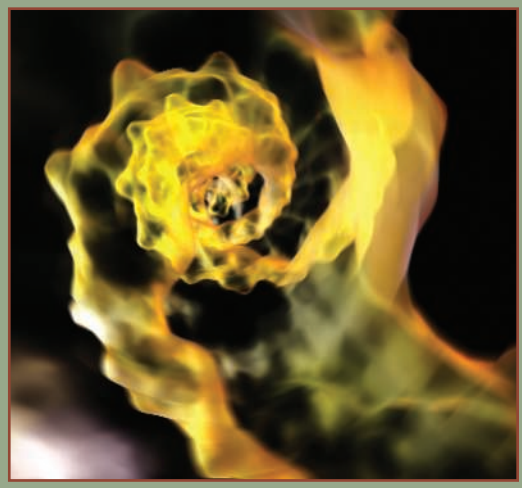

SPIRAL IV

If you could climb the twisted ladder of a DNA molecule and look down, you might see something like the image above. Kenneth Eward, a science artist at BioGrafx Scientific & Medical Images in Ovid, Michigan, used x-ray crystallographic data from DNA molecules to paint a unique portrait of the double helix. The image omits the chemical bonds that crisscross the center of the molecule, so that the structural features of the helix can be seen more easily.

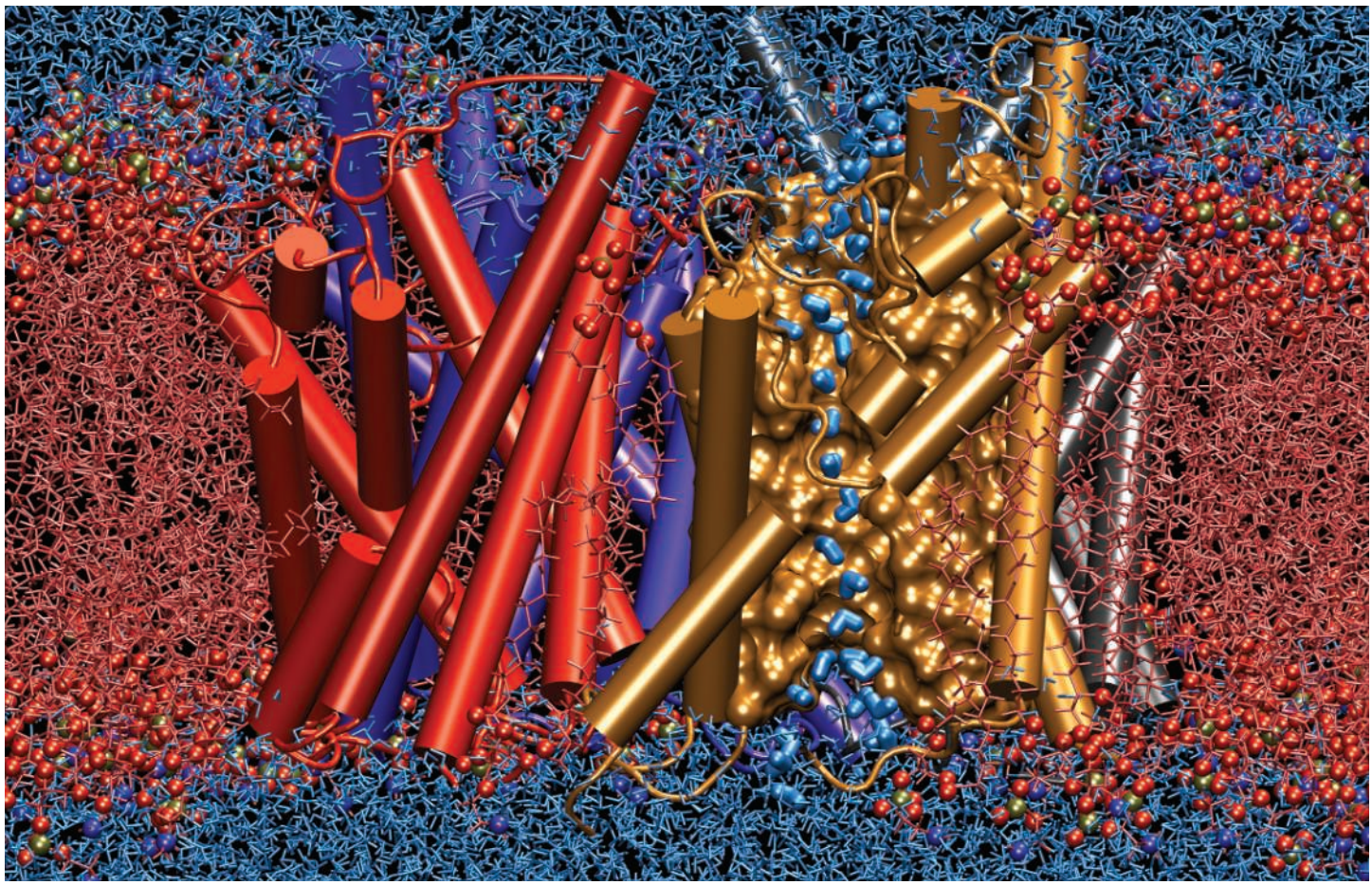

Published by AAAS

INFORMATIONAL GRAPHICS

MOUNT ETNA

David Fierstein,
David Fierstein Illustration, Santa Cruz, California

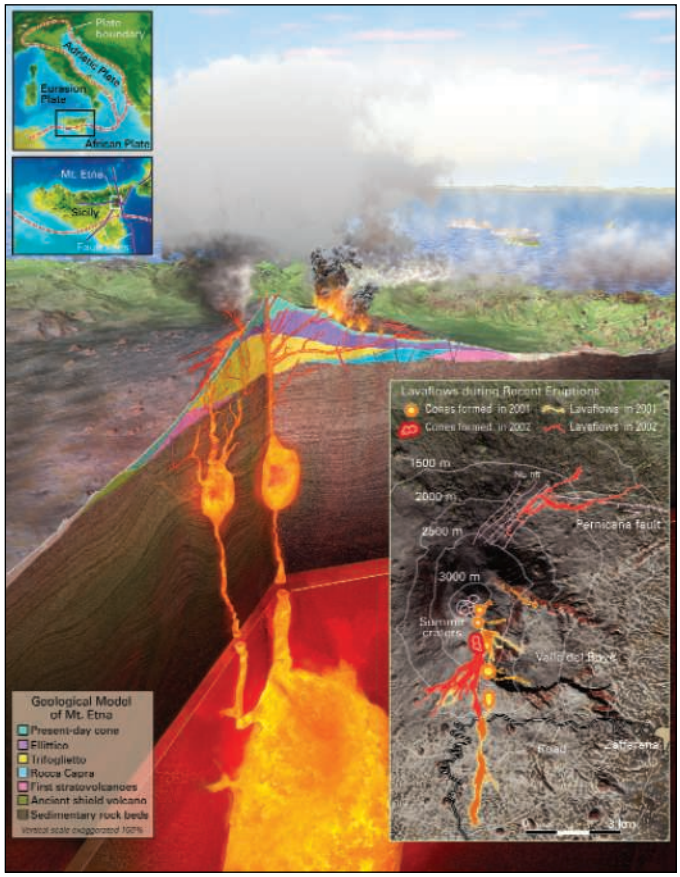

Science illustrator David Fierstein cuts to the core of one of the world's most unusual volcanoes in his illustration of Mount Etna. The image merges the latest scientific data with state-of-the-art 3D modeling software to give a comprehensive view of the volcano's rich and violent history.

Located on the east coast of Sicily, Mount Etna is Europe's largest volcano and one of the most productive in the world. Eruptions in the past 3 years alone have destroyed tourist complexes and threatened nearby towns. New evidence suggests that Mount Etna is growing increasingly violent and may someday rival Mount St. Helens and Pinatubo in ferocity.

Fierstein's graphic documents the changing nature of the volcano by combining this new evidence with prior research. The insets at the upper left illustrate how the unique geological location of the volcano allows it to produce large volumes of magma, and the panel at the lower right provides details about recent lava flows and eruptions. The central image chronicles the evolution of Mount Etna from a relatively flat shield volcano to the mountainous cone that looms over the countryside today. Fierstein says the large, glowing magma pools in this image are the most salient part of the graphic, in that they highlight Mount Etna's hypothesized "dual plumbing system," which may give clues to the volcano's future activity.

"This image is a great example of how to illustrate a complex set of relationships," says panel of judges member Thomas Lucas. Fellow panelist Boyce Rensberger agrees: "It shows you everything you'd want to know," he says, "except, perhaps, for the people screaming down below."

MULTIMEDIA—INTERACTIVE: HONORABLE MENTION

BRACHIAL PLEXUS

Doctors who inject anesthetic to numb selected body parts literally take a shot in the dark. Many of the body's nerves lie so deep that anesthesiologists must use unreliable cues, such as pulse and bone position, to guide them. But now physicians may be able to improve their accuracy by using anesthesiologist Paul Bigeleisen's interactive DVD. The presentation combines ultrasound, virtual-reality animation, and see-through videography to provide a detailed road map of the peripheral nervous system in a living patient. Bigeleisen, who practices at Strong Memorial Hospital in Rochester, New York, endeavored to make the tutorial visually appealing so users would look forward to learning the material.

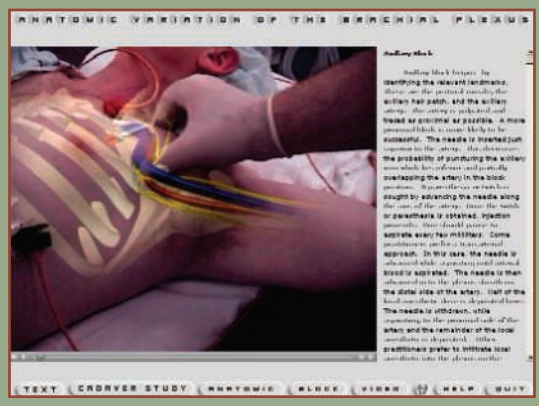

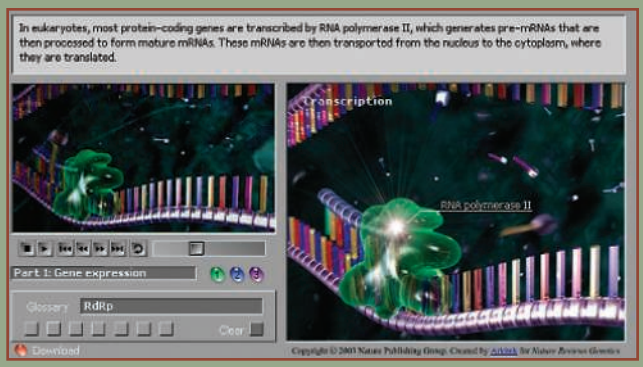

RNAi—A BALLET OF MOLECULAR MACHINES

It slices, it dices, and it may someday turn genetic disease into a thing of the past. RNA interference is a complex set of cellular processes that converts a foreign piece of double-stranded RNA into a potent gene blocker. Science animators Doug Huff and Beth Anderson of Arkitek Studios in Seattle, Washington, shed light on these processes in a narrated interactive video that takes viewers inside a living cell as double-stranded RNA is introduced. Viewers can toggle among three different acts of the ballet and get more information on each of the machines from a pop-up glossary. The animators placed equal emphasis on beauty and detail, so that the video would both satisfy molecular biologists and capture the attention of a wide audience.

Published by AAAS

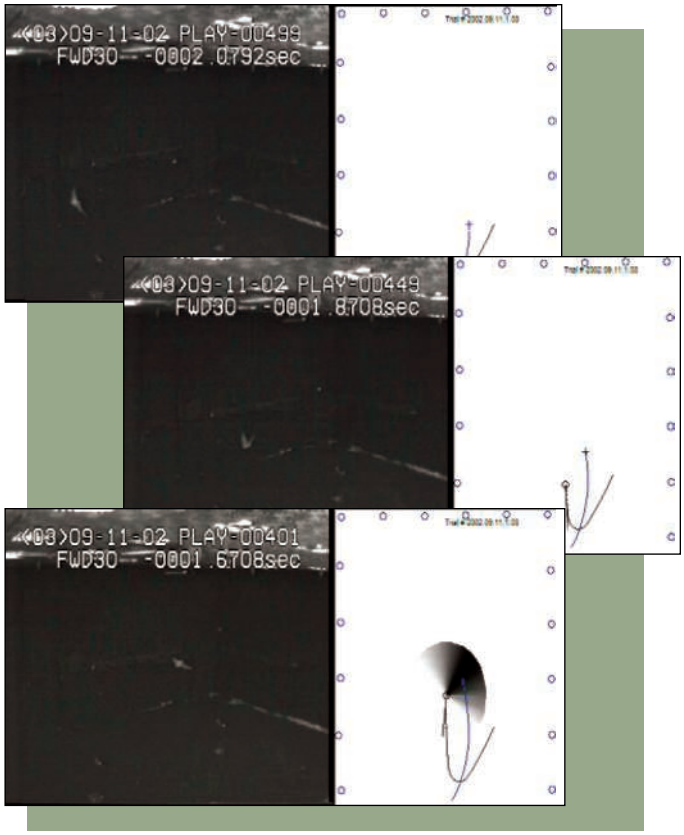

MULTIMEDIA—NONINTERACTIVE

BAT INTERCEPTS FLYING INSECT

Cynthia F. Moss and Kaushik Ghose,
University of Maryland, College Park

Under infrared light, a large, winged object locks onto and overtakes a small blip while a radarlike display tracks the entire proceeding. This isn't a military exercise; it's an experiment designed to understand how bats use sonar to capture their prey.

Bats emit high-frequency sounds when hunting and navigating, but no one knew how they aimed these sonar beams until neuroethologist Cynthia Moss and graduate student Kaushik Ghose created a bat cave in their laboratory at the University of Maryland, College Park. The researchers padded a large room with acoustic foam and set up two high-speed infrared cameras and 16 strategically placed microphones. Then they introduced a large brown bat and a praying mantis.

The drama unfolds in a two-frame multimedia presentation. In the left frame, a slowed-down movie captures the visual action, complete with bat chirps and a crunch when the mantis meets its fate. On the right, an animated diagram traces the hunt from above and incorporates the microphone data to pinpoint the direction of the bat's sonar (represented by the darker bars on the gray-scale cone). The presentation reveals that a bat "locks its beam on a target" when hunting, says Ghose, who notes that the behavior is akin to baseball players keeping their eye on the ball.

"This is a unique visualization of an amazing event," says panel of judges member Thomas Lucas. He says the judges were impressed with the combination of video, sound, and sonar that puts the viewer in the bat's world. "This is something we never get to see," says Lucas. "It always happens in the dark."

HONORABLE MENTION

THE ELBE RIVER FLOOD 2002

Geographer Nils Sparwasser and colleagues at the German Aerospace Center in Oberpfaffenhofen send viewers on a bird's-eye journey over Eastern Europe in August 2002 as entire cities are consumed by the worst flooding to hit the region in more than 100 years. The group incorporated optical and radar data from 10 satellites to create the three-dimensional presentation. Disaster organizations may soon use similar displays to predict flood damage and evacuate endangered residents.

SPATIOTEMPORAL ARBOVIRAL SURVEILLANCE IN FLORIDA DURING 2003

A map of Florida comes to life in this animated video by biologist Gregory Ross and colleagues at the University of Florida, Gainesville. Clouds of red, yellow, and green transiently materialize over various regions of the state as antibodies against the West Nile and eastern equine encephalitis viruses appear in sentinel chicken flocks throughout the year. Mosquito-control agencies and health departments can use this animated map to track and combat the mosquitoes that carry these viruses.

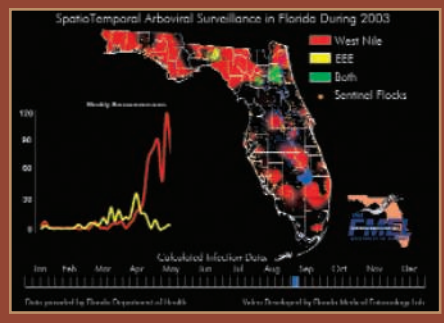

Published by AAAS

Letters to the Editor

Letters (~300 words) discuss material published in *Science* in the previous 6 months or issues of general interest. They can be submitted through the Web (www.submit2science.org) or by regular mail (1200 New York Ave., NW, Washington, DC 20005, USA). Letters are not acknowledged upon receipt, nor are authors generally consulted before publication. Whether published in full or in part, letters are subject to editing for clarity and space.

How Did the Horned Lizard Get Its Horns?

IN THEIR BREVIA "HOW THE HORNED LIZARD got its horns," K. V. Young *et al*. present an important example of natural selection in the wild, suggesting that loggerhead shrike predation drove the evolution of elongated horns in the flat-tailed horned lizard (2 Apr., p. 65). Although the authors acknowledge that selective forces other than shrike predation may also be involved, they make no mention of the possibility that one of these potential forces could have been the first instigator of the directional selection for horn elongation. Under this hypothetical scenario, the horns would have then only subsequently served to reduce shrike predation. Other likely cases of preadaptation [or exaptation (*1*)] have been described in vertebrates (*2*–*5*), some of which involve important transitions in evolutionary history. Perhaps the role of preadaptation in evolution is of great importance and is deserving of more widespread appreciation. Given the possibility of a preadaptation scenario in the evolution of crown horns in horned lizards, I find it ironic that Young *et al*. commented on the weakness of "just-so stories" (*6*) and also chose a title that reads remarkably like the titles of Kipling's stories. Until presented with evidence suggesting that the horns were mere nubs until the onset of shrike predation, I will remain convinced that "How the horned lizard got its horns" is a poor choice for what is presumably meant to be an informative title.

WILLIAM R. FOUTS

Department of Biology, Nevada State College, 1125 Nevada State Drive, Henderson, NV 89015, USA.

References

1. S. J. Gould, S. Vrba, *Paleobiology* **8**, 4 (1982).
2. K. P. Dial, *Science* **299**, 402 (2003).
3. S. J. Gould, *The Panda's Thumb* (Norton, New York, 1980).
4. D. J. Futuyma, *Evolutionary Biology* (Sinauer, Sunderland, MA, ed. 3, 1998).
5. N. H. Shubin *et al*., *Science* **304**, 90 (2004).
6. R. Kipling, *Just So Stories* (Doubleday, New York, 1902).

IN THEIR BREVIA "HOW THE HORNED LIZARD got its horns" (2 Apr., p. 65), K. V. Young *et al*. claim to have direct evidence of the defensive function of the long bony horns that fringe the lateral and posterior margins of the head of the flat-tailed horned lizard (*Phrynosoma mcalli*). They show elegantly and convincingly that loggerhead shrikes (*Lanius ludovicianus*) prey on lizards with relatively short horns (corrected for body size) and that this source of mortality produces directional selection favoring longer horns. Unfortunately, the authors incorrectly conclude that "defense against shrike predation is one factor driving the radical elongation of horns in some species of horned lizards." This conclusion is incorrect because they did not show that the lizards use their horns to defend themselves against shrikes, nor did they show that longer horns are better for defense. Suppose that lizards with longer horns also are more vigilant, escape faster, spend less time in the open, are more cryptic, or have other traits that reduce the chance they are seen, caught, killed, and eaten by shrikes. Any of these correlated traits could also explain the observed pattern of predation and selection. Observations of how shrikes attack lizards and how lizards defend themselves, and measurements of predation rates on lizards with experimentally shortened and lengthened horns are needed to test the validity of the intuitively attractive suggestion that the horns of horned lizards are defensive. At present, this explanation for the adaptive function for horns remains a "just-so story."

JOHN H. CHRISTY

Smithsonian Tropical Research Institute, Apartado 2072, Balboa, Ancon, Panama. E-mail: chirstyj@naos.si.edu

IN THEIR BREVIA "HOW THE HORNED LIZARD got its horns" (2 Apr., p. 65), K. V. Young *et al*. explain the causal processes of how the flat-tailed horned lizards (*Phrynosoma mcalli*) developed parietal horns as a defense against the impaling capabilities of the loggerhead shrike (*Lanius ludovicianus*). However, the actual selection factor that the horns help to defend the lizards from—how shrikes kill their vertebrate prey—was not discussed. Shrikes prey differentially on invertebrates and vertebrates. A shrike (*Lanius* spp.) kills its vertebrate prey (*1*, *2*), including species that may weigh as much as an adult shrike (30 to 75 g depending on the species of shrike), with a bite directed at the portion of the prey's neck immediately posterior to the skull. The bite disarticulates the vertebral column. When the prey is dead, a shrike will fly to a convenient perch where the prey is either impaled on a sharp point or dragged and lodged into a fork of a branch (*3*). This allows a shrike to pull the prey apart with its bill into portions that can be swallowed.

CREDIT: K. V. YOUNG

Flat-tailed horned lizard in defensive posture.

Natural selection can only occur if individuals survive a given experience and are able to transmit that information to conspecifics or their progeny (*4*). Given my long experience in the field with shrikes, the attack period is the only possible event when a horned lizard could experience and escape the attacks of the shrike to the nape. Further, it is also possible that attacks by inexperienced juvenile shrikes, allowing for a greater percentage of escapes (*3*), on the horned lizards gave rise to the selection for elongated horns. It also does not make evolutionary sense for a trait to be incorporated into a prey species, as a result of a predator's behavior, that results in all cases in its death (i.e., the impaling stage). Hence, although I accept the authors' conclusion that "defense against shrike predation is one factor driving the radical elongation of horns," I suggest that the parietal horns developed as a defense against shrike attacks to the nape region and not against their being impaled after they are dead. Thus, the posterior-directed (and perhaps even the lateral-directed) cranial horns of a *Phrynosoma* lizard are a potential danger to a shrike, aimed as they are at a shrike's eye when it goes in for a lethal bite at the lizard's neck.

REUVEN YOSEF

International Bird Research Centre in Eilat, Department of Life Sciences, Ben-Gurion University of the Negev, Eilat 88000, Israel.

References

1. T. J. Cade, E. C. Atkinson, *Birds N. Am.* **671** (2002).
2. R. Yosef, *Birds N. Am.* **231** (1996).
3. R. Yosef, *Vogelwarte* **42**, 25 (2003).
4. M. W. Strickberger, *Evolution* (Jones & Bartlett, Boston, 1990).

Response

THE TITLE OF OUR PAPER WAS MEANT AS AN allusion to the *Just So Stories* of Kipling (*1*), which are often used as a shorthand criticism for unsubstantiated adaptive arguments. It is a bold statement, and we thought it so clearly over the top that it would not be taken as a literal explanatory title. The problem of identifying adaptations and their causes has (at least) two schools of thought, one that focuses on the source of the original character state change (as described by Fouts), and one that focuses on current value and selection (as described in our Brevia). Heritable traits that have current adaptive value, as is the case for the horns of flat-tailed horned lizards (*Phrynosoma mcalli*), will continue to change through natural selection, thereby leading to continued adaptation and explaining in part how horned lizards got elongated horns. The question of whether any horns on the head of horned lizards existed before shrike predation drove them to elongated states (i.e., were "preadapted") is an interesting one, but one that is only answerable through comparative analyses with full phylogenetic information and ancestral environmental conditions (*2*). Although we have not performed such an analysis and could probably never reconstruct the ancestral predation conditions, it is worth noting that of the 13 species of horned lizards currently extant, *P. mcalli* has the longest relative horn lengths and belong to the most derived species group (*3*, *4*), while some other species in the genus (e.g., *P. douglassi*) have virtually no parietal or squamosal horns (i.e., the nubs mentioned by Fouts).

Christy correctly points out the two primary shortcomings of any covariance analysis of selection: It is impossible to rule out every unknown unmeasured character that could drive the observed selection, and covariance analyses usually cannot assign a mechanism of selection because they are not manipulative studies (*5*). In the case of shrike predation selecting on horn length in lizards, however, we have measured a fitness component undeniably assignable to predation by a single predator. We also know that lizards routinely use their horns behaviorally in defense, jabbing them backward into anything that restrains them, often with enough force to draw blood from human fingers. It seems most parsimonious to conclude that the fitness advantages conferred by longer horns with respect to shrike predation accrue because of their defensive function, rather than to invoke some unknown correlated character that generates the observed covariance.

Yosef describes the predation behavior of shrikes attacking their prey and in doing so explains some of the critical natural history driving the natural selection we observed. We regret that space limitations prevented us from fully describing the fascinating behavior of shrikes, and the comments of Yosef help to fill in some of these blanks and support the interpretations in our paper. The impaling behavior of shrikes provides a unique sampling of successful predation, but we never intended to imply that horn length served to prevent the impaling process per se.

The defensive behavior of flat-tailed horned lizards is consistent with the interpretation that longer horns deter attacks by shrikes. When attacked or grasped, flat-tailed horned lizards stab their spines into the offending object. In the case of human fingers, this behavior often results in bleeding and immediate release of the lizard. The predation behavior of shrikes, which typically attack near the neck, would place vulnerable areas of the predator's face within range of the parietal and squamosal horns of flat-tailed horned lizards. Lizards with relatively longer horns would be expected to be more likely to be able to reach and inflict damage on a predator, thereby interrupting the predation sequence and escaping.

EDMUND D. BRODIE III,[1] KEVIN V. YOUNG,[2] EDMUND D. BRODIE JR.[2]

[1]Department of Biology, Indiana University, Bloomington, IN 47405–3700, USA. [2]Department of Biology, Utah State University, Logan, UT 84322–5305, USA.

References

1. R. Kipling, *Just So Stories* (Doubleday, New York, 1902), p. 249.
2. H. W. Greene, *Fieldiana Zool.* **31**, 1 (1986).
3. K. Zamudio, W. L. Hodges, *Mol. Phylogenet. Evol.* **31**, 961 (2004).
4. R. R. Montanucci, *Contrib. Sci. Nat. Hist. Mus. Los Angeles County* **390**, 1 (1987).
5. E. D. Brodie III, A. J. Moore, F. J. Janzen, *Trends Ecol. Evol.* **10**, 313 (1995).

The Importance of Educating Girls

IN HIS EDITORIAL "SUSTAINABLE DEVELOPMENT" (30 Apr., p. 649), J. Sachs eloquently describes scientists' increasing concern about the difficulty of providing for a growing global population in sustainable ways.

It will be much easier to achieve decent, sustainable living standards if population growth slows more rapidly. Extensive research from diverse countries shows that while family planning and basic health care clearly play major (and reinforcing) roles, expanding education for women where female education levels are now relatively low is probably the single most effective way to encourage a shift to smaller, healthier, and better educated families (*1*,

2). Education boosts women's earning capacity roughly as it does men's (*3*–*5*). Education also improves women's "bargaining position" in the family and society. As education and resulting higher earning capacity increase the opportunity cost of women's time, couples tend to have fewer children and to invest more in the health and education of each child. A World Bank study of 100 countries finds that when women gain four years of education, on average, fertility per woman drops by about one birth (*6*), and another study of 65 countries finds that doubling the proportion of women with a secondary education from 19 to 38% would reduce average fertility rates from 5.3 to 3.9 children (and improve child mortality too) (*2*).

Yet despite the benefits of female education, the UN estimates that 104 million school-age children—60 million of them girls—are not in school each year (*7*). The World Bank reports that in sub-Saharan Africa, more than half of girls do not complete a primary education (*8*). One reason is that even basic education carries considerable costs to parents—tuition may come to one-fourth of poor families' incomes. (Even when education is supposedly free, "extra fees" and indirect costs for schooling may burden poor families.) Yet the benefits of education accrue mainly to the girls when they grow up, to the families they have in their turn, and to their societies, not immediately to the parents who decide on schooling. The benefits may well seem distant and dicey to the parents, particularly in cultures where girls "marry out" and where poverty is widespread and the quality of available education is very poor.

Many countries—from Bangladesh, to China, to Mexico—have strong programs to improve education for girls and boys. But far more needs to happen to bring more girls into school, ensure that they stay beyond primary school, and provide them decent quality education. Although many if not most people support such efforts, it's a question of priority.

As Lawrence Summers emphasized when at the World Bank and the Treasury Department, once all its benefits are considered, female education may well be the highest return investment available to the developing world (*9*). The impact of female education on family size and well-being—and so also on population growth and the prospects for sustainable development—is enormous. Female education thus deserves far more priority in public policy both in particular countries and internationally. An international effort under UN aegis is under way to achieve "Basic Education for All" by year 2015. Whether this effort accomplishes its goal depends on greater national and international political commitment, on increased financial support, on real education reforms, and thus on greater public understanding.

BARBARA HERZ

Moose, WY, USA.

References

1. B. Herz, G. B. Sperling, *What Works in Girls' Education: Evidence and Policies from the Developing World* (Council on Foreign Relations, New York, 2004).
2. K. Subbarao, L. Raney, *Econ. Dev. Cultural Change* **44** (no. 1), 105 (1995).
3. G. Psacharopoulos, H. A. Patrinos, "Returns to Investment in Education: A Further Update," World Bank Policy Research Working Paper 2881 (World Bank, Washington, DC, 2002).
4. T. P. Schultz, *World Dev.* **30** (no. 2), 207 (2002).
5. T. P. Schultz, in *Women's Education in Developing Countries: Barriers, Benefits, and Policy*, E. King, M. A. Hill, Eds. (Johns Hopkins Univ. Press, Baltimore, MD, 1993).
6. S. Klasen, "Does Gender Inequality Reduce Growth and Development? Evidence from Cross-Country Regressions," Policy Research Report on Gender and Development Working Paper No. 7 (World Bank, Washington, DC, 1999).
7. UNESCO, *Education for All Global Monitoring Report 2003/4* (UNESCO, Paris, 2003).
8. B. Bruns, A. Mingat, R. Rakotomalala. "Achieving Universal Primary Education by 2015: A Chance for Every Child" (World Bank, Washington, DC, 2003).
9. L. H. Summers, "Investing in All the People: Educating Women in Developing Countries," EDI Seminar paper No. 45 (World Bank, Washington, DC, 1994).

Future Global Warming Scenarios, Take 2

IN HIS LETTER "FUTURE GLOBAL WARMING scenarios" (16 Apr., p. 388), W. S. Broecker critiques our recent study for the Department of Defense on the national security implications of abrupt climate change (*1*). We admire Broecker and his work, which importantly informed the scientific underpinning of the study, and although we agree with the substance of his comments on the science of climate change, his critique does not accurately reflect the content of the report—or its intent.

First, we make no predictions. As our opening paragraph explicitly states: "The purpose of this report is to imagine the unthinkable—to push the boundaries of current research on climate change so we may better understand the potential implications on United States national security… We have created a climate change scenario that although not the most likely, is plausible, and would challenge United States national security in ways that should be considered immediately."

Broecker is correct in asserting that the most likely scenario is one of regional climate change (locations uncertain) many decades from now. But that would have little impact on today's strategic planning for national security. That is why we examined the plausibility of a low-likelihood,

near-term abrupt climate change scenario across all the major geographies.

Why should abrupt climate change matter to the Department of Defense? Because thinking the unthinkable is fundamental. In 2000, the senior writer of this report led one of the teams that explored "National Security in the 21st Century" with the Hart-Rudman Commission. The Commission's report, published in the summer of 2001, concluded that a major terrorist attack on U.S. soil was likely in the next quarter century and that we were ill prepared to either detect or stop it. At the time, this was considered a low-probability event; today, the government is under considerable fire for not seriously considering such scenarios.

Our climate change study was conducted and shared in that spirit. It was not an attempt to do climate science or influence climate policy. But its conclusions strongly suggest that it is in our national security interests to increase support for climate science so that we can gain better insight into the timing, nature, and likelihood of abrupt climate change.

PETER SCHWARTZ AND DOUG RANDALL
Global Business Network, 5900 X Hollis Street, Emeryville, CA 94608, USA.

Reference
1. P. Schwartz, D. Randall, "Abrupt climate change," report prepared by Global Business Network (GBN) for the Department of Defense, available at www.gbn.org/ArticleDisplayServlet.srv?aid=26231.

CORRECTIONS AND CLARIFICATIONS

Perspectives: Draft versions of the PDFs for three Perspectives (Busse, Stolow, and Levin) in the issue of 10 Sept. were inadvertently posted. The correct versions were posted on 13 Sept. at approximately 4 p.m. The HTML and print versions of these articles were correct. If you downloaded a PDF of one of these Perspectives prior to the above date, please return to *Science* Online to obtain the correct version.

Random Samples: "Reason to exist" (13 Aug., p. 941). Susan Ganter, the new executive director of the Association for Women in Science (AWIS), is on leave from her position as associate professor of mathematical sciences at Clemson University and remains involved in educational and research activities. The item wrongly implied that she no longer has an affiliation with Clemson and that she would not be continuing her work in mathematics and education.

Special Issue on Immunotherapy: Viewpoint: "Therapeutic vaccines for chronic infections" by B. Autran *et al.* (9 July, p. 205). The purple lines in panels (B) and (C) of Fig. 1 were printed incorrectly. The correct figure appears here. Also, the authors would like to acknowledge support from the European Union.

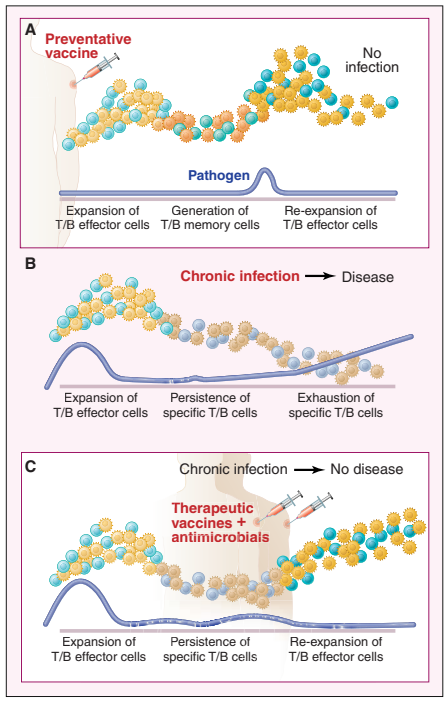

Reports: "Antigen bias in T cell cross-priming" by M. C. Wolkers *et al.* (28 May, p. 1314). Two of the symbols in Fig. 3B were denoted incorrectly. The closed triangles represent RMA-S sE7-GFP-NP cells, and the closed circles represent RMA-S sNP-GFP-E7 cells.

TECHNICAL COMMENT ABSTRACTS

COMMENT ON "Role of NMDA Receptor Subtypes in Governing the Direction of Hippocampal Synaptic Plasticity"

Dmitri A. Rusakov, Annalisa Scimemi, Matthew C. Walker, Dimitri M. Kullmann

Liu *et al.* (Reports, 14 May 2004, p. 1021) reported that NMDA receptors containing NR2A and NR2B subunits are selectively coupled to long-term potentiation (LTP) and long-term depression (LTD), respectively. Because NR2B (but not NR2A) receptors occur outside synapses, and can be activated by glutamate spillover, this principle may underlie synaptic homeostasis.

Full text at www.sciencemag.org/cgi/content/full/305/5692/1912b

RESPONSE TO COMMENT ON "Role of NMDA Receptor Subtypes in Governing the Direction of Hippocampal Synaptic Plasticity"

Tak Pan Wong, Lidong Liu, Morgan Sheng, Yu Tian Wang

Although we agree with Rusakov *et al.* that activation of extra-synaptic NR2B receptors by glutamate spillover may lead to heterosynaptic LTD, our data also support a role of synaptic NR2B receptors in homosynaptic LTD. The proposed role of extrasynaptic NMDA receptor-mediated LTD in synaptic homeostasis may thus be temporally limited.

Full text at www.sciencemag.org/cgi/content/full/305/5692/1912c

Comment on "Role of NMDA Receptor Subtypes in Governing the Direction of Hippocampal Synaptic Plasticity"

Liu *et al*. (*1*) recently showed that blockade of *N*-methyl-D-aspartate (NMDA) subtype glutamate receptors containing either NR2A or NR2B subunits leads to a selective defect in either long-term potentiation (LTP) or long-term depression (LTD), respectively. Their report provides an elegant demonstration of complementarity of function of the receptor subtypes (*2*). We would like to draw attention to a potentially important implication of the results for network behavior. NR2A-containing receptors, unlike NR2B-containing receptors, are located almost exclusively within synapses (*3*–*5*). Therefore, the balance of LTP and LTD in a cell could reflect the degree to which synaptic, as opposed to extrasynaptic, receptors are activated. Liu *et al*. modestly omitted reference to a previous study from the same group supporting precisely this principle (*6*).

Taken together with recent evidence that extrasynaptic spillover of glutamate is detected exclusively by NR2B-containing NMDA receptors (*7*–*9*), these findings provide a novel mechanism for homeostatic regulation of excitatory transmission (*10*) and for sharpening pattern storage in the neuronal network. An elevation in ambient glutamate, released from multiple synapses and sensed by extrasynaptic NR2B-containing receptors, should trigger widespread LTD if accompanied by neuronal depolarization (Fig. 1). This does not preclude induction of LTP at synapses where glutamate is released and opens synaptic NR2A-containing receptors. The higher affinity of NR2B- than NR2A-containing receptors for glutamate (*11*) is well suited to their proposed role in weakening transmission as a function of heterosynaptic activity.

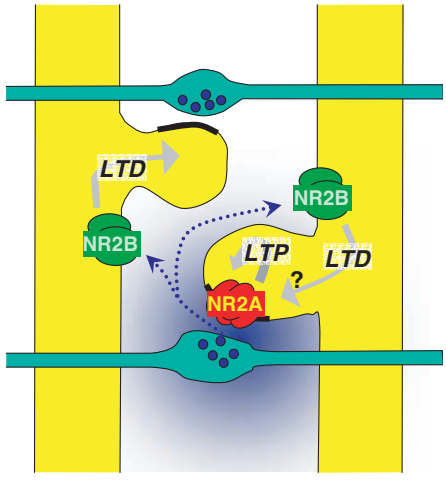

Fig. 1. NR2B-containing receptors (unlike NR2A-containing receptors) occur in the extrasynaptic membrane. Glutamate escaping from synapses selectively activates NR2B-containing receptors (dotted arrows). The selective coupling of NR2A- and NR2B-containing receptors to LTP and LTD, respectively (*1*), provides a mechanism for homeostatic plasticity if homosynaptic LTP is accompanied by heterosynaptic LTD. The model also implies that LTP induction overrides or precludes LTD at the same synapse, indicated by the question mark.

Differential activation of NR2A- and NR2B-containing receptors by synaptic and extrasynaptic glutamate also has distinct consequences for gene transcription (*12*). Finally, because the relative density of synaptic and extrasynaptic NR2A- and NR2B-containing receptors changes with age (*3*, *13*, *14*), their complementary roles in synaptic plasticity may be developmentally regulated.

Dmitri A. Rusakov*
Annalisa Scimemi
Matthew C. Walker
Dimitri M. Kullmann*
Institute of Neurology
University College London
Queen Square
London WC1N 2BG, UK
**To whom correspondence should be addressed.*
E-mail: d.kullmann@ion.ucl.ac.uk (D.M.K.); d.rusakov@ion.ucl.ac.uk (D.A.R.)

References

1. L. Liu *et al.*, *Science* **304**, 1021 (2004).
2. T. V. P. Bliss, R. Schoepfer, *Science* **304**, 973 (2004).
3. G. Stocca, S. Vicini, *J. Physiol.* **507**, 13 (1998).
4. K. R. Tovar, G. L. Westbrook, *J. Neurosci.* **19**, 4180 (1999).
5. F. Steigerwald *et al.*, *J. Neurosci.* **20**, 4573 (2000).
6. H. C. Lu, E. Gonzalez, M. C. Crair, *Neuron* **32**, 619 (2001).
7. N. O. Dalby, I. Mody, *J. Neurophysiol.* **90**, 786 (2003).
8. A. Scimemi, A. Fine, D. M. Kullmann, D. A. Rusakov, *J. Neurosci.* **24**, 4767 (2004).
9. N. A. Lozovaya *et al.*, *J. Physiol.* **558**, 451 (2004).
10. G. G. Turrigiano, S. B. Nelson, *Nature Rev. Neurosci.* **5**, 97 (2004).
11. T. Kutsuwada *et al.*, *Nature* **358**, 36 (1992).
12. G. E. Hardingham, Y. Fukunaga, H. Bading, *Nature Neurosci.* **5**, 405 (2002).
13. E. D. Kirson, Y. Yaari, *J. Physiol.* **497**, 437 (1996).
14. J. H. Li *et al.*, *Eur. J. Neurosci.* **10**, 1704 (1998).

4 June 2004; accepted 11 August 2004

Response to Comment on "Role of NMDA Receptor Subtypes in Governing the Direction of Hippocampal Synaptic Plasticity"

As a result of the differential (intrasynaptic versus extrasynaptic) localization and agonist affinity of NR2A-containing and NR2B-containing *N*-methyl-D-aspartate receptors (NMDARs), Rusakov *et al*. (*1*) propose that the production of long-term potentiation (LTP) versus long-term depression (LTD) in a cell might depend on the degree to which synaptic and extrasynaptic NMDARs are activated. We alluded to this idea in a previous study (*2*) but did not discuss it further in (*3*).

Although a substantial amount of NR2B subunits are localized at extrasynaptic sites (*4*–*6*), they are also expressed in hippocampal synapses of adult rats (*7*). We argue that it is the activation of these synaptic NR2B-containing NMDARs that produced the CA1 LTD in our study (*3*) for the following reasons. First, we demonstrated that about 30 to 40% of evoked NMDAR-mediated synaptic currents at CA1 synapses were sensitive to NR2B antagonists (*3*) and, more important, that a similar proportion of spontaneously occurring miniature excitatory postsynaptic currents (mEPSCs) were sensitive to the same antagonists (Fig. 1). Because mEPSCs are primarily activated by glutamate spontaneously released from presynaptic terminals (as opposed to spillover from adjacent synapses), functional NR2B-containing NMDARs must have been present within CA1 synapses in the adult rats used in our study. Second, if activation of extrasynaptic NMDA receptors by glutamate spillover is responsible for the induction of LTD, one might expect that high-frequency stimulation, rather than low-frequency stimulation, would be more likely to produce LTD, because it should cause more spillover. However, high-frequency and low-frequency stimulation produce LTP and LTD, respectively. Finally, the CA1 LTD shown in (*3*) is the homosynaptic type that has a high degree of input specificity. Such specificity can only occur after the activation of synaptic NMDARs because the activation of extrasynaptic NMDARs by glutamate spillover would be expected to produce a heterosynaptic LTD in nearby synapses. As noted in (*1*), that the majority of extrasynaptic NMDARs are NR2B-containing might explain why bath application of NMDA produces LTD in hippocampal neurons in both brain slices (*8*) and primary cultures (*2*). Together, these results are consistent with the idea that, regardless of their synaptic or extrasynaptic localization, sufficient activation of NR2B-containing receptors can lead to the induction of CA1 LTD.

We agree with Rusakov *et al*. (*1*) that the higher affinity for glutamate of NR2B receptors (*9*) makes extrasynaptic NR2B-containing NMDARs well suited to sense glutamate spillover from strongly activated synapses. This could be one of the mechanisms underlying homeostatic regulation of excitatory transmission (*10*), but there are potential pitfalls to consider. Because the induction of NMDAR-dependent LTD typically requires a temporal stimulation threshold of at least several minutes (*3*, *11*, *12*), the activation of extrasynaptic NR2B-containing receptors may not be sufficiently sensitive as a feedback mechanism for the maintenance of synaptic homeostasis. Moreover, heterosynaptic LTD in an unstimulated pathway after the induction of LTP in another pathway appears not to require the activation of NMDARs (*13*). Nonetheless, Rusakov *et al*. raise interesting ideas that should provoke more research into the physiological effects of activation of extrasynaptic NMDARs during conditions of glutamate spillover.

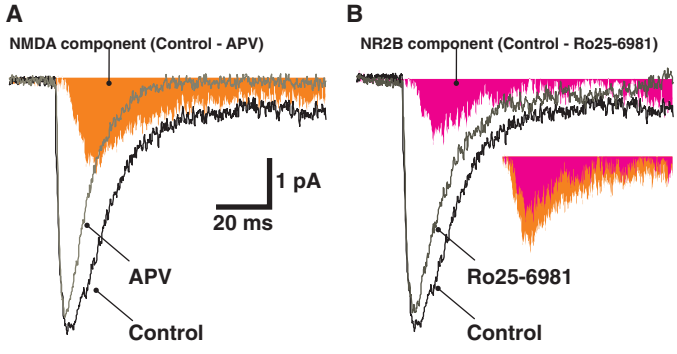

Fig. 1. Evidence for the presence of functional synaptic NR2B-containing NMDA receptors in CA1 hippocampal neurons from 3-week-old rats. Spontaneous mEPSCs were recorded in whole-cell voltage-clamp mode at a holding membrane potential of −60 mV in the presence of tetrodotoxin (0.3 μM) and bicuculline (10 μM) in artificial cerebral spinal fluid with no Mg^{2+} added. (**A**) Examples of mEPSC traces (averaged from 100 individual events) obtained in the absence and presence of the broad spectrum NMDA receptor antagonist APV (50 μM) demonstrate that, under this recording condition, mEPSCs comprise both α-amino-3-hydroxy-5-methyl-isoxazole-4-propionic acid (AMPA) and NMDA receptor–mediated components. The AMPA component (APV), isolated by recording of mEPSCs in the presence of APV, was completely blocked by non-NMDA receptor antagonist DNQX (data not shown). The NMDA component (orange) was obtained by subtracting the AMPA component (APV) from control mEPSCs (control). (**B**) Examples of averaged mEPSC traces illustrate pharmacological isolation of the component of mEPSCs mediated by NR2B-containing NMDA receptors (pink). The NR2B component was obtained by subtracting mEPSCs recorded in the presence of a specific NR2B-containing NMDA receptor antagonist Ro25-6981 (1 μM; Ro25-6981) from control mEPSCs (control). The inset shows the overlay of the NR2B component [pink area in (B)] with the total NMDA component [orange area in (A)]. On average, the NR2B-containing receptor-mediated component accounts for 38.9 ± 6.7% of the synaptic NMDA current (n = 3).

Tak Pan Wong
Lidong Liu
Brain Research Centre and Department of Medicine
University of British Columbia
2211 Wesbrook Mall
Vancouver, BC, V6T 2B5, Canada

Morgan Sheng
The Picower Center for Learning and Memory
RIKEN-MIT Neuroscience Research Center
Howard Hughes Medical Institute
Massachusetts Institute of Technology
77 Massachusetts Avenue (E18-215)
Cambridge, MA 02139, USA

Yu Tian Wang*
Brain Research Centre and Department of Medicine
University of British Columbia
**To whom correspondence should be addressed.*
E-mail: ytwang@interchange.ubc.ca

References

1. D. A. Rusakov, A. Scimemi, M. C. Walker, D. M. Kullmann, *Science* **305**, 1912 (2004); www.sciencemag.org/cgi/content/full/305/5692/1912b.
2. W. Lu *et al.*, *Neuron* **29**, 243 (2001).
3. L. Liu *et al.*, *Science* **304**, 1021 (2004).
4. J. H. Li *et al.*, *Eur. J. Neurosci.* **10**, 1704 (1998).
5. F. Steigerwald *et al.*, *J. Neurosci.* **20**, 4573 (2000).
6. K. R. Tovar, G. L. Westbrook, *J. Neurosci.* **19**, 4180 (1999).
7. G. Köhr *et al.*, *J. Neurosci.* **23**, 10791 (2003).
8. H. K. Lee, K. Kameyama, R. L. Huganir, M. F. Bear, *Neuron* **21**, 1151 (1998).
9. T. Kutsuwada *et al.*, *Nature* **358**, 36 (1992).
10. G. G. Turrigiano, S. B. Nelson, *Nature Rev. Neurosci.* **5**, 97 (2004).
11. T. Mizuno, I. Kanazawa, M. Sakurai, *Eur. J. Neurosci.* **14**, 701 (2001).
12. B. Mockett, C. Coussens, W. C. Abraham, *Eur. J. Neurosci.* **15**, 1819 (2002).
13. M. Scanziani, R. C. Malenka, R. A. Nicoll, *Nature* **380**, 446 (1996).

7 July 2004; accepted 31 August 2004

ECOLOGY

A Checkered History

Chris D. Jiggins

On the Wings of Checkerspots
A Model System for Population Biology
Paul R. Ehrlich and Ilkka Hanski, Eds.
Oxford University Press, New York, 2004. 391 pp. $64.50, £40. ISBN 0-19-515827-X.

The spring day in 1960 when Paul Ehrlich caught his first bay checkerspot, *Euphydryas editha*, on Jasper Ridge in California was perhaps the butterfly ecology equivalent of Thomas Hunt Morgan bottling his first *Drosophila melanogaster*. Up until then, population ecology had tended to concentrate on very common species or those with boom and bust population cycles, and Ehrlich was looking for an unexceptional study organism with small, stable populations that would exemplify a "normal" species. He could hardly have envisaged that this butterfly would mark the beginning of over 30 years of intensive study of related species on both sides of the Atlantic. *On the Wings of Checkerspots* documents that research effort, which focused primarily on two species: *E. editha* in North America and the Glanville fritillary, *Melitaea cinxia*, in Europe. Sadly, the story also includes the eventual extinction, in the late 1990s, of the bay checkerspot populations at Jasper Ridge.

It is only by understanding the natural history of a species that general ecological theory can be tested in the wild. As an example that is discussed in the volume, there is a considerable theoretical literature on the impact of spatial habitat heterogeneity on population dynamics and persistence, but only scarce empirical evidence relates to this problem, much of it provided by checkerspots. On the Åland Islands in Finland, *Melitaea cinxia* has two major hosts, *Plantago lanceolata* and *Veronica spicata*. Local patches tend to be dominated by one or the other, leading to a heterogeneous patchwork of habitats. Many years of detailed annual censuses in this connected network of butterfly populations have led to the development of models that can be used to investigate the impact of this spatial heterogeneity on population extinction and colonization (*1*). It was found that an empty patch dominated by *Plantago* was more likely to be colonized by *M. cinxia* if the surrounding patches were also dominated by that host plant, and the equivalent pattern was found for *Veronica* patches. Experiments demonstrated that this differential success is due to local adaptation of butterflies in their host preferences (*2*). (In retrospect, it is perhaps unsurprising that if colonists are better adapted to the local conditions when they arrive at a patch, then they are more likely to establish a new population.)

This apparently simple result has far-reaching implications. Consider a network in which 80% of the checkerspot populations live in patches dominated by *Plantago* and 20% in *Veronica*-dominated sites. The *Veronica*-adapted genotypes can only persist if patches of their preferred habitat are sufficiently close to one another for frequent recolonization. If these patches are all isolated by surrounding *Plantago*, then the *Veronica*-adapted genotypes are likely to go extinct on a regional scale. The host-plant preferences also affect the survival probability of the whole system, because by making the *Veronica* habitat unavailable, the overall carrying capacity of the network is only 80% of what it could have been under a different spatial distribution of patches. Thus understanding the specific details of how *Melitaea cinxia* adapts to its hosts provides an elegant demonstration of how habitat heterogeneity impacts both the genetics of local adaptation and the probability of population survival.

Although the Jasper Ridge populations of *Euphydryas editha* came to a sorry end, it is to be hoped that their demise was not entirely in vain. There has been a strong emphasis on understanding population survival and extinction in checkerspot research that should be heeded by conservationists. For example, the repeated patterns of population extinction and colonization that have been so well documented in the Åland islands make it possible to separate the many factors that influence extinction risk. In particular, the relative influences of genetic and demographic factors on extinction are beginning to be understood in this system (*3*). This book should be required reading for all conservation biologists.

Furthermore, future butterfly ecologists will be inspired by the detailed observations of checkerspot natural history, which provide some of the most entertaining aspects of the volume. My favorite was Mike Singer's description of female *Euphydryas editha* dropping to the ground like stones and probing around hopelessly for nonexistent low-growing leaves on which to lay their eggs. This comic tragedy was the result of a recent host switch from the low-growing lousewort *Pedicularis semibarbata* to the erect annual *Collinsia torreyi*. Both species provided the chemical stimulus for oviposition behavior, but only the former has the low-growing leaves to which the butterflies are behaviorally adapted. The elegance of adaptation is easy to take for granted until things go wrong.

Threatened model metapopulation. The bay checkerspot (*Euphydryas editha bayensis*) inhabits sunny open grasslands in the San Francisco Bay area.

Studies of the checkerspot butterflies have provided major contributions to evolutionary and ecological theory over the last 30 years, notably in the fields of insect-plant coevolution and population dynamics. The editors and contributors have managed quite an achievement in bringing this work together with an overview of many aspects of checkerspot biology (including larval biology, reproductive dynamics, population genetics, phylogenetics, and comparative analysis). Furthermore, although the book is an edited volume with 15 contributors, it was obviously well planned and reads more like the work of a single author. Its structure could be a model for anyone wanting to write an overview of their particular research system. I strongly recommend *On the Wings of Checkerspots* to anyone interested in evolution, ecology, or entertaining and informative stories about butterflies.

The reviewer is in the Institute of Evolutionary Biology, University of Edinburgh, Ashworth Laboratories, West Mains Road, Edinburgh, EH9 3JT, UK. E-mail: chris.jiggins@ed.ac.uk

References
1. I. Hanski, *Oikos* **87**, 209 (1999).
2. I. Hanski, M. C. Singer, *Am. Nat.* **158**, 341 (2001).
3. J. Saccheri *et al.*, *Nature* **392**, 491 (1998).

INVERTEBRATE BIOLOGY

Lobster Tales

Esther Sternberg

For anyone who has ever savored a tender morsel of lobster drenched in butter and wondered what happened before the lobster reached the fork, *The Secret Life of Lobsters* provides a glimpse into this gastronomically most popular crustacean's world. The book has something for everyone, from behavioral neuroscientists to those interested in the tensions between people who catch lobsters and people who want to preserve their habitat. Journalist Trevor Corson writes in the tradition of John McPhee. He seamlessly interweaves tales of lobster biology and ecology with ocean geology and geography, alternating these with sketches of lobstermen and scientists whose livelihoods and careers depend on understanding *Homarus americanus*.

The Secret Life of Lobsters
How Fishermen and Scientists Are Unraveling the Mysteries of Our Favorite Crustacean
by Trevor Corson

HarperCollins, New York, 2004. 299 pp. $24.95, C$34.95. ISBN 0-06-055558-0.

Like the lobsters themselves, Corson starts with mating behavior. As background, he provides a brief synopsis of early attempts to understand "how lobster sex works"—a vexing question given that the animal's essential parts are completely covered by an impenetrable shell. The answer is intriguing and amusing, as are the clever methods that modern scientists have devised to obtain it. These descriptions also illustrate how intimately the lobsters' sense of "smell" is linked to their mating and molting behaviors. The importance of this sensory pathway and its links to other behavioral responses surface again and again throughout the book. For example, molecules wafting into a lobster's antennules allow it to detect the intensity of chemical signals and move toward their source—whether "a tasty morsel of food or an alluring lobster of the opposite sex."

Sex leads to reproduction, and reproduction is the basis of provisioning New England's seas with more juvenile lobsters (which may eventually grow into those one to two pounders that land steaming on our plates). Because Corson's stories show not only how lobsters behave but also how they interact with their habitat and environment, the reader comes to appreciate how we cannot simply stop at detailed analyses of the neurophysiological basis of behavior, but must ultimately consider any behavior in the context of the wider world. This is most evident in Corson's descriptions of fighting.

It seems that, other than sex, the male lobster's greatest preoccupation is obtaining and defending a rocky shelter. To steal a home and then keep rivals out, male lobsters frequently engage in often violent contests, in which they may fight to the death or rip off each other's claws. Corson tells the fascinating story of how the vanquished male learns to recognize his winning opponent, another example of lobster behavior that depends on the critical sense of smell. Along with a shelter, the prize for the winner includes a line of females waiting patiently outside his door to mate. And the means by which a female lobster turns an aggressive male into an attentive and caring one (ready at her beck and call to protect her during and after mating) offers yet another example of the tight link between sensory inputs and behavioral responses that are critical for the survival of the species.

Through a quirk of anatomy, the lobster's bladder is located directly behind its eyes. Near the bladder is a gland that empties directly into the urinary tract, secreting chemicals and hormones that provide each lobster with its unique signature odor. When two male lobsters get into a fight, they literally get into a pissing match: "What the researchers discovered…was that dueling lobsters accompanied their most punishing blows during combat by intense squirts of piss at the opponent's face. What was more, in scenes akin to a showdown at the OK Corral, the winner of the physical combat almost always turned out to be the lobster that had urinated first." Lobsters use this approach to mating as well: "The dominant male waited in his shelter, peeing out the door of his apartment at the females who came calling. A female would poke her head in and pee back at her prospective mate, a love potion in her urine suppressing his bellicosity and putting him in the mood for courtship."

The fact that shelters are central to the behaviors of lobsters has other important implications. It turns out that only certain dimensions of crevices or burrows will do. Young lobsters range far and wide on the ocean floor to find appropriate housing, to mate, and to avoid being gobbled up by predators when they are small. Those of us who spend our lives on dry land tend not to think about the landscape beneath the waves. Just off the shore of the Maine coastline, one finds sandy bottoms, pebbly bottoms, and rocky bottoms. It has been found that topographies with just the right-sized rocks lie beneath lobster fishing grounds that lobstermen have known for centuries to be the most fertile. Indeed, in his tales of the lobstermen and their families, Corson describes how they, too, jealously guard their territories, with an unwritten code passed on through the generations.

Through these human stories, Corson illuminates the personal aspects of the conflicts among the lobstermen, environmentalists, and the scientists who would understand the "patterns, processes and mechanisms" that determine the lobster catch. The reader finds that all are concerned with the same problem—preventing the disappearance of this ancient crustacean—although they approach their common goal from their varied individual perspectives.

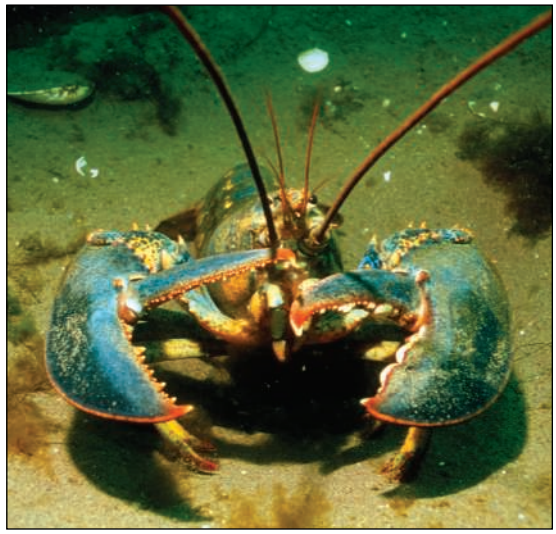

CREDIT: PETER SCOONES/SCIENCE PHOTO LIBRARY

My one complaint about Corson's fast-paced narrative is that the book lacks an index, which would have helped readers locate the many juicy tidbits of information embedded within it. (Those wishing to cook their own lobster will find an appendix that provides humane instructions, based on our knowledge of the animal's central nervous system, for doing so.)

The Secret Life of Lobsters reminds us that behavior only makes sense in the context of physical and social surroundings. Corson's engaging tales of lobster biology reveal the survival value of individual sensory inputs and behavioral patterns that allow lobsters to recognize and react to other lobsters and to negotiate the topography of the ocean floor. The book also demonstrates the intimate connections between humans and lobsters—and the need for lobstermen and scientists to work together (and compromise) if the lobster is to survive.

The reviewer is the author of *The Balance Within: The Science Connecting Health and Emotions*. Web site: www.esthersternberg.com

Published by AAAS

ECOLOGY

Globalization, Migration, and Latin American Ecosystems

T. Mitchell Aide and H. Ricardo Grau

The floods of 24 May 2004 and the tragic loss of thousands of lives in southeastern Haiti and Jimaní, Dominican Republic, provide important lessons for scientists, conservationists, and politicians. The same storm did not have such a devastating effect in neighboring Puerto Rico or in other regions of Dominican Republic, mainly because the highlands are forested. The mountains of southeastern Haiti, the major source of the flood, are quite a different story—they are virtually treeless. Sixty years ago, most of the mountains of Puerto Rico were also treeless, but forest recovered as the economy shifted from agricultural to industry and services (*1*). A similar process has occurred in Dominican Republic during the last 20 to 30 years; an increase in job opportunities in the cities associated with expanding tourism and textile industries stimulated rural-urban migration and forest recovery on the abandoned lands in the mountains. Other areas in Latin America are experiencing similar land-use dynamics as socioeconomic globalization extends its effects.

Enhanced online at www.sciencemag.org/cgi/content/full/305/5692/1915

In Latin America, conservation efforts have focused on lowland deforestation for cattle grazing and slash-and-burn agriculture, but the relative importance of these drivers of deforestation is declining. Today, soybean production—the majority of which is shipped to China for animal consumption—is the major cause of deforestation of millions of hectares of seasonally dry forests in Brazil, Bolivia, Paraguay, and Argentina (*2*, *3*). At the same time, rural-urban migration is leaving marginal grazing and agricultural lands abandoned. In rural areas, an important conservation strategy has been to invest in community-based sustainable development projects. These projects have had limited success in improving socioeconomic conditions and may delay rural-urban migration and ecosystem recovery. Current economic and demographic trends suggest that social and conservation policies should focus on preparing rural migrants for an urban environment and should promote ecosystem recovery in the lands that are abandoned.

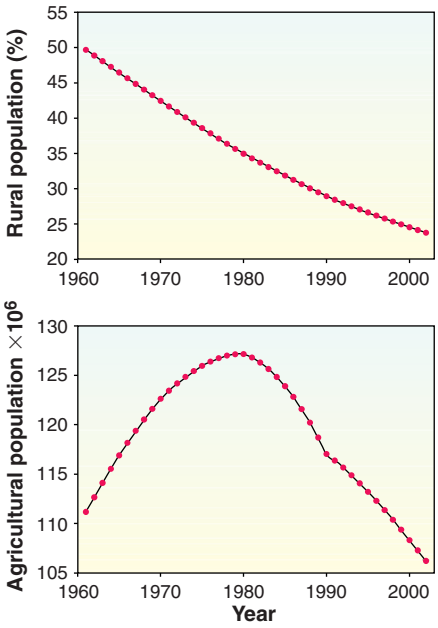

Changes in the rural and agricultural populations of Latin America and Caribbean (*14*). The agricultural population is defined as individuals whose livelihood directly depends on agriculture, hunting, fishing, or forestry.

During the last 40 years, the proportion of the population of Latin America and the Caribbean living in rural areas has dropped from about half to less than one-quarter (see figure above). More important, since 1980, the population whose livelihood directly depends on agriculture, hunting, fishing, or forestry has declined by about 20 million people (see figure above). Migration is particularly intense among those of economically active ages (*4*), who have the strongest impact on natural resources, and a growing proportion of the remaining "rural" inhabitants who depend on government subsidies, state employment, and money transfers from family members abroad.

What are the major factors driving rural-urban migration? In fertile lowlands and valleys, small farms have been bought and converted to large-scale modern agriculture, which frequently results in a decrease in the labor demand and rural-urban migration. In these areas, agriculture will continue to be the major use of land. The expansion of high-yield agriculture has decreased the prices of many crops and is indirectly influencing land-use practices in other regions. In Latin America, lower prices of corn, grain, coffee, potatoes, and beef have made it very difficult for small-scale farmers to compete, and this has contributed to the abandonment of marginal grazing and agricultural lands, particularly in the mountains. In other areas, rural migration has been stimulated by armed conflicts (Colombia), large-scale natural catastrophes such as hurricanes (Honduras), and international migration. Possibly, the most important factor influencing rural-urban migration, particularly for young people, is the cultural and economic attraction of urban life. Regardless of the motive for migrating, the abandonment of agricultural and grazing lands will facilitate ecosystem recovery. These recovering ecosystems will provide ecological services for the growing urban population and could support much of the biodiversity that has attracted widespread conservation interest to this region.

These economic, demographic, and land-use/land-cover dynamics or "forest transition" (*5*) are similar to what has occurred in Europe and North America; economies shift from agriculture to industry, cities grow, consumption increases, rural areas are abandoned, and forests recover. What is different is that Latin America has some of the highest levels of biodiversity in the world. Increasing forest in the mountains, and expanding cities and high-yield agriculture in the lowland and valleys present new opportunities and challenges for conservation; however, the consequences of this economic/demographic/ecological transition have received little attention. Most current tropical conservation research focuses on the drivers of deforestation (e.g., agriculture expansion, timber extraction, infrastructure development) (*6*), and its ecological consequences: carbon emissions (*7*), habitat destruction and fragmentation (*8*), and biodiversity loss (*9*). Although deforestation continues in many regions of Latin America, a decreasing rural population has tremendous implications for conservation as reduced human pressure often allows ecosystem and biodiversity recovery.

Many tropical ecosystems can recover fast with little or no intervention when previous land use has not severely degraded the

T. M. Aide is in the Department of Biology, University of Puerto Rico, San Juan, PR 00931–3360. E-mail: tmaide@yahoo.com. H. R. Grau is in the Laboratorio de Investigaciones Ecológicas de las Yungas, Universidad Nacional de Tucuman Casilla de Correo 34 (4107), Yerba Buena, Tucuman, Argentina. E-mail: chilograu@yahoo.com.ar

Published by AAAS

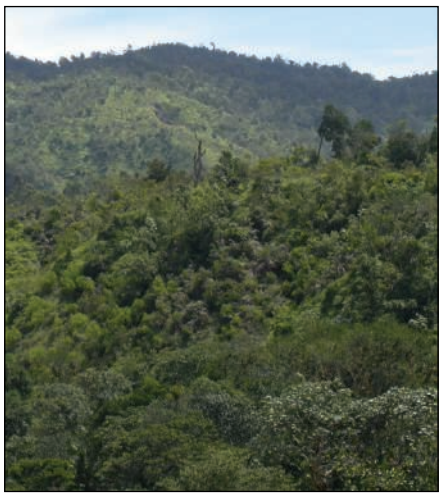

Recent transformation of subtropical dry forest (Chaco) in northwest Argentina into soybean fields contrasted with (right) forest regeneration in abandoned agricultural lands in a montane region of Dominican Republic.

soils. For example, in Puerto Rico, forest-cover increased from <10% to >40% in about 60 years, following the abandonment of agricultural and grazing lands (*1*). Virtually all the recovering forests are in the mountains, reducing erosion and floods, improving water quality, and providing habitat for many organisms. Rapid ecosystem recovery has also occurred in the 400-year-old pastures and fields formerly covered with dry forest in the Area de Conservación (ACG), northwestern Guanacaste, Costa Rica. In the 1980s, reductions in global trade tariffs reduced beef prices, and cattle production in Guanacaste declined by 90% facilitating the addition of 60,000 hectares to the ACG. By removing cattle and controlling anthropogenic fires, in 20 years, seed dispersal from forest fragments has converted a landscape previously dominated by cattle pasture on highly degraded soil into young forest (*10*). Furthermore, the fauna, including a stable population of jaguars, is recovering (*11*). Similar patterns of ecosystem recovery following rural-urban migration have been documented in forested (e.g., Patagonia, northwest Argentina, Ecuador, Mexico, Honduras, and Dominican Republic) and nonforested ecosystems (e.g., montane deserts and Andean tundra ecosystems of Bolivia, Argentina, and Peru). Although the potential for wide-scale recovery is encouraging, the land-use history of many areas has caused severe degradation, and recovery can be slow or arrested when invasive species, such as African grasses or ferns, dominate recently abandoned pastures or agricultural fields. Although other factors (e.g., global climate change) will influence the future of ecosystems in Latin America, the interactions we have described between natural and social systems suggest that research and management of ecological recovery/restoration should become better integrated into land-use policy and conservation agendas.

The global human population is expected to grow to about 9 billion people during the next 50 years, and resource consumption rates are increasing. Thus, we must efficiently use the world's resources to balance the growing human population and their food, health, and educational needs with the need to conserve the world's biodiversity and ecosystems services (*12*). Present strategies of opposing high-yield agriculture and discouraging rural-urban migration do not help to resolve these challenges. The globalization process, including high-yield agriculture, has neglected many environmental and social issues. These issues must be resolved, but at the same time, we must continue to invest in research and development to ensure the most efficient and long-term use of our agricultural lands. If agricultural activities are concentrated in the most productive soils, then other areas, particularly areas with marginal soils or steep slopes, can be dedicated to producing water and providing habitat for bioconservation and recreation. This balancing act will be difficult to achieve, but it will be much easier if we continue to improve agriculture efficiency and support population urbanization where social issues (e.g., health, education, and job opportunities) can be resolved more efficiently.

Effects of the 24 May 2004 flood on the border town of Jimaní, Dominican Republic.

The growing human population, biodiversity loss, and economic globalization are expected by many people to result in an ominous future for our planet. We do not have to accept this scenario, but we do have to understand how these and other important factors interact to create alternative scenarios, and to enact effective policies that ensure a more promising future. Technological improvements that have increased agricultural productivity and land-use efficiency and an increase in rural-urban migration are positive signs.

One week after the tragic floods in Haiti and Dominican Republic, we have read dozens of newspaper reports and only two have mentioned the extensive deforestation in Haiti and its relation to the floods. Clearly the emphasis has been on the human tragedy, and there are many immediate problems that must be resolved, but we should not allow this event to pass without learning from it. Twenty years ago, few people would have predicted a simultaneous increase in forest cover and Gross Domestic Product (GDP) in Dominican Republic and Puerto Rico (*13*). These examples challenge the conservation paradigm of a negative effect of economic growth on forest cover. To be effective, conservation action and land-use policy need to be more responsive to the dynamics of a changing world and to the opportunities that globalization provides. The social and ecological systems of Haiti, Latin America, and the developing world depend on these actions.

References and Notes

1. H. R. Grau *et al.*, *Bioscience* **12**, 1159 (2003).
2. P. M. Fearnside, *Environ. Conserv.* **28**, 23 (2001).
3. H. R. Grau *et al.*, *Environ. Conserv.* in preparation.
4. D. Preston, in *Latin America Development: Geographical Perspectives*, D. Preston, Ed. (Longman Scientific & Technical, Harlow, England, 1996), pp. 165–187.
5. A. S. Mather, C. Needle, *Area* **30**, 117 (1998).
6. H. J. Geist, E. F. Lambin, *Bioscience* **52**, 143 (2002).
7. R. A. Houghton, *Tellus* **51B**, 298 (1999).
8. W. Laurence *et al.*, *Conserv. Biol.* **16**, 605 (2002).
9. R. P. Dirzo, P. H. Raven, *Annu. Rev. Environ. Res.* **28**, 137 (2003).
10. D. H. Janzen, *Handbook of Ecological Restoration,* vol. 2, *Restoration in Practice*, M. R. Perrow, A. J. Davy, Eds. (Cambridge Univ. Press, Cambridge, 2002), pp. 559–583.
11. D. H. Janzen, personal communication.
12. P. E. Waggoner, J. H. Ausubel, *Popul. Dev. Rev.* **27**, 239 (2001).
13. A. E. Lugo, *Landscape Ecol.* **17**, 601 (2002).
14. FAOSTAT data, 2004, accessed 29 May 2004.

15. Support was provided by an Institutional Research Award from NASA and the Inter-American Institute for Global Change Research. We thank A. Grau, M. del Carmen Ruiz-Jaen, and N. Rios for their comments on the manuscript.

GEOPHYSICS

Silent Heralds of Megathrust Earthquakes?

Alfred Hirn and Mireille Laigle

During an earthquake, rupture propagates along the fault plane within a few tens of seconds. Much slower rupture, lasting for weeks or months, has recently been observed in slip transients or slow earthquakes (*1*, *2*). These events are also dubbed "silent earthquakes," because seismometers cannot sense any seismic waves during rupture. Silent earthquakes share their source region with that of low-frequency seismic waves (*3*–*5*), akin to the seismic tremor known to occur in volcanoes where it is attributed to fluids trapped in cracks or conduits.

Silent earthquakes and seismic tremor do not cause strong, sudden ground motion, and are hence not considered hazardous. However, they occur in subduction zones where 90% of Earth's destructive seismic energy is released in large-magnitude ($M >$ 7.0) megathrust earthquakes. Monitoring and interpreting such events may improve our understanding of the stress build-up in subduction zones and help in forecasting large future earthquakes (*6*). The documented examples of this activity are in regions where megathrust events are expected: the Nankai subduction zone in Japan and, most recently, the Cascadia subduction zone in the Pacific, off Washington state and western Canada (*7*).

In Japan, low-noise seismometer arrays have discovered deep nonvolcanic seismic tremor in the Nankai subduction zone, where at least nine great ($M > 8.0$) earthquake sequences have occurred in the historical record at intervals of one or two centuries, with devastating consequences. The tremor is attributed to water that has been liberated by metamorphism of the subducting Philippine sea plate and is trapped under the forearc crust (*3*). Intraslab earthquakes have been linked to such metamorphism (*8*). Seismic exploration has also elucidated the interplate fault region and its possible water content (*9*, *10*). For example, high pore-fluid pressure has been imaged in the Tokai segment (*6*) and suggested as a cause of the silent earthquake detected there.

In the Cascadia subduction zone, a silent earthquake was detected (*1*) with space-geodetic, Global Positioning System (GPS) arrays, which sense the slow motion of Earth's surface over several hundred kilometers. Seismic tremor occurred in the same time span, from sources in the region where the silent earthquake slip occurred. This activity, called episodic tremor and slip (ETS), was predicted to recur in Cascadia every 14 months, with the latest event predicted for July 2004 (*11*). The expected ETS event was observed from 8 to 24 July, with the slip migrating northward from Puget Sound, Washington, to Vancouver Island at the northern end of the Cascadia subduction zone. Two significant (M = 5.8 and 6.4) earthquakes were also detected off Vancouver Island. The event was preceded by another, unexpected episode of tremor and slip beginning in late April; this event may have moved southward into northern California and terminated at the southern end of the subducting slab (*7*).

The belt of tremor sources associated with the Nankai subduction zone (see the

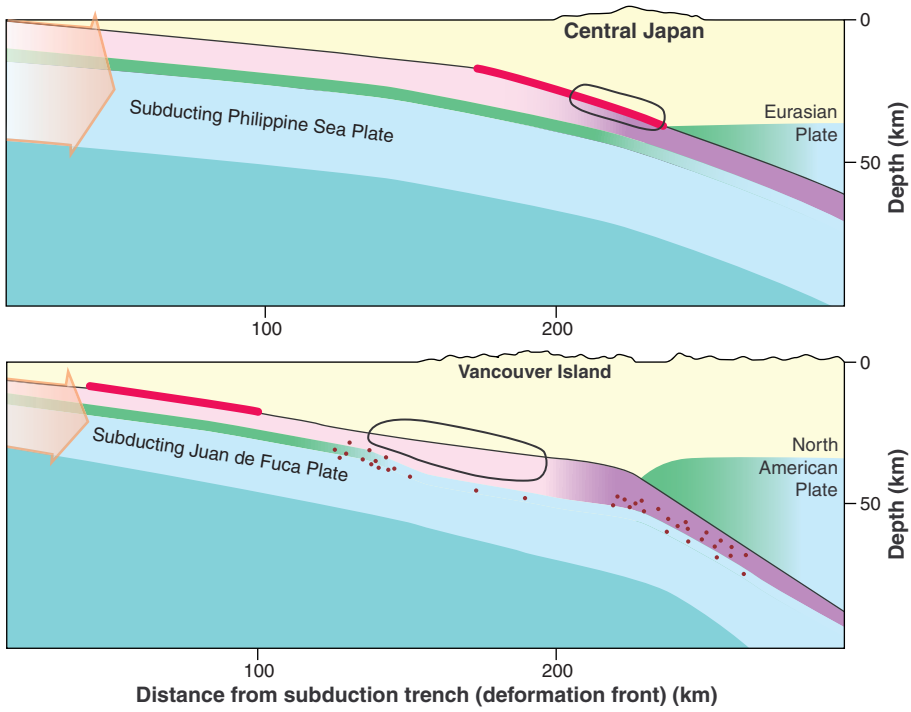

Cross sections of the Nankai and Cascadia subduction zones. The two panels show the forearc regions between the subduction trench and volcanic arc, which are 50 km on either side of the figure. Megathrust earthquakes are thought to occur on the seismogenic part of the dipping interplate boundary (red lines). Silent earthquakes and nonvolcanic seismic tremor sources are thought to occur in the circled regions. In the Cascadia subduction zone, these events occur downdip of the megathrust seismogenic zone (**bottom**), whereas in the Tokai part of the Nankai subduction zone, they occur on the megathrust seismogenic zone (**top**). They are likely related to water fed under the forearc crust by dehydration of the subducting plate. No such events are recorded in the Kanto part of the Nankai subduction zone, as discussed in the text.

The authors are at the Laboratoire de Sismologie Expérimentale, CNRS 7580 Département de Sismologie de l'Institut de Physique du Globe de Paris, 4 pl. Jussieu, 75252 Paris, France. E-mail: hirn@ipgp.jussieu.fr, laigle@ipgp.jussieu.fr

Published by AAAS

figure, top panel) also terminates abruptly to the northeast of Tokai, consistent with a lateral edge to the subducting slab. The slab itself appears to be split apart widely downstream of Mount Fuji. No seismic tremor is detected in the region east of Mount Fuji to the outskirts of Tokyo, the site of the 1923 Kanto (M = 7.9) earthquake, where the other part of the slab is subducting. In the latter area, water thus appears not to be trapped under the forearc crust, but originates in a deeper section of the slab and reacts with the forearc mantle to form serpentinite (*12*). The liberation of water at larger depth than in the other cases cited may be explained by the cold Pacific plate that rapidly subducts beneath the slab and cools the overlying mantle. Water thus moderates the size of the megathrust earthquake by limiting the extent of rupture to above the stably gliding serpentinized arc mantle (*13*).

When seismic tremor signals the presence of water beneath the forearc crust, water may also contribute to the development of silent earthquakes. Along the Nankai belt of tremor sources, silent earthquakes occur only on the Tokai segment (see the figure, top panel), in the same region where a megathrust earthquake is believed to be overdue. Megathrust earthquakes result from a stick-slip frictional instability on the interplate fault (*14*). A stick-slip segment can be unclamped by lowering the effective compressive normal stress. It can then still participate in the megathrust earthquake rupture, but the latter cannot nucleate on it. Such a scenario has been suggested to occur in the upperpart of the Hellenic subduction zone, due to the extra weight of a slab that is rolling back (*15*).

The deeper part of the Tokai megathrust rupture zone could be similarly unclamped, here by an increase of pore-fluid pressure on the interplate fault, as imaged by Kodaira *et al*. (*6*). In their simple earthquake-slip model, the block unclamped by pore-fluid pressure under the forearc crust would experience silent earthquakes before the megathrust earthquake. The absence of silent earthquakes on the other segments of Nankai is then consistent with more recent rupture on these segments. Silent earthquakes could herald their evolution to preseismic stage, because the seismic tremor indicates water availability, although this may be modulated by local structure.

In the Cascadia subduction zone, seismic tremor and silent earthquakes occur downdip of where the interplate is presently locked (see the figure, bottom panel). This is very different from Nankai, as is the specific one-to-one coincidence of their occurrence as events on the order of a week or more with migration or propagation over hundreds of kilometers along the unlocked interplate where it is not in stick-slip condition. They appear to be confined to the forearc crust, consistent with water being trapped here from the slab beneath, and the long-term slip could comprise here a succession of transient episodes of fluid flow at the interplate boundary. Further down, water enters the arc mantle instead, and the resulting serpentinite above the interplate enables smooth, continuous gliding (*13*).

These newly discovered seismic phenomena and inferred structural signatures provide an unprecedented opportunity to understand subduction and elucidate the processes that lead to major earthquakes. The search for silent earthquakes and seismic tremor should now be extended to other subduction zones, while the unexpected episode of tremor and slip mentioned above illustrates the need for more in-depth studies in Nankai and Cascadia. New continuous GPS arrays and low-noise seismometer arrays extending to the ocean-bottom are required. Furthermore, seismic exploration should be used to further elucidate the architecture and water content of interplates and their walls.

References and Notes

1. H. Dragert, K. Wang, T. S. James, *Science* **292**, 1525 (2001).
2. S. Osawa *et al.*, *Science* **298**, 1009 (2002).
3. K. Obara, *Science* **296**, 1679 (2002).
4. A. Katsumata, N. Kamaya, *Geophys. Res. Lett.* 10.1029/2002GL015981 (2003).
5. G. Rogers, H. Dragert, *Science* **300**, 1942 (2003).
6. S. Kodaira *et al.*, *Science* **304**, 1295 (2004).
7. See www.pnsn.org.
8. L. P. Preston *et al.*, *Science* **302**, 1197 (2003).
9. M. R. Nedimovic, R. H. Hyndman, K. Ramachandran, G. D. Spence, *Nature* **424**, 416 (2003).
10. A. J. Calvert, *Nature* **428**, 163 (2004).
11. M. M. Miller, T. Melbourne, D. J. Johnson, W. Q. Sumner, *Science* **295**, 2423 (2002).
12. S. Kamiya, Y. Kobayashi, *Geophys. Res. Lett.* **27**, 819 (2000).
13. R. D. Hyndman, M. Yamano, D. A. Oleskevitch, *Island Arc* **6**, 244 (1997).
14. C. H. Scholz, *Nature* **391**, 37 (1998).
15. M. Laigle, M. Sachpazi, A. Hirn, *Tectonophysics*, 10.1016/j.tecto.2004.07.009 (2004).

BIOMEDICINE

A Fresh Look at BSE

Bruce Chesebro

Mad cow disease, or bovine spongiform encephalopathy (BSE), is the cattle form of a family of progressive brain diseases. These diseases include scrapie in sheep, Creutzfeldt-Jakob disease (CJD) in humans, and chronic wasting disease (CWD) in deer and elk. They are also known as either "prion diseases" because of the association of a misfolded cellular prion protein in pathogenesis or "transmissible spongiform encephalopathies" (TSEs) because of the spongelike nature of the damaged brain tissue (*1*).

The recent discovery of two BSE-infected cows, one in Canada and one in the United States, has dramatically increased concern in North America among meat producers and consumers alike over the extent to which BSE poses a threat to humans as well as to domestic and wild animals. The European BSE epidemic of the late-1980s seems to have been initiated a decade earlier in the United Kingdom by changes in the production of meat and bone meal (MBM) from rendered livestock, which led to contamination of MBM with the BSE infectious agent. Furthermore, the fact that UK farmers fed this rendered MBM to younger animals and that this MBM was distributed to many countries may have contributed to the ensuing BSE epidemic in the United Kingdom and internationally (*2*).

Despite extensive knowledge about the spread of BSE through contaminated MBM, the source of BSE in Europe remains an unsolved mystery (*2*). It has been proposed that BSE could be derived from a cross-species infection, perhaps through contamination of MBM by scrapie-infected sheep tissues (see the figure). Alternatively, BSE may have been an endemic disease in cattle that went unnoticed because of its low level of horizontal transmission. Lastly, BSE might have originated by "spontaneous" misfolding of the normal cellular prion protein into the disease-associated abnormal isoform (*3*), which is postulated to be the infectious agent or "prion."

Spontaneous protein misfolding is not a new phenomenon as proteins are known to sometimes misfold after synthesis. Cells in turn have devised ingenious ways to deal with this problem. These include molecular chaperone proteins that bind to misfolded proteins and help them to unfold, and organelles called proteosomes that degrade misfolded or unwanted proteins. However, although misfolded prion proteins have been generated in test tubes as well as in cultured cells, it has been difficult to

The author is in the Laboratory of Persistent Virus Diseases, Rocky Mountain Laboratories, National Institute of Allergy and Infectious Diseases, Hamilton, MT 59840, USA. E-mail: bschesebro@nih.gov

demonstrate that such misfolded abnormal prion proteins are infectious (*4*, *5*). Even the most recent data do not prove conclusively that infectivity has been generated in vitro because misfolded synthetic prion proteins were not able to transfer disease directly to wild-type mice (*6*). To obtain infectivity and subsequent prion disease, the misfolded proteins had to be inoculated and incubated for 1 to 2 years in transgenic mice that overexpressed a mutant version of the prion protein. Previous data from this group showed that transgenic mice expressing high amounts of prion protein developed neurological disease without inoculation of misfolded prion protein (*7*). Thus, at the biochemical level, the critical attributes of the misfolded prion protein required for infectivity are not known, and misfolding of prion protein alone may not be sufficient to generate an infectious agent (*8*).

Nevertheless, the idea that BSE might originate due to the spontaneous misfolding of prion proteins has received renewed interest in the wake of reports suggesting the occurrence of atypical BSE (*9*–*11*). These results imply that new strains of cattle BSE might have originated separately from the main UK outbreak. Where and how might such strains have originated? Although such rare events cannot be studied directly, any number of sources of the original BSE strain could also explain the discovery of additional BSE strains in cattle (see the figure). However, it would be worrisome if spontaneous BSE were really a valid etiology because such a mechanism would be impossible to prevent—unlike other possible scenarios that could be controlled by large-scale eradication of TSE-positive animals.

Another way to look at this problem is to examine evidence for possible spontaneous TSE disease in other animals besides cattle. Spontaneous BSE would be extremely difficult to detect in cattle, where horizontal spread is minimal. However, in the case of the sheep TSE disease, scrapie, which spreads from ewes to lambs at birth as well as between adults, spontaneous disease should be detectable as new foci of clinical infection. In the early 1950s scrapie was eradicated in both Australia and New Zealand, and the mainland of both these countries has remained scrapie-free ever since. This scrapie-free status is not the result of selection of sheep resistant to scrapie because sheep from New Zealand are as susceptible as their UK counterparts to experimental scrapie infection (*12*). These experiments of man and nature appear to indicate that spontaneous clinical scrapie does not occur in sheep. Similarly, because CWD is known to spread horizontally, the lack of CWD in the deer or elk of eastern North America but its presence in western regions would also argue against a spontaneous disease mechanism. This is particularly noteworthy in New Zealand, where there are large numbers of deer and elk farms and yet no evidence of spontaneous CWD. If spontaneous scrapie does not occur in sheep or deer, this would suggest that spontaneous forms of BSE and sporadic Creutzfeldt-Jakob disease (sCJD) are unlikely to be found in cattle or humans. The main caveat to this notion is that spontaneous disease may arise in some animal species but not others. In humans, sCJD—which is considered by some researchers to begin by spontaneous misfolding of the prion protein—usually takes more than 50 years to appear. Thus, in animals with a shorter life-span, such as sheep, deer, and cattle, an analogous disease mechanism might not have time to develop.

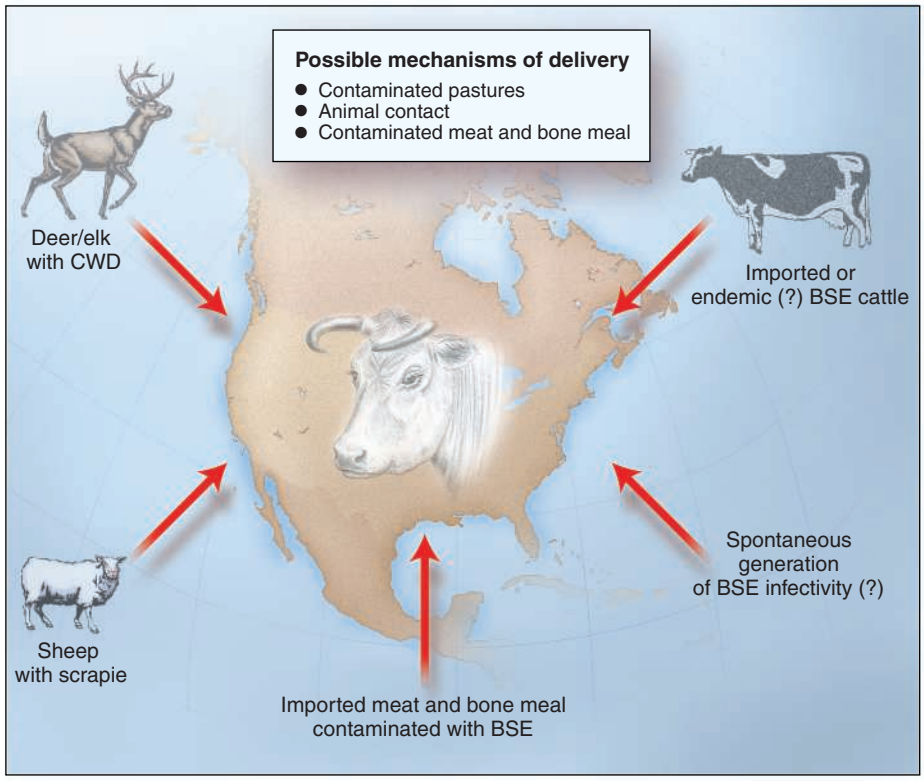

Five possible sources of BSE in North American cattle. Sheep, deer, and elk could spread prion diseases (TSEs) to cattle through direct animal contact or contamination of pastures. Endemic BSE has not been proven to exist anywhere in the world, but it is difficult to exclude this possibility because of the inefficient spread of BSE infectivity between individual animals (*2*). BSE caused by spontaneous misfolding of the prion protein has not been proven.

What can we conclude so far about BSE in North America? Is the BSE detected in two North American cows sporadic or spontaneous or both? "Sporadic" pertains to the rarity of disease occurrence. "Spontaneous" pertains to a possible mechanism of origin of the disease. These are not equivalent terms. The rarity of BSE in North America qualifies it as a sporadic disease, but this low incidence does not provide information about cause. For the two reported North American BSE cases, exposure to contaminated MBM remains the most likely culprit. However, other mechanisms are still possible, including cross-infection by sheep with scrapie or cervids with CWD, horizontal transmission from cattle with endemic BSE, and spontaneous disease in individual cattle. Based on our understanding of other TSEs, the spontaneous mechanism is probably the least likely. Thus, "idiopathic" BSE—that is, BSE of unknown etiology—might be a better term to describe the origin of this malady.

What does all this imply about testing cattle for BSE in North America? Current testing in the United States indicates that BSE is rare (one positive result in 40,000 cattle tested). However, additional testing of 200,000 head of slaughtered cattle over the next 1 to 2 years, as recently proposed by the U.S. Department of Agriculture (USDA), should tell us the incidence more precisely. Nevertheless, if any rare cases are detected, we may still not know their origin. If evidence arises of a focal occurrence of BSE, we might gain important insight into unexpected sources of contamination. However, because current tests do not seem to be able to detect BSE in infected animals less than 30 months of age, even more extensive testing will not com-

CREDIT: KATHARINE SUTLIFF/*SCIENCE*

pletely guarantee the negative status of younger animals in the food chain. Therefore, the alternative option of testing all slaughtered cattle, as implemented in some countries such as Japan, would appear to provide little additional benefit. This fact has been acknowledged as the basis for a new agreement between the United States and Japan aimed at reestablishing the beef trade between the two countries.

One problem with the current U.S. testing program was the announcement a few months ago of unconfirmed positive BSE tests in two additional North American animals that were subsequently found to be negative when tested with the more accurate method of Western blotting. The public release of information about unconfirmed positive tests detected by the rapid test used for mass screening may be a good idea in the interest of openness, but it has the potential to create unwarranted anxiety. If unconfirmed positives are a frequent occurrence, it would seem reasonable to follow a more cautious approach and wait until confirmatory testing is complete before publicly announcing the details.

Based on the experience of many European countries, the mainstays of controlling BSE in cattle and avoiding spread to humans are threefold: first, eliminate feeding of ruminant tissues to ruminants; second, remove high-risk cattle tissues from human food; and third, continue to test for BSE in cattle in order to monitor progress with the elimination of the disease on a local and national basis. In the next 12 months, after extensive USDA test results are available, the extent of any possible BSE spread in the United States will be better documented. But, in fact, the United States and Canada have already instituted the most important steps to prevent the spread of cattle BSE in advance of the results—that is, a ban on feeding ruminant MBM to other ruminants and removal of high-risk tissues from meat for human consumption. It is hoped that the new data will not deviate enough from previous predictions to require further measures for management of this problem. The most important line of defense against any possible spread of BSE will be to maintain strict vigilance in the implementation of the current regulations.

References

1. S. B. Prusiner, *Proc. Natl. Acad. Sci. U.S.A* **95**, 13363 (1998).
2. P. G. Smith, R. Bradley, *Br. Med. Bull.* **66**, 185 (2003).
3. C. Weissmann, A. Aguzzi, *Curr. Opin. Neurobiol.* **7**, 695 (1997).
4. A. F. Hill *et al.*, *J. Gen. Virol.* **80**, 11 (1999).
5. R. Chiesa *et al.*, *J. Virol.* **77**, 7611 (2003).
6. G. Legname *et al.*, *Science* **305**, 673 (2004).
7. D. Westaway *et al.*, *Cell* **76**, 117 (1994).
8. B. Chesebro, *Science* **279**, 42 (1998).
9. A. G. Biacabe *et al.*, *EMBO Rep.* **5**, 110 (2004).
10. Y. Yamakawa *et al.*, *Jpn. J. Infect. Dis.* **56**, 221 (2003).
11. C. Casalone *et al.*, *Proc. Natl. Acad. Sci. U.S.A.* **101**, 3065 (2004).
12. E. F. Houston *et al.*, *J. Gen. Virol.* **83**, 1247 (2002).

PHYSICS

Superfluidity in a Crystal?

Tony Leggett

Imagine that you place a small solid body—say, a coin—on the axis of an old-fashioned gramophone turntable, and set the latter into slow rotation. You would expect the coin to rotate with the turntable. But it will not do so if it is made of solid ^{4}He, according to Kim and Chan (see report in this week's issue on page 1941) (*1*).

In superfluid liquid helium, such a failure to rotate or, more technically, nonclassical rotational inertia (NCRI) was predicted by London 50 years ago (*2*). It was eventually verified experimentally by Hess and Fairbank (*3*), who set helium in a suspended bucket into rotation above the temperature T_c at which superfluidity sets in, and then cooled it (with the bucket still rotating at angular velocity ω) through T_c. They found that, provided ω is less than a critical value ω_c, the apparent moment of inertia of the helium—that is, the ratio of its angular momentum to ω—is not given by the classical value $I_{classical}$—but rather by

$$I(T) = I_{classical}[1 - f_s(T)] \qquad (1)$$

where $f_s(T)$ is the "superfluid fraction" as measured in other types of experiment (such as those on persistent currents or second sound). In liquid helium, $f_s(T)$ tends to 1 in the zero-temperature limit and to 0 when $T = T_c$. More recently, related behavior has been seen (*4*) in a Bose-Einstein condensate of an alkali gas.

The phenomenon of NCRI is, by definition, characteristic of the equilibrium state of the system, and is quantum-mechanical in origin; it should be carefully distinguished from the apparently similar phenomenon of persistent currents, which is a metastable effect. [The famous oscillating-disk experiment of Andronikashvili (*5*) is essentially a persistent-current experiment, because the angular velocity of the disks is much greater than ω_c, and the observed nonrotating state of the superfluid therefore cannot be the true equilibrium state].

The phenomenon of NCRI in liquid helium and in alkali gases is generally believed to be well understood [see, for example, (*6*)]. However, the explanation rests on two crucial assumptions: first, that the single-atom wave functions are extended over the whole system, and second, that the system has undergone Bose-Einstein condensation (BEC), that is, a finite fraction of all the atoms occupy the same one-particle state.

Can NCRI occur in a crystalline solid? This seemingly bizarre possibility was suggested as long ago as 1969 (*7*), and over the past 35 years, a number of experiments have searched for it without success. Kim and Chan measured the resonance frequency of a torsional oscillator that contains an annulus filled with solid ^{4}He. Below 230 mK, the frequency experiences a relative increase that depends on the temperature and drive amplitude and reaches a maximum of about four parts in 10^5. Having ex-

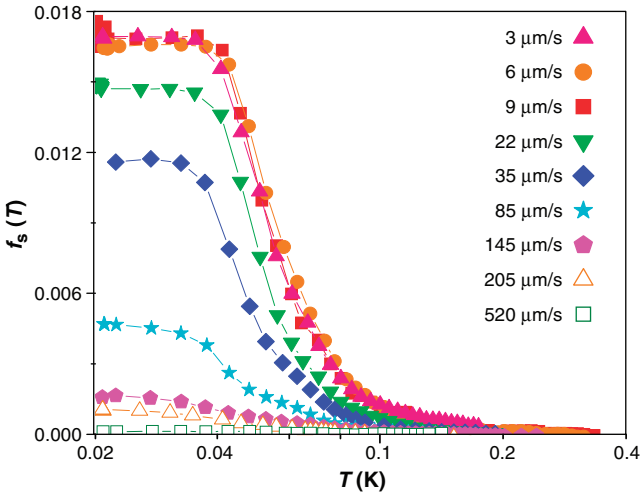

Signs of superfluidity. The superfluid fraction $f_s(T)$ inferred from the data in (*1*) as interpreted by Eq. 1, as a function of temperature for different values of the maximum velocity of the walls. The pressure is 41 bars. [Adapted from (*1*)]

The author is in the Department of Physics, University of Illinois, Urbana, IL 61801, USA. E-mail: aleggett@uiuc.edu

cluded, by various control experiments, other explanations, they conclude that the data indicate a change in the moment of inertia of the superfluid, which, according to Eq. 1, corresponds to a maximum superfluid fraction of ~1.7% (see the figure).

This experiment is in some sense intermediate between the Hess-Fairbank and Andronikashvili experiments: The angular velocity is lower than the critical value at the lowest drive amplitudes, but exceeds it for the higher ones. Furthermore, the temperature is established first and the sample rotated subsequently (rather than vice versa as in the Hess-Fairbank experiment). Hence, even when the rotational velocity is below critical, one cannot exclude the possibility that one is seeing a metastable effect (even this would be very surprising and interesting) rather than the thermodynamic equilibrium behavior, that is, true NCRI. In principle, it should be possible to test this possibility in future experiments that more closely resemble the Hess-Fairbank scheme. In any case, the most plausible interpretation, and the one drawn by the authors, is that NCRI is indeed occurring, with a superfluid fraction of ~1.7%.

If this conclusion is correct, the implications are revolutionary. If we make the standard assumption that, at sufficiently low temperatures (so that we can neglect thermal vacancies), each lattice site in a crystalline solid is occupied by a single atom, and if we moreover neglect exchange processes between neighboring atoms, then the system possesses neither of the two properties mentioned above as essential for NCRI in liquids or gases.

Thus, we appear to have only a few possibilities for explaining the observed behavior: First, the number of atoms is not equal to the number of lattice sites, that is, even at zero temperature there is a finite concentration of zero-point vacancies (which might then form extended vacancy waves and eventually undergo BEC). This hypothesis was the basis of the original 1969 suggestion (*7*), but experiments have since put severe limits on the number of such vacancies (*8*). Second, the experimental sample contains a large (possibly nonequilibrium) number of larger defects such as dislocations. Third, the number of atoms is indeed equal to the number of lattice sites, but as a result of exchange processes between neighboring atoms (which are known to occur at a non-negligible rate in solid ^{3}He), the system can nevertheless display NCRI.

This last scenario—which prior to the experiment of Kim and Chan would probably have been dismissed as implausible by the vast majority of workers in the field—raises a number of theoretical issues, including the question whether BEC is a necessary condition for NCRI in a bulk three-dimensional system such as helium. In any case, if the interpretation Kim and Chan give of their raw data is correct (and quite probably even if it is not!), their experiment will force theorists to revise dramatically the generally accepted picture of crystalline solid ^{4}He.

References

1. E. Kim, M. H. W. Chan, *Science* **305**, 1941 (2004); published online 2 September 2004 (10.1126/science.1101501).
2. F. London, *Superfluids* (Wiley, New York, 1954), vol. II, p. 144.
3. G. B. Hess, W. M. Fairbank, *Phys. Rev. Lett.* **19**, 216 (1967).
4. F. Chevy, K. W. Madison, J. Dalibard, *Phys. Rev. Lett.* **85**, 2223 (2000).
5. E. L. Andronikashvili, *J. Phys. USSR* **10**, 201 (1946).
6. A. J. Leggett, *Rev. Mod. Phys.* **73**, 307 (2001), section VI.
7. A. F. Andreev, I. M. Lifshitz, *Sov. Phys. JETP* **29,** 1107 (1969).
8. M. W. Meisel, *Physica B* **178**, 121 (1990).

Published online 2 September 2004
10.1126/science.1103584

ECOLOGY

Where Rivers Meet

Claude Gascon and Michael Leonard Smith

Seen from space, the Amazon basin is a green mat interrupted only by the branches of a massive river system (see the figure). Since the Amazonian expeditions of Alfred Russel Wallace in the 1850s, biogeographers have sought to clarify the forces driving the remarkable morphological and genetic diversity of terrestrial species in the Amazon basin, the world's richest biome (*1*, *2*). Several million years of evolution have produced a mosaic of overlapping morphologically and genetically distinct terrestrial species, resulting in areas of endemism (*3*). Much research has investigated the diversity of Amazonian terrestrial species, whereas freshwater species restricted to the Amazon and its many tributaries have been little studied. This oversight is now remedied by Fernandes *et al*. (*4*), who report on page 1960 of this issue the results of their comprehensive survey of electric fish species across a 2000-km transect of the Amazon basin.

The concentration of fish species in the Amazon beckons both biogeographers, who see in this diversity the power to resolve the details of geological changes and evolutionary processes, and conservationists, who wish to target their investments to places that offer the greatest payoffs in species protected per unit effort (*5*). The basic impediment to the endeavors of these two groups is the size of the Amazon basin—it is a big, wet place—and the stunning richness of its fish fauna. At what point can we feel we have mastered enough of the details to draw conclusions about the basic patterns of fish diversity and community structure within the basin? One approach is to concentrate sampling to all species within a monophyletic group (clade). Such a group has unitary properties and, if properly sampled, provides a logically coherent unit of analysis. This is just the approach taken by Fernandes *et al.* (*4*) in their remarkably thorough sampling of more than a thousand deep-water trawling stations along a 2000-km stretch of the mainstem Amazon and its tributaries. As their clade, they selected electric fishes belonging to the neotropical order Gymnotiformes, which reaches a peak of diversity in the Amazon basin.

Fernandes *et al.* studied the local effects of tributaries on the diversity of electric fishes. They made repeated trawls just upstream (above), in, and just downstream (below) of the confluence points where 13 major tributaries enter the Amazon mainstem. Their comprehensive survey yielded 43 electric fish species. The investigators discovered that tributaries have a large, but local, positive effect on mainstem species richness at confluences. Contrary to the downstream species-accumulation hypothesis (*6*), the authors did not detect an increase in the number of fish species as they sampled the Amazon further downstream. This suggests that the effects of tributaries are local and do not translate into an overall increase in species richness as one moves downstream.

The authors investigated the local effects of tributaries by comparing species diversity in the three types of station placement at each confluence (above, in, and below the tributary). Diversity was highest in the tributaries themselves, suggesting that the Amazon encounters distinct biogeographical units as it cuts across the basin. In addition, Fernandes and colleagues found that stations just below the tributary confluence points had significantly higher diversity than stations just above them. There are a number of possible explanations. When very large rivers meet, they may be able to retain their identities and perhaps their distinctive biotas for some distance, acting like two rivers in a shared channel (see the figure). Yet repeated mix-

The authors are with Conservation International, Washington, DC 20036, USA. E-mail: c.gascon@conservation.org; m.smith@ conservation.org

CREDIT: NASA

A bird's eye view of the mighty Amazon. The confluence of the Amazon River (mainstem, brown) and the Rio Negro River (tributary, black) at the city of Manaus. From space, most of the forested areas (green) appear homogeneous, as do many of the rivers. However, large-scale evidence points to the heterogeneous nature of the Amazon basin and the effects of this heterogeneity on distribution patterns of terrestrial and aquatic biodiversity. For freshwater systems, major tributaries join the mainstem Amazon River and increase species diversity immediately downstream of the confluence, but not upstream. This may be due to the river confluence providing conditions enabling both fish faunas (tributary and mainstem) to coexist over certain distances. The image suggests this possibility: The two rivers meet but remain distinct for a large distance downstream.

ing of such biotas, together with increased food availability and habitat stability, suggests that species should accumulate in a downstream direction.

Their extremely large sample enabled Fernandes *et al.* to carry out a test of this hypothesis on an unprecedented scale. They combined upstream and downstream samples at each confluence to obtain comprehensive estimates of richness at each site, and used rarefaction methods to estimate species richness in each section of the 2000-km stretch of river that they studied. They did not find any evidence to support the species accumulation hypothesis. Inspection of the species × site matrix data (kindly provided by the authors) shows that 18 electric fish species (41.2%) drop out progressively as one proceeds downstream, whereas only 5 species (11.6%) are added to the overall list from downstream stations. Despite the spikes in species richness below the confluence points where the tributaries enter the Amazon mainstem, diversity apparently returns to a lower state in the reaches between tributaries.

The pattern of electric fish diversity across a transect of the Amazon basin is strikingly similar to the general patterns of species richness seen in small terrestrial vertebrates of the Amazon basin. For example, amphibian species richness shows the greatest diversity on the flanks of the Andes, with attenuation eastward, that is, downstream (*7*). An increase in diversity from one site to another also characterizes much of the Amazon fauna, both terrestrial and aquatic, from the foothills to the lowlands. The exact driving forces behind these diversity patterns may vary by taxa (ancient geologic ridges in the case of some amphibians and small mammals, major rivers in the case of many primates, and tributaries in the case of freshwater fishes), but the biogeography and conservation implications are the same. First, we need to better bridge our evolutionary and ecological understanding of the forces driving species diversity for each group of taxa in order to better inform conservation planning. Second, freshwater aquatic biodiversity (especially that of fishes) is understudied and needs priority research like the Fernandes *et al*. study to establish a better and more comprehensive understanding of species distribution patterns. Finally, this and other studies continue to emphasize that lowland Amazonia is a very heterogeneous region and that its biodiversity is not evenly distributed, nor does it follow neat and clear overlapping patterns across taxonomic groups.

If we are to better manage the Amazon, we need to decide where to conserve biodiversity. We can only answer that question with detailed species-based information and analyses of distribution patterns of the kind presented by Fernandes and colleagues. Any other approach will be like trying to go up a river without a paddle.

References

1. J. M. Ayres, T. H. Clutton-Brock, *Am. Nat.* **140**, 531 (1992).
2. C. Gascon *et al.*, *Proc. Natl. Acad. Sci. U.S.A.* **97**, 13672 (2000).
3. J. M. C. Silva *et al.*, *Bull. Br. Ornith. Club* **115**, 200 (1995).
4. C. C. Fernandes *et al.*, *Science* **305**, 1960 (2004).
5. N. Myers *et al.*, *Nature* **403**, 853 (2000).
6. W. J. Matthews, *Patterns in Freshwater Fish Ecology* (Chapman & Hall, New York, 1998).
7. W. E. Duellman, *Ann. Mo. Bot. Gard.* **75**, 79 (1988).

MATERIALS SCIENCE

Smart Biomaterials

Daniel G. Anderson, Jason A. Burdick, Robert Langer

More than 2000 years ago, the Romans, Chinese, and Aztecs used biomaterials such as gold for dentistry. Yet it is only with the development of synthetic polymer systems in the past few decades that biomaterials have begun to find broad applications in modern medicine (*1*). A new wave of advances in cell biology, chemistry, and materials science is enabling the production of a new generation of smart biomaterials.

Minute nanofibers of various structures and chemistries are formed through simple self-association and organization of peptides and proteins (*2*). Several bioactive extracellular protein domains have been identified that can be incorporated as small peptides into nanofibers through simple modification of the peptide amino acid sequence. Nanofibers can be designed to present these peptide sequences at high density. Three-dimensional (3D) macroscopic gel-like solids can also present high densities of such bioactive peptides.

Applying molecular self-assembly, Silva *et al*. report a new 3D material capable of directing the differentiation of neural progenitor cells to a specific lineage without the help of growth factors (*3*) (see the figure, A). Stem and progenitor cells have the ability to differentiate into derivative tissues and have great potential for tissue repair or replacement. Typically, differentiation is controlled by soluble compounds such as growth factors. Silva *et al*. synthesized self-assembling peptide amphiphiles that present the pentapeptide epitope isoleucine-lysine-valine-alanine-valine (IKVAV). IKVAV is an amino acid sequence found in laminin, which promotes neurite adhesion, sprouting, and growth. These peptide amphiphiles self-assemble in aqueous media to form nanofibers with diameters of 5 to 8 nm and lengths several orders of magnitude higher. Macroscopically, these intermeshed fibers form highly hydrated 3D gels that are able to direct the rapid differentiation of encapsulated neural progenitors into neurons while discouraging the production of astrocytes. The inhibition of astrocyte prolifera-

The authors are in the Department of Chemical Engineering, Massachusetts Institute of Technology, Cambridge, MA 02139, USA. E-mail: rlanger@mit.edu

tion may prevent glial scar formation, which inhibits the regeneration and elongation of axons after central nervous system trauma.

Although the discovery of specific bioactive peptides has enabled the rational design of materials with the ability to control cell behavior, it is often unclear which chemical properties are necessary to provide this control. A high-throughput synthesis and screening platform for the testing of polymer-cell interactions can accelerate the discovery of such materials (*4*) (see the figure, B). Researchers have screened a library of polymers synthesized in nanoliter volumes for their effects on human embryonic stem (hES) cell growth and differentiation. There were numerous unexpected interactions: Some materials supported high levels of hES cell differentiation into epithelial-like cells, and others supported hES cell growth only in the absence of certain growth factors. Future studies combining rationally designed combinatorial libraries of biomaterials and high-throughput screening methods should allow the identification of new methods to control cellular behavior in tissue-engineered constructs. The ability to induce specific cellular behaviors (such as differentiation) with a material, as opposed to a diffusible compound such as a growth factor, provides the first opportunity to control precisely where differentiation occurs in an engineered tissue. In the future, this positional control of cellular behavior may facilitate the production of tissues composed of multiple lineages derived from a single stem cell type.

In addition to biomaterials that direct specific cellular behaviors, researchers are also developing smart biomaterials that respond to specific cellular signals. Hydrogels containing both matrix metalloproteinase (MMP) degradable sites and tethered adhesive ligands have been manufactured (*5*). The presence of these MMP sites allows native cells to control gel remodeling such that these cells replace the synthetic gel material with tissue. When these biomaterials are further supplemented with specific growth factors, such as bone morphogenetic proteins, these gels support the infiltration of cells and the formation of mineralized tissue for the healing of critical-sized cranial defects in rats. These materials exhibit many of the benefits of naturally derived gels such as collagen (for example, the ability to be remodeled and biocompatibility), yet avoid some undesirable properties of natural extracellular matrix gels (such as nonspecific protein adsorption).

Advances in microfabrication have also provided new approaches for developing smart biomaterials and drug delivery systems. For example, implantable silicon microchips with 100 drug-containing wells have been created (*6*). Each well can release drug on demand by application of a low voltage. Fully degradable versions of drug delivery microchips have also been reported (*7*). The incorporation of sensors into computer-controlled drug delivery systems like these may lead to responsive, fully automated drug therapies.

From a clinical standpoint, many of the advantages of these next-generation biomaterials are lost if the material cannot be implanted correctly. For example, proper contact between bone and implant is extremely important for the apposition and integration of bone tissue. To this end, biomaterials are being developed to allow easy application in one form (such as a liquid) that is rapidly converted into another (a solid or gel) at the appropriate destination. Some examples of this are biomaterials that solidify in vivo with exposure to light, temperature, or pH changes (*8*, *9*). Biodegradable shape-memory polymers (*10*) are also under development. These materials are composed of at least two separated phases, each with a different thermal transition temperature. These distinct phase transition temperatures allow the materials to "memorize" a permanent shape at body temperature that can be substantially different from a temporary shape at room temperature. Materials such as these may greatly simplify the use of biomaterials in surgical procedures, as they can be implanted at room temperature in a minimally invasive form (for example, laparoscopically) and then expand to a final shape after reaching body temperature.

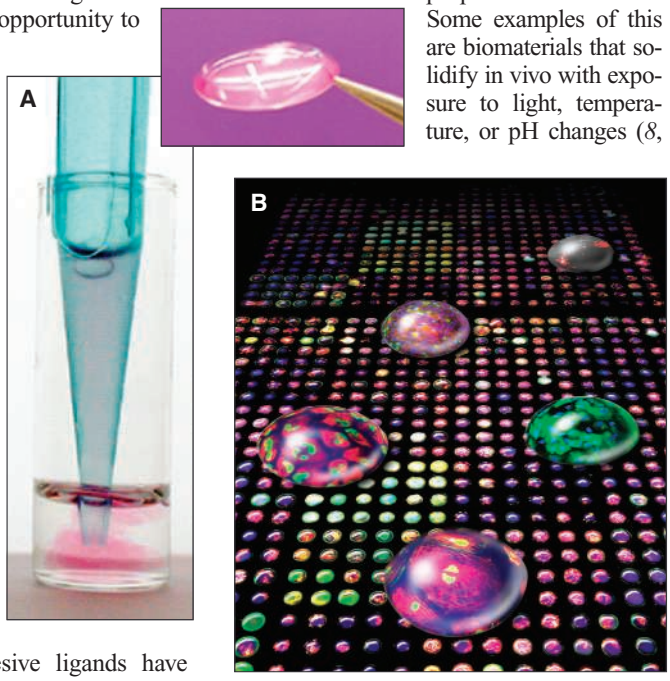

Smart biomaterials get smarter. (**A**) A gel is formed by mixing a 1:1 volume ratio of murine neural progenitor cells suspended in culture medium and a 1% (by weight) solution of peptide amphiphile molecules that self-assemble into nanofibers. The cells remain viable after their encapsulation by the nanofibers and proceed to differentiate rapidly and selectively into neurons. (**B**) Polymeric microarray with fluorescently labeled human embryonic stem cells. Several individual spots with different cell types are magnified.

In addition to materials with responsive bulk properties, researchers are also developing smart surfaces. One example is a surface that can reversibly switch between hydrophilic and hydrophobic in response to an electric potential (*11*). A key design feature of this surface is the carefully controlled intermolecular spacing of a molecule with a negative terminus—(16-mercapto)hexadecanoic acid (2-chlorophenyl)diphenylmethyl ester (MHAE)—on a gold surface. With the proper spacing, the surface responds to negative electric potential by extending itself to display the hydrophilic, negatively charged terminus. Upon application of a positive charge, the gold surface attracts the negatively charged terminus, bending MHAE molecules to display their hydrophobic moieties. In the future, coatings such as these may enable production of medical devices and sensors with digitally responsive surfaces.

The work described here shows that we are no longer limited to off-the-shelf materials for biomedical applications. We have moved beyond the days of the first artificial heart created from polyetherurethanes, the same material originally used in ladies' girdles (*12*). We expect that biomaterials will become increasingly influenced by advances in cell biology and chemistry, and that the combination of these smart biomaterials with biosensors (*13*), new drug delivery systems (*14*), growth factors (*15*), and DNA (*16*) will boost the development and clinical application of new medical devices.

References

1. R. Langer, D. A. Tirrell, *Nature* **428**, 487 (2004).
2. S. Zhang, *Nature Biotechnol.* **21**, 1171 (2003).
3. G. A. Silva *et al.*, *Science* **303**, 1352 (2004).
4. D. G. Anderson *et al.*, *Nature Biotechnol.* **22**, 863 (2004).
5. M. P. Lutolf *et al.*, *Nature Biotechnol.* **21**, 513 (2003).
6. J. T. Santini Jr. *et al.*, *Nature* **397**, 335 (1999).
7. A. C. R. Grayson *et al.*, *Nature Mater.* **2**, 767 (2003).
8. K. S. Anseth, J. A. Burdick, *MRS Bull.* **27**, 130 (2002).
9. J. L. Drury, D. J. Mooney, *Biomaterials* **24**, 4337 (2003).
10. A. Lendlein, R. Langer, *Science* **296**, 1673 (2002).
11. J. Lahann *et al.*, *Science* **299**, 371 (2003).
12. N. A. Peppas, R. Langer, *Science* **263**, 1715 (1994).
13. P. McFadden, *Science* **297**, 2075 (2002).
14. W. M. Saltzman, W. L. Olbricht, *Nature Rev. Drug Discov.* **1**, 177 (2002).
15. K. Y. Lee *et al.*, *Nature* **408**, 998 (2000).
16. L. D. Shea *et al.*, *Nature Biotechnol.* **17**, 551 (1999).

CREDIT: PANEL A: S. STUPP

Self-Organized Patchiness and Catastrophic Shifts in Ecosystems

Max Rietkerk,[1]* Stefan C. Dekker,[1] Peter C. de Ruiter,[1] Johan van de Koppel[2]

Unexpected sudden catastrophic shifts may occur in ecosystems, with concomitant losses or gains of ecological and economic resources. Such shifts have been theoretically attributed to positive feedback and bistability of ecosystem states. However, verifications and predictive power with respect to catastrophic responses to a changing environment are lacking for spatially extensive ecosystems. This situation impedes management and recovery strategies for such ecosystems. Here, we review recent studies on various ecosystems that link self-organized patchiness to catastrophic shifts between ecosystem states.

Ecosystems are exposed to changes in climate, nutrient loading, or biotic exploitation. How ecosystems undergo such environmental changes on different scales of space and time is one of the main frontiers in ecology. Although environmental change can be slow and gradual, it may lead to sudden catastrophic change in the structure and functioning of ecosystems (*1*). Such catastrophes are commonly attributed to the existence of two alternative stable states in ecosystems (*2*), meaning that the dynamics of these systems are determined by two attracting states. Here, we define this as bistability.

[1]Department of Environmental Sciences, Copernicus Institute, Utrecht University, P.O. Box 80115, 3508 TC Utrecht, Netherlands. [2]Spatial Ecology Department, Netherlands Institute of Ecology, P.O. Box 140, 4400 AC Yerseke, Netherlands.

*To whom correspondence should be addressed. E-mail: m.rietkerk@geog.uu.nl

Positive feedback control between consumers (e.g., plants) and limiting resources (e.g., water, nutrients) is considered to be the principle underlying catastrophic ecosystem shifts (*1*–*3*). This picture emerged from models that ignore spatial interactions. Hence, these so-called mean field models predict bistability in ecosystems as a consequence of positive feedback. We interpret this as local bistability. Such mean field analysis is particularly helpful for understanding catastrophic shifts in homogeneous or well-mixed ecosystems. The sudden loss of transparency in shallow lakes provides an illustrative example (*4*, *5*). However, verifications and predictive power of catastrophic shifts are lacking for spatially extensive, heterogeneous ecosystems. As a result, sustainable management and recovery strategies for such ecosystems have been difficult to devise; they require an understanding of the relation between feedback and spatial scale.

We review recent ecosystem studies that include feedback control and spatial scale (Table 1 and Fig. 1). These studies link feedback control to self-organized patchiness of consumers and resources, and they show that a resource concentration mechanism invoked by consumers explains the diversity of spatial structures in these ecosystems. Such consumers have previously been called "ecosystem engineers" (*6*). Spatial self-organization is not imposed on any system but emerges from fine-scale interactions owing to internal causes (*7*). Moreover, model outcomes show that ecosystems where this resource concentration mechanism operates exhibit bistability between a specific spatially structured and homogeneous ecosystem state. We define the bistability at large spatial scales predicted by these spatially explicit models as global bistability.

Similar to the mean field models, global bistability in spatially explicit models is associated with catastrophic shifts at large spatial scales between coexisting stable states. Hence, these results stress the importance of self-organized patchiness for a better understanding of catastrophic shifts. Increased resource scarcity leads to spatial reorganization of consumers and resources in these model ecosystems, and an ecosystem state develops with localized structures observed in reality. Once resource scarcity reaches a threshold, the system shifts toward a homogeneous state

Table 1. Overview of references describing self-organized patchiness in some major ecosystems and the mechanisms involved.

Ecosystem	References	Pattern characteristics (scale)	Mechanisms involved
Arid	(*8*, *11*)	Spots, labyrinths, gaps (1 m) and stripes (10 m) (Fig. 1C)	Redistribution of soil water due to positive feedback among plant biomass, extent of root system, and water uptake
	(*9*, *14*)	Periodic spots and bands (10 to 100 m)	Short-range facilitation and long-range competition for limiting water
	(*12*)	Spots, labyrinths, gaps, and stripes (10 to 100 m) (Fig. 1, A and B)	Redistribution of surface water due to positive feedback between plant cover and water infiltration
	(*13*)	Disordered spots and clustered spots on hillslope contours (10 to 100 m)	Competition for limiting water
Savanna	(*15*)	Isolated spots of trees and shrubs in grass matrix (10 to 100 m) (Fig. 1, D and E)	Short-range facilitation and long-range competition for limiting nutrients
Peatland	(*24*)	String patterns (10 m)	Ponding of surface water upstream from hummocks combined with positive feedback between hummock occurrence and water table depth
	(*25*)	Maze and string patterns perpendicular to flow direction (10 m) (Fig. 1, F and G)	Convective transport of limited nutrients in the groundwater toward areas with higher plant biomass, driven by differences in transpiration rate

without consumers functioning as ecosystem engineers. Increasing resource availability does not recover these localized structures, because the resource concentration mechanism fails. This phenomenon is called hysteresis, meaning that specific spatial structures may develop in real ecosystems that only arise when resource availability is decreased, but not when increased. Therefore, we propose the hypothesis that imminent catastrophic shifts in ecosystems can be predicted by self-organized patchiness.

Arid Ecosystems

Self-organized patchiness and the resource concentration mechanisms involved have been reported from various ecosystems (Table 1 and Fig. 1), among which arid ecosystems are the most prominent (*8*–*14*). The self-organized patchiness in these ecosystems differs in scale and shape. Patterns reported are gaps, labyrinths, stripes (''tiger bush'') (Fig. 1, A to C), and spots (''leopard bush'').

The general mechanism underlying this self-organized patchiness is a positive feedback between plant growth and availability of water. Higher vegetation density allows for higher water infiltration into the soil (because of root penetration) and lower soil evaporation (because of shading). As a result, vegetation persists once present, but bare soil is too hostile for recolonization after the vegetation disappears, implying that the present state of the vegetation depends on its history (*3*).

Recent studies link this positive feedback with subsequent redistribution of water resources (*10*–*12*). Lateral flow of subsurface soil water at a scale of 0.1 m, driven by differences in evapotranspiration, explains regular patterning of grasses in the Negev desert (*11*) (Fig. 1C). Redistribution of surface runoff water at a scale of 10 m, driven by differences in water infiltration, elucidates the formation of self-organized patchiness in arid bushlands (*12*) (Fig. 1, A and B). These observations show that similar patterns of self-organized patchiness may emerge at different scales. Ecosystem transitions involve a sequence of emerging patterns of various forms induced by decreased rainfall. Vegetation states include homogeneous cover, gaps, labyrinths or stripes, and spots, in that order (*11*, *12*, *14*). More important, in these models the vegetation shifts catastrophically from the spotted state to a bare homogeneous state if rainfall is decreased beyond a threshold. This can be attributed to global bistability of the spotted and bare states. Hence, a predictable form of self-organized patchiness may indicate imminent catastrophic shift to a bare homogeneous state. Increased rainfall may not recover the spotted state, because the resource concentration mechanism (concentration of soil water under vegetated patches) fails (*11*).

Savanna Ecosystems

In nutrient-poor Savanna ecosystems, periodic and aperiodic isolated spots of trees and shrubs

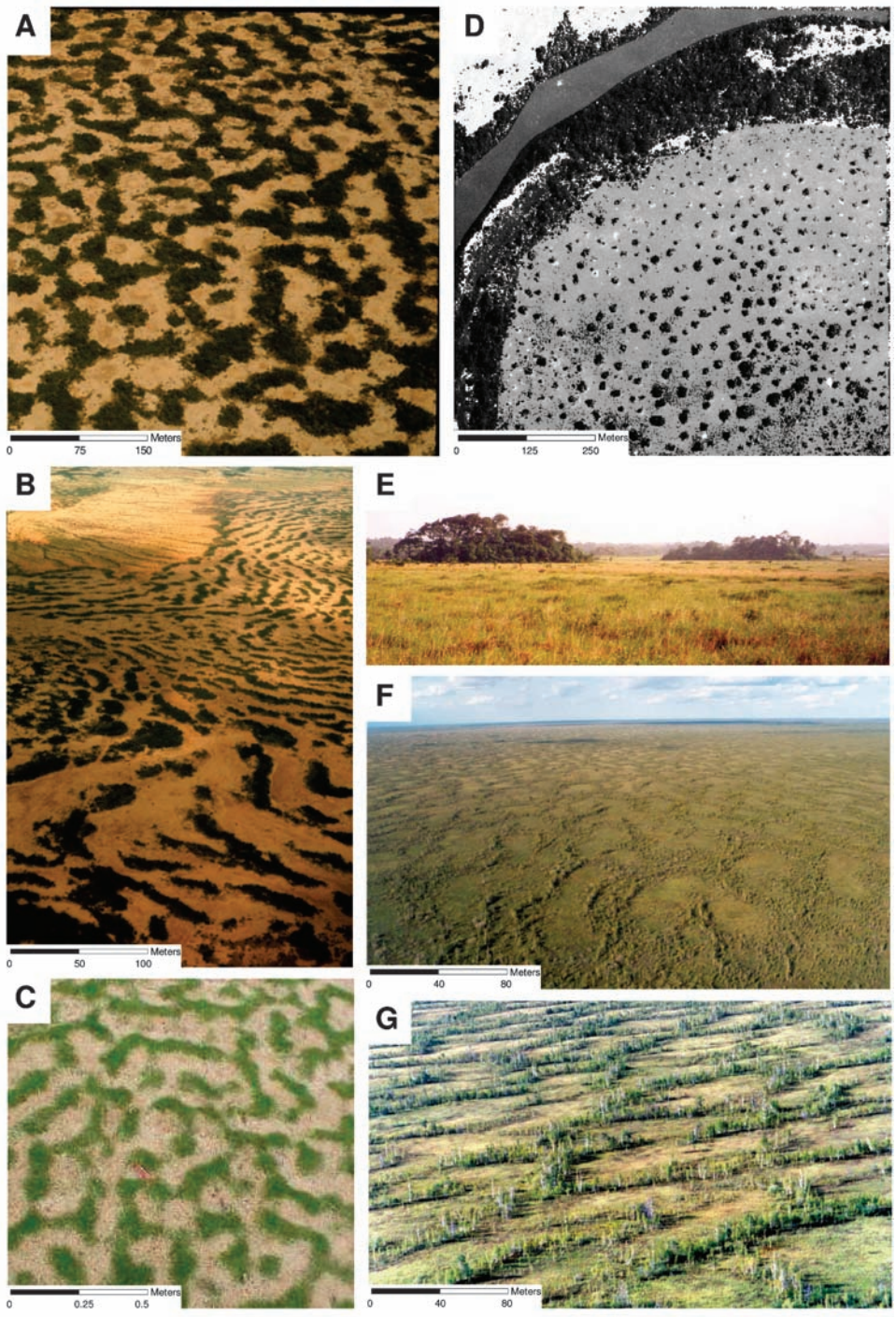

Fig. 1. Field observations. (**A** to **C**) Arid ecosystems: (A) Labyrinth of bushy vegetation in Niger [(*12*), © 2002 University of Chicago]; (B) Striped pattern of bushy vegetation in Niger; (C) Labyrinth of perennial grass *Paspalum vaginatum* in Israel [(*11*), © 2001 American Physical Society]. (**D** and **E**) Savanna ecosystems: Aerial and ground photographs of spots of tree patches in Ivory Coast and French Guiana, respectively [(*15*), © 2002 American Physical Society]. (**F** and **G**) Peatlands: Regular maze patterns of shrubs and trees in western Siberia [(*25*), © 2004 University of Chicago]. Scales of oblique aerial photographs [all panels except (E)] are order-of-magnitude approximations of distance in the *x* direction shown in the scale bars.

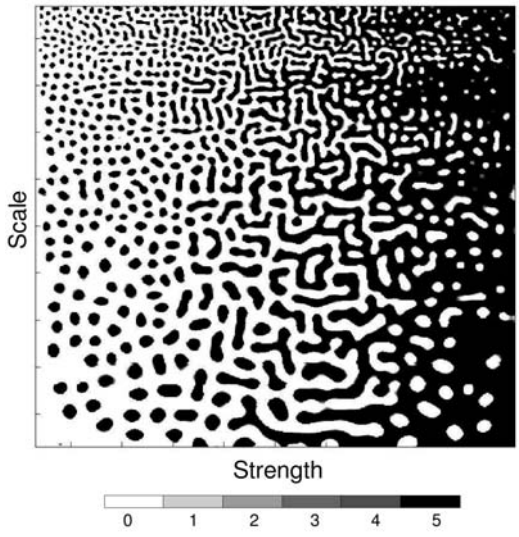

Fig. 2. Model results from a modified version of the Thiery *et al*. (*30*) cellular automaton, showing stable isotropic vegetation patterns after time step $t = 15$ (supporting online text and movie S1). Grid size is 500×500 cells. Black areas represent vegetation in maximum state 5; white areas represent bare soil in minimum state 0. Simulations were started by randomly introducing vegetation state 2 on 5% of the cells. Vegetation patterns are the result of fine-scale positive feedback and coarse-scale negative feedback. On the *x* axis, the strength of the positive feedback is increased; on the *y* axis, the scale of influence is decreased. Patterns change from spots to labyrinths and gaps at different spatial scales.

at a scale of 10 to 100 m in grassland are observed (*15*) (Fig. 1, D and E). Lejeune *et al*. (*15*) proposed an interaction-redistribution model of vegetation dynamics generating these patterns even under homogeneous conditions. Their model is grounded on the balance between short-range facilitation and long-range competition. The mechanistic base is provided by observations that in nutrient-poor environments, trees and shrubs can have positive effects on each other and on themselves because of local nutrient accumulation as well as the ability of long superficial roots to track scarce nutrients from the surroundings (*16*–*18*).

Other plausible mechanisms coupling short-range facilitation with long-range competition are nutrient retention by the binding of soil by roots, raindrop interception, and runoff retention, all of which prevent erosion (*3*). This forms the mechanistic base of the concept of ''islands of fertility'' (*19*), explaining soil fertility under canopies of trees and shrubs by local nutrient accumulation and recycling. The observed patterns are interpreted as localized structures arising from global bistability between a ''bare'' state (no trees and shrubs) and a self-organized patchy state. Hence, Lejeune *et al*. (*15*) predicted the possibility of a stable homogeneous state and a self-organized patchy state for the same resource availability, with catastrophic shifts between these states. As resource availability diminishes, the vegetation goes through a predictable sequence of emerging patterns comparable to that described above for arid ecosystems (*11*, *12*, *14*, *15*).

Peatland Ecosystems

Bogs in North America and Eurasia commonly show various spatial patterning (*20*, *21*), including regular string patterns of densely vegetated bands at a scale of 10 m (hummocks forming ridges) oriented perpendicular to the slope, alternating with more sparsely vegetated wetter zones (hollows forming pools) (*22*–*24*). Other regular patterns recently reported are maze patterns: bands densely vegetated by vascular plants at a scale of 10 m in a more sparsely vegetated matrix of predominantly nonvascular plants (*25*) (Fig. 1, F and G). A general mechanism underlying patterning in these ecosystems is a positive feedback between plant productivity and groundwater depth on elevated, drier sites, mainly due to increased production of vascular plants.

Rietkerk *et al*. (*25*) proposed the convective transport of nutrients in the groundwater toward areas with higher vascular plant biomass, driven by differences in transpiration, as a mechanism to explain regular string and maze patterns. If plant productivity is limited by nutrient flow, this local ''nutrient accumulation'' mechanism may lead to self-organized patchiness such as the observed string patterns on slopes and maze patterns on flat ground. Mean field models including this positive feedback allow for the occurrence of local bistability (thin peat with high water table coexisting with thick peat with low water table) for the same precipitation level, and catastrophic shifts between these states (*26*, *27*). Rietkerk *et al*. (*25*) predicted the possibility of global bistability (nonhomogeneous equilibrium with vascular plants and homogeneous equilibrium without vascular plants) for the same precipitation and nutrient input level, and catastrophic shifts between these states. Here, the vegetation also goes through a sequence of predictable patterns with decreasing nutrient input.

Self-Organized Patchiness and Catastrophic Shifts

Mean field models that ignore the relation between feedback and spatial scale predict local bistability and catastrophic shifts in the ecosystems discussed here (*1*, *3*, *26*–*28*). Recent studies show that spatially explicit models including the resource concentration mechanism predict global bistability associated with catastrophic shifts at large spatial scales and self-organized patchiness. Observations confirm the model results. A variety of mechanisms in ecosystems lead to resource concentration through consumer-resource feedback. The consumers harvest resources from their surroundings; in the ecosystems discussed here, harvest is facilitated by mass flow of resources toward consumers, triggered by the consumers themselves. Furthermore, consumers spread relatively slowly as compared to flow of resources. A general pattern emerging from these observations is that consumers are positively associated with resource abundance at short spatial range, but negatively at long spatial range (*29*). Thus, a common principle applies to these locally reinforced consumers, in that there is a positive feedback effect that is short-ranged and a negative feedback effect that is long-ranged. This is a necessary condition for self-organized patchiness to form (*14*).

We generated new results from a simple cellular automaton based on the model of Thiery *et al*. (*30*) exemplifying how such scale-dependent feedback can explain a diversity of patterns in ecosystems (Fig. 2, supporting online text, and movie S1). The differences in structure and scale of patchiness are the result only of varying strength and scale of feedback influence (*14*), illustrating the general nature of the underlying scale-dependent mechanisms explaining self-organized patchiness in ecosystems.

The notion of scale-dependent feedback controlled by the resource concentration mechanism is crucial for a predictive theory of catastrophic shifts in ecosystems. This suggests that catastrophic shifts can be predicted by self-organized patchiness (Fig. 3). Therefore, the concepts of catastrophic shifts and self-organized patchiness are tightly linked, whereby a scale-dependent feedback is triggered by resource concentration.

Ecosystems with scale-dependent feedback resemble the activator-inhibitor system first described by Turing (*31*). In the ecosystems discussed here, the inhibition effect results from the large-scale depletion of a resource that is consumed during the localized production of the activator (consumer). The activator effect results from the local positive feedback control between the consumer and its limited resource (water or nutrient availability). These ecosystems represent a class of activator-inhibitor system that has been recognized earlier as ''activator-depleted substrate systems'' (*32*). Indeed, theoretical analyses of an activator-depleted substrate system also predict global bistability and catastrophic shifts between spotted and uniform states (*33*). Experimental evidence of global bistability and

hysteresis between states of spots and stripes comes from such a system as well (*34*, *35*).

Most theoretical approaches to self-organized patchiness in ecosystems are based on the same framework of models as are used to explain pattern formation in chemical systems and biological pattern formation on sea shells (*32*) and animal coats (*36*). Here, we concentrated on the overlap between ecosystems exhibiting both self-organized patchiness and catastrophic shifts due to global bistability. The resource concentration mechanism invoked by ecosystem engineers provides a general explanation, because ecosystem engineers at low densities may be unable to harvest resources from the surroundings. We suggest that all ecosystems with self-organized patchiness resulting from a resource concentration mechanism will also exhibit catastrophic shifts.

Challenges Ahead

Linking self-organized patchiness with catastrophic shifts by the resource concentration mechanism may help to bridge the present gaps among theory, observation, and management (*2*). The link may be crucial to a predictive theory of catastrophic shifts from which early-warning systems can be developed on the basis of spatial explicit time-series data. This is because predictable forms of self-organized patchiness may indicate imminent catastrophic shifts if resource input decreases in time (Fig. 3). For instance, the spotted state may develop only when resource input is decreased, not when it is increased. This means that a snapshot in time of a spotted state would already indicate imminent catastrophic shift.

Human management strategies could be directed toward preserving and restoring self-organized patchiness and its natural resource concentration function (*12*, *37*). Vegetation structures in resource-poor agroecosystems, such as the African Sahel, may lose this function because of overgrazing by cattle, leading to catastrophic shifts to a desertified ecosystem state. Adequate grazing management of rangelands and patchy crop production to conserve resources in marginally arable lands may help to optimize productivity, thereby preventing such catastrophic shifts.

Although this is a promising perspective, we are far from quantitative predictions. For that, we need to move away from models that ignore space and therefore generate only qualitative predictions. A key question concerns how local geological and soil differences, seasonality in rainfall, and random processes affect self-organized patchiness and ecosystem resistance against catastrophic shifts. Furthermore, the fact that self-organized patchiness and catastrophic shifts may occur at different spatial and temporal scales (*11*, *12*) provides new perspectives for fine-scale and relatively short-term experiments to predict large-scale self-organized patchiness and catastrophic shifts in ecosystems.

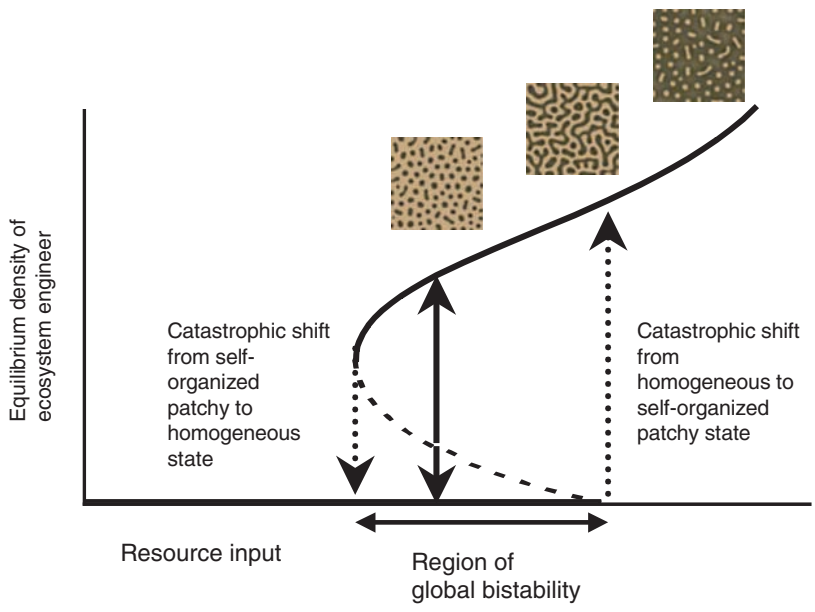

Fig. 3. Model showing how ecosystems may undergo a predictable sequence of emerging self-organized patchiness as resource input decreases or increases (*11*, *12*, *14*, *25*). Thick solid lines represent mean equilibrium densities of consumers functioning as ecosystem engineers. Dotted arrows represent catastrophic shifts between self-organized patchy and homogeneous states, and vice versa. Dark colors in the insets represent high density. The range of resource input for which global bistability and hysteresis exists is between these dotted arrows. Solid arrows represent development of the system toward the coexisting self-organized patchy state or homogeneous state, depending on initial ecosystem engineer densities.

References and Notes

1. M. Scheffer *et al.*, *Nature* **413**, 591 (2001).
2. M. Scheffer, S. R. Carpenter, *Trends Ecol. Evol.* **18**, 648 (2003).
3. M. Rietkerk, J. van de Koppel, *Oikos* **79**, 69 (1997).
4. M. Scheffer *et al.*, *Trends Ecol. Evol.* **8**, 275 (1993).
5. S. R. Carpenter *et al.*, *Ecol. Appl.* **9**, 751 (1999).
6. C. G. Jones *et al.*, *Oikos* **69**, 373 (1994).
7. P. Rohani *et al.*, *Trends Ecol. Evol.* **12**, 70 (1997).
8. C. Klausmeier, *Science* **284**, 1826 (1999).
9. P. Couteron, O. Lejeune, *J. Ecol.* **89**, 616 (2001).
10. R. HilleRisLambers *et al.*, *Ecology* **82**, 50 (2001).
11. J. Von Hardenberg *et al.*, *Phys. Rev. Lett.* **87**, 198101 (2001).
12. M. Rietkerk *et al.*, *Am. Nat.* **160**, 524 (2002).
13. N. M. Shnerb *et al.*, *Phys. Rev. Lett.* **90**, 038101 (2003).
14. O. Lejeune *et al.*, *Int. J. Quantum Chem.* **98**, 261 (2004).
15. O. Lejeune *et al.*, *Phys. Rev. E* **66**, 010901 (2002).
16. A. J. Belsky, *Ecology* **75**, 922 (1994).
17. R. M. Callaway *et al.*, *Nature* **417**, 844 (2002).
18. J. F. Bruno *et al.*, *Trends Ecol. Evol.* **18**, 119 (2003).
19. W. H. Schlesinger *et al.*, *Ecology* **77**, 364 (1996).
20. R. A. Lindsay *et al.*, *Aquilo Ser. Bot.* **21**, 69 (1985).
21. L. R. Belyea, J. Lancaster, *J. Ecol.* **90**, 223 (2002).
22. Y. Sakaguchi, *Bull. Dept. Geogr. Univ. Tokyo* **12**, 35 (1980).
23. D. R. Foster *et al.*, *Nature* **306**, 256 (1983).
24. D. K. Swanson, D. F. Grigal, *Oikos* **53**, 509 (1988).
25. M. Rietkerk *et al.*, *Am. Nat.* **163**, 699 (2004).
26. D. W. Hilbert *et al.*, *J. Ecol.* **88**, 230 (2000).
27. L. R. Belyea, R. S. Clymo, *Proc. R. Soc. London Ser. B* **268**, 1315 (2001).
28. M. Rietkerk *et al.*, *Oikos* **80**, 241 (1997).
29. M. Rietkerk *et al.*, *Plant Ecol.* **148**, 207 (2000).
30. J. M. Thiery *et al.*, *J. Ecol.* **83**, 497 (1995).
31. A. Turing, *Philos. Trans. R. Soc. London Ser. B* **273**, 37 (1952).
32. H. Meinhardt, *The Algorithmic Beauty of Sea Shells* (Springer, Berlin, 1995).
33. S. L. Judd *et al.*, *Physica D* **136**, 45 (2000).
34. V. Castets *et al.*, *Phys. Rev. Lett.* **64**, 2953 (1990).
35. Q. Ouyang *et al.*, *J. Phys. Chem.* **96**, 6773 (1992).
36. J. D. Murray, *Mathematical Biology*, vol. 19 of *Biomathematics Texts* (Springer-Verlag, Berlin, 1989).
37. J. Ludwig *et al.*, *Landscape Ecology, Function and Management: Principles from Australia's Rangelands* (CSIRO, Collingwood, Victoria, Australia, 1997).

38. We thank W. Bleuten, P. Couteron, C. Klausmeier, E. Lapshina, O. Lejeune, E. Meron, and M. Wassen for sharing photographs, and M. Scheffer, P. Herman, and two anonymous referees for thoughtful comments that increased the clarity of the manuscript. Supported by a VIDI grant of the Netherlands Organization of Scientific Research (NWO-ALW) (M.R.).

Supporting Online Material

www.sciencemag.org/cgi/content/full/305/5692/1926/DC1
SOM Text
Movie S1

A Triassic Aquatic Protorosaur with an Extremely Long Neck

Chun Li,[1]* Olivier Rieppel,[2] Michael C. LaBarbera[3]

By the Middle Triassic, a number of reptile lineages had diversified in shallow epicontinental seas and intraplatform basins along the margins of Pangea, including the giraffe-necked protorosaurid reptile *Tanystropheus* from the Western Tethys (modern Europe and the Middle East). Here we report another long-necked fossil, *Dinocephalosaurus orientalis*, a protorosaur earlier named (on the basis of an isolated skull) for its appearance (*1*). Unlike some other protorosaurs, this taxon represents a fully aquatic species.

The new specimen preserves much of the postcranial skeleton. The neck is ~1.7 m long, but the trunk is less than 1 m (the tail was not preserved) (Fig. 1). Together with ichthyosaurs and fishes, *Dinocephalosaurus* was found in Middle Triassic (Anisian stage, 230 million years ago) marine limestone in southern China (the Guanling Formation near Xinmin, Guizhou Province).

Neck elongation is a derived character of protorosaurs, a group that originated in the Permian and diversified in the Triassic. *Dinocephalosaurus* shares additional diagnostic characters with protorosaurs, such as elongated cervical ribs and very low neural spines on the neck vertebrae. The limbs of *Dinocephalosaurus* indicate fully aquatic (marine) habits, and they differ from all other protorosaurs in that they retain juvenile characteristics in the adult stage, as in many other aquatic tetrapods. The limbs are relatively short and broad; the distal carpal and tarsal elements remain unossified (except for one). The astragalus and calcaneum of the tarsus form simple rounded ossifications without any complex contact between them. The fifth metatarsal is a simple straight ossification. Unlike *Dinocephalosaurus*, *Tanystropheus* and its closest allies show a combination of a short fifth metatarsal with a much-elongated first phalanx in the fifth toe that mimics a metatarsal in its structure.

The neck of *Dinocephalosaurus* incorporates 25 elongated vertebrae (*Tanystropheus* has 12). The longest neck vertebra is 2.75 times longer than an anterior dorsal vertebra (in adult *T. longobardicus*, this ratio is 7 to 8). As in *Tanystropheus*, the cervical ribs are long and slender, running parallel to the ventrolateral edges of the neck. As the cervical rib length increases from front to back and the vertebrae become shorter posteriorly, the number of intervertebral joints bridged by the ribs increases.

Cladistic analysis based on published data (*2*) shows that *Dinocephalosaurus* nests within the Protorosauria but outside the most derived members of the group, which include *Tanystropheus* (supporting online text). The elongation of the neck is convergent in *Dinocephalosaurus* and *Tanystropheus*, as is also indicated by the anatomy. *Tanystropheus* adopted an extreme "giraffe-neck" developmental program (*3*) with only a moderate increase in the number of cervical vertebrae, whereas *Dinocephalosaurus* shows a lesser elongation of individual neck vertebrae but an increase in their number, as is also known in plesiosaurs. The adaptive significance of neck elongation in *Tanystropheus* has generated much speculation (*4*, *5*), but in *Dinocephalosaurus*, it presumably served a functional role. Extending the head vertically in order to gulp air at the surface would have been impossible; hydrostatic pressure would have prevented lung inflation. To breathe, the animal would have had to move with the neck held nearly horizontal at the air-water interface, the head emerging from the water. Such a posture increases the "hull length" of the animal, reducing wave-induced resistance to locomotion.

The slender neck also positions the head well in front of the sturdy body, such that *Dinocephalosaurus* could have closely approached potential prey before the profile of the predator would have become apparent in dimly lit water. Given the length and slenderness of the cervical ribs, moderate lateral flexion of the neck must have been possible. Contraction of muscles [originating from cervical ribs and bridging the intervertebral joints (*6*)] would have rapidly straightened the neck while the ribs would have simultaneously splayed outward. The consequent increase of the esophageal volume would have created suction such that the animal would have essentially swallowed the pressure wave created as its head lunged forward. This would have resulted in an almost perfect strike at a prey item in water. Unlike other protorosaurs, but similar to extant crocodiles, *Dinocephalosaurus* shows concave-convex dental margins with fanglike teeth on both upper and lower jaws. This tooth arrangement would have helped the animal to secure its prey once caught.

Fig. 1. The Middle Triassic marine protorosaur *D. orientalis* is known from a skull [**(bottom inset)** IVPP fossil no. V13767] and a nearly complete skeleton (IVPP V13898). The structure of its hindlimb **(top inset)** documents fully aquatic habits.

References and Notes

1. C. Li, *Acta Geol. Sin.* **77**, 419 (2003).
2. O. Rieppel, N. C. Fraser, S. Nosotti, *Atti Soc. Ital. Sci. Nat.* **144**, 359 (2003).
3. G. Parra-Olea, D. B. Wake, *Proc. Natl. Acad. Sci. U.S.A.* **98**, 7888 (2001).
4. M. A. Taylor, *Nature* **341**, 688 (1989).
5. K. Tschanz, *Palaeontology* **31**, 997 (1988).
6. K. Tschanz, thesis, University of Zurich (1986).
7. We thank Z. Zhou for reading the paper, W. Gao for photography, and J. Ding for preparing the fossil. Supported by the National Natural Science Foundation of China grant nos. 40302007 and 40342020.

Supporting Online Material
www.sciencemag.org/cgi/content/full/305/5692/1931/DC1
SOM Text
References and Notes

19 May 2004; accepted 2 August 2004

[1]Institute of Vertebrate Paleontology and Paleoanthropology (IVPP), Chinese Academy of Sciences, Post Office Box 643, Beijing 100044, China. [2]Department of Geology, The Field Museum, Chicago, IL 60605–2496, USA. [3]Department of Organismal Biology and Anatomy, The University of Chicago, Chicago, IL 60637, USA.

*To whom correspondence should be addressed. E-mail: lichun@pa.ivpp.ac.cn

Solar Wind–Induced Atmospheric Erosion at Mars: First Results from ASPERA-3 on Mars Express

R. Lundin,[1]* S. Barabash,[1] H. Andersson,[1] M. Holmström,[1] A. Grigoriev,[1] M. Yamauchi,[1] J.-A. Sauvaud,[2] A. Fedorov,[2] E. Budnik,[2] J.-J. Thocaven,[2] D. Winningham,[3] R. Frahm,[3] J. Scherrer,[3] J. Sharber,[3] K. Asamura,[4] H. Hayakawa,[4] A. Coates,[5] D. R. Linder,[5] C. Curtis,[6] K. C. Hsieh,[6] B. R. Sandel,[6] M. Grande,[7] M. Carter,[7] D. H. Reading,[7] H. Koskinen,[8] E. Kallio,[8] P. Riihela,[8] W. Schmidt,[8] T. Säles,[8] J. Kozyra,[9] N. Krupp,[10] J. Woch,[10] J. Luhmann,[11] S. McKenna-Lawler,[12] R. Cerulli-Irelli,[13] S. Orsini,[13] M. Maggi,[13] A. Mura,[13] A. Milillo,[13] E. Roelof,[14] D. Williams,[14] S. Livi,[14] P. Brandt,[14] P. Wurz,[15] P. Bochsler[15]

The Analyzer of Space Plasma and Energetic Atoms (ASPERA) on board the Mars Express spacecraft found that solar wind plasma and accelerated ionospheric ions may be observed all the way down to the Mars Express pericenter of 270 kilometers above the dayside planetary surface. This is very deep in the ionosphere, implying direct exposure of the martian topside atmosphere to solar wind plasma forcing. The low-altitude penetration of solar wind plasma and the energization of ionospheric plasma may be due to solar wind irregularities or perturbations, to magnetic anomalies at Mars, or both.

The evolution of the martian atmosphere and its possibly substantial hydrosphere is affected by interactions with the solar wind and interplanetary plasma. Various theories have been proposed to explain the change from an earlier wetter and warmer Mars (*1*). A number of processes have been suggested to explain the removal of volatiles such as H_2O and CO_2, such as thermal (Jeans) escape, hydrodynamic escape (*2*), nonthermal escape (*3*, *4*), or catastrophic impact erosion (*5*). Jeans escape promotes mainly light ions such as hydrogen, providing mass escape rates at least an order of magnitude lower than nonthermal escape processes. Nonthermal escape (NTE) is here defined as all processes in which energization and escape of particles are related to nonthermal processes governed by solar wind forcing. Estimates of NTE have led to accumulated water volumes equivalent to a global ocean of a few meters' depth (*6*), in agreement with the Phobos-2 observations (*7*). However, Lammer *et al.* (*8*) showed that the intense extreme ultraviolet radiation and solar wind of the early Sun should lead to higher escape. They modeled an escape of water from Mars since 3.5 billion years ago equivalent to a global ocean with a thickness of ~14 to 34 m. The heavy loss of volatiles from Mars may also be associated with the lack of a strong intrinsic magnetic field like that of the Earth, which prohibits direct solar wind impact on the ionosphere and topside atmosphere (*9*).

The main objective of the ASPERA-3 experiment on Mars Express (MEX) is to study the solar wind scavenging of the ionosphere and topside atmosphere of Mars, by direct measurements of inflowing solar wind plasma and outflowing energized ionospheric plasma (the planetary wind) and by remotely imaging the flow of energetic neutral atoms (ENAs) generated by charge exchange in the exosphere of Mars. Here we focus on in situ results obtained from the electron spectrometer (ELS) and the ion mass analyzer (IMA) experiment. The ELS instrument measures electrons in the energy range 0.01 to 20 keV with high-energy resolution ($\Delta E/E$ = 0.07). The IMA experiment measures ions with limited mass resolution (m/q = 1, 2, 4, 8, 16, >25, where m is mass and q is electric charge) in the energy range 0.05 to 35 keV/q.

ASPERA-3 plasma observations. Our observations were made during the early commissioning phase of MEX, from 23 January 2004 to 22 March 2004. The induced magnetosphere boundary (IMB) is defined as the envelope of the induced martian magnetosphere, i.e., the stopping boundary for the solar wind, whereas the interior is dominated by plasma of planetary origin. We used this definition of the IMB because of the lack of magnetic field measurements on board MEX, avoiding potential conflicts with defined features such as the magnetic flux pile-up boundary (*10*). The ion data (Fig. 1) display a cyclic behavior that originates in the electrostatic elevation deflection scans versus time. The time resolution for each three-dimensional (3D) (~2π) ion distribution was ~3 min. The electron data were secured in 2D and measured in a plane with a 360° field of view. The lower ionosphere data show photoelectron lines emerging as a result of ionospheric CO_2^+ (Fig. 1). The photoelectron boundary (PEB) separates ionospheric electrons from shocked sheath electrons (at higher altitudes). Above the PEB and IMB, the spacecraft encounters intense fluxes of shocked solar wind ions. Finally, beyond the bow shock (BS), electrons are cooler and the solar wind ions (H^+ and He^{++}) represent cold beams.

The entire region inside the IMB is characterized by energized heavy ions accelerated up to several keV down to pericenter altitudes (~270 km). In the pass shown in Fig. 1, solar wind ions (protons) were stopped at ~500 km, i.e., at the IMB. However, because the energization of ions was observed down to the pericenter (270 km), direct solar wind forcing must also be capable of reaching these heights. The lack of complementary plasma instrumentation on MEX makes any suggested identification of the energy sources concerned very speculative. The electron data present an ordinary quiet ionosphere with only minor perturbations. This suggests low wave activity, making the energization of heavy ionospheric ions even more puzzling. Other observations of energization of ionospheric ions near the pericenter are correlated with

[1]Swedish Institute of Space Physics, Box 812, S-98 128, Kiruna, Sweden. [2]Centre d'Etude Spatiale des Rayonnements, BP-4346, F-31028 Toulouse, France. [3]Southwest Research Institute, San Antonio, TX 78228–0510, USA. [4]Institute of Space and Astronautical Science, 3-1-1 Yoshinodai, Sagamichara, Japan. [5]Mullard Space Science Laboratory, University College London, Surrey RH5 6NT, UK. [6]University of Arizona, Tucson, AZ 85721, USA. [7]Rutherford Appleton Laboratory, Chilton, Didcot, Oxfordshire OX11 0QX, UK. [8]Finnish Meteorological Institute, Box 503 FIN-00101 Helsinki, Finland. [9]Space Physics Research Laboratory, University of Michigan, Ann Arbor, MI 48109–2143, USA. [10]Max-Planck-Institut für Sonnensystemforschung, D-37191 Katlenburg-Lindau, Germany. [11]Space Science Laboratory, University of California, Berkeley, CA 94720–7450, USA. [12]Space Technology Limited, National University of Ireland, Maynooth, County Kildare, Ireland. [13]Instituto di Fisica dello Spazio Interplanetari, I-00133 Rome, Italy. [14]Applied Physics Laboratory, Johns Hopkins University, Laurel, MD 20723–6099, USA. [15]University of Bern, Physikalisches Institut, CH-3012 Bern, Switzerland.

*To whom correspondence should be addressed. E-mail: rickard.lundin@irf.se

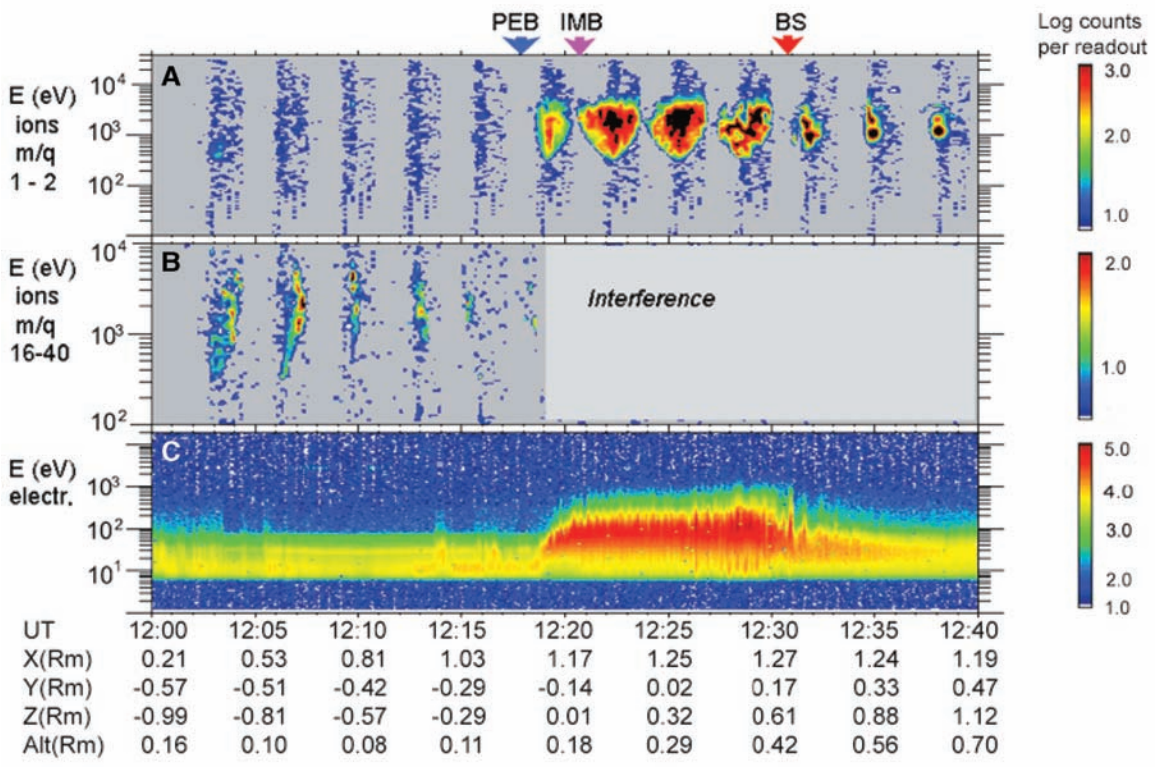

Fig. 1. MEX pericenter pass (~12:08 UT) traversing the ionosphere PEB, the IMB, and the BS. The three panels depict (**A**) H^+, (**B**) heavy ions such as O^+, and (**C**) electron energy-time spectra from the IMA and ELS spectrometers of ASPERA-3. "Interference" in the middle panel indicates contamination in the heavy ion mass channels by intense fluxes of H^+; therefore, the data there have been removed. X(Rm), Y(Rm), Z(Rm), and Alt(Rm) indicate spacecraft coordinates in the Mars solar ecliptic coordinate system. electr., electrons; Rm, Mars radii.

electron perturbations similar to those found in the sheath. Another possible energization process is solar wind electromotive forcing (such that ionospheric ions are accelerated by an externally applied solar wind electric field). Yet a third possibility is that the ions are accelerated not locally but elsewhere, perhaps upstream in the martian exosphere after being first transformed to ENAs by charge exchange (*11*, *12*). Because ENAs may propagate relatively unperturbed over long distances, possibly well away from the generation region in the exosphere, they may transform back to ions through the charge exchange process. In such a way, charge exchange could enable energized ions to, in essence, transfer to other sites, even to lower altitudes. The problem with this suggested mechanism is that the expected fluxes should be rather low, whereas the heavy ion fluxes actually recorded are very high.

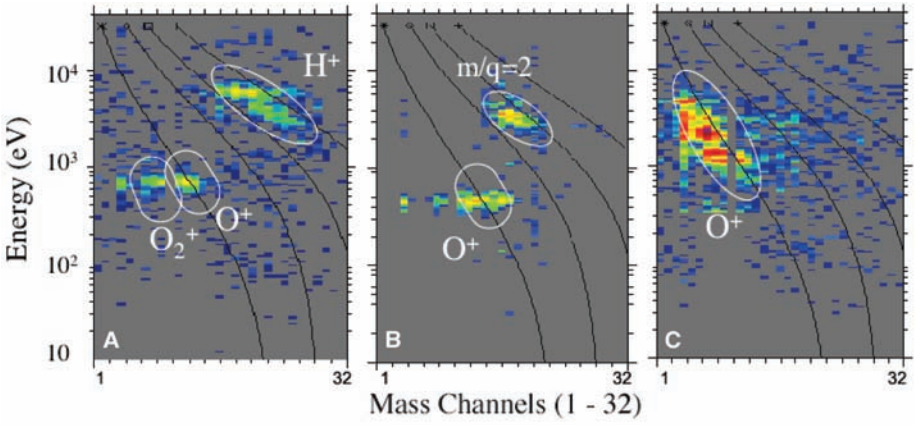

Fig. 2. Three examples of energy-m/q spectra for energized ions. Skewed lines indicate nominal mass identifications for m/q of 1, 2, 4, and 16, respectively. (**A**) 27 February 2004, 2- to 7-keV H^+ and ~700-eV heavy ions (O^+ and O_2^+) at an altitude of ~290 km. (**B**) 25 January 2004, ~500-eV heavy ions and keV ions with $m/q = 2$ (possibly He^{++}, H_2^+, and D^+) at an altitude of 900 km. (**C**) 22 March 2004, strong energization of heavy ions at an altitude of ~330 km.

The composition of energized ionospheric ions reflects the source altitude of the ions (*13*). On 27 February 2004, we measured H^+ with several keV together with ~700-eV heavy ions (O^+ and molecular ions, possibly O_2^+) at an altitude of ~290 km (Fig. 2A). The intense H^+ ion flux suggests a solar wind origin, illustrating that solar wind ions may intrude down to an altitude of ~290 km in the dayside martian ionosphere. Figure 2B (25 January 2004) shows a strong peak at $m/q \sim 2$ with energy of ~4 keV, in addition to energized heavy ions (O^+) of ~500 eV. Normally, $m/q = 2$ is associated with solar wind He^{++}, but a lack of the dominant solar wind species, protons, suggests either that the protons were ''removed'' (possibly through charge exchange), leaving He^{++} essentially unaffected, or that the peak corresponds to martian D^+ or H_2^+. Because the altitude is 900 km, we can immediately exclude the possibility of proton removal by charge exchange. The relatively high flux, of the order 10^6 $(cm^2\ s\ steradian\ keV)^{-1}$, excludes D^+, leaving us with the final possibility, that the peak is due to H_2^+. If this is correct, it implies energization and upward transport of H_2^+ from relatively low altitudes where the ionospheric temperatures are lower. Low-energy ionized molecular hydrogen was found by the ASPERA experiment on Phobos-2 (*14*) near Phobos, a moon of Mars, possibly as a result of outgassing. However, the quite high energy of the MEX $m/q = 2$ peak is puzzling. We are therefore faced with the possibility that the m/q peak is due to He^{++}, while still lacking a good explanation for the dearth of protons. The strong energization of heavy ions (predominantly O^+) at an altitude of ~330 km (Fig. 2C) results in a relatively broad energy distribution, ~1 to 5 keV, quite different from the heavy ion acceleration in Fig. 2, A and B. From the energy distribution point of view, this resem-

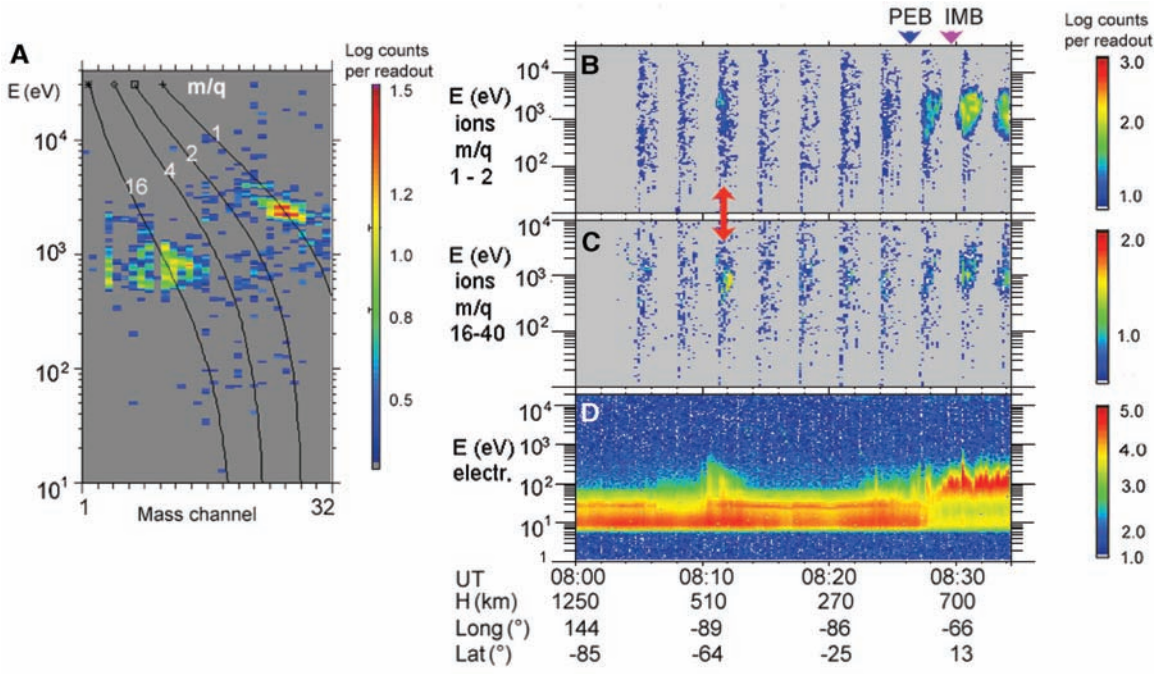

Fig. 3. Spectra for 1 March 2004, showing energized heavy ions (~0.8 to 1 keV) and electrons at an altitude of ~460 km, simultaneously with H^+ (~2 keV) of solar wind origin. (**A**) An energy-mass spectrum of the event marked by the red double arrow in (B) and (C) (08:10 to 08:13 UT). (**B** to **D**) Energy-time spectra for (B) H^+ and He^{++}, (C) heavy ions, $m/q >$ 16, and (D) electrons. H, height; Long, longitude; Lat, latitude.

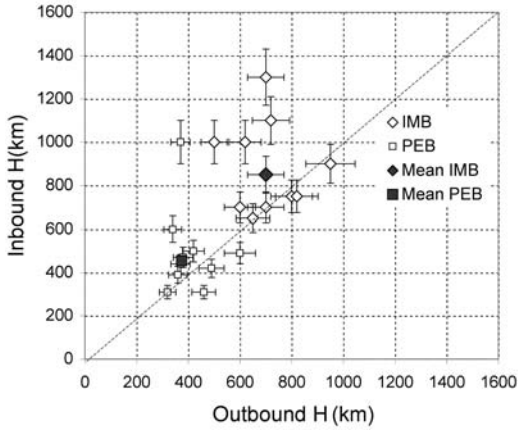

Fig. 4. Altitude statistics for the dayside martian PEB and IMB. To illustrate the variability (in space and time) of the boundaries, the inbound boundary altitude is plotted versus the outbound boundary altitude.

bles transverse (to the ambient magnetic field) energization of ionospheric plasma in the terrestrial upper ionosphere. However, in the absence of magnetic field data, we can only conclude that the heavy ions flow as in the external sheath. We noted previously that the electron data show low wave activity, suggesting that the energization is nonlocal, possibly resulting from upstream activities.

On 1 March 2004, we observed a more typical case of local plasma energization, i.e., energization of heavy ions associated with sheathlike or energized electrons (~08:10 UT) (Fig. 3). This energization was separated from the ambient ionospheric electrons, at altitudes that imply the PEB is not stable versus time. We also observed an almost identical, well-separated electron perturbation that occurred simultaneously at Mars Global Surveyor (MGS), when the spacecraft were separated by ~1800 km. This implies a temporal phenomenon, most likely a consequence of a solar wind perturbation. Consequently, solar wind irregularities may have a strong impact not only on the location of the PEB and IMB plasma boundaries, but also on the energization and escape of ionospheric plasma at Mars. This isolated event occurred geographically well away from magnetic anomalies at Mars, although we also observed cases above magnetic anomalies like on MGS (*15*, *16*). However, the dayside magnetic field well above an anomaly is perturbed by the external (sheath) magnetic field, so the connection to the low-altitude magnetic anomaly is not trivial. For instance, the magnetic flux tube of an anomaly is swept tailward by the solar wind interaction. Therefore, what appears to be ion energization over a region void of magnetic anomalies may in fact be due to energization processes over a magnetic anomaly further upstream. Our preliminary results are therefore inconclusive with regard to the magnetic anomalies and ionospheric ion energization.

The altitude statistics of the dayside martian PEB and IMB were determined by combining ion and electron data (Fig. 4). We used the lower end of the photoelectron transition region for the PEB, and the upper bound of the region where sheath plasma (ions and electrons) strongly decreases inward as the IMB. The IMB is consistent with the boundaries inferred from Phobos-2 data and given various names such as ''magnetopause'' or ''planetopause'' (*7*, *17*). The IMB marks the stopping boundary for sheath electrons, thereby resembling the magnetic flux pile-up boundary (*10*). Inbound traversals were plotted versus outbound traversals to illustrate the temporal and spatial variability of the boundaries. During our study period, MEX inbound traversals of the IMB occurred in the prenoon sector at clock angles ~330° to 350° in the early period and ~260° to 280° in the later period. The corresponding outbound clock angles of the IMB were ~30° to 50° and ~0° to 15°, respectively. This implies a stronger inbound-outbound asymmetry with respect to the noon meridian in the later period. The mean values for inbound and outbound traversals are 455 km (in) and 375 km (out) for the PEB and 850 km (in) and 700 km (out) for the IMB; i.e., there is a slight asymmetry with higher IMB and PEB altitudes for inbound crossings. The mean IMB and PEB asymmetry is probably related to tailward magnetosphere flaring. The varying heights of the IMB and PEB along the symmetry line may correspond to slow variations of the solar wind dynamic pressure. However, the fine structure in Fig. 4 and, in particular, observations of multiple boundary crossings demonstrate the variability of the solar wind penetration process and also the lack of stability of the boundaries.

Table 1 gives some preliminary statistics of the solar wind ion access and the ionospheric ion energization inside the PEB and IMB. We binned the number of measurement sequences (~3 min) in which solar wind ions were observed inside the IMB and in which solar wind ion fluxes were below the measurement threshold. In a similar manner, the number of sequences with or without energized ionospheric ions inside the IMB and PEB, respectively, was determined. The dayside IMB is not a rigid boundary for solar wind ions. In about half of the cases, we observed solar wind ions at altitudes lower than where the IMB should have been, according to the electron data. We observed accelerated ionospheric ions well inside the IMB and sometimes also inside the PEB.

Localized precipitation of solar wind ions and the energization and erosion of ionospheric ions deep inside the ionosphere (Fig. 5 and Table 1) illustrate the variability of the dayside ionosphere at Mars. The mean PEB and IMB boundaries represent average states of the dayside ionosphere. The combined solar wind plasma precipitation and energization of ionospheric plasma suggests a rather corrugated ionosphere at Mars, with strong depletion zones that may vary with time scales on the order of a few minutes. The high variability of the IMB and PEB may be due to ionospheric peak thermal pressure insufficient to withhold the solar wind ram pressure (*18*), combined with external forcing instabilities such as the Kelvin-Helmholtz instability.

Discussion. We have presented ASPERA-3 observations of ions and electrons from the first two months of MEX commissioning near Mars, focusing on data from pericenter passes in the noon/postnoon meridian. On the basis of 11 pericenter passes, we summarize our findings as follows:

1) Solar wind plasma protrudes fairly deep into the martian ionosphere and atmosphere, occasionally down to pericenter altitudes ~270 km above the surface of Mars.

2) Acceleration processes responsible for the erosion and loss of the martian ionosphere may go deep down in the ionosphere, with the planetary wind from the dayside region sweeping tailward at altitudes as low as ~270 km.

3) Accelerated or outflowing heavy ions (e.g., O^+) with several keV in energy are found at 300 km in altitude.

4) The planetary wind also comprises molecular species, mainly as heavy ion molecules (e.g., CO_2^+ and O_2^+). This is consistent with ionospheric ion energization processes that reach low altitudes.

These findings raise a number of questions regarding ionospheric escape processes at Mars. Solar wind forcing extending deep into the ionosphere agrees with the Viking 2 lander results; the Viking 2 entry into the ionosphere displayed a sharp density cutoff above ~300 km in altitude (*13*). ASPERA-3 data show that energization and erosion of ionospheric plasma may even start below 300 km, at heights with high densities of molecular ions (*19*). Our ASPERA-3 data also confirm previous findings from Phobos-2 of molecular ions (*7*, *14*). The origin of escaping ions is related to the upper atmosphere photochemistry at Mars. The origin of, for example, escaping O^+ ions (possibly from CO_2 or H_2O) is not clear. However, the main origin of atmospheric hydrogen must be water. The combined escape of H^+ and O^+, as evidenced by measurements in the central plasma tail by Phobos-2 (*17*), is therefore evidence for a slow dehydration of Mars.

The composition of the heavy molecular ions is a matter for further investigation. For instance, how much of the escaping molecular ions are O_2^+ and how much are CO_2^+? Considering that the dominant atmospheric constituent is CO_2, it is important to establish the loss rate of carbon from the martian atmosphere. At this early stage, we cannot exclude that a large fraction of the molecular ion outflow is CO_2^+ and CO^+. It will be difficult to separate C^+ from O^+ with IMA, making it hard to shed light on the carbon loss issue. Hot carbon densities in the exosphere have been discussed by Nagy *et al*. (*20*), who note that the outflow of carbon may be substantial during high solar activity.

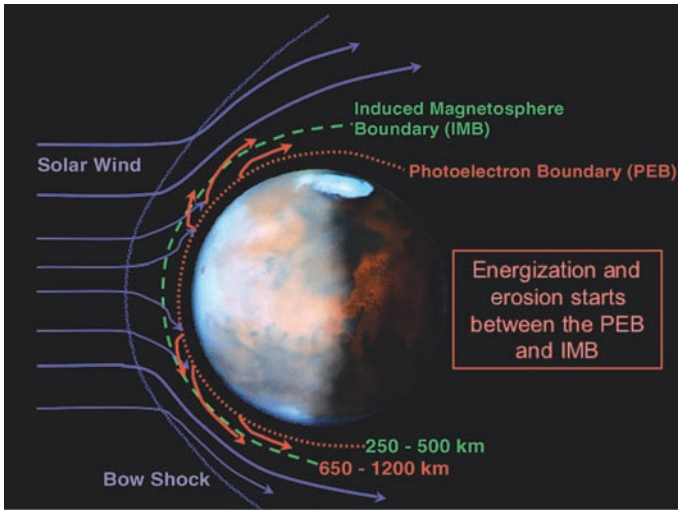

Fig. 5. Diagram illustrating ASPERA-3 findings of the solar wind–induced planetary ion erosion from the dayside ionosphere of Mars, showing how planetary ions pick up speed at altitudes located between the PEB and the IMB.

Table 1. Preliminary statistics of ASPERA-3 pericenter data.

	Solar wind ions and IMB	Accelerated ions and IMB	Accelerated ions and PEB
Inside the boundary	37	33	13
Outside the boundary	38	42	28

References and Notes

1. R. Kerr, *Science* **289**, 714 (2000).
2. E. Chassifiere, *Icarus* **124**, 537 (1996).
3. H. Pérez-de-Tejada, *J. Geophys. Res.* **92**, 4713 (1987).
4. J. G. Luhmann, S. J. Bauer, *Geophys. Monogr. Am. Geophys. Union* **66**, 417 (1992).
5. H. J. Melosh, A. M. Vickery, *Nature* **338**, 487 (1989).
6. H. Pérez-de-Tejada, *J. Geophys. Res.* **103**, 31499 (1998).
7. R. Lundin *et al.*, *Nature* **341**, 609 (1989).
8. H. Lammer *et al.*, *Int. J. Astrobiol.* **2**, 195 (2003).
9. R. Lundin, *Science* **291**, 1909 (2001).
10. D. Vignes *et al.*, *Geophys. Res. Lett.* **27**, 49 (2000).
11. S. R. Barabash *et al.*, in *Mars Express: The Scientific Payload*, A. Wilson, Ed. (ESA Special Publication SP-1240, 2004); available at http://sci.esa.int/science-e/www/object/index.cfm?fobjectid=34885.
12. M. Holmström, S. Barabash, E. Kallio, *J. Geophys. Res.* **107**, 1029 (2002).
13. W. B. Hanson, S. Sanatani, D. R. Zuccaro, *J. Geophys. Res.* **82**, 4351 (1977).
14. O. Norberg, R. Lundin, S. Barabash, in *Proceedings of the COSPAR Colloquium 4*, T. I. Gombosi, Ed. (Elsevier, Oxford, 1992), pp. 299–304.
15. M. J. Acuña *et al.*, *Science* **284**, 790 (1999).
16. D. L. Mitchell *et al.*, *J. Geophys. Res.* **106**, 23419 (2001).
17. R. Lundin *et al.*, *Geophys. Res. Lett.* **17**, 873 (1990).
18. J. G. Luhmann, C. T. Russell, F. L. Scarf, L. H. Brace, W. C. Knudsen, *J. Geophys. Res.* **92**, 8545 (1987).
19. M. B. McElroy, T. Y. Kong, Y. L. Yung, *J. Geophys. Res.* **82**, 4379 (1977).
20. A. F. Nagy, M. W. Liemohn, J. L. Fox, *J. Geophys. Res.* **106**, 21565 (2001).
21. The ASPERA-3 experiment on the European Space Agency (ESA) Mars Express is a joint effort among 15 laboratories in 10 countries, all supported by their national agencies. We thank all these agencies, as well as the various departments and institutes hosting these efforts. We wish to acknowledge in particular the Swedish National Space Board and NASA for their support of the Swedish Institute of Space Physics. We are indebted to the ESA for their courage in embarking on MEX, the first ESA mission to the Red Planet.

23 June 2004; accepted 20 August 2004

PHYTOCHROME-INTERACTING FACTOR 1 Is a Critical bHLH Regulator of Chlorophyll Biosynthesis

Enamul Huq,[1,2] Bassem Al-Sady,[2] Matthew Hudson,[2] Chanhong Kim,[3] Klaus Apel,[3] Peter H. Quail[2]*

Photosynthetic organisms must achieve a delicate balance between the light energy absorbed by chlorophyll and their capacity to channel that energy into productive photochemical reactions. Release of excess absorbed energy in the cell can cause lethal photooxidative damage. We identified a basic helix-loop-helix (bHLH) transcription factor, designated PHYTOCHROME-INTERACTING FACTOR 1 (PIF1), that negatively regulates chlorophyll biosynthesis. *pif1* mutant seedlings accumulate excess free protochlorophyllide when grown in the dark, with consequent lethal bleaching upon exposure to light. PIF1 interacts specifically with the photoactivated conformer of phytochromes A and B, suggesting a signaling pathway by which chlorophyll biosynthetic rates are tightly controlled during the critical initial emergence of seedlings from subterranean darkness into sunlight.

The colonization of land by terrestrial flowering plants has included the evolution of a capacity for the buried seed to germinate and grow upward in subterranean darkness toward the soil surface. This is accomplished with the use of a developmental strategy termed skotomorphogenesis, whereby germinated seedlings grow heterotrophically on seed reserves in the absence of chlorophyll accumulation and functional chloroplast development. Upon reaching the soil surface, the seedlings undergo a marked developmental transition, termed deetiolation, toward the normal photomorphogenic pattern of fully green plants. This transition is triggered by light and involves coordinate inhibition of hypocotyl cell elongation, unfolding of the apical hook, stimulation of cotyledon cell expansion, activation of functional chloroplast development, and chlorophyll accumulation.

The first exposure of emergent seedlings to sunlight is a point of particular vulnerability in the life cycle, requiring a sequence of tightly regulated responses. In preparation for the transition to photoautotrophic growth, subterranean seedlings accumulate a small pool of protochlorophyllide, the immediate precursor of chlorophyll, to permit rapid assembly of functional photosynthetic machinery upon initial light exposure. However, the size of this pool must be stoichiometrically linked to the level of the enzyme protochlorophyllide oxidoreductase, which catalyzes the light-induced conversion of protochlorophyllide to chlorophyll. Accumulation of free protochlorophyllide in excess over available protochlorophyllide oxidoreductase levels can result in lethal photooxidative damage, because light energy absorbed by these free molecules can be dissipated within the cell as reactive oxygen species or free radicals (*1*–*2*). Therefore, coordinate regulation of the chlorophyll biosynthetic pathway and the capacity for enzymatic conversion of protochlorophyllide to chlorophyll is particularly crucial during the initial deetiolation process.

The light signals that induce the deetiolation transition are perceived by members of the cryptochrome (cry) and phytochrome (phy) families of informational photoreceptors. We focused on defining the signaling and transcriptional networks involved in transducing the signals perceived by the five-member phy family (phyA through phyE) in *Arabidopsis*. These molecules monitor the incident red (R) and far-red (FR) light impinging on the plant by switching reversibly between two conformers—the inactive Pr and active Pfr forms—upon sequential R and FR photon absorption. The activated molecules subsequently transduce the perceived information to photoresponsive nuclear genes. Studies in recent years have defined and led to the cloning of a considerable number of genetic loci apparently involved in the signaling process (*3*–*5*), and a number of phytochrome-interacting factors (PIFs) that bind directly to the photoreceptor molecules have been identified (*3*, *6*). Current evidence suggests that the signal transduction mechanism involves light-induced translocation of the photoreceptor molecule from the cytoplasm into the nucleus, and subsequent physical interaction with PIF3, a member of the bHLH family of transcriptional regulators, with consequent modulation of target gene expression (*7*–*10*). Although initially reported to act positively in phy signaling (*9*, *11*, *12*), PIF3 has recently been found to have a complex role in seedling deetiolation, acting both positively and negatively in different facets of the process (*13*–*15*). In addition, recent data indicate that the translocated phy molecule induces degradation of PIF3 (*14*), thereby presumptively affecting transcriptional activity indirectly by reducing PIF3 abundance. Three other bHLH factors—PIF4 (*16*), HFR1 (*17*), and PIL1 (*18*)—have also been implicated in phy-regulated responses.

However, definitive identification of the mechanism involved in phy signaling to nuclear interactors is presently lacking, and the number of bHLH factors and their target genes that are potentially involved in phy-related activities remains to be defined. Based on the premise that closely related proteins may have similar functions, we investigated a new bHLH family member, designated PIF1 [*Arabidopsis* Genome Initiative (AGI) locus number At2g20180], with high sequence similarity to PIF3 (*11*), for possible involvement in the light-induced seedling deetiolation process.

PIF1 negatively regulates chlorophyll biosynthesis. To determine whether PIF1 is functionally involved in phy-regulated seedling development, we isolated homozygous *pif1* transferred DNA (T-DNA) insertion lines and generated *PIF1* overexpression lines. Sequence analyses showed that the T-DNA is inserted in the second exon, causing deletion of the bHLH domain in both the *pif1-1* and *pif1-2* alleles (Fig. 1A). Northern blot analyses showed a stable band of 0.9 kb for the *pif1-1* allele and no detectable band for the *pif1-2* allele (Fig. 1B), suggesting that at least the latter is a null allele.

Although the overexpression lines displayed some perturbation in normal seedling growth, neither T-DNA–insertion mutant showed any detectable alteration in photoresponsiveness under the extended irradiation conditions used from germination onward (fig. S1, A and B). These data suggest that PIF1 is not necessary for normal seedling deetiolation under these conditions but is capable of interfering with this process when overexpressed.

In contrast, we observed a marked bleaching phenotype in *pif1* mutant seedlings that had first been germinated and grown in the dark for several days before transfer to white light (Fig. 1C). Because this phenotype is qualitatively reminiscent of *flu* mutants, which bleach in light as a result of the accumulation of excess protochlorophyllide (*19*),

[1]Section of Molecular Cell and Developmental Biology and Institute of Molecular Biology, University of Texas at Austin, Austin, TX 78712, USA. [2]Department of Plant and Microbial Biology, University of California, Berkeley, CA 94720, USA and U.S. Department of Agriculture/Agricultural Research Service, Plant Gene Expression Center, 800 Buchanan Street, Albany, CA 94710, USA. [3]Institute of Plant Sciences, Swiss Federal Institute of Technology (ETH), Universitatstrasse 2, 8092 Zurich, Switzerland.

*To whom correspondence should be addressed. E-mail: quail@nature.berkeley.edu

we examined the *pif1* mutant for protochlorophyllide levels using low-temperature (77 K) fluorescence spectra analysis (*2*, *19*). The data show that the level of protochlorophyllide in dark-grown *pif1-1* is about two times as high as that in the wild-type seedlings (Fig. 1D). Importantly, the *pif1* mutants also show levels of free protochlorophyllide four to six times as high as wild-type seedlings in the short term after initial transfer to white light (up to 3 hours shown in Fig. 1, E and F). However, *pif1* seedlings showed little or no residual chlorophyll or chlorophyll precursors under prolonged incubation in light, reflecting the bleaching process (fig. S2, A and B). Thus, the bleaching phenotype of *pif1* is apparently due to the overaccumulation of free protochlorophyllide in the postgermination dark period and seems to indicate that photooxidative damage in light is caused by the photosensitizing activity of this tetrapyrrole intermediate.

In time-course experiments, we observed that the severity of the bleaching phenotype increased markedly with increasing time in darkness before transfer to light (Fig. 2A). Young seedlings germinated for 1 or 2 days in darkness before transfer to light exhibited no detectable bleaching, whereas seedlings held in darkness for 3 to 6 days displayed an increasingly severe phenotype. These data suggest that PIF1 may function as a negative regulator of the chlorophyll biosynthetic pathway, acting to prevent the accumulation of excess protochlorophyllide in prolonged darkness. To test this proposition more directly, we examined the rate of light-induced chlorophyll accumulation in young *pif1* mutant seedlings in which insufficient protochlorophyllide had previously accumulated to cause bleaching. The *pif1* seedlings accumulated chlorophyll significantly more rapidly than did wild-type seedlings under these conditions (Fig. 2B). This increase is not due to enhanced cotyledon expansion, given that the *pif1* mutants have cotyledon areas similar to those of the wild-type seedlings (fig. S3). Conversely, *phyA* and *phyB* null mutants accumulated chlorophyll more slowly than did the wild-type seedlings (Fig. 2C), consistent with a positive role for each photoreceptor in this process. Together, the data indicate that PIF1 does indeed negatively regulate the chlorophyll biosynthetic pathway and that phyA and phyB may act to repress PIF1 activity in the light (Fig. 2D).

The increasing lethality in *pif1* seedlings with increasing preillumination darkness suggests that PIF1 may have evolved to protect seedlings germinating at depth in subterranean darkness from the deleterious effects of uncontrolled protochlorophyllide accumulation before reaching the surface. This is more directly apparent when the seedling survival rate is quantified as a function of hypocotyl length at first exposure to light for wild-type compared with *pif1* seedlings (Fig. 3). The data show that the presence of PIF1 in wild-type seedlings confers a marked presumptive selective advantage for seeds germinating at 10 mm or more below the soil surface (Fig. 3). Consistent with this notion, PIF1 overexpressors exhibit a substantially enhanced capacity to resist lethal bleaching compared with that of the wild-type seedlings after considerably longer preillumination dark periods (>10 days) (*20*).

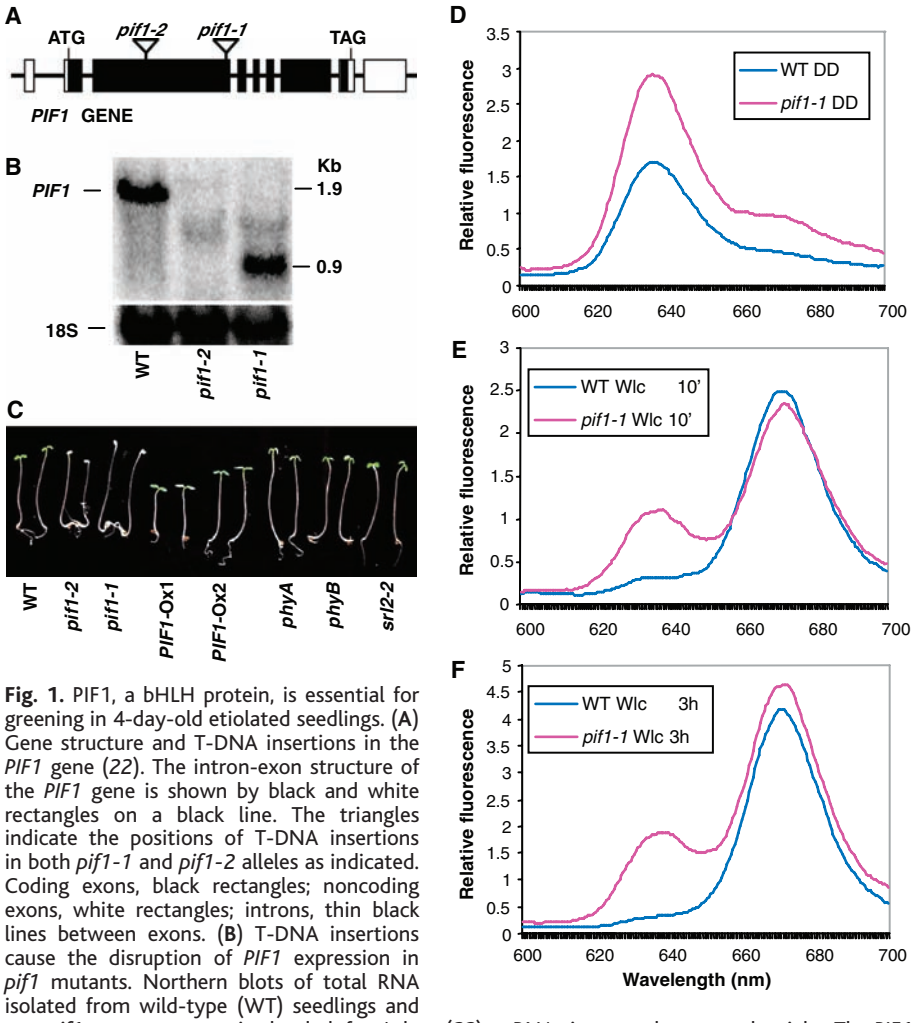

Fig. 1. PIF1, a bHLH protein, is essential for greening in 4-day-old etiolated seedlings. (**A**) Gene structure and T-DNA insertions in the *PIF1* gene (*22*). The intron-exon structure of the *PIF1* gene is shown by black and white rectangles on a black line. The triangles indicate the positions of T-DNA insertions in both *pif1-1* and *pif1-2* alleles as indicated. Coding exons, black rectangles; noncoding exons, white rectangles; introns, thin black lines between exons. (**B**) T-DNA insertions cause the disruption of *PIF1* expression in *pif1* mutants. Northern blots of total RNA isolated from wild-type (WT) seedlings and two *pif1* mutants grown in the dark for 4 days (*22*). mRNA sizes are shown on the right. The PIF1 open-reading-frame region was used as a probe. 18*S* ribosomal RNA was used to show the amount of RNA loaded in each lane. (**C**) Visible phenotypes of the *pif1* mutants, wild-type (Col), and *PIF1* overexpression (Ox) lines grown for 5 days in the dark and then transferred to white light (50 μmol m^{-2} s^{-1}) for 2 days (*22*). *phyA*, *phyB*, and *srl2-2* mutants were grown under the same conditions (controls). Seedling images are to scale. (**D** to **F**) *pif1* has a higher level of protochlorophyllide (635-nm peak) than the wild-type seedlings. Fluorescence spectra of acetone extracts from wild-type and *pif1-1* mutant seedlings that were grown for 4 days in the dark (D) or dark-grown seedlings transferred to white light for 10 min (E) or 3 hours (h) (F) with the use of an excitation wavelength of 440 nm. DD, dark; Wlc, white light.

PIF1 interacts with photoactivated phyA and phyB. To explore the mechanism(s) by which PIF1 might regulate the chlorophyll biosynthetic pathway, we investigated the molecular interactions between PIF1 and the two principal phytochromes regulating seedling deetiolation. Figure 4, A and B, shows that PIF1 interacts strongly and specifically with the biologically active Pfr form of both phyA and phyB, as determined by an in vitro coimmunoprecipitation assay. PIF1 has reduced affinity for signaling-compromised missense mutant forms of phyA and phyB, suggesting that this interaction is biologically important (Fig. 4, A and B). Because the other two phy-interacting bHLH proteins thus far reported, PIF3 and PIF4, both displayed strongly preferential binding to phyB compared with phyA (*16*, *21*), we directly compared the apparent binding affinities of these two PIFs with those of PIF1 toward the two phy's. The data show that PIF1 and PIF3 have similar affinities for phyB, which are somewhat higher than PIF4 (Fig. 4C). In

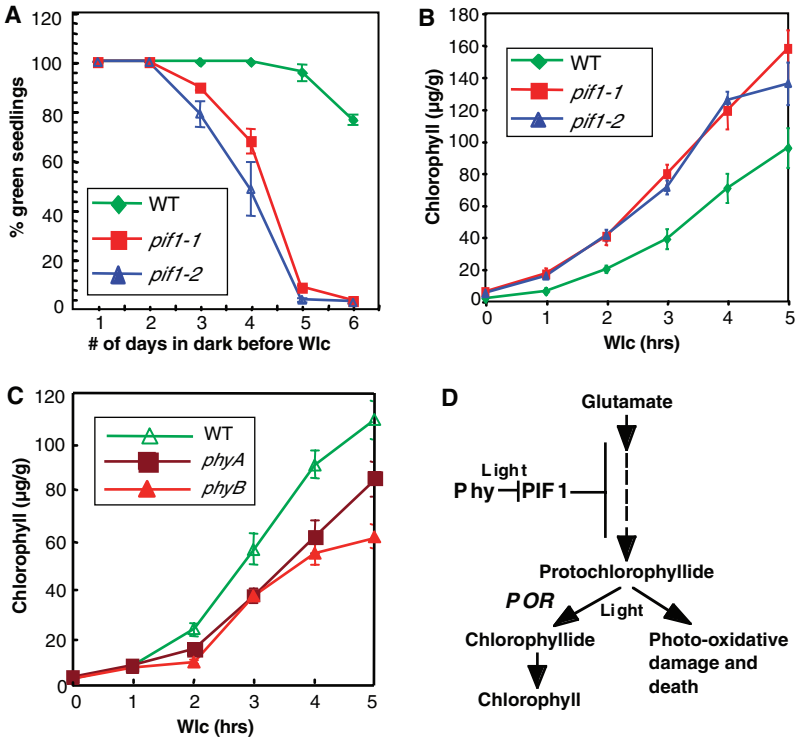

Fig. 2. Perturbation of chlorophyll biosynthesis is responsible for the bleaching phenotype of *pif1* mutants. (**A**) *pif1* seedlings fail to green if grown in the dark for 4 to 6 days before transfer to white light. (**B**) PIF1 modulates control of chlorophyll biosynthesis in response to light. Young *pif1* mutant seedlings accumulate chlorophyll at higher rates compared with accumulation rates of wild–type seedlings in response to light. Two-day-old dark-grown wild-type or *pif1* mutant seedlings were transferred to continuous white light (Wlc) for different periods of time and total chlorophyll was extracted in N′N′-dimethylformamide, according to Inskeep and Bloom (*23*). Standard error of means for three different experiments are shown. (**C**) Photoreceptor mutants accumulate chlorophyll at a reduced rate compared with that of wild-type seedlings. Three-day-old etiolated wild-type (Col-O), *phyA*, and *phyB* mutant seedlings (in Col-O background) were transferred to Wlc for different time periods and total chlorophyll was measured as described in (B). Error bars in (A) to (C) show mean ± SEM. (**D**) Model outlining potential role of PIF1 in controlling chlorophyll biosynthesis. PIF1 either directly or indirectly represses the biosynthesis of protochlorophyllide in the dark, or increases its stability. Phy's directly interact with PIF1 upon light activation, potentially repressing PIF1 transcriptional activity in a light-dependent manner and thereby increasing chlorophyll biosynthesis in response to light. POR, photochlorophyllide oxidoreductase.

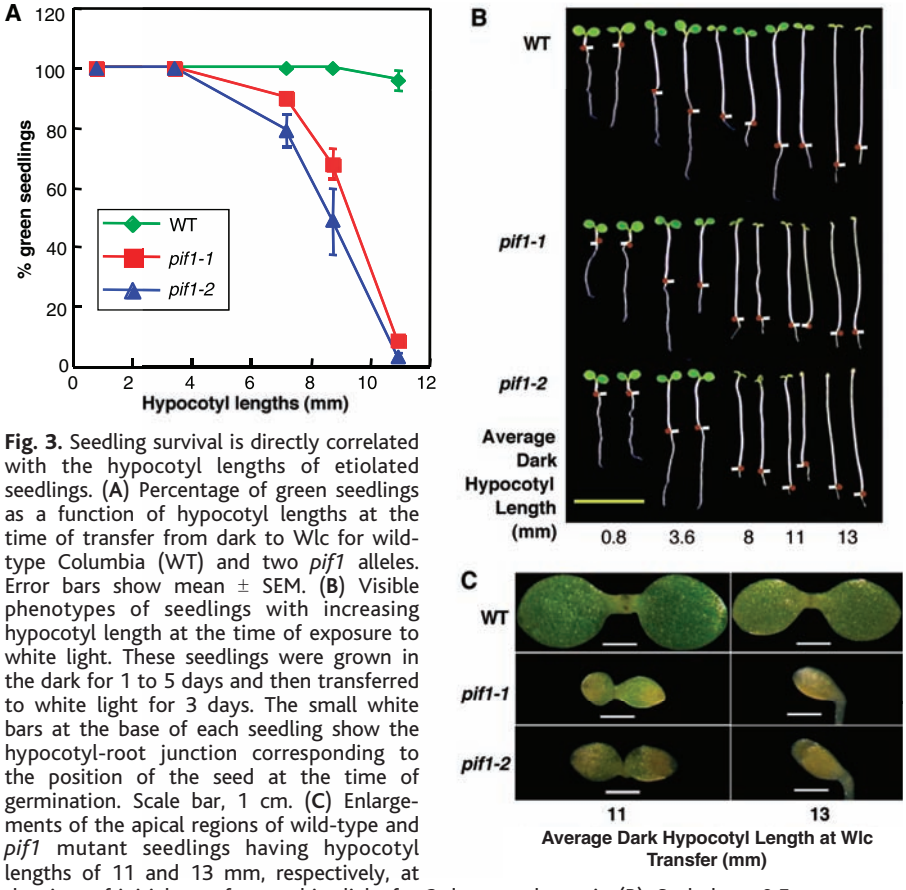

Fig. 3. Seedling survival is directly correlated with the hypocotyl lengths of etiolated seedlings. (**A**) Percentage of green seedlings as a function of hypocotyl lengths at the time of transfer from dark to Wlc for wild-type Columbia (WT) and two *pif1* alleles. Error bars show mean ± SEM. (**B**) Visible phenotypes of seedlings with increasing hypocotyl length at the time of exposure to white light. These seedlings were grown in the dark for 1 to 5 days and then transferred to white light for 3 days. The small white bars at the base of each seedling show the hypocotyl-root junction corresponding to the position of the seed at the time of germination. Scale bar, 1 cm. (**C**) Enlargements of the apical regions of wild-type and *pif1* mutant seedlings having hypocotyl lengths of 11 and 13 mm, respectively, at the time of initial transfer to white light for 3 days, as shown in (B). Scale bars, 0.5 mm.

contrast, PIF1 has affinity for phyA more than 10 times as high as that of PIF3 or PIF4 (Fig. 4C). These results establish PIF1 as a distinct member of the phy-interacting bHLHs thus far described, with a potential role in both phyA and phyB signaling. The data suggest that different bHLH proteins may interact differentially with different phy family members, thereby providing the potential for selective channeling of photosensory signaling information to different subsets of target genes.

As PIF1 is a member of the bHLH family, we investigated its subcellular localization and whether it can directly bind to DNA. Not unexpectedly, the data indicate that PIF1 localizes to the nucleus (fig. S4). Previously, we have shown with gel-shift assays that both PIF3 and PIF4 bind to the G-box DNA sequence motif (CACGTG) found in many light-regulated promoters and that phyB can bind DNA-bound PIF3 in the Pfr form to generate a specific super-shifted complex in these assays (*9*, *16*). Our present data show that PIF1 can also bind to this G-box motif in sequence-specific fashion (fig. S5A). However, in contrast to PIF3, DNA-bound PIF1 displayed no detectable interaction with either phyB or phyA by gel-shift assay (fig. S5B). Thus, PIF1 apparently cannot bind to both the G-box DNA and activated phy molecules simultaneously under these experimental conditions, which is similar to previously reported behavior for PIF4 (*16*). These data suggest that the mechanism of phy-mediated control of gene expression through PIF1 and PIF3 might be different. Alternatively, if the recently reported light-induced degradation of PIF3 (*14*) is general among other phy-interacting bHLHs, it is possible that this basic process can occur regardless of whether the factor is DNA-bound or free and that it is different in this respect between the different bHLHs.

PIF1 transcriptional activation activity is negatively modulated by phyA and phyB. To determine whether PIF1 can function in phy-modulated gene regulation, we investigated whether it can activate transcription in a transient assay in a light-responsive manner. For this purpose, PIF1 was expressed as a fusion protein with the GAL4 DNA binding domain under the control of the strong cauliflower mosaic virus 35S (CaMV35S) promoter (Fig. 5A). The reporter construct consisted of a minimal promoter with the GAL4 DNA binding site driving a Luciferase reporter gene. A Renilla Luciferase gene under the control of a CaMV35S promoter was also used as an internal control. These constructs were expressed transiently in 3-day-old dark-grown *Arabidopsis* seedlings after particle bombardment, and Luciferase activity was assayed after 16 hours of incubation under pulses of red light (Rp), continuous red light (Rc) (*20*), continuous far-red light (FRc), or dark. PIF1 stimulated up to seven times as much Luciferase expression as that of the controls in dark-incubated seedlings, indicating that this factor does indeed have the capacity to function as a transcriptional activator in vivo (Fig. 5, B to D). Intriguingly, both Rp and FRc light treatments significantly suppressed the transcriptional activator activity of PIF1 in a phyB- and phyA-dependent manner, respectively (Fig. 5, B to D), indicating that each of these two photoreceptors, endogenously present in the target cells, was capable of negatively regulating the transcriptional activity of PIF1 in response to the relevant light signals. The yeast GAL4 transcriptional activator DNA binding domain (DBD)–GAL4 activation domain fusion (DBDAD), although active in the *Arabidopsis* cells, showed no such responsiveness to the light signals (Fig. 5B). Because DNA-bound PIF1 did not interact with either phy molecule (fig. S5B), these data suggest that the function of the direct physical interaction between unbound PIF1 and phyA and phyB might be to modulate PIF1 transcriptional activity through interference, sequestration, or degradation to modulate chlorophyll biosynthesis in response to light.

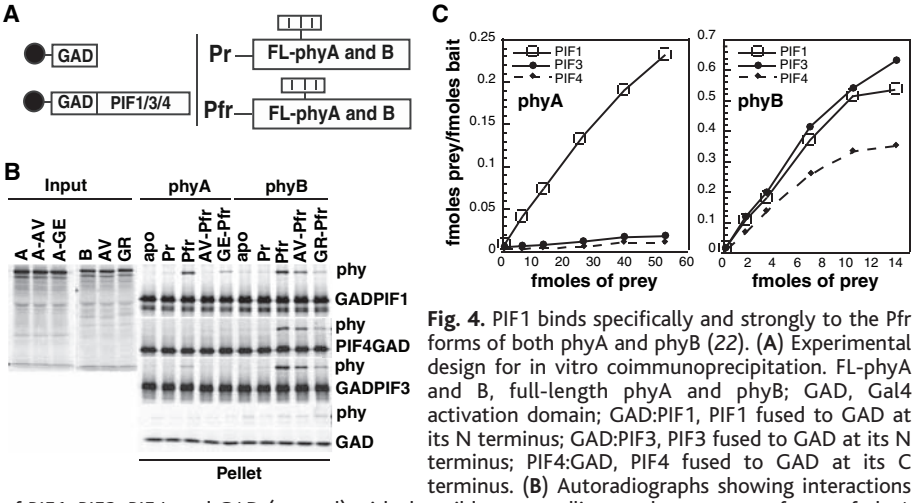

Fig. 4. PIF1 binds specifically and strongly to the Pfr forms of both phyA and phyB (*22*). (**A**) Experimental design for in vitro coimmunoprecipitation. FL-phyA and B, full-length phyA and phyB; GAD, Gal4 activation domain; GAD:PIF1, PIF1 fused to GAD at its N terminus; GAD:PIF3, PIF3 fused to GAD at its N terminus; PIF4:GAD, PIF4 fused to GAD at its C terminus. (**B**) Autoradiographs showing interactions of PIF1, PIF3, PIF4, and GAD (control) with the wild-type seedlings and two mutant forms of phyA and phyB, respectively. Left panel shows the input, and right panel shows the pellet fraction from the in vitro coimmunoprecipitation assay. A and B under input represent phyA and phyB, respectively; apo, phy without chromophore; AV/GR and AV/GE are missense mutants of phyA and phyB, respectively. GAD, GAD:PIF1, GAD:PIF3, and PIF4:GAD are described in (A). (**C**) Concentration curves showing the increased binding with increasing amount of phyA or phyB in the Pfr form (prey) with either GAD:PIF1, GAD:PIF3, or PIF4:GAD (bait). The same amount of bait (~12 fmol) was used for each construct in each tube. The absolute amount of each bait and prey used was calculated from a standard curve with the use of known amounts of ^{35}S-methionine. fmoles of prey/fmoles of bait is plotted against increasing amount of prey used.

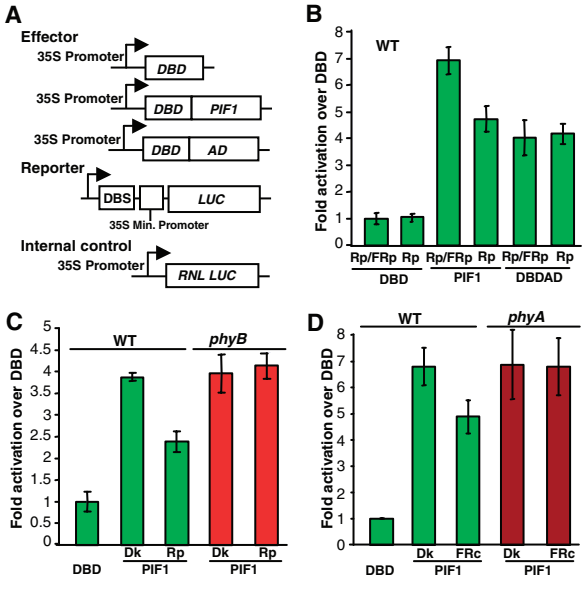

Fig. 5. PIF1 transcriptional activation activity is regulated by phyA and phyB in a light-dependent manner (*22*). (**A**) Constructs used for the experiment. AD, GAL4 activation domain; DBS, GAL4 DNA binding site; LUC, firefly Luciferase; RNL LUC, Renilla Luciferase. Three-day-old etiolated *Arabidopsis* seedlings of Col wild type (WT) (**B**), wild type and *phyB* (**C**), or wild-type and *phyA* mutants (**D**) were bombarded with effector constructs constitutively expressing a DBD-PIF1 fusion (DBDPIF1), DBDAD, or DBD alone. Seedlings were treated for 15 min with FR light and then exposed to 5-min pulses of R light alone (Rp) every 2 hours (9×40 μmol m^{-2} s^{-1}) [(B) and (C)] or R pulses followed immediately by a FR pulse (Rp/FRp) (9×55 μmol m^{-2} s^{-1}) (B), or continuous FR light (FRc) (20 μmol m^{-2} s^{-1}) (D) or darkness (Dk) for 14 hours [(C) and (D)]. Each histogram column represents the mean of eight biological replicates and the variation is expressed as standard error. Transcriptional activity was measured with the use of a dual-Luciferase assay system (Promega). The photon-count ratio of the reporter firefly (LUC+ in pGLL reporter plasmid) and *Renilla* (RNL internal control plasmid) luciferases measured in the presence of the effector DBD alone (pMN6 plasmid) is set as 1× fold activation. Fold transcriptional activity is determined by the photon-count ratios of these two reporter luciferases driven by the DBDPIF1 or DBDAD effectors, divided by this ratio for DBD alone.

Fine-tuning chlorophyll biosynthesis: Mechanisms and potential evolutionary implications. Collectively, the data suggest that PIF1 may function as a negative regulator of the chlorophyll biosynthetic pathway in the dark, and that this activity is negatively regulated by light (Fig. 2D). According to this model, light-induced photoconversion of phy molecules to the Pfr form would trigger interaction with PIF1, in some way reducing the transcriptional activation activity of PIF1. This would, in turn, result in partial release of the negative regulation of PIF1, which would allow plants to produce higher rates of chlorophyll synthesis in the light (Fig. 2B). On this basis, PIF1 would appear to function as a critical modulator by which plants optimize chlorophyll biosynthesis in response to environmental light conditions and protect against accumulation of potentially toxic levels of intermediates. Given the similarity of the *pif1* phenotype to that of the *flu* mutants (*19*), we examined whether PIF1 might regulate *FLU* gene expression. However, no difference in *FLU* transcript levels between wild-type and *pif1-1* seedlings was detected on Northern blots (*20*), suggesting that other components in the pathway are potential targets.

The proposed protective biological function of PIF1 may have emerged early in angiosperm evolution to provide a selective advantage in certain environments where seed burial was critical to survival. The capacity to germinate and emerge from subterranean darkness may have been particularly important in the successful radiation of the seed producers into drier, more hostile environments. Seed burial can provide long-term survival through protection from predators and hostile surface conditions until environmental conditions are favorable for germination and can facilitate establishment of a robust underground root system before seedling emergence, thereby increasing survival potential.

phy signaling through a bHLH transcriptional network. The reverse-genetic strategy of targeting *Arabidopsis* bHLH-family members, which are phylogenetically related to PIF3, for potential involvement in phy-regulated development is providing emerging evidence of a small network of these factors differentially involved in regulating and integrating different facets of the seedling deetiolation process. PIF3 (*11*), PIF4 (*16*), HFR1 (*17*), PIL1 (*18*), and PIF1 are all involved in this process, but each appears to have a differential role. Moreover, together with the recent evidence of phy-induced PIF3 degradation (*14*), our data here for PIF1 suggest that modulation of constitutively active transcription factor activity might be one of the mechanisms by which the phy family of photoreceptors induces photomorphogenesis in response to light.

References and Notes

1. S. Reinbothe, C. Reinbothe, K. Apel, N. Lebedev, *Cell* **86**, 703 (1996).
2. R. G. L. op den Camp *et al.*, *Plant Cell* **15**, 2320 (2003).
3. P. H. Quail, *Nature Rev. Mol. Cell. Biol.* **3**, 85 (2002).
4. H. Wang, X.-W. Deng, *The Arabidopsis Book*, C. R. Somerville, E. M. Meyerowitz, Eds. (American Society of Plant Biologists, Rockville, MD, 2004), 10.1199/tab.0074.1, http://aspb.org/publications/arabidopsis.
5. M. M. Neff, C. Fankhauser, J. Chory, *Genes Dev.* **14**, 257 (2000).
6. P. H. Quail, *Sem. Cell Dev. Biol.* **11**, 457 (2000).
7. F. Nagy, E. Schaefer, *Annu. Rev. Plant Biol.* **53**, 329 (2002).
8. S. Kircher *et al.*, *Plant Cell* **14**, 1541 (2002).
9. J. Martinez-Garcia, E. Huq, P. H. Quail, *Science* **288**, 859 (2000).
10. M. Ni, J. M. Tepperman, P. H. Quail, *Nature* **400**, 781 (1999).
11. M. Ni, J. M. Tepperman, P. H. Quail, *Cell* **95**, 657 (1998).
12. K. J. Halliday, M. Hudson, M. Ni, M.-M. Qin, P. H. Quail, *Proc. Natl. Acad. Sci. U.S.A.* **96**, 5832 (1999).
13. J. Kim *et al.*, *Plant Cell* **15**, 2399 (2003).
14. D. Bauer *et al.*, *Plant Cell* **16**, 1433 (2004).
15. E. Monte, P. Quail, unpublished data.
16. E. Huq, P. H. Quail, *EMBO J.* **21**, 2441 (2002).
17. C. D. Fairchild, M. A. Schumaker, P. H. Quail, *Genes Dev.* **14**, 2377 (2000).
18. M. G. Salter, F. A. Keara, G. C. Whitelam, *Nature* **426**, 680 (2003).
19. R. Meskauskiene *et al.*, *Proc. Natl. Acad. Sci. U.S.A.* **98**, 12826 (2001).
20. E. Huq, P. H. Quail, data not shown.
21. Y. Zhu, J. M. Tepperman, C. D. Fairchild, P. H. Quail, *Proc. Natl. Acad. Sci. U.S.A.* **97**, 13419 (2000).
22. Materials and methods are available as supporting material on *Science* Online.
23. W. P. Inskeep, P. R. Bloom, *Plant Physiol.* **77**, 483 (1985).

24. We thank K. Chang and C. Lanzatella for technical assistance, J. Tepperman for help with nuclear localization assays, V. Symonds for help with photography, and the *Arabidopsis* Biological Resource Center, Ohio, for providing seed stocks. Supported by grants from NIH no. GM47475, the Torrey Mesa Research Institute, San Diego, U.S. Department of Energy Basic Energy Sciences no. DE-FG03-87ER13742 and U.S. Department of Agriculture Current Research Information Service no. 5335-21000-010-00D to P.H.Q. and a set-up fund from University of Texas at Austin to E. H. Molecular interaction data have been deposited in the Biomolecular Interaction Network Database with accession codes 151737, 151738, 151739, and 151740.

Supporting Online Material

www.sciencemag.org/cgi/content/full/305/5692/1937/DC1
Materials and Methods
Figs. S1 to S5
References

28 April 2004; accepted 4 August 2004

REPORTS

Observation of Superflow in Solid Helium

E. Kim and M. H. W. Chan*

We report on the observation of nonclassical rotational inertia in solid helium-4 confined to an annular channel in a sample cell under torsional motion, demonstrating superfluid behavior. The effect shows up as a drop in the resonant oscillation period as the sample cell is cooled below 230 millikelvin. Measurement of 17 solid samples allows us to map out the boundary of this superfluid-like solid or supersolid phase from the melting line up to 66 bars. This experiment indicates that superfluid behavior is found in all three phases of matter.

At temperatures below 2.176 K, liquid ^{4}He enters into a superfluid state and flows without any friction (*1*, *2*). The onset of superfluidity is associated with Bose-Einstein condensation (*3*, *4*), where the ^{4}He atoms, which are bosons, condense into a single momentum state and acquire quantum mechanical coherence over macroscopic length scales. Bose-Einstein condensation of alkali atoms in the vapor phase was achieved (*5*) in 1995, and there is strong evidence for superfluidity in these systems (*6*–*8*). Perhaps counter to intuition, superfluid-like behavior is thought possible even in solid helium (*9*–*14*). A recent torsional oscillator measurement found evidence of superfluid flow in solid helium confined in porous Vycor glass (*15*) with pore diameter of 7 nm. There is, however, concern that the observed effect may be due to a liquid-like layer of helium atoms adsorbed on the surface of the pores (*16*). Here we report observation of superflow in bulk solid helium. Our experiment shows that the superfluid-like behavior is a general and intrinsic property of solid helium and not the result of confinement in any particular medium.

The resonant period of the high mechanical quality factor torsional oscillator (*17*) (Fig. 1) is given by $2\pi[(I/G)^{1/2}]$, where I is the moment of inertia of the torsion cell, which contains ^{4}He, and G is the torsion spring constant of the Be-Cu torsion rod. The torsion cell has an annular channel in which ^{4}He can be introduced and pressurized to the solid phase. Ultrahigh-purity ^{4}He, with a stated ^{3}He impurity of 0.3 parts per million, is used in our experiment. When ^{4}He enters the superfluid or supersolid phase and acquires nonclassical rotational inertia (NCRI), a fraction of the helium decouples from the oscillation, thereby reducing the rotational inertia I and the resonant period. We have measured a total of 17 solid ^{4}He samples with pressure ranging from 26 bars, close to the melting boundary, to 66 bars; all showed supersolid decoupling below 230 mK.

The resonant period as a function of temperature is shown for a solid sample pressurized to 51 bars (Fig. 2A). Measurements

Department of Physics, Pennsylvania State University, University Park, PA 16802, USA.

*To whom correspondence should be addressed. E-mail: chan@phys.psu.edu

were made with different drive voltages, inducing different amplitudes and speeds of oscillation. We calculated and labeled the different runs by the maximum speed in a cycle of oscillation as computed at the mean radius of the annular channel, v_{max}. We display our data on a logarithmic rather than a linear scale to better highlight results in the low-temperature region. The resonant period showed a linear dependence on temperature from 0.3 K up to 1.5 K. A linear dependence on temperature extending down to 0.1 K, with a shallower slope, was also found for the empty cell. The empty-cell period is smaller than the filled-cell value by 3012 ns at 0.3 K. When the lock-in amplifier is adjusted for measurement with a different oscillation speed, the resonant period often shows a shift of a few ns. However, the period versus temperature curves for different speeds have identical slopes and can be made to collapse onto each other, as shown in the figure, by shifting the period values at any temperature between 0.3 and 1.5 K.

Below 250 mK, the period begins to drop below the linear background extrapolated from higher temperature. The negative period shift, or the difference between the measured period and the period given by linear background ($\tau - \tau^*$), increases smoothly but rapidly with decreasing temperature and saturates below 40 mK. The resonant period curves measured with v_{max} equal to 4 and 6 μm/s are identical and appear as a single curve down to the lowest temperature. At 14 μm/s and above, the period shift decreases with v_{max} and falls below the level of detection for the run with v_{max} equal to 420 μm/s.

Although a constant ac voltage was used to excite the oscillation for each run of a specific v_{max}, a broad minimum in the amplitude of the oscillation (and hence also v_{max}) is seen over the temperature range where $\tau - \tau^*$ is changing most rapidly. This minimum is seen for all solid samples studied, irrespective of the oscillating speed. For clarity we show in Fig. 2A the amplitude curves for only three runs, namely with v_{max} at 4, 33, and 117 μm/s. In some runs, the low-temperature amplitude recovers to the high-temperature value; in others, it is lower. The v_{max} values labeling the various curves in Fig. 2A are calculated at the low-temperature limit. This minimum in amplitude is a signature of dissipation and is reminiscent of that found in two-dimensional, thin, superfluid liquid ^{4}He films adsorbed on a planar surface (*17*–*19*). In addition to the minimum, the amplitude also shows a smooth decrease with increasing temperature above 0.3 K. This feature is not related to the dissipation of superflow seen when the torsional cell is filled with solid ^{3}He.

If the resonant period drop is due to solid helium in the annulus entering the supersolid phase, then in the reference frame of the torsional cell the supersolid fraction would be executing oscillatory superflow around the annulus. If a barrier is present in the annulus, superflow around the annulus cannot be established and the decrease in the resonant period should be vastly reduced. The result of this control experiment on a solid sample of 36 bars measured with a cell with a barrier in the annulus is shown in Fig. 2B. Because the physical dimensions of this torsion cell—including the diameter and the width of the (blocked) annulus—are larger than those of the barrier-free or unblocked cell, the expected period shift in the absence of the barrier is also larger. The expected total period shift in the absence of the barrier is 95 ± 15 ns. Instead, a period shift of 1.4 ± 0.2 ns, or 1.5 ± 0.5% of the expected value, is seen. A superfluid sample confined in a finite cavity, due to irrotational flow, will exhibit decoupling even if the cavity does not make a complete path around the axis of rotation (*20*). A calculation of this irrotational flow effect, mimicking the geometry and dimensions of the blocked channel, found a decoupling of 0.8% (*21*), on the order of the measured value. Another possible source of this decoupling is the small gap of several μm that was left unfilled by epoxy resin when the torsion rod was attached to the torsion cell. The reason for this gap is that we wanted to make sure the hole from the torsion rod to the annulus remained open for the introduction of ^{4}He. We estimate that this gap may contribute up to 0.5 ns of the observed decoupling. We repeated the measurement with liquid helium with this blocked cell. The period of oscillation increased by 5270 ns when the annulus was filled with normal liquid. In the low-temperature limit, all the liquid should be superfluid; however, the total decoupling

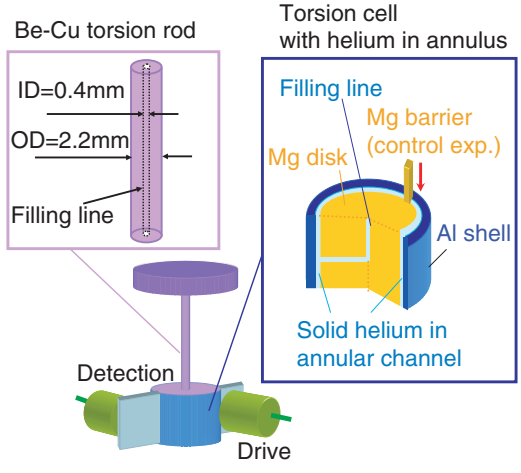

Fig. 1. Torsional oscillators: The cylindrical drive and detection electrodes are coupled capacitively to the two planar electrodes attached as fins on the two sides of the cylindrical torsion cell. Oscillation of the torsion cell induces an ac voltage on the detection electrode. This voltage enables a lock-in amplifier to keep the oscillation in resonance. The outside diameter, width, and height of the channel in the barrier-free torsion cell are 10 mm, 0.63 mm, and 5 mm, respectively. The mechanical quality factor of the oscillator is 2×10^6, allowing the determination of the resonant period to 0.2 ns out of a resonant period of 1 ms. The outside diameter, width, and height of the (blocked) channel of a second torsion cell with the barrier are 15 mm, 1.1 mm, and 5 mm, respectively. The mechanical quality factor and period precision values are similar to those of the barrier-free torsion cell.

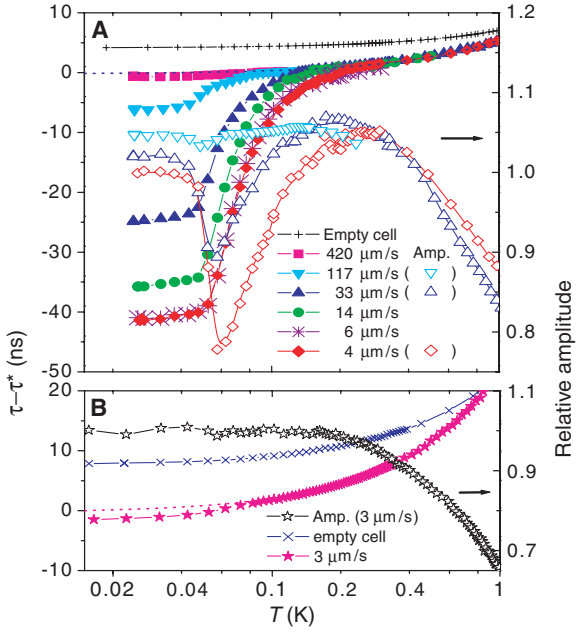

Fig. 2. Resonant period and amplitude of oscillation as a function of temperature for the unblocked (**A**) and blocked (**B**) cell. The period readings are shifted relative to τ^*, the resonant period at 300 mK. The values of τ^* for the open cell with helium are 1,099,477 ns, 1,099,480 ns, 1,099,482 ns, 1,099,483 ns, 1,099,488 ns, and 1,099,485 ns when the maximum oscillation speed are, respectively, 4, 6, 14, 33, 117, and 420 μm/s. The empty-cell period at 300 mK is 1,096,465 ns, 3012 ns less than that when the cell is full. The value of τ^* for the blocked cell with solid helium at 36 bars at 300 mK is 2,242,940 ns. The resonant period when it is empty at 300 mK is 2,235,890 ns.

we observed is only 90 ns. In other words, the observed fractional decoupling in the blocked cell filled with superfluid is comparable to that found for solid helium. This similarity suggests that superflow in solid ^{4}He, as in superfluid, is also irrotational. In contrast to the data obtained with the barrier-free or unblocked cell, there is no observable minimum in the amplitude. We have also made measurements with high-purity (99.999%) solid ^{3}He in the barrier-free torsion cell and found no drop in the resonant period and no amplitude minimum.

In Fig. 3 we plot the nonclassical rotational inertia fraction (*11*) (*NCRIF*) as a function of temperature for 3 of the 17 samples we studied. *NCRIF* is defined as the period shift $\tau - \tau^*$ (Fig. 2A) divided by the increase in period due to the filling of the annulus with the specific ^{4}He sample. The family of curves in Fig. 3, A to C, show *NCRIF* determined with different values of v_{max}. *NCRIF* obtained with v_{max} smaller than a certain critical value, v_c, collapses into a single curve. Exceeding v_c, *NCRIF* is found to decrease with v_{max}. The value of v_c of the samples at 41 and 65 bars (Fig. 3, B and C) and 51 bars (Fig. 2A) is close to 5 μm/s. A much higher v_c, close to 38 μm/s, is found for the 26-bars sample. The value of *NCRIF* in the low-temperature limit (at 20 mK) as a function of v_{max} for five different solid samples is also shown (Fig. 3D). The results shown in Figs. 3 and 2A can be understood by thinking of v_c as the critical velocity of superflow. When the torsional cell is oscillating with v_{max} below v_c, a fraction of the helium (i.e., the supersolid fraction) is stationary and does not contribute to rotational inertia. The collapsed *NCRIF* curves at these low speeds are therefore plots of the supersolid fraction, ρ_s/ρ, as a function of temperature. When the cell is oscillating with v_{max} exceeding v_c, supersolid decoupling occurs only during the portion of the oscillation cycle when the instantaneous speed is less than v_c, and thus gives rise to a smaller *NCRIF* and smaller period shift.

Liquid helium undergoing superflow around an annulus of radius R satisfies the Onsager-Feynman quantized circulation relation (*22*), $2\pi R \cdot v_s = (h/m) \cdot n$, where v_s is the superflow velocity, h is Planck's constant, m is the mass of helium atom, and the integer n is the circulation quantum number. For R = 5 mm, as in our annulus, v_s = 3.6 μm/s for n = 1. The fact that this velocity is on the same order of magnitude as the critical velocity v_c defined above indicates that the decrease in *NCRIF* with increasing v_{max} is associated with the appearance of vortices of a single or few unit(s) of quantum circulation in the superflow.

The temperature dependence of ρ_s/ρ at different pressures—that is, the (collapsed) *NCRIF* curves measured with the lowest speeds (Fig. 3, A to C)—shows a "universal" behavior of a smooth but increasingly rapid rise with decreasing temperature and then a saturation in the low-temperature limit. Thirteen other samples (in addition to the samples featured in Figs. 2 and 3) with pressure falling between 26 and 66 bars, all showing the same "universal" supersolid behavior, were studied with either one or two low oscillation speeds, typically with v_{max} close to or smaller than 5 μm/s. The low-temperature supersolid fraction, ρ_{so}/ρ, for all 17 solid samples (fig. S1) ranges from 0.0075 to 0.0175 and clusters between 0.01 and 0.015. The scatter in the result makes it difficult to conclude whether there is a real trend of increasing ρ_{so}/ρ with pressure. We speculate that the variation in ρ_{so}/ρ is related to the less than ideal crystallinity of the solid helium samples. Given the temperature gradient and different wall materials that exist in the torsional cell and the capillary leading to the cell, solid helium grown by the blocked capillary method is likely to be polycrystalline with grain boundaries that may affect the coherence of the superflow and possibly the magnitude of the supersolid fraction. The largest ρ_{so}/ρ value, 0.017, is comparable to that found for the experiment with helium confined in Vycor (0.025) (*15*). The Vycor value includes a multiplicative factor of 5 to correct for the tortuous pore structure of the Vycor glass. The theoretical estimate of the zero-temperature supersolid fraction varies from 1 part per million to 40% (*11*, *23*–*26*).

In addition to the comparable amplitude, the temperature dependence of the ρ_s/ρ of ^{4}He in Vycor resembles that found in bulk solid samples (*15*). These similarities suggest that the observed superflow in these two systems is an intrinsic low-temperature property of solid helium. One may argue that the decrease in the resonant period is not due to superflow but due to solid helium (with a soft shear mode) not following the acceleration of the torsional cell. This means the viscous penetration depth (δ) of solid helium must be less than 3.5 nm, the typical radius of the pores in Vycor glass. Its viscosity, $\eta = \delta^2\rho\omega$ (where ρ = 0.2 g/cc and $\omega = 2\pi \cdot 1024$ Hz are the density of solid helium and the angular frequency of the torsional motion, respectively), must be less than 1.5×10^{-11} Pa·s.

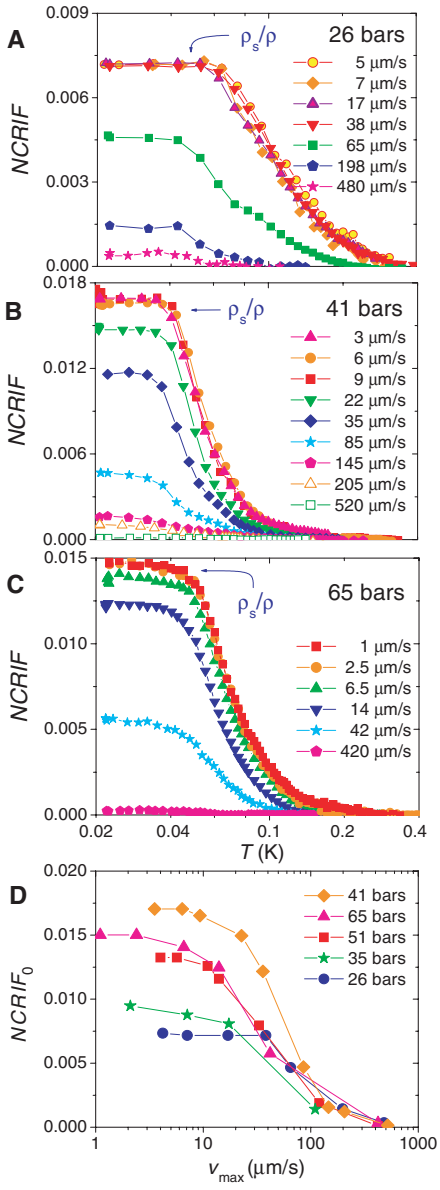

Fig. 3. (A to C) *NCRIF* as a function of temperature for three solid samples at different maximum oscillation speeds v_{max}. The observed period increases due to filling of the cell with ^{4}He at 300 mK are, respectively, 2785 ns, 2886 ns, and 3143 ns for solid samples at 26, 41, and 65 bars. *NCRIF* curves measured with oscillation speed less than the critical velocity of superflow collapse into a single curve. These curves represent the supersolid fraction, ρ_s/ρ, as a function of temperature. (**D**) *NCRIF* in the low-temperature limit as a function of v_{max}.

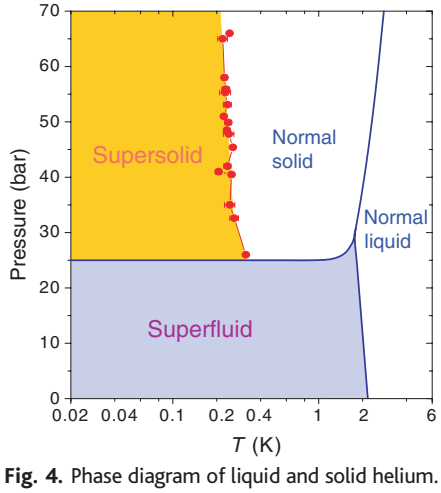

Fig. 4. Phase diagram of liquid and solid helium.

This number is one-seventh of the value reported in (*1*) as the upper limit of viscosity of superfluid helium. For comparison, the viscosity of normal fluid ^{4}He is 2×10^{-6} Pa·s. This calculation invalidates this soft shear mode interpretation and supports the superflow interpretation.

The smooth decay in ρ_s/ρ with increasing temperature near 250 mK makes it difficult to determine with precision the supersolid transition temperature T_c. We estimate the value of T_c by assuming a linear dependence of ρ_s/ρ on temperature near T_c and then use the data with ρ_s/ρ between 0.01 and 0.1 to fit for T_c. The resultant transition temperatures, with uncertainty of 20 mK, are likely to be lower than the "true" values. The transition temperatures we have found show a weak pressure dependence decreasing from 315 mK at 26 bars down to 230 mK at pressures exceeding 40 bars. The phase diagram of ^{4}He, including both the superfluid and supersolid phases, is shown in Fig. 4.

A number of experiments have searched for the supersolid phase in bulk solid helium without success (*27*). A recent experiment found an unexpected interaction between acoustic and heat pulses in solid ^{4}He with several tens of parts per million of ^{3}He (*28*). The result led to the interpretation of a Bose condensate of thermally activated vacancies at temperatures above 200 mK and therefore is not related to the findings reported here. A prior torsional oscillator experiment (*29*) reported the absence of any supersolid decoupling in a solid ^{4}He sample that contains 411 parts per million of ^{3}He—a concentration, as we found in the Vycor experiment (*15*), sufficient to quench the supersolid phase. The authors of this prior experiment also reported that they failed to find evidence of the supersolid phase in samples of high-purity ^{4}He (*29*). Our results disagree with this conclusion. Other experiments involve the search of motion of a falling dense object in solid helium or flow of solid helium from one chamber of higher pressure to one of lower pressure (*30–34*). A likely explanation of why these experiments found null results is that such pressure-driven mass flow requires a difference in the supersolid fraction between regions or chambers of different pressures. Our measurements showed that the supersolid fraction is insensitive to the pressure of the solid ^{4}He samples.

We noted above that Bose-Einstein condensation is found together with superfluidity in bulk liquid helium and in alkali gases. In contrast, superfluidity at $T > 0$ is found in two-dimensional liquid helium films without Bose-Einstein condensation (*18*). An intriguing question is whether the supersolid phase is associated with Bose-Einstein condensation.

References and Notes

1. P. Kapitza, *Nature* **141**, 74 (1938).
2. J. F. Allen, A. D. Misener, *Nature* **141**, 75 (1938).
3. P. Nozières, D. Pines, *Theory of Quantum Liquids* (Addison-Wesley Reading, MA, 1989), vol. 2, chap. 6.
4. P. E. Sokol, in *Bose-Einstein Condensation*, A. Griffin, D. W. Snoke, S. Stringari, Eds. (Cambridge Univ. Press, Cambridge, 1995).
5. M. Anderson, J. R. Ensher, M. R. Matthews, C. E. Wieman, E. A. Cornell, *Science* **269**, 198 (1995).
6. M. R. Matthews *et al.*, *Phys. Rev. Lett.* **83**, 2498 (1999).
7. A. P. Chikkatur *et al.*, *Phys. Rev. Lett.* **85**, 483 (2000).
8. F. Chevy, K. W. Madison, J. Dalibard, *Phys. Rev. Lett.* **85**, 2223 (2000).
9. A. F. Andreev, I. M. Lifshitz, *Sov. Phys. JETP* **29**, 1107 (1969).
10. G. V. Chester, *Phys. Rev. A.* **2**, 256 (1970).
11. A. J. Leggett, *Phys. Rev. Lett.* **25**, 1543 (1970).
12. K. S. Liu, M. E. Fisher, *J. Low Temp. Phys.* **10**, 655 (1973).
13. M. Liu, *Phys. Rev. B* **18**, 1165 (1978).
14. D. E. Galli, L. Reatto, *J. Low Temp. Phys.* **124**, 197 (2001).
15. E. Kim, M. H. W. Chan, *Nature* **427**, 225 (2004).
16. J. R. Beamish, *Nature* **427**, 204 (2004).
17. D. J. Bishop, J. D. Reppy, *Phys. Rev. Lett.* **40**, 1727 (1978).
18. J. M. Kosterlitz, D. J. Thouless, *J. Phys. C* **6**, 1181 (1973).
19. V. Ambegaokar, B. I. Halperin, D. R. Nelson, E. D. Siggia, *Phys. Rev. Lett.* **40**, 783 (1978).
20. A. L. Fetter, *J. Low Temp. Phys.* **16**, 533 (1974).
21. E. J. Mueller, personal communication.
22. R. P. Feynman, in *Progress in Low Temperature Physics I* (North-Holland, Amsterdam, 1955), chap. 2.
23. J. F. Fernandez, M. Puma, *J. Low Temp. Phys.* **17**, 131 (1974).
24. R. A. Guyer, *Phys. Rev. Lett.* **26**, 174 (1970).
25. W. M. Saslow, *Phys. Rev. Lett.* **36**, 1151 (1976).
26. D. Ceperley, G. V. Chester, M. H. Kalos, *Phys. Rev. B* **17**, 1070 (1978).
27. M. W. Meisel, *Physica B* **178**, 121 (1992).
28. J. M. Goodkind, *Phys. Rev. Lett.* **89**, 095301 (2002).
29. D. J. Bishop, M. A. Paalanen, J. D. Reppy, *Phys. Rev. B* **24**, 2844 (1981).
30. A. Andreev, K. Keshishev, L. Mezhov-Deglin, A. Shal'nikov, *Pis'ma Zh. Eksp. Teor. Fiz.* **9**, 507 (1969) [*Sov. Phys. JETP Lett.* **9**, 306 (1969)].
31. V. L. Tsymbalenko, *Pis'ma Zh. Eksp. Teor. Fiz* **23**, 709, (1976) [*Sov. Phys. JETP Lett.* **23**, 653 (1976)].
32. D. S. Greywall, *Phys. Rev. B* **16**, 1291 (1977).
33. G. Bonfait, H. Godfrin, B. Castaing, *J. Phys. (Paris)* **50**, 1997 (1989).
34. N. E. Dyumin, S. V. Svatko, V. N. Grigor'ev, *Fiz. Nizk. Temp.* **15**, 524 (1989).

35. We thank J. R. Banavar, J. R. Beamish, D. J. Bishop, M. E. Fisher, J. M. Goodkind, J. K. Jain, A. J. Leggett, E. Mueller, M. A. Paalanen, J. D. Reppy, W. M. Saslow, K. Shirahama, and D. S. Weiss for informative discussions. Supported by the NSF Condensed Matter Physics Program.

Supporting Online Material

www.sciencemag.org/cgi/content/full/1101501/DC1
Fig. S1

15 June 2004; accepted 12 August 2004
Published online 2 September 2004;
10.1126/science.1101501
Include this information when citing this paper.

Visualization of Dislocation Dynamics in Colloidal Crystals

Peter Schall,[1]* Itai Cohen,[1,2] David A. Weitz,[1,2] Frans Spaepen[1]

The dominant mechanism for creating large irreversible strain in atomic crystals is the motion of dislocations, a class of line defects in the crystalline lattice. Here we show that the motion of dislocations can also be observed in strained colloidal crystals, allowing detailed investigation of their topology and propagation. We describe a laser diffraction microscopy setup used to study the growth and structure of misfit dislocations in colloidal crystalline films. Complementary microscopic information at the single-particle level is obtained with a laser scanning confocal microscope. The combination of these two techniques enables us to study dislocations over a range of length scales, allowing us to determine important parameters of misfit dislocations such as critical film thickness, dislocation density, Burgers vector, and lattice resistance to dislocation motion. We identify the observed dislocations as Shockley partials that bound stacking faults of vanishing energy. Remarkably, we find that even on the scale of a few lattice vectors, the dislocation behavior is well described by the continuum approach commonly used to describe dislocations in atomic crystals.

Dislocations in a crystalline lattice are central to our understanding of yield, work hardening, fracture, fatigue, and time-dependent elasticity in atomic crystals (*1*). Such dislocations are line defects that mark the boundary of a surface at which one part of the crystal has been uniformly translated with respect to the other (*2–4*). A complete understanding of dislocations and their dynamics requires an analysis that bridges a range of length scales (*5*). On the atomic scale, the interatomic potential determines the structure of the dislocation core. On the medium-range scale, the strain field of the dislocations determines their interactions. On the macroscopic scale, the behavior of the dislocations determines the deformation of the crystal. It is difficult to observe dis-

[1]Division of Engineering and Applied Sciences, [2]Department of Physics, Harvard University, 9 Oxford Street, Cambridge, MA 02138, USA.

*To whom correspondence should be addressed. E-mail: pschall@deas.harvard.edu

locations simultaneously on these length scales. Transmission electron microscopy (TEM) is best suited for in situ observations on the medium-range scale. Computer simulations can bridge the length scales, but the size of their systems and length of the evolution time remain limited. Thus, there remains a need for techniques that link investigations of dislocations on these different length scales.

We show that colloidal crystals offer a unique opportunity for just such a bridging of length scales. Because colloidal particles are several orders of magnitude larger than atoms, they can be studied in real time and their positions in three dimensions can be determined accurately by confocal microscopy (*6*). Concentrated hard-sphere colloidal suspensions form crystals to increase their entropy, thereby lowering their free energy. Such crystals have a finite stiffness (*7*), which is essential for the existence of dislocations. To study these dislocations on the medium scale, we developed a laser diffraction microscopy (LDM) technique that images the strain field in a manner analogous to TEM in atomic systems. Confocal microscopy and LDM make a powerful combination for studying dislocation dynamics simultaneously over two qualitatively different length scales.

We focus on misfit dislocations formed when a film is grown via particle sedimentation on a substrate with a different lattice parameter. This configuration allows us to introduce the dislocations in a controlled way and to study nucleation and propagation of dislocations (*8*) during a process analogous to the industrially important epitaxial growth of thin atomic crystalline films. In thin epitaxial films, the misfit strain ε_0 is accommodated purely elastically and results in a uniform strain ε_{el}. The total elastic energy increases linearly with the film thickness. At some critical thickness h_c, the crystal can lower its energy by incorporating dislocations that relieve some of the elastic strain. As the film thickness increases, an increasing portion of the misfit strain is accommodated.

We determine the important parameters of the dislocation array: number per length, Burgers vector, position and range of the strain field, and mobility. We find that many of these features can be accounted for by the continuum theory used for epitaxial growth of atomic thin films. Some features, however, are unique to colloidal crystals, such as the negligibly small stacking fault energy and the slight variation of the lattice parameter with height (due to the pressure head of the upper layers).

We grow colloidal face-centered cubic (fcc) single crystals by slowly sedimenting colloidal particles onto a patterned template (*9*). We use silica particles with a diameter of 1.55 μm and a polydispersity of less than 3.5% (*10*). We prepare a pattern (*11*) with lattice constant d_0 = 1.63 μm that nearly matches the equilibrium interparticle separation for colloidal crystals that are about 30 μm thick. This preferred lattice spacing changes slightly with film thickness as a result of the difference in the pressure head (*12*).

We add 3.5 ml of the dilute suspension, which after sedimentation gives rise to about 11 crystalline layers corresponding to a film 13 μm thick. After several days, we remove two-thirds of the supernatant and replace it with another dose of the dilute silica suspension. Using this procedure, we grow the crystal by 9-μm increments until the film is 31 μm thick.

We image dislocations in the crystalline films with a simple LDM setup that is inspired by the TEM techniques used to investigate dislocations in atomic systems (*13*). We use a HeNe laser with a wavelength of 632 nm, which scatters coherently from the colloidal crystal. When the incident beam is perpendicular to the template, a symmetric fcc (100) diffraction pattern is observed. By slightly tilting the sample to change the direction of the incident beam, we maximize the intensity in the (220) diffracted spot. We then use two lenses to project the light in the diffracted beam onto a screen (Fig. 1A). The image on the screen corresponds to a region in the crystal that is illuminated by the incident beam. A perfect crystal shows a uniformly bright image. When the crystal contains dislocations, however, dark lines appear in the image: The bending of lattice

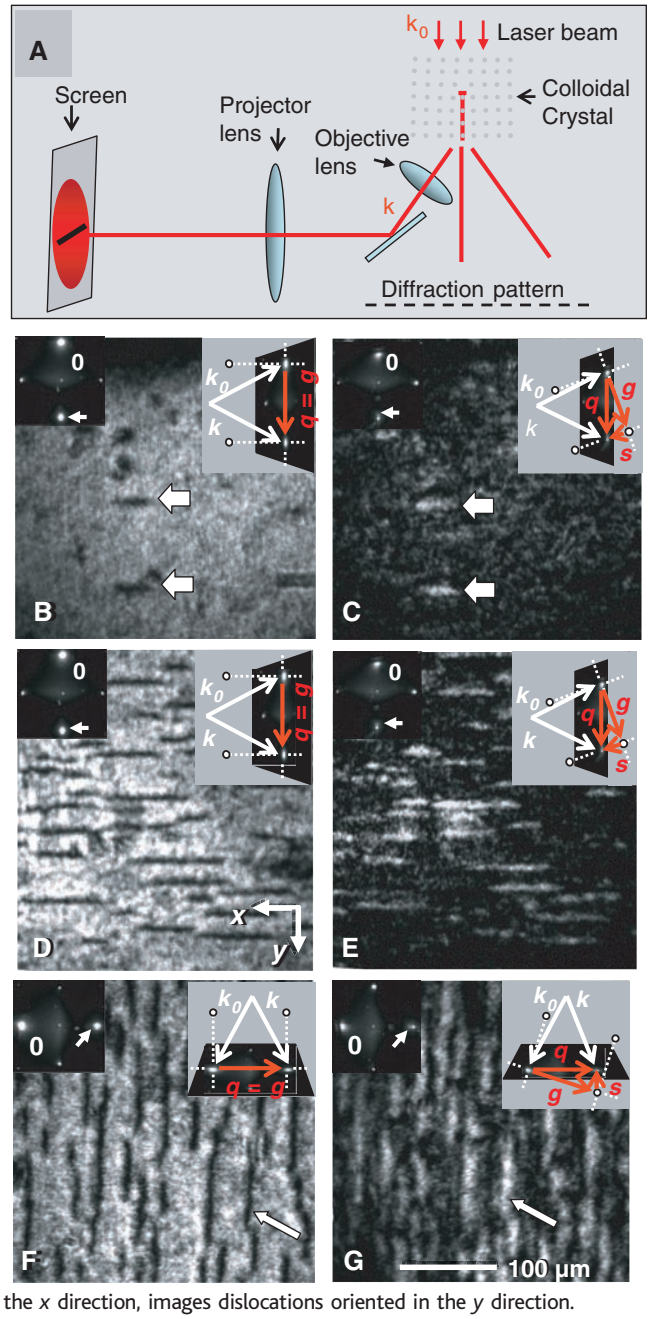

Fig. 1. Laser diffraction microscopy (LDM) technique and images. (**A**) Schematic of the LDM instrument: A laser beam is sent through a colloidal crystal. One of the diffracted beams is imaged on a screen by means of an objective and a projector lens. (**B** and **C**) LDM images of the colloidal crystal grown on the template with the ideal lattice constant d_0 = 1.63 μm. Arrows indicate dislocations. The upper left inset shows the diffraction pattern from the crystalline film; 0 indicates the transmitted beam, and an arrow indicates the diffracted beam used for imaging. The upper right inset illustrates the wave vectors of the incident and diffracted beams $\mathbf{k}_0$ and $\mathbf{k}$, the diffraction vector $\mathbf{q} = \mathbf{k} - \mathbf{k}_0$, and the corresponding reciprocal lattice vector $\mathbf{g}$. In (B) the diffraction vector $\mathbf{q}$ coincides with the reciprocal lattice vector $\mathbf{g}$ and the diffracted beam intensity is maximum. In (C), the sample is tilted, so that $\mathbf{q}$ differs from $\mathbf{g}$ by the excitation error $\mathbf{s} = \mathbf{q} - \mathbf{g}$, which gives rise to an inversion of the image contrast. (**D** to **G**) LDM images of a colloidal crystalline film grown on a stretched template with lattice constant d_1 = 1.65 μm. (D) and (E) show that using the (220) diffraction vector, which lies along the *y* direction, gives images of dislocations oriented in the *x* direction. (F) and (G) show that choosing the $(\bar{2}20)$ diffraction vector, which lies along the *x* direction, images dislocations oriented in the *y* direction.

planes in the strain field of the dislocation gives rise to a local change in the Bragg condition and results in a dark line in the image of the diffracted beam. A LDM image of a 0.3 mm by 0.3 mm section of the colloidal crystal grown on the template with the ideal lattice constant d_0 = 1.63 μm is shown in Fig. 1B. Even these crystals, grown on templates with an ideal lattice constant, contain some dislocations (indicated by arrows). Such dislocations are most frequently observed near the template border.

We can further exploit the analogy with the TEM technique and use contrast inversion to verify that the dark lines in Fig. 1B indeed result from scattering due to the dislocations. When the sample is tilted slightly further, the Bragg condition is no longer fulfilled in the perfect lattice and is instead locally satisfied in the region corresponding to the dislocation strain field. Thus, the image contrast on the screen inverts (Fig. 1C). The additional tilt of the sample introduces an excitation error, $\mathbf{s} = \mathbf{q} - \mathbf{g}$ (Fig. 1C, upper right inset), which causes the intensity in the diffracted beam to decrease (Fig. 1C, upper left inset). Close to the dislocation, however, the bending of lattice planes locally scatters light into the direction of the diffracted beam, making the dark lines appear light.

To investigate the effect of a lattice mismatch, we grew a crystal on a template with lattice constant d_1 = 1.65 μm, which is 1.5% larger than d_0. The crystal grown on the stretched template exhibited a similarly low density of dislocations at a crystal thickness of 22 μm. Strikingly, as the crystal was grown to a thickness of 31 μm, a large number of dislocations nucleated and grew (Fig. 1, D and E). We determined the average dislocation line separation in the direction perpendicular to the dislocation lines, Λ, from the images. Λ^{-1} is the number of dislocations per unit length. Measuring Λ in three different 0.3 mm by 0.3 mm regions, we obtained an average value of 53 (±10) μm for the 31-μm crystal.

Remarkably, although the template was stretched in both spatial directions, dislocation lines were seen in one direction only (Fig. 1, D and E). The dislocation contrast is visible only if the particle displacements in the dislocation strain field have a component parallel to the diffraction vector used for imaging. The (220) diffraction vector chosen for imaging in Fig. 1, B to E, lies along the *y* direction; therefore, only lattice distortions with a component along the *y* direction showed up in the image. When we instead chose the $(\bar{2}20)$ diffraction vector, which lies along the *x* direction, we observed a second set of dislocations (Fig. 1, F and G). Comparing the images in Fig. 1, D and F, we conclude that the strain field of the dislocations is strictly perpendicular to the imaged dislocation lines.

To elucidate the defect structure on the microscopic scale, we used confocal microscopy to image the individual particles and to determine their positions (*6*). The 31-μm-thick fcc colloidal crystal grown on the stretched template contains characteristic defects. At these defects, the nearest neighbor particle configuration changes so that particles have three opposing nearest neighbor pairs, as is the case in the hexagonal close-packed (hcp) lattice, rather than six as in the fcc lattice. A reconstruction of a 55 μm by 55 μm by 17 μm section of the crystal is shown in Fig. 2A. The *x*, *y*, and *z* axes correspond to the $(1\bar{1}0)$, (110), and (001) directions of the fcc lattice, respectively. Particles with three opposing nearest neighbor pairs are shown in red, and those with six opposing nearest neighbor pairs in blue. The red particles lie along intersecting planes embedded in the fcc lattice. By displaying only the red particles, we show that the planes are hcp (Fig. 2B). The red planes sandwich a stacking fault where the stacking order of the hcp planes changes from *ABC-ABCABC* to *ABCBCABCA*. The stacking fault lies along the (111) plane where the dislocations move most easily as a result of the shallow potential wells. This defines the glide plane of the dislocations in the fcc structure.

For a closer look at the strain field associated with the stacking faults, we display a typical *y*-*z* cut through a stacking fault. The fault ends above the template and is terminated by a dislocation (Fig. 2C). The first row of particles sits in the template holes. In the second row of particles, we recognize the emergence of a strain field in the *y*-*z* plane associated with a dislocation line oriented perpendicular to this plane. The dislocation core (⊥) lies about two lattice constants above the template. The Burgers circuit illustrated by the red line, which would close in the perfect lattice, exhibits a closure failure around the dislocation core. The Burgers vector **b**, which connects the starting and ending points of the Burgers circuit, is $1/6(\bar{1}\bar{1}2)$. This type of dislocation is known as a Shockley partial dislocation and is the most prominent dislocation observed in fcc

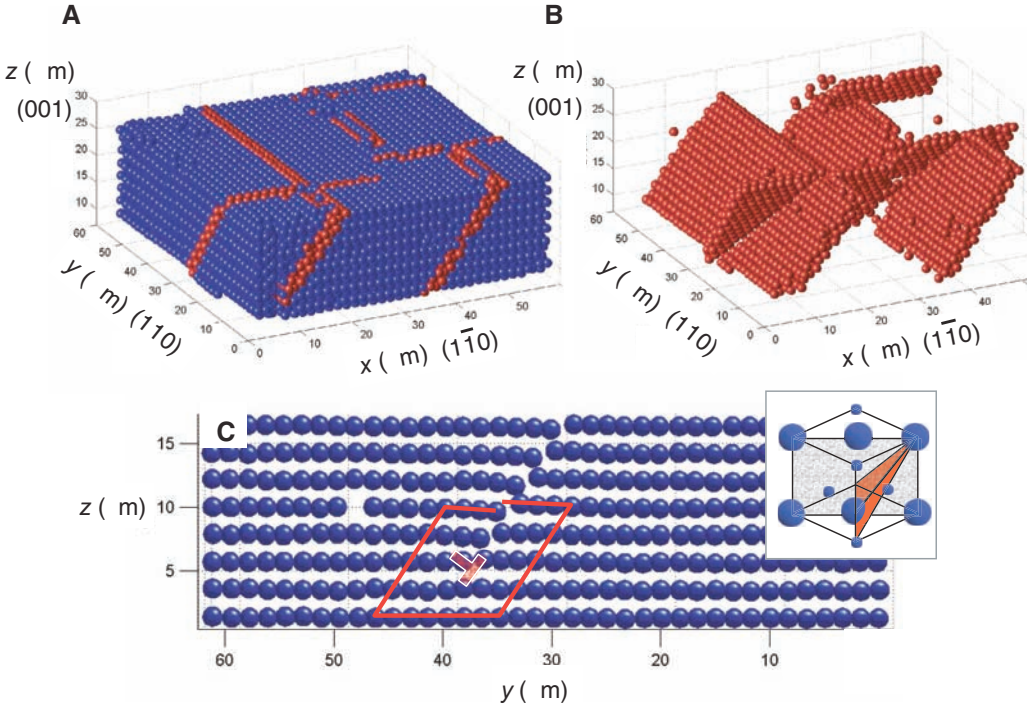

Fig. 2. (**A**) Reconstruction of a 55 μm by 55 μm by 17 μm section of the colloidal crystal grown on the stretched template. The red particles delineate stacking faults embedded in an otherwise perfect fcc lattice. (**B**) Crystal reconstruction showing only the particles adjacent to the stacking faults. (**C**) A reconstructed *y*-*z* section through a stacking fault. The stacking fault is terminated by a Shockley partial dislocation whose core position is indicated by ⊥. The red loop indicates a Burgers circuit. The upper right inset is a three-dimensional illustration of the fcc unit cell. The *y*-*z* plane is gray; the hcp plane parallel to the stacking fault is red.

metals (*14*). In metals, Shockley partial dislocations usually appear in pairs, held together by a stacking fault of nonzero energy. In contrast, in the hard-sphere colloidal crystal, the stacking faults extend to the crystal surface. This difference results from the vanishingly low energy cost associated with stacking faults in hard-sphere crystals (*15*), where second nearest neighbor interactions are almost negligible.

To calculate the critical film thickness h_c, where the crystal starts to nucleate dislocations in order to relieve some of the elastic strain, we consider the crystalline film to be an isotropic, linear elastic medium with Young modulus E, shear modulus μ, and Poisson ratio ν. The widely used one-dimensional dislocation models for misfit dislocations in atomic thin films (*16*, *17*) give $h_c = \mu b \ln(R/r_c)/[4\pi E\varepsilon_0(1-\nu)\cos\alpha]$, where r_c and R are the core and outer radii of the dislocation strain field, respectively (*18*), ε_0 is the misfit strain imposed by the template, and α is the angle between the Burgers vector and its projection onto the template. We take r_c to be $b/4$ (*1*, *19*), R to be the film thickness (*17*), and ε_0 to be 0.015. Because $E/\mu = 2(1+\nu)$ for an isotropic elastic medium (*1*) and the Poisson ratio can be set at $\nu = 1/3$ (*7*), we find $h_c = 22$ μm. Consistent with this prediction, at a thickness of 22 μm the colloidal crystalline film is still free of dislocations. However, as the film thickness is increased to 31 μm, the film develops a large number of dislocations (Fig. 1, D to G), again consistent with the model. The misfit strain associated with the dislocations is $\varepsilon = b\cos\alpha/\Lambda$. Using $b = 0.94$ μm, $\cos\alpha = 1/\sqrt{3}$, and $\Lambda = 53$ μm, we find $\varepsilon = 0.010$, which corresponds to two-thirds of the total misfit strain $\varepsilon_0 = 0.015$ (*20*).

A further test of the continuum model is to calculate the height at which the dislocations rest above the template. A dislocation is driven toward the template by the force $F_{el} = \frac{1}{2}\Lambda E\varepsilon_0^2$, which results from the elastic stress in the layers below the dislocation core, which are still strained (*21*). The boundary condition, set by the requirement that the particles in the first layer must adopt the template spacing, gives rise to an image force that repels the dislocation away from the template. The image force acting on a dislocation whose Burgers vector $\mathbf{b}'$ is parallel to the template and whose core rests at a distance z above the template is $F_i = \mu b'^2/[4\pi(1-\nu)z]$ (*1*). We estimate this force for our system by neglecting the vertical component of the Burgers vector and taking $b' = b\cos\alpha$. The image force balances the elastic force when the dislocation rests at a distance $z_0 = \mu(b\cos\alpha)^2/[2\pi\Lambda E(1-\nu)\varepsilon_0^2]$ from the template. Using $\Lambda = 53$ μm, $b = 0.94$, $\cos\alpha = 1/\sqrt{3}$, and $\varepsilon_0 = 0.015$, we find $z_0 = 2.1$ μm, in good agreement with our observation of $z_0 = 3$ μm. Thus, surprisingly, the predictions of continuum theory, which are typically applied on length scales above 100 lattice constants, hold even for a very small number of layers.

We also used LDM to study the dislocation dynamics during the epitaxial growth of the film. We started with a crystal 22 μm thick, added a final dose of particles, waited 14 hours, and then tracked the evolution of dislocations over a period of 2.5 hours (movie S1). Three snapshots from the movie are shown in Fig. 3, A to C. The images show the spreading of existing dislocations and the nucleation and growth of new ones. Figure 4A shows the dislocation length as a function of time for the four dislocations indicated in Fig. 3C. Initially, the dislocations grow rapidly, at a rate of about 1 μm s^{-1}. As the dislocation length increases, however, the growth rate decreases and eventually falls to zero.

To quantitatively analyze this spreading behavior, it is necessary to account for the forces acting on a dislocation. A diagram depicting a typical dislocation line in our thin film is shown in Fig. 4B. The dislocation consists of an edge segment that runs parallel to the template and joins two screw segments that terminate at the crystal surface. The edge dislocation expands through the lateral motion of the screw segments (*22*). Figure 4B also depicts the forces acting on one of the screw segments. The expansion of a dislocation is driven by the Peach-Koehler force F_{PK} due to the elastic stress (*22*) and is resisted by the dislocation line tension F_l (*1*) and a drag force F_d associated with moving the screw segment through the crystal. For colloidal crystals, F_d has been shown to be

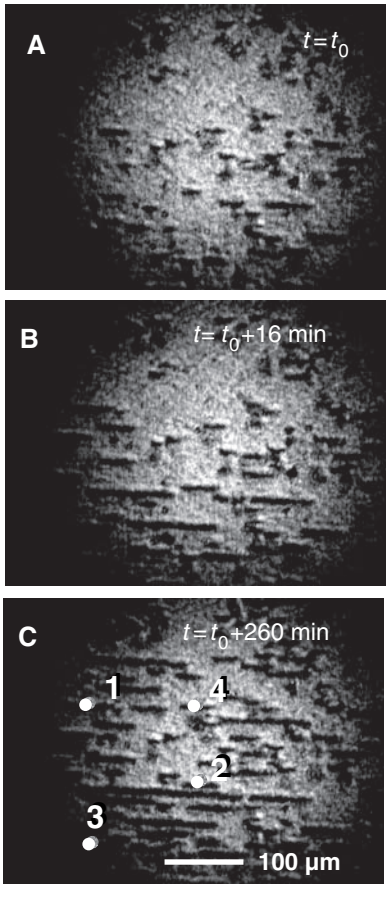

Fig. 3. (**A** to **C**) Snapshots from an LDM movie (movie S1) taken during the epitaxial growth of a colloidal crystal film grown on the stretched template. The time t_0 corresponds to 14 hours after adding a final dose of particles. The dots in (C) mark four dislocations whose growth is tracked and displayed in Fig. 4.

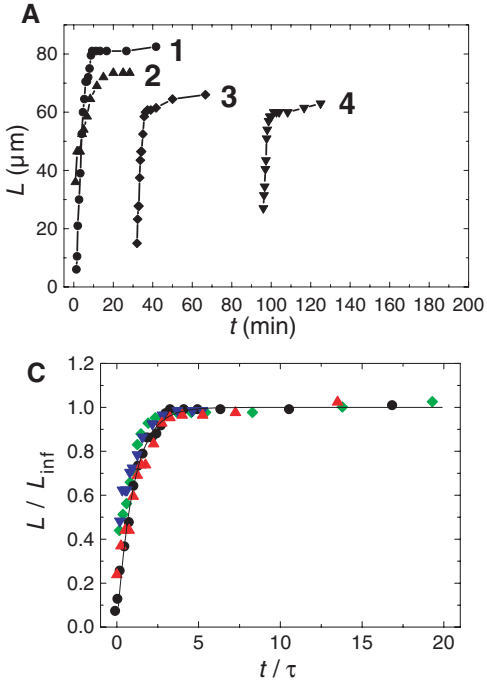

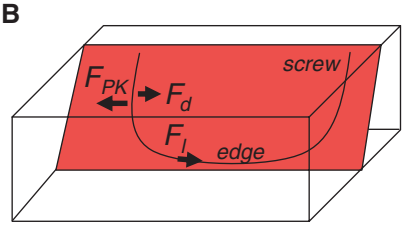

Fig. 4. (**A**) Length versus time for the four dislocations marked in Fig. 3C. (**B**) Schematic diagram of a dislocation line that lies in a hcp plane shown in red. The dislocation edge segment runs parallel to the template and joins two screw segments that terminate at the crystal surface. The forces acting on the dislocation line are marked. (**C**) The symbols indicate the rescaled dislocation length L/L_{inf} versus rescaled time t/τ for the four growth curves marked in (A). The solid line is the theoretical prediction of the model and has the functional form $[1 - \exp(t/\tau)]$.

the dominant force associated with the motion of such screw dislocations (*19*). At the onset of dislocation growth, we estimated the magnitude of each of the forces to be on the order of 100 fN. The length of a dislocation as a function of time can be calculated from the force balance, $F_{PK} = F_l + F_d$ (*23*). As the dislocation grows and accommodates an increasing portion of the misfit strain, the elastic force driving the expansion decreases. Thus, the force balance predicts that $L = L_{inf}[1 - \exp(-t/\tau)]$, where L_{inf} is the final dislocation length and τ is a constant, proportional to the ratio of the viscosity of the solvent to the elastic modulus.

To test this prediction, we scaled the entire data set and plotted L/L_{inf} versus t/τ (Fig. 4C). The data are in excellent agreement with the theoretical prediction. As a final check, we used the average value of τ, which we determined to be 130 (±40) s, to estimate the elastic modulus of the colloidal crystal (*23*). This estimate yields a value of 0.3 Pa, in reasonable agreement with theoretical estimates that predict a value on the order of 1 Pa (*7*). This is one of the only techniques available for directly determining the elastic modulus of thin colloidal crystal films.

The combination of imaging techniques presented and the close similarity of dislocations in colloidal and atomic crystals lays the groundwork for investigating further important phenomena that cannot be directly studied on the atomic scale, such as the nucleation and interaction of dislocations in very constrained systems. The remarkable and unexpected correspondence between continuum model predictions and the phenomena we observe on the scale of just a few lattice constants suggests that continuum models may also be applied to describe dislocation behavior even in highly constrained structures, such as those being made as nanoscale science pushes to ever smaller devices. Finally, the effects of the vanishing stacking fault energy and the pressure head on dislocations in colloidal crystals highlight some of the unique features of this class of condensed matter.

References and Notes

1. J. P. Hirth, J. Lothe, *Theory of Dislocations* (Wiley, New York, ed. 2, 1982).
2. G. I. Taylor, *Proc. R. Soc. A* **145**, 362 (1934).
3. E. Orowan, *Z. Phys.* **89**, 605 (1934).
4. M. Polanyi, *Z. Phys.* **89**, 660 (1934).
5. J. Lepinoux, D. Maziere, V. Pontikis, G. Saada, Eds., *NATO Science Series E, Multiscale Phenomena in Plasticity: From Experiments to Phenomenology, Modeling and Materials Engineering* (Kluwer Academic, Dordrecht, Netherlands, 2000), vol. 367.
6. A. D. Dinsmore, E. R. Weeks, V. Prasad, A. C. Levitt, D. A. Weitz, *Appl. Opt.* **40**, 4152 (2001).
7. D. Frenkel, A. J. C. Ladd, *Phys. Rev. Lett.* **59**, 1169 (1987).
8. R. Hull, J. C. Bean, D. J. Werder, R. E. Leibenguth, *Appl. Phys. Lett.* **52**, 1605 (1988).
9. A. van Blaaderen, R. Ruel, P. Wiltzius, *Nature* **385**, 321 (1997).
10. The silica particles (Micromod, Sicastar, 1.5 μm) are suspended in an index-matching mixture of water and dimethyl sulfoxide at an initial volume fraction of 0.03%. We add a small amount of a fluorescein-NaOH mixture to the solvent, allowing us to image the particles with fluorescence under the confocal microscope; the particles appear as dark spheres in a light background.
11. We use standard photolithographic processes to prepare a template with a square array of 3000 by 3000 holes in a polymethyl methacrylate layer 500 nm thick over an area of about 5 mm by 5 mm.
12. For example, we estimate that increasing the film thickness from 20 μm to 30 μm produces a 0.4% decrease in the preferred lattice spacing.
13. D. B. Williams, C. B. Carter, *Transmission Electron Microscopy: A Textbook for Materials Science* (Plenum, New York, 1996).
14. D. Hull, D. J. Bacon, *Introduction to Dislocations* (Pergamon, New York, 1984).
15. S. Pronk, D. Frenkel, *J. Chem. Phys.* **110**, 4589 (1999).
16. F. C. Frank, J. H. van der Merwe, *Proc. R. Soc. London Ser. A* **198**, 216 (1949).
17. J. W. Matthews, A. E. Blakeslee, *J. Cryst. Growth* **27**, 118 (1974).
18. In accordance with the one-dimensional dislocation model, we assume that the x and y directions are uncoupled and study the accommodation of the misfit strain in one spatial direction. The elastic energy stored in a strained film of thickness h is $U_{el} = \frac{1}{2}\varepsilon_{el}^2 Eh$ per unit area, where the elastic strain is $\varepsilon_{el} = \varepsilon_0 - \varepsilon$, and ε is the strain relieved by the dislocations. The energy cost per unit area associated with the misfit dislocations is $U_l = (\Lambda^{-1})\{\mu b^2 \ln(R/r_c)/[4\pi(1-\nu)]\}$, where b is the magnitude of the Burgers vector of the dislocations, and r_c and R are the core and outer radii of the dislocation strain field, respectively (*1*). Minimizing the total energy $U_{el} + U_l$ with respect to the number of dislocations per unit length Λ^{-1}, we find that, for film thicknesses greater than h_c, the equilibrium dislocation density is $\Lambda^{-1} = [\varepsilon_0/(b \cos\alpha)] - \{\mu \ln(R/r_c)/[4\pi(1-\nu)E \cos^2\alpha\, h]\}$. As the film thickness increases, the dislocation density approaches the limit $[\varepsilon_0/(b \cos\alpha)]$, where the entire misfit strain is accommodated by dislocations. The critical film thickness, where $\Lambda^{-1} = 0$, is $h_c = \mu b \ln(R/r_c)/[4\pi E\varepsilon_0(1-\nu)\cos\alpha]$; this yields a critical thickness $h_c = 22$ μm.
19. M. Jorand, F. Rothen, P. Pieranski, *J. Phys. (Paris)* **46**, 245 (1985).
20. We note that this value for the strain ε is larger than that predicted for this 31-μm-thick film grown on a template where $\varepsilon_0 = 0.015$. However, the model prediction depends sensitively on the value of the misfit strain ε_0. For example, a 0.005 increase in the misfit strain can account for the discrepancy. Such an increase can result from the change in pressure head when the film thickness changes from 20 μm to 30 μm.
21. The elastic energy stored in the thin crystal layer below the dislocations is $U_{el} = \frac{1}{2}\varepsilon_0^2 Ez$ per area and decreases with decreasing distance, z, of the dislocations to the template. Hence, a single dislocation experiences the elastic force $F_{el} = \frac{1}{2}\Lambda E\varepsilon_0^2$.
22. J. W. Matthews, S. Mader, T. B. Light, *J. Appl. Phys.* **41**, 3800 (1970).
23. The forces acting on the screw dislocation are given by $F_{PK} = 2\mu(1+\nu)hb \cos\alpha\, \varepsilon_{el}/(1-\nu)$, $F_l = \mu b^2 \ln(R/r_c)/[4\pi(1-\nu)]$, and $F_d = (h/\sin\alpha)\gamma v$, where $\gamma = \eta b^2/4\pi r_c^2$, v is the velocity of the screw dislocations, and η is the solvent viscosity. As the dislocation expands, it accommodates an increasing portion of the misfit strain. The rate at which the strain is accommodated is $d\varepsilon/dt = \rho_{screw}\, b \cos\alpha\, v$, where ρ_{screw} is the number of mobile screw dislocations per unit area of the film. From the force balance $F_{PK} = F_l + F_d$, we find that $\varepsilon(t) = \varepsilon_{inf}[1 - \exp(-t/\tau)]$, where the constant $\varepsilon_{inf} = \varepsilon_0 - \{b \ln(R/r_c)/[8\pi(1+\nu)h \cos\alpha]\}$ corresponds to the final misfit strain accommodated by the dislocation, and the time constant $\tau = (1-\nu)\gamma/(Eb^2 \cos^2\alpha \sin\alpha\, \rho_{screw})$. Because ε is proportional to the dislocation length L, this equation predicts the time dependence of L. To calculate the elastic modulus from the measured time constant τ, we determine the density of mobile screw dislocations by counting the number of dislocations that are expanding, multiplying by 2, and dividing by the area corresponding to the field of view. We obtain $\rho_{screw} = 3 \times 10^{-4}$ μm^{-2}. Taking $\eta = 3.0 \times 10^{-3}$ Pa·s (*24*), we obtain a value of 0.3 Pa for the elastic modulus.
24. Y. Higashigaki, D. H. Christensen, C. H. Wang, *J. Phys. Chem.* **85**, 2531 (1981).

25. We thank R. Christianson and D. Blair for their help with the image analysis, and E. Chen and Y. Lu for their help in manufacturing the templates. Supported by a Lynen Fellowship from the Alexander von Humboldt Foundation (P.S.), by NSF grant DMR-0243715, and by Harvard MRSEC grant DMR-0213805.

Supporting Online Material

www.sciencemag.org/cgi/content/full/305/5692/1944/DC1
Movie S1

30 June 2004; accepted 20 August 2004

Ice Flow Direction Change in Interior West Antarctica

Martin J. Siegert,[1]* Brian Welch,[2] David Morse,[3] Andreas Vieli,[1] Donald D. Blankenship,[3] Ian Joughin,[4] Edward C. King,[5] Gwendolyn J.-M. C. Leysinger Vieli,[1] Antony J. Payne,[1] Robert Jacobel[2]

Upstream of Byrd Station (West Antarctica), ice-penetrating radar data reveal a distinctive fold structure within the ice, in which isochronous layers are unusually deep. The fold has an axis more than 50 kilometers long, which is aligned up to 45° to the ice flow direction. Although explanations for the fold's formation under the present flow are problematic, it can be explained if flow was parallel to the fold axis ~1500 years ago. This flow change may be associated with ice stream alterations nearer the margin. If this is true, central West Antarctica may respond to future alterations more than previously thought.

Ice-penetrating radar provides information on ice thickness, subglacial morphology, and internal layering, caused by electromagnetic-wave reflections from dielectric contrasts (such as high-acidity horizons formed from the aerosol product of volcanic events contained within ancient snow). Internal layers are believed to be isochronous, as

they obey the rules of stratigraphy (*1*). They are often traceable continuously over several hundred kilometers. In slow-flowing regions of ice sheets, internal layers commonly drape over topography (i.e., their vertical position relates to bed relief). In ice streams and their tributaries, however, internal layers may deform in a manner unrelated to bed topography (*2*, *3*). In one location upstream of the tributaries of Ice Stream D in West Antarctica (Fig. 1), the internal layer pattern differs markedly from the bed topography. Along the present ice flow line, internal layers drop in elevation by up to 800 m (over horizontal distances of ~5 km) without substantial variation in bed morphology (Fig. 2A), and then return to their approximate original elevation downstream. This highly unusual internal layer fold is observed in several radar transects, and the axis of the fold is aligned roughly linearly (XY in Fig. 1). At Y, the alignment is at ~45° to the current flow direction, whereas ice flows roughly parallel to the axis at X (Fig. 1). Internal layers are easily traceable in the radar data, allowing the internal layer depths to be determined along XY. This longitudinal section shows the steady internal layer convergence to the bed from X to Y, in contrast to the short-wavelength, high-amplitude fold in the cross direction AA′ and BB′ (Fig. 2), which also demonstrates how the fold amplitude increases from X to Y (fig. S1).

Under the present glaciological setting, six processes that may distort internal layers within a grounded ice sheet can be ruled out as explanations for the fold. First, basal topography is relatively subdued upstream of the layer distortion and so, under the present glaciological regime, there is little ice flow around subglacial obstacles. Second, strain rate variations in the ice can cause internal layer distortions known as Raymond bumps (*4*). These occur at the ice sheet divide, require a frozen bed (*5*), and increase in size with depth quadratically. Raymond bumps differ from the measured layers, which are located ~180 km from the ice divide and increase in size linearly with ice depth (fig. S1). Moreover, as we discuss later, the radar data show evidence of warm subglacial conditions. Third, changes to the surface accumulation rate can cause internal layer distortions where there is an alteration to the ice sheet surface slope (*6*). There is, however, no noticeable surface-slope variation around the measured layers (*7*), and furthermore, the slope of the fold's axial plane (dipping upstream, Fig. 3A and fig. S1) is the opposite of what would be expected from a nonuniform but stationary pattern of surface accumulation. Fourth, interferometric synthetic aperture radar (InSAR) data (*8*, *9*) reveal little ice sheet convergence or divergence over the fold, thus ruling out converging or diverging ice flow as an explanation. Fifth, isochrones may dip toward the ice base across the transition between regions of no-sliding and sliding and toward the ice surface across a transition from sliding to no-sliding (*10*). Although the structure at BB′ could be accounted for under this mechanism, the fold's amplitude is so great at AA′ that it could not have formed without substantial acceleration (and then deceleration) to the ice flow. InSAR data show no such velocity anomaly around AA′, so it appears unlikely that ice flow over no-sliding/sliding/no-sliding zones could have formed the fold at this location. Sixth, the convergence of internal layers with the ice base can be assigned to enhanced geothermal heating and the resulting basal melting of ice (*11*). We calculate that the convergence of the

[1]Centre for Polar Observation and Modelling, Bristol Glaciology Centre, School of Geographical Sciences, University of Bristol, Bristol BS8 1SS, UK. [2]Physics Department, St. Olaf College, Northfield, MN 55057, USA. [3]Institute for Geophysics, John A. and Katherine G. Jackson School of Geosciences, The University of Texas, 4412 Spicewood Springs Road, Austin, TX 78759, USA. [4]Jet Propulsion Laboratory, Mail Stop 300-235, 4800 Oak Grove Drive, Pasadena, CA 91109, USA. [5]Physical Sciences Division, British Antarctic Survey, High Cross, Madingley Road, Cambridge CB3 0ET, UK.

*To whom correspondence should be addressed. E-mail: m.j.siegert@bristol.ac.uk

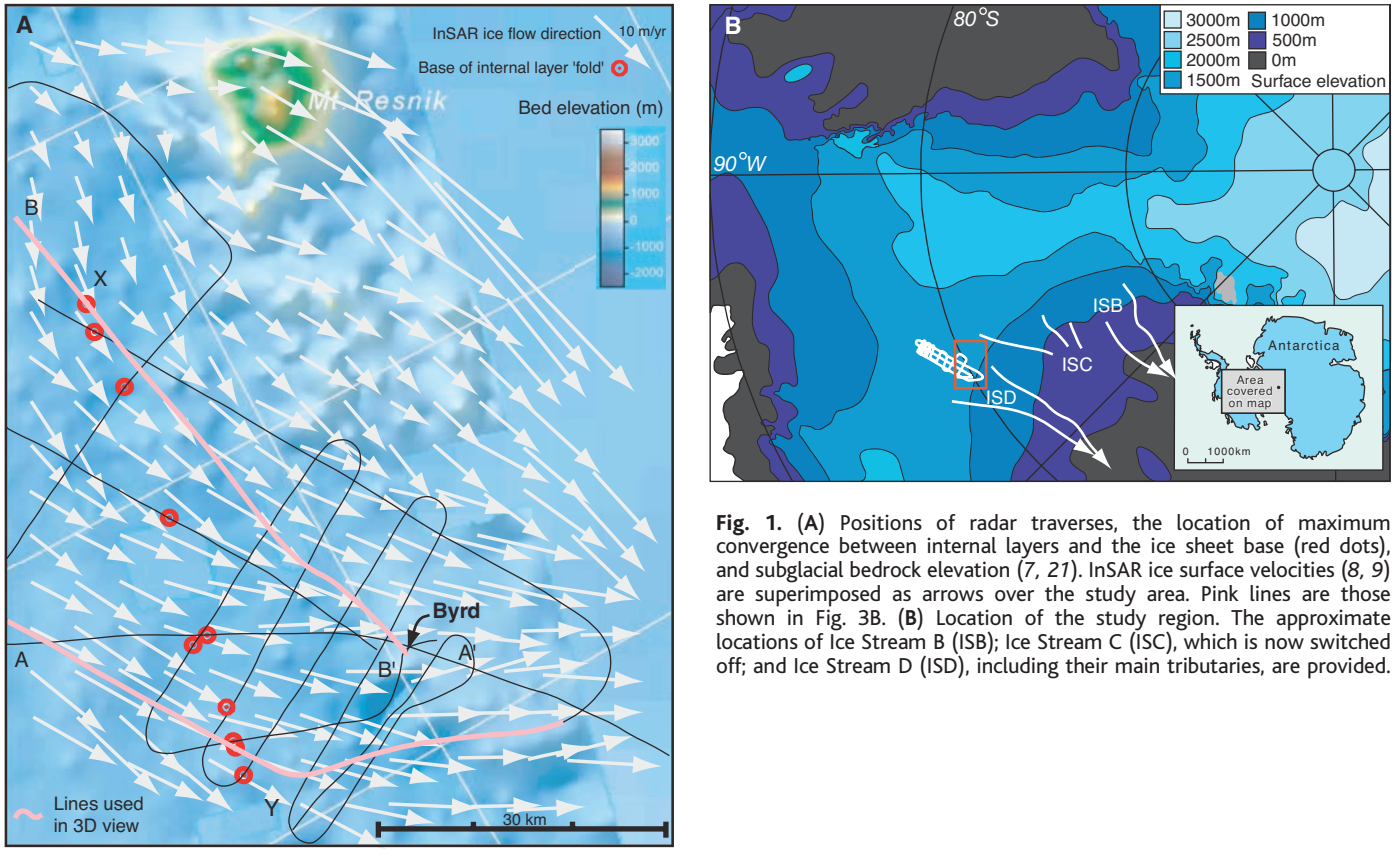

Fig. 1. (**A**) Positions of radar traverses, the location of maximum convergence between internal layers and the ice sheet base (red dots), and subglacial bedrock elevation (*7*, *21*). InSAR ice surface velocities (*8*, *9*) are superimposed as arrows over the study area. Pink lines are those shown in Fig. 3B. (**B**) Location of the study region. The approximate locations of Ice Stream B (ISB); Ice Stream C (ISC), which is now switched off; and Ice Stream D (ISD), including their main tributaries, are provided.

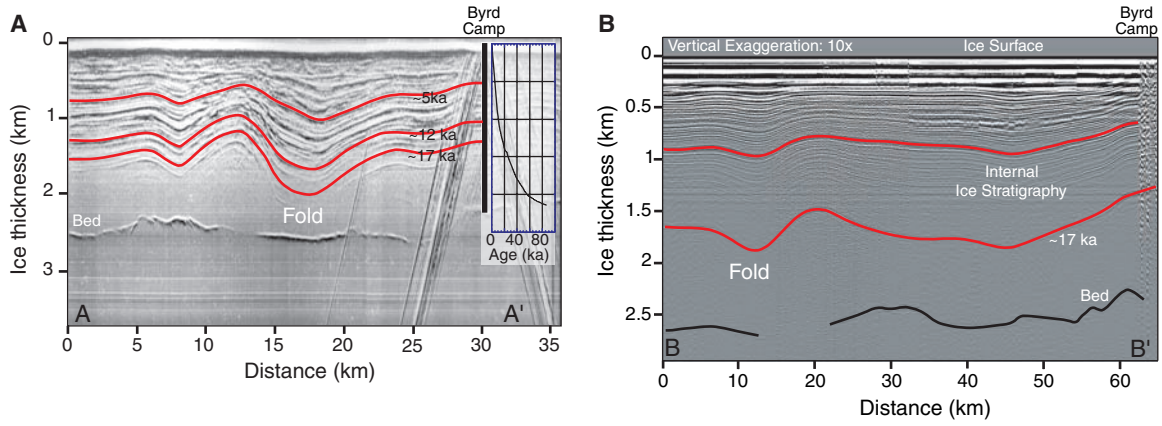

Fig. 2. (**A**) Radar data upstream of the Byrd ice core along AA′ (located in Fig. 1). These radar data were collected by members of the Scott Polar Research Institute (Cambridge, UK) in 1974 to 1975, using a frequency of 60 MHz and a pulse width of 250 ns. Radar reflections off the various buildings of Byrd Station are seen as surface hyperbolas. Layers have been dated at their intersection with the ice core site at Byrd Station (*22*). ka, thousand years ago. (**B**) Radar data along BB′ (located in Fig. 1). These data were collected by the US-ITASE program in 2001, using a frequency of 3 MHz (*23*). The deepest layer (highlighted in red) is an unusually bright internal layer between ice depths of 1250 and 1750 m, which has an age of 17,000 years (*22*). The intersection of the radar transect with XY is where the internal layer fold is at its deepest (i.e., the trough minima).

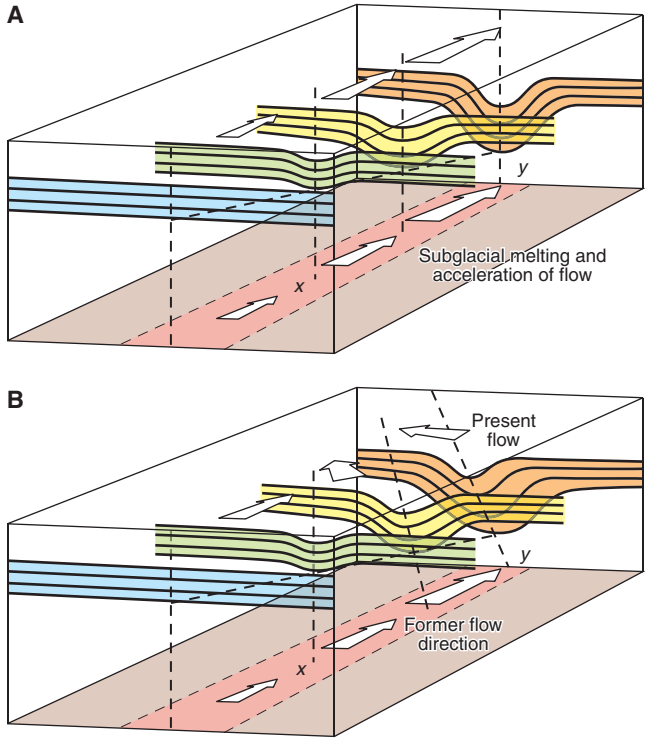

Fig. 3. Conceptual development of the englacial fold. (**A**) The fold forms as a consequence of ice flow across a no-sliding/sliding zone and subglacial melting. The fold axis forms parallel to ice flow and the amplitude of the fold increases from X to Y. (**B**) Ice flow change results in flow across the fold axis, which causes secondary deformation to the fold. At Y, the deformation is greatest (the axis here is aligned 45° to ice flow), which results in the tilting of the axial plane (dipping upstream). The fold axis remains roughly linear, which is consistent with the fact that fast ice flow (basal sliding) no longer occurs here.

internal layers with the ice base would require melt rates of up to 6 cm year^{-1}. Such melt rates are an order of magnitude greater than those calculated for the Siple Coast region through consideration of ice flow and heat transfer (*12*). Although we can use basal melting to explain how isochrones can be drawn down to greater depths, it cannot explain how the layers appear at much higher elevations immediately downstream.

The presence of subglacial water (the product of basal melting) is supported, however, by the relative strengths of bed echoes. Internal layer convergence with the bed is associated with bed returns as strong as one would expect from an ice-water interface (Fig. 2A). In point of fact, near the ice divide, radar data reveal a small subglacial lake (*13*), the surface of which has an echo strength similar to that beneath the internal layer fold. Subglacial melting cannot, therefore, be ruled out as a process contributing to the shape of the internal layers.

As there is no apparent explanation for the fold under the current glaciological setting, explanations involving an alternative (former) glaciological setting are examined. The rationale for this is as follows. First, the current ice sheet configuration in West Antarctica is thought to have been achieved ~6000 years ago, after a prolonged period during which the grounded margin was positioned near the present ice shelf terminus (*14*–*16*). Hence, the flow pattern around Byrd Station may have been different 6000 years ago. Second, investigations of Ice Stream C have shown that internal layer structures (similar to those in Fig. 2) within regions of enhanced ice flow can be traced along the line of ice flow (*3*). Because of ice sheet convergence, the layer structures compress laterally down the flowline. As the fold upstream of Byrd Station appears similar to the structures observed in Ice Stream C (i.e., a traceable englacial structure with extended fold axes and no apparent link to bed perturbation), we propose that the fold axis is a paleoflow line (Fig. 1) (translated only partially by subsequent sliding, as discussed later). This rationale reopens the possibility of two explanations discounted previously: (i) ice flow around subglacial topography, and (ii) processes acting on the ice as it flows from X to Y (Fig. 1).

The most obvious subglacial feature that may be responsible for the internal layer distortion is Mount Resnik, a huge subglacial mountain located 30 km from X (Fig. 1). However, the fold axis, XY, points to ice flow originating well upstream of Mount Resnik, making the mountain an unlikely source for the fold. Elsewhere, subglacial topography is subdued. The only remaining explanations involve englacial processes acting on the ice as it flows along the fold axis.

We propose that, when the flow was parallel to the axis, the fold may have been developed by a combination of basal melting and, because the fold increases in intensity from X to Y (fig. S1), sideways compression in a manner similar to that demonstrated for internal layers in Ice Stream C (*3*). We propose further that the formation of the fold was at, or upstream of, the fold in BB′ and due to flow across a no-sliding/sliding transition (*10*) (fig. S2). For this explanation to be correct, enhanced (ice stream tributary) flow must have occurred between X and Y. Such flow may require a wet ice base (to

allow basal sliding), which is consistent with the observation that there may be subglacial water directly beneath the fold axis.

Regardless of the actual mechanism responsible for the fold, it most probably formed before the establishment of the modern ice flow regime (*15*, *16*). At position X (Fig. 1), the inferred ice flow path (the fold axis) is close to the present-day ice flow vector and the fold is aligned vertically (Fig. 2B). Conversely, the fold axis across AA′ is aligned ~40° to the present flow vector, and the fold's axial plane is at a substantial angle to the vertical (increasing downstream to a maximum of 45°, dipping away from the direction of present ice flow) (Fig. 3 and fig. S1). We propose that when ice flowed parallel to the fold axis, the axial plane would have been vertical (as it is at X). Subsequently, under the present flow regime, the fold may be reworked by ice deformation acting to tilt the axial plane and basal sliding, which may "translate" the axis laterally. As the fold axis is straight, we contend that subglacial sliding is presently a minor component of ice flow. Ice deformation at 3 m $year^{-1}$, acting for 1000 years, would be sufficient to tilt the axial plane at X by ~45° (fig. S1). Timing of this order makes it possible that the change from paleo- to modern flow regimes is associated with measured alterations to ice streams C and D that occurred ~1500 years ago (*17*).

Currently, ice flows across much of the fold axis toward the southern tributary of Ice Stream D. Under the former ice flow regime, the direction of ice flow would have been toward the northern tributary of the same ice stream. Although evidence for ice flow change at the ice sheet margin has been observed on several occasions (*18*, *19*), this represents evidence of a major shift in the flow direction at the center of an ice sheet. The driver of this change could be associated with activation of the southern tributary of Ice Stream D a few thousand years ago. This activation may be related to the relaxation of the ice sheet from its pre-Holocene configuration that has been hypothesized from numerical modeling (*20*) or to changes to the internal ice sheet dynamics. In either case, the evidence for past flow change shows that interior regions of ice sheets may be affected by ice flow conditions downstream.

References and Notes

1. M. J. Siegert, R. C. A. Hindmarsh, G. S. Hamilton, *Quat. Res.* **59**, 114 (2003).
2. R. W. Jacobel, A. M. Gades, D. L. Gottschling, S. M. Hodge, D. L. Wright, *J. Glaciol.* **39**, 528 (1993).
3. F. Ng, H. Conway, *Geology* **32**, 481 (2004).
4. C. F. Raymond, *J. Glaciol.* **29**, 357 (1984).
5. E. C. Pettitt, P. H. Jacobson, E. D. Waddington, *Ann. Glaciol.* **37**, 370 (2003).
6. D. G. Vaughan, H. F. J. Corr, C. S. M. Doake, E. D. Waddington, *Nature* **298**, 323 (1999).
7. D. L. Morse, D. D. Blankenship, E. D. Waddington, T. A. Neumann, *Ann. Glaciol.* **35**, 36 (2002).
8. I. Joughin *et al.*, *Science* **286**, 283 (1999).
9. I. Joughin, S. Tulaczyk, R. Bindschadler, S. F. Price, *J. Geophys. Res.* **107**, 2289 (2002).
10. J. Weertman, *Quat. Res.* **6**, 203 (1976).
11. M. Fahnestock, W. Abdalati, I. Joughin, J. Brozena, P. Gogineni, *Science* **294**, 2338 (2001).
12. I. Joughin, S. Tulaczyk, D. R. MacAyeal, H. Engelhardt, *J. Glaciol.*, in press.
13. M. J. Siegert, J. A. Dowdeswell, M. R. Gorman, N. F. McIntyre, *Antarct. Sci.* **8**, 281 (1996).
14. H. Conway, B. L. Hall, G. H. Denton, A. M. Gades, E. D. Waddington, *Science* **286**, 280 (1999).
15. R. P. Ackert Jr. *et al.*, *Science* **286**, 276 (1999).
16. J. O. Stone *et al.*, *Science* **299**, 99 (2003).
17. R. W. Jacobel, T. A. Scambos, C. F. Raymond, A. M. Gades, *J. Geophys. Res.* **101**, 5499 (1996).
18. M. Fahnestock, T. Scambos, R. Bindschadler, G. Kvaran, *J. Glaciol.* **46**, 652 (2000).
19. R. W. Jacobel, T. A. Scambos, N. A. Nereson, C. F. Raymond, *J. Glaciol.* **46**, 102 (2000).
20. P. Huybrechts, *Quat. Sci. Rev.* **21**, 203 (2002).
21. M. B. Lythe, D. G. Vaughan, the BEDMAP Consortium, *J. Geophys. Res.* **106**, 11335 (2001).
22. T. Blunier, E. J. Brook, *Synchronization of the Byrd and Greenland (GISP2/GRIP) Records* [International Geosphere–Biosphere Programme Past Global Changes (IGBP PAGES)/World Data Center A for Paleoclimatology, Data Contribution Series #2001-003, 2001], available at www1.ncdc.noaa.gov/pub/data/paleo/icecore/antarctica/byrd/.
23. B. C. Welch, R. W. Jacobel, *Geophys. Res. Lett.* **30**, 1444 (2003).

24. We thank J. Dowdeswell, Director of the Scott Polar Research Institute, for access to radar records held there in archive. Supported by the Natural Environment Research Council (NERC) Centre for Polar Observation and Modelling, NERC grant no. NER/A/S/2001/01011, and a Philip Leverhulme Prize to M.J.S. U.S.–International Trans-Antarctic Scientific Expedition (US–ITASE) work was supported by National Science Foundation grant no. OPP-9814574.

Supporting Online Material

www.sciencemag.org/cgi/content/full/305/5692/1948/DC1
Materials and Methods
Figs. S1 and S2
Table S1
References and Notes

4 June 2004; accepted 23 August 2004

Fractionation of the Platinum-Group Elements During Mantle Melting

Conny Bockrath,* Chris Ballhaus, Astrid Holzheid

Experiments in sulfide-silicate systems demonstrate that two sulfide phases are stable in the asthenospheric upper mantle: a crystalline osmium-iridium-ruthenium–enriched monosulfide and a rhodium-platinum-palladium–enriched sulfide melt. During silicate melt segregation, monosulfide stays in the solid residue, dominating the noble metal spectrum of residual mantle. The sulfide melt is entrained as immiscible droplets in the segregating silicate melt, defining the noble metal inventory of the basaltic component.

When primitive mantle, chondritic with respect to the platinum-group elements (PGEs) (*1*), undergoes partial melting, the noble metals become fractionated. Os, Ir, and Ru are retained in the mantle residue, whereas Re, Pt, and Pd are sequestered to the basaltic melt (*2*). There is consensus that sulfide plays a major role in the fractionation process (*3*, *4*) because the PGEs of the mantle reside to a large extent in sulfide (*5*). But how fractionation is possible in the presence of sulfide, or whether sulfide must be eliminated to release any PGEs to the silicate melt (*6*), are unresolved issues. We present evidence that the cycling of PGEs into silicate melt is controlled by physical parameters. The key observation is that molten sulfide behaves physically incompatibly during silicate melt segregation.

Our experiments used as starting composition $(Fe,Ni,Cu)_{1-x}S$ monosulfide synthesized from metal powders and S in evacuated SiO_2 glass tubes at 900°C (*7*). The composition was (in atomic %) 35.6 Fe, 11.8 Ni, 0.7 Cu, and 51.9 S. Ni was calculated assuming that the sulfide is in equilibrium with upper-mantle olivine containing 90 mol % forsterite and 3000 parts per million (ppm) Ni (*8*, *9*). Cu was added assuming that 50% of the Cu in primitive mantle [~20 ppm (*1*)] resides in sulfide. Metal/S was set to 0.93, reflecting a sulfide in moderately oxidized mantle in equilibrium with the fayalite-magnetite-quartz oxygen buffer. The composition was melted between 1040° and 1400°C at 1 atm to 3.5 GPa (*10*).

Phase equilibria at run conditions may be deduced from quench textures (Fig. 1) and from phase compositions (SOM Text). Subsolidus runs resulted in aggregates of ~80-μm-sized polygonal, homogeneous monosulfides that tended to disintegrate after removal from the capsule (Fig. 1A). Experiments with partial sulfide melting, i.e., in the two-phase field, quenched out two phases,

Institut für Mineralogie, Universität Münster, Corrensstrasse 24, 48149 Münster, Germany.

*To whom correspondence should be addressed. E-mail: bockrat@nwz.uni-muenster.de

Table 1. Summary of PGE abundance calculations.

Element	Monosulfide (ppm)*	D_{PGE} Mss-sulfide melt†	Sulfide melt (ppm)‡	Residual sulfide (ppm)§	Basaltic melt (ppb)‖	Mantle residue (ppb)#
Ir	5.3	10.0	0.97	9.7	1.5	3.7
Ru	7.6	9.0	1.52	13.7	2.3	5.3
Rh	1.6	3.0	0.78	2.3	1.2	0.9
Pt	11.0	0.12	19.6	2.4	30.2	0.9
Pd	5.5	0.14	9.6	1.3	14.7	0.5

*PGE content of bulk sulfide in primitive mantle (~600 ppm), assuming that PGEs reside in sulfide. †Monosulfide-sulfide melt partition coefficients (*7*). ‡PGEs in sulfide melt after 50% sulfide melting. §PGEs in monosulfide. ‖PGEs in model basalt after 20% silicate melting and incorporation of all sulfide melt. #PGE spectrum of mantle residue after silicate melt segregation.

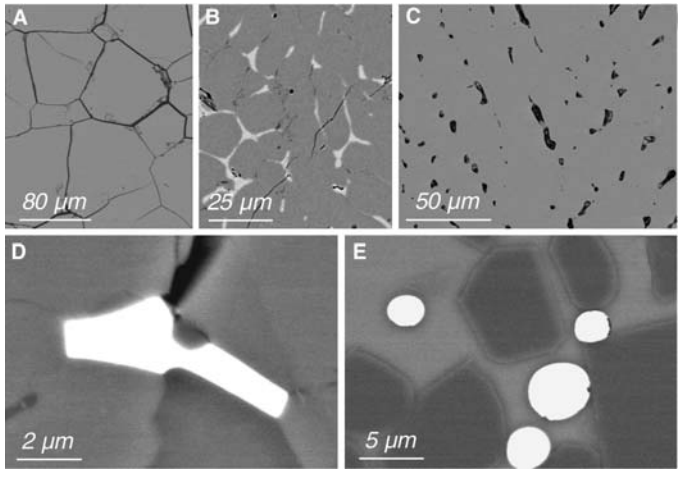

Fig. 1. Backscattered images of experiments with pure sulfide (**A** to **C**) and with sulfide in mantle matrix (**D** and **E**). (A) Subsolidus run with equant monosulfide grains (1100°C, 1.2 GPa). (B) Supersolidus run with roundish FeS-rich monosulfide and bright Cu-Ni–rich interstitial intermediate solid solution, from the two-phase monosulfide-melt field (1350°C, 2 GPa). (C) Skeletal monosulfides from a superliquidus run with quench vapor bubbles (1275°C, 1 GPa). (D) Crystalline monosulfide intergrown with olivine (gray) and glass (darker gray). (E) Sulfide melt droplets and olivine immersed in silicate melt.

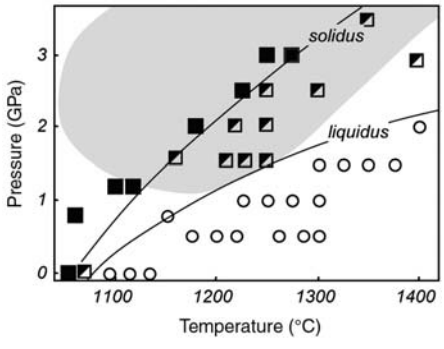

Fig. 2. Phase relations of the $(Fe,Ni,Cu)_{1-x}S$ monosulfide quoted in the text. Solidus ± 10°C, liquidus ± 20°C. Filled squares, subsolidus sulfides; half-filled squares, monosulfide-melt pairs; open circles, superliquidus skeletal monosulfides. Shaded area approximates the *P-T* region of the silicate solidi with and without volatiles *(33, 34)*.

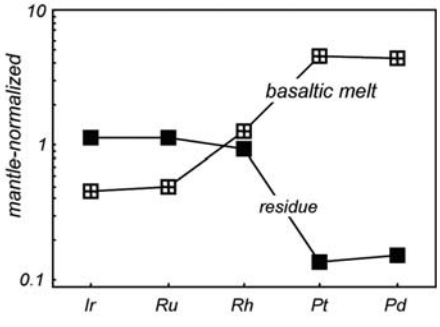

Fig. 3. Calculated PGE spectra of basaltic melt and mantle residue, after 20% batch melting and complete incorporation of sulfide melt in the silicate melt (Table 1).

FeS-rich monosulfide and Cu-Ni–enriched intermediate solid solution (Fig. 1B). Superliquidus runs crystallized single-phase, homogeneous dendritic monosulfides whose grain boundaries are decorated by gas bubbles, notably at pressures below 1.5 GPa (1C). The melting reaction of $(Fe,Ni,Cu)_{1-x}S$ monosulfide is divariant in *P-T* space (Fig. 2) and widens with increasing pressure. Both solidus (±10°C) and liquidus (±20°C) have positive slopes slightly shallower than the univariant melting curve of pure $Fe_{1-x}S$ (*11*).

To constrain the physical behavior of sulfide during partial silicate melting, we carried out further experiments with sulfide in a silicate matrix composed of 60 weight % (wt %) olivine (Fo_{90}), 20 wt % orthopyroxene (En_{90}), 15 wt % clinopyroxene (cr-diopside), and 5 wt % spinel (cr-al-spinel) (*12*), analogous to fertile upper mantle. Added to this was 0.2 to 2 wt % monosulfide $[(Fe,Ni,Cu)_{1-x}S]$. The charges were equilibrated in graphite capsules at temperatures above the dry silicate solidus from 0.5 to 3.0 GPa for 4 to 24 hours. These experiments confirm the stability of two sulfides in a convecting upper mantle and they add important textural information: Crystalline monosulfides formed angular grains encased in silicates (Fig. 1D), whereas sulfide melt quenched to droplets concentrated along grain boundaries of silicates and in silicate melt (Fig. 1E). Average droplet diameters of molten sulfide were ~1.5 μm. The droplets did not vary with the amount of sulfide in the charge, nor did they coalesce with time (up to 24 hours) to larger aggregates (*13*).

Our experiments confirm the textural observation (*3*, *4*, *14*, *15*) that two sulfides may coexist in the upper mantle. Furthermore, they offer an effective way of fractionating the PGEs between mantle and basaltic melt. Crystalline monosulfides, enriched in Os-Ir-Ru, are left behind in the residue because of their tendency to adhere to silicates. Immiscible sulfide droplets, moderately depleted in Os-Ir-Ru but enriched in Rh-Pt-Pd, are dispersed in silicate melt and can be segregated from the melting region along with silicate melt. In the presence of entrained sulfide, the PGE abundances of a basalt are controlled by the amount of sulfide entrained and the PGE concentration in the sulfide. The PGE ratios in a basalt reflect the extent of metal partitioning between monosulfide and sulfide melt (*7*). The contribution of PGEs to a basalt by sulfide-silicate partitioning (*6*) is negligibly small.

To fractionate the PGEs with this mechanism, three conditions must be met. First, the upper mantle undergoing partial melting must remain at sulfur saturation until the silicate melt can be segregated. Fertile mantle is estimated to have 200 to 250 ppm S (*1*), present as sulfide. The solubility of S in a typical oceanic basalt is, at atmospheric pressure, ~1000 ppm (*16*). A basaltic melt that originates by 20% by volume silicate batch melting can remove from the mantle source by way of sulfide dissolution about 200 ppm S, which is close to the estimated S content of fertile mantle. In reality, however, partial mantle melting is fractional, so at least the low-degree melt fractions contributing to a basalt will be S-saturated when they leave their source regions. This will impose a fractionated PGE signature onto the basalt even if sulfide did not persist in some regions of the melting column. Furthermore, the solubility of S falls by a factor of 2 from 1 atm to 1.5 GPa (*17*, *18*), making total sulfide dissolution more difficult at depth. Second, it must be physically possible to entrain dense sulfide melt against its tendency to settle in less dense silicate melt. The settling speed of 1.5-μm-large sulfide droplets, i.e., the average

droplet diameter determined in this study, is calculated with Stoke's law to ~15 cm per year (*19*). Magma ascent rates in partially molten mantle matrix, in contrast, are on the order of several meters per year (*20*, *21*), thus easily overcoming the settling rate of immiscible sulfide droplets dispersed in silicate melt. Third, absolute PGE abundances and PGE ratios in basalts must be consistent with sulfide entrainment. Using Ir and Pd as examples, we calculate PGE abundances of a mantle residue and a basaltic melt that originated by 20% by volume batch melting of a chondritic mantle source (Table 1 and Fig. 3). We assume that the sulfide phase is melted on average by 50% and that all molten sulfide is entrained when the silicate melt is segregated. The S content of the primitive mantle, recalculated as FeS, gives 600 ppm sulfide. If all the Ir and Pd of the fertile mantle—i.e., 3.2 and 3.27 parts per billion (ppb), respectively (*1*)—reside in sulfide, the sulfide phase before partial melting contains 5.3 ppm Ir and 5.5 ppm Pd. When partial melting occurs, the PGEs will be fractionated between monosulfide and sulfide melt according to their partition coefficients ($D_{Ir}^{mss\text{-}L} \sim 10$, $D_{Pd}^{mss\text{-}L} \sim 0.14$) (*7*), producing a sulfide melt with 1 ppm Ir and 9.6 ppm Pd. This melt will be in equilibrium with residual monosulfide with 9.7 ppm Ir and 1.3 ppm Pd. For a 20% by volume of silicate melting, where the basaltic melt entrains all of the sulfide melt in the mantle source, the basalt on the surface will contain 1.5 ppb Ir and 14.7 ppb Pd. The mantle residue will have 3.7 ppb Ir and 0.5 ppb Pd.

The calculated Ir and Ru concentrations in the residue are insensitive to sulfide melt extraction (Table 1 and Fig. 3), in agreement with natural abundances in peridotite xenoliths and massive peridotites (*1*, *5*, *22*, *23*). The melt extraction produces slight Ir-Ru enrichment relative to primitive mantle, but this is due entirely to the volume loss of the mantle when silicate melt is extracted. Silicate melt extraction also produces subchondritic Pt/Ir and Pd/Ir chondrite-normalized ratios, reflecting the affinity of Pt and Pd toward the sulfide melt (SOM Text). The model basalt spectrum resembles that of highly magnesian melts like picrites and komatiites (*24*). Calculated mantle-normalized Ir/Pd and Pt/Pd values (Table 1) are higher than in most basalts; however, as discussed above, basalts originate by fractional rather than batch melting (*25*), which results in Ir/Pd ratios lower than calculated here. More importantly, basalts continue to fractionate their PGEs as they decompress to the surface, unlike our model basalt; once sulfide entrained from the mantle source is dissolved during decompression (*17*, *26*), its PGEs are released to the silicate melt and are then fractionated by silicate solubilities. The PGEs least soluble in silicate melt—i.e., Os, Ir, and Pt (*27*, *28*)—will partly precipitate as metallic alloys, lowering Ir/Pd and Pt/Pd to values more typical of basalts (SOM Text).

References and Notes

1. H. Palme, H. St. C. O'Neill, in *Treatise of Geochemistry,* vol. 2, *The Mantle and Core,* R. W. Carlson, Ed. (Elsevier, Amsterdam, 2003), p. 1.
2. S.-J. Barnes, A. J. Naldrett, M. P. Gorton, *Chem. Geol.* **53**, 303 (1985).
3. O. Alard, W. L. Griffin, J.-P. Lorand, S. E. Jackson, S. Y. O'Reilly, *Nature* **407**, 891 (2000).
4. J.-P. Lorand, O. Alard, *Geochim. Cosmochim. Acta* **65**, 2789 (2001).
5. D. G. Pearson, D. Canil, S. B. Shirey, in *Treatise of Geochemistry,* vol. 2, *The Mantle and Core,* R. W. Carlson, Ed. (Elsevier, Amsterdam, 2003), p. 171.
6. M. E. Fleet, J. H. Crocket, W. E. Stone, *Geochim. Cosmochim. Acta* **60**, 2397 (1996).
7. C. Ballhaus, M. Tredoux, A. Spaeth, *J. Petrol.* **42**, 1911 (2001).
8. The exchange coefficient of the equilibrium $2FeS + Ni_2SiO_4 \rightleftharpoons 2NiS + Fe_2SiO_4$ was assumed to be 12 (*9*).
9. C. D. Doyle, A. J. Naldrett, *Econ. Geol.* **82**, 208 (1987).
10. Ambient-pressure experiments were done in evacuated SiO_2 glass tubes; the piston cylinder press experiments used SiO_2 glass capsules sealed with a Pyrex glass plug.
11. B. Ryshenko, G. C. Kennedy, *Am. J. Sci.* **273**, 803 (1973).
12. Ground mineral separates from the Mongolian spinel peridote xenolith Mo101, analyzed by Press *et al.* (*29*).
13. Consistent with results of Bremond *et al.* (*30*), who suggested that sulfide coalescence is prevented by the high surface tension of sulfide melt.
14. A. Luguet, J.-P. Lorand, M. Seyler, *Geochim. Cosmochim. Acta* **67**, 1553 (2003).
15. K. W. Burton, P. Schiano, J. L. Birck, C. J. Allegre, *Earth Planet. Sci. Lett.* **172**, 311 (1999).
16. H. St. C. O'Neill, J. A. Mavrogenes, *J. Petrol.* **43**, 1049 (2002).
17. J. A. Mavrogenes, H. St. C. O'Neill, *Geochim. Cosmochim. Acta* **63**, 1173 (1999).
18. A. Holzheid, T. L. Grove, *Am. Min.* **87**, 227 (2002).
19. Density of sulfide melt is assumed to be 4700 kg m^{-3}, density of silicate melt 2800 kg m^{-3}, and viscosity of silicate melt 5 kg m^{-1} s^{-1}.
20. G. Schubert, D. L. Turcotte, P. Olson, *Mantle Convection in the Earth and Planets* (Cambridge Univ. Press, Cambridge, 2001).
21. T. Elliot, M. Spiegelman, *Earth Planet. Sci. Lett.* **118**, 1 (1993).
22. J. W. Morgan, R. J. Walker, A. D. Brandon, M. F. Horan, *Meteorit. Planet. Sci.* **36**, 1257 (2001).
23. D. G. Pearson, G. J. Irvine, D. A. Ionov, F. R. Boyd, G. E. Dreibus, *Chem. Geol.* **208**, 29 (2004).
24. I. Puchtel, M. Humayun, *Geochim. Cosmochim. Acta* **64**, 4227 (2000).
25. M. Rehkämper *et al.*, *Earth Planet. Sci. Lett.* **172**, 65 (1999).
26. C. Ballhaus, *Earth Planet. Sci. Lett.* **132**, 75 (1995).
27. H. St. C. O'Neill, D. B. Dingwell, A. Borisov, B. Spettel, H. Palme, *Chem. Geol.* **120**, 255 (1995).
28. A. Borisov, H. Palme, *Am. Mineral.* **85**, 1665 (2000).
29. S. Press, G. Wirr, H. A. Seck, D. Eonov, V. I. Kovalenko, *Geochim. Cosmochim. Acta* **50**, 2587 (1986).
30. J. D. Bremond d'Ars, N. A. Arndt, E. Hallot, *Earth Planet. Sci. Lett.* **186**, 371 (2001).
31. T. J. Falloon *et al.*, *J. Petrol.* **29**, 1257 (1988).
32. R. J. Kinzler, T. L. Grove, *J. Geophys. Res.* **97**, 6885 (1992).
33. The position of dry fertile solidus from experiments by Falloon *et al.* (*31*) and Kinzler *et al.* (*32*).
34. T. J. Falloon, D. H. Green, *Geology* **18**, 195 (1990).

35. This report is dedicated to the late Eugen Stumpfl to honor his contribution to PGE mineralogy. We thank N. Arndt, J.-P. Lorand, C. Putnis, K. Mezger, E. Scherer, two anonymous reviewers, and especially A. Meibom for their comments. Financial support by the Deutsche Forschungsgemeinschaft (Ba 964/15) is acknowledged.

Supporting Online Material

www.sciencemag.org/cgi/content/full/305/5692/1951/DC1
SOM Text
Table S1
References

11 May 2004; accepted 16 August 2004

Distance Communication Transfer of HIV Prevention Interventions to Service Providers

Jeffrey A. Kelly,[1]* Anton M. Somlai,[1] Eric G. Benotsch,[1] Timothy L. McAuliffe,[1] Yuri A. Amirkhanian,[1] Kevin D. Brown,[1] L. Yvonne Stevenson,[1] M. Isa Fernandez,[2] Cheryl Sitzler,[1] Cheryl Gore-Felton,[1] Steven D. Pinkerton,[1] Lance S. Weinhardt,[1] Karen M. Opgenorth[1]

Most acquired immunodeficiency syndrome (AIDS) service providers are in countries with little access to scientific developments relevant to their programs. It is critical to transfer advances from the scientific arena to service providers on a global scale. Human immunodeficiency virus (HIV) prevention organizations in 78 countries were randomized to receive either a control condition or a technology transfer condition with an interactive distance learning computer training curriculum and individualized distance consultation. Of 42 nongovernmental organizations in the technology transfer condition, 29 adopted the science-based program in their communities or trained other agencies to also use it. Advanced communication technologies can create a cost-effective infrastructure to disseminate new intervention models to service providers worldwide.

Many studies have shown the positive effects of behavioral interventions in reducing HIV risk practices and disease (*1*–*3*). However, scholarly journals are rarely accessible to service providers, and articles published in them do not include sufficient detail to allow

providers to successfully implement the approaches. Service providers often cannot adopt complex new practice methods through didactic information alone (*4*). Dissemination approaches are more successful when providers gain skills and receive ongoing support for the use of a new method (*5*). A randomized trial evaluating technology transfer approaches with U.S. nongovernmental organizations (NGOs) found that providing intervention manuals had much less effect on new program adoption than NGO staff receiving face-to-face training followed by implementing consultation (*6*). However, a critical practical question is how to efficiently reach thousands of NGO service providers worldwide.

Distance education programs often show effects comparable to those in traditional teaching (*7*). We extended these methods to determine whether online and offline technologies can assist acquired immunodeficiency syndrome (AIDS) NGOs in resource-poor countries with implementing a research-based community-level HIV prevention intervention. An immediate study objective was to determine whether the distance training approach helped NGOs to implement the science-based program in their own communities. Its broader objective was to test a technology transfer infrastructure model that could routinely move methods from the research field to service providers on a global scale.

Study participants were 86 leading AIDS NGOs in 78 countries (29 countries in Africa, 25 in Central/Eastern Europe and Central Asia, and 24 in Latin America and the Caribbean) located through service provider databases and expert recommendations. Most had limited budgets and few staff and relied on international donors and volunteers.

NGOs assigned high priority to inexpensive prevention outreach approaches. For these reasons, we selected the popular opinion leader (POL) model for dissemination (*8*). This community-level intervention has its basis in the principle that population risk behavior can be reduced when enough naturally liked and trusted persons within the target population are trained to communicate effective risk-reduction personal endorsement messages to others (*8*, *9*). The model is characterized by distinctive core elements and includes using ethnography to identify large numbers of opinion leaders, training POLs to deliver theory-based messages that personally endorse and instill positive attitudes about safer behavior, and encouraging POLs to deliver these messages to friends and acquaintances in everyday conversations. The intervention can be applied across populations, countries, and cultures; does not require literacy; and can be carried out by paraprofessionals. It is adaptable because, regardless of culture, all community populations have opinion leaders whose views can influence others. Initial contacts made with study NGOs indicated a high level of enthusiasm about this model.

Two-part baseline interviews were carried out by telephone with NGO directors. The first part elicited a general overview of the organization and programs carried out during the past 6 months. We then identified all programs that were possible candidates for change as a result of the dissemination activities, including those that involved community AIDS education, peer education, or teaching community volunteers to serve as AIDS outreach educators. The second part of the baseline interview probed for the presence of each POL core element in each candidate program. Written interview summaries were coded by a team of three HIV prevention researchers for the presence of core elements.

NGOs were then randomized within regions into control and experimental conditions. NGOs were paired with a behavioral science consultant on our staff who was from the region or was familiar with its culture. Consultation through telephone, Web site communications, e-mail, or instant messaging initially concerned the organization's needs and reasons for study participation. This allowed the consultant to understand the NGO's circumstances and allowed NGO staff, even though far away, to personalize their relationships with us.

Control NGO directors attended an orientation meeting that described the POL intervention and explained that they would receive training in 18 months. Each NGO received a computer, subsidized Internet service, access to a study Web site to network with other NGOs about new programs, and briefing papers on topics such as effective grant writing, program evaluation, needs assessment methods, and organizational management.

Experimental condition organizations received the same supports plus a transfer program carried out by using distance communication technologies, with all materials and communications in English, French, Russian, or Spanish. Each experimental NGO received a self-paced curriculum for the POL intervention on compact disk (CD). The curriculum described key intervention procedures, modeled techniques, and used discussion points to engage users in planning intervention implementation with a community population of their choice. The CD had print, video, animation, and voice-over to explain critical points and discuss practical implementation issues. It also included printable copies of all materials needed to replicate the intervention. Many directors also requested and received supplemental print curricula. Most NGOs required 3 to 4 weeks to complete the curriculum.

Postcurriculum consultation continued for 6 months. Consultants answered questions about the intervention and how to culturally tailor it to meet local circumstances. Some NGOs planned immediate intervention implementation. Others used consultation to develop grant applications to funding agencies. NGOs differed in their plans to develop entirely new programs based on the model, to modify existing programs, or to function as nodes, sharing the training with other in-country agencies. Consultation did not pressure organizations to adopt the intervention but instead followed a provider-centered approach to help each NGO achieve its own goals.

In-depth follow-up telephone interviews were repeated 15 months after the baseline assessment by interviewers unaware of an NGO's condition. Directors were first asked whether they had initiated a new program or modified an existing one on the basis of their study experiences. All candidate programs were again assessed for the presence of POL core elements. The study's main outcomes were the percentage of NGOs in each condition that developed a new program or modified an existing program (Mantel-Haenszel χ^2 statistic) and the change in total number of POL core elements in candidate programs (repeated measures analysis of variance).

Out of a total of 42 NGO directors in the experimental group, 37 directors (88%) used

[1]Center for AIDS Intervention Research (CAIR), Department of Psychiatry and Behavioral Medicine, Medical College of Wisconsin, Milwaukee, WI 53226, USA. [2]Department of Public Health, University of Miami, Miami, FL 33101, USA.

*To whom correspondence should be addressed. E-mail: kdemming@mcw.edu

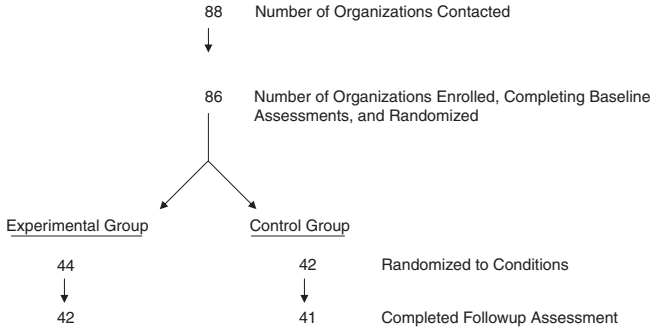

Fig. 1. Study flow chart of the number of organizations contacted.

the CD, and they did so for an average of 6.8 hours and viewed 69% of its content. All read the print curriculum, spent a mean of 15.6 hours doing so, and read 93% of it. An average of 10.7 other NGO staff and volunteers also used the curriculum. Consultants communicated with NGOs a mean of 5.9 times (range from 1 to 17), each lasting 30 min.

The CD was evaluated as very useful by 30 directors (72%); the print materials were evaluated as such by 37 directors (88%); and the distance consultation, by 28 (67%). Of the 42 experimental condition NGOs, 37 held staff meetings to plan new programs based on the model, 34 chose target populations, and 31 identified community venues for carrying out the intervention. Grants were written to funders by 24 NGOs (57%) to support intervention implementation.

At follow-up, 18 of the 42 experimental condition NGOs (43%) but only 7 of the 41 controls (17%) had developed a new HIV prevention program based on the model that was disseminated [$\chi_{M\text{-}H}^2 = 5.28$, $P = 0.022$, odds ratio (OR) = 4.0, and confidence intervals (CI) = 1.3, 12.0]. POL core elements were incorporated into an existing prevention program by 23 (55%) experimental NGOs compared with 11 (27%) control NGOs ($\chi_{M\text{-}H}^2 = 7.14$, $P = 0.008$, OR = 4.6, and CI = 1.6, 13.4). Nearly twice as many NGOs in the technology transfer condition ($n = 27$, 64%) as controls ($n = 14$, 34%) either developed a new program or modified an existing program based on the disseminated model ($\chi_{M\text{-}H}^2 = 7.70$, $P = 0.006$, OR = 5.0, and CI = 1.7, 14.5).

Successful transfer of the disseminated intervention should also be reflected in increased incorporation of its core elements. Across all study NGOs, 67 candidate HIV prevention programs offered at both baseline and follow-up could be matched. Experimental and control NGOs had respective means of 1.03 and 1.35 core elements in their baseline programs. At follow-up, experimental NGOs incorporated significantly more core elements ($M = 2.81$) in candidate prevention programs than control NGOs [$M = 1.90$, $F(1,61) = 4.27$, and $P = 0.04$]. New programs developed by experimental NGOs at follow-up incorporated a mean of 2.69 POL core elements.

NGOs also often networked with other in-country providers to share information they gained during project participation. Of the 42 experimental NGOs, 23 (55%) gave copies of the CD or print curriculum to other community-based providers. Twelve NGOs shared the CD curriculum with a total of 81 other organizations, and 21 NGOs gave print manuals to 143 other organizations. Twelve experimental NGOs (29%) held training sessions on the model for a total of 73 other in-country agencies, and 19 (45%) met with their governments about the model. The intervention was incorporated into government HIV prevention strategic plans in 26% of the NGO countries.

When new intervention approaches are found efficacious in the research arena, they must be moved into the hands of service providers. It is important to distinguish between our interactive curriculum and passive uses of Web sites to simply supply information. We also believe that the personalized cultural consultation offered in this project was critical for helping providers tailor and implement the new method. Advantages of Internet- and computer-based dissemination methods include potential cost-effectiveness for reaching very large numbers of international providers, ability to produce new training packages whenever new advances are made, equity of opportunity for training by organizations even in resource-poor countries, and availability of on-demand training.

Our outcomes relied on director reports of NGO programs, which could be biased. However, 18 of the experimental NGOs (43%) spontaneously shared with us materials, photographs, and funding applications that corroborate their reports. It is clear that most NGOs did not adopt the dissemination intervention in its entirety and that their use of core elements was selective. Lack of funding was an implementation barrier cited by 25 of the 42 experimental NGOs (60%), and providers most often incorporated core elements that did not require additional cost or personnel. We do not know whether the omission of certain elements adversely impacted the effectiveness of programs implemented by the NGOs. Future research should study how service providers use and adapt science-based models and the effectiveness of these interventions when carried out by providers in the field. Our findings show that advanced communication technologies can link service providers worldwide with training, technical assistance, and consultation in the use of new approaches originating in the research arena (*10*).

References and Notes

1. *Interventions to Prevent HIV Risk Behaviors* (NIH Consensus Development Conference Statement Online, 1997 February 11 to 13), 15(2), pp. 1–41.
2. Centers for Disease Control and Prevention (CDC) HIV/AIDS Prevention Research Synthesis Project, *Compendium of HIV Prevention Interventions with Evidence of Effectiveness* (CDC, Atlanta, GA, 1999).
3. Center for Substance Abuse Prevention, *National Registry of Effective Prevention Programs* (Substance Abuse and Mental Health Services Administration, Rockville, MD, 2001). Available online at http://preventionpathways.samhsa.gov/nrepp/default.htm.
4. J. Grimshaw, I. Russell, *Lancet* **342**, 1317 (1993).
5. D. Davis *et al.*, *JAMA* **282**, 867 (1999).
6. J. Kelly *et al.*, *Am. J. Public Health* **90**, 1082 (2000).
7. K. Umble, R. Caruero, B. Yang, W. Atkinson, *Am. J. Public Health* **90**, 1218 (2000).
8. J. Kelly *et al.*, *Lancet* **350**, 1500 (1997).
9. E. Rogers, *Diffusion of Innovations* (Free Press, New York, 1983).
10. Detailed materials and methods are found on *Science* Online.

11. Supported by grants R01-MH62982 and P30-MH52776 from the National Institute of Mental Health.

Supporting Online Material
www.sciencemag.org/cgi/content/full/305/5692/1953/DC1
Materials and Methods
Tables S1 to S4

26 May 2004; accepted 13 August 2004

Avian Extinction and Mammalian Introductions on Oceanic Islands

Tim M. Blackburn,[1]* Phillip Cassey,[1] Richard P. Duncan,[2] Karl L. Evans,[3] Kevin J. Gaston[3]

The arrival of humans on oceanic islands has precipitated a wave of extinctions among the islands' native birds. Nevertheless, the magnitude of this extinction event varies markedly between avifaunas. We show that the probability that a bird species has been extirpated from each of 220 oceanic islands is positively correlated with the number of exotic predatory mammal species established on those islands after European colonization and that the effect of these predators is greater on island endemic species. In contrast, the proportions of currently threatened species are independent of the numbers of exotic mammalian predator species, suggesting that the principal threat to island birds has changed through time as species susceptible to exotic predators have been driven extinct.

The colonization of each land mass by humans has broadly coincided with an increase in the extinction rate of the native biota (*1–6*). The oceanic island bird species lost to extinction after human colonization are estimated to number in the hundreds to thousands (*3*, *7–10*). Although the exact causes of these extinctions are debated (*11–15*), human colonization is typically associated with habitat destruction and fragmentation and with other processes that can eliminate species, including overexploitation of populations (*5*, *16*).

These processes may also be driven by the nonnative predator and herbivore species that humans introduce. In particular, the introduction of mammalian predators has caused the extinction of many populations and species of oceanic island birds (*3*, *17–20*) that, having evolved in their absence, lack appropriate antipredator responses.

The probability that a bird species has been extirpated from an island varies substantially among islands (Fig. 1A). This variation has normally been ascribed to differences in the characteristics of individual islands, such as area, isolation, elevational range, or date of human colonization (*9*, *21–24*). Isolation may increase extinction susceptibility, because the avifaunas of isolated islands are likely to have evolved for longer in the absence of predators, and so their species are more likely to react naïvely to exotic mammalian predators when they arrive. Large islands support larger populations of native bird species, which are thus less prone to extinction (*25*). Larger islands (or those with a greater elevational range) are also more likely to provide refugia from forces that promote extinction. Islands colonized longer ago may have more unrecorded prehistoric extinctions and so appear to have fewer extinctions, because only species that are relatively resistant to extinction remain [the filter effect (*21*)]. However, islands also vary substantially in the number of exotic mammal species, from none to >20 species. This variation may also drive variation in extinction probability. Here, we test this hypothesis using data from 220 oceanic islands worldwide (*26*) (table S1). Most mammalian introductions have occurred in the period after European colonization of an island, so we focus on bird extinctions that have occurred in this historic period. This increases the reliability of our results because historic extinctions are well documented, whereas prehistoric extinctions suffer from the incompleteness of the (sub)fossil record.

Our results show that islands with more exotic mammal predator species have lost a greater proportion of their avifauna since European colonization. The probability of extinction from an island's avifauna since European colonization increases with the number of exotic mammal predator species introduced (estimate ± SE = 0.24 ± 0.05, $P < 0.01$; the estimate is a linear parameter estimate from a general linear mixed model with binomial errors). The numbers of exotic mammalian predators and herbivores on an island are highly positively correlated (Pearson's $r = 0.67$, $n = 220$ islands, $P < 0.01$); however, the probability of extinction is unrelated to changes in the number of exotic mammal herbivore species (estimate ± SE = 0.02 ± 0.07, $P = 0.51$). This suggests that the predator relationship is not a simple consequence of more extensive environmental modification that leads to both more native extinction and exotic establishment. Introduced mammal predators are known to have caused specific island bird extinctions, but our results are consistent with introduced predators being a major cause of bird extinctions on oceanic islands around the world. Islands with more exotic predator species have suffered correspondingly greater losses.

We restrict analysis to historic extinctions, yet some exotic mammal species were established on islands before European colonization (e.g., the Pacific rat *Rattus exulans*), and many bird extinctions were prehistoric. A significant effect of predator species number is still observed when the analysis is expanded to include prehistoric mammal introductions and bird extinctions (multiple regression, predators: estimate ± SE = 0.24 ± 0.06, $P < 0.01$; herbivores: estimate ± SE = 0.01 ± 0.07, $P = 0.81$).

The apparent influence of predators could be an artifact of colinearity between the number of predator species introduced and biogeographic variables that have previously been shown to relate to extinction probability across islands, such as area or isolation (*9*, *21–24*). The number of predator species introduced to an island does indeed covary positively with island size ($r = 0.63$, $n = 197$ islands, $P < 0.01$) and maximum elevation ($r = 0.42$, $n = 183$, $P < 0.01$). However, because extinction probability should be lower on large and elevationally diverse islands, negative relationships would be expected if this colinearity were causing the predator effect. Moreover, multiple regression analyses that include island characteristics and number of exotic mammal predator species reveal that the effect of predators is robust to the inclusion of other variables that might determine avian extinction probability and that predator species number is the strongest predictor (Table 1).

Previous studies have found that islands with more exotic bird species have lost more native bird species (*27*). This relationship is argued to be an indirect consequence of extensive environmental modification that increases the habitat available for exotic bird species and negatively affects native

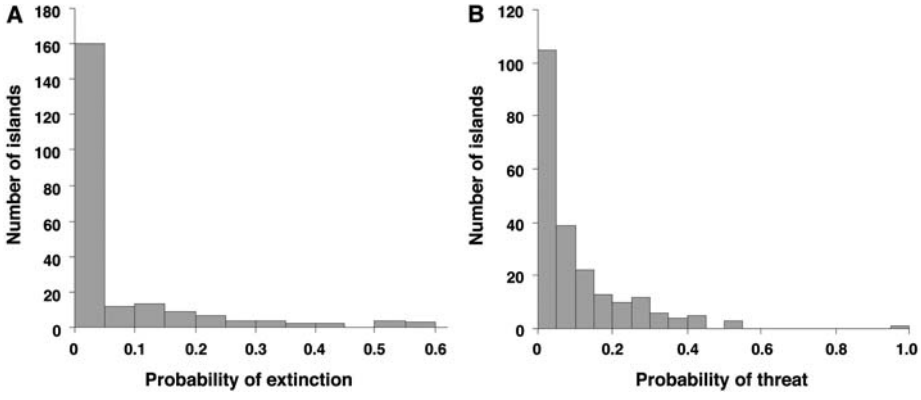

Fig. 1. Interisland variability in the probability of historic extinction and current threat for bird species. (**A**) The frequency distribution across islands ($n = 220$ islands) of the probability that a species in the historic fauna has become extinct from an island (the proportion extinct). Here and throughout the paper, extinction refers to the loss of a species from an island and so does not necessarily equate to global extinction. (**B**) The frequency distribution across islands ($n = 220$) of the probability that a species in the extant fauna is threatened with extinction (the proportion threatened). Threat refers to the risk of global extinction (*30*).

Table 1. The minimum adequate multivariate model (MAM) for historical probability of extinction in native island bird species. The MAM was derived by backward deletion of nonsignificant terms from a full model that also included island isolation, latitude, and human colonization date. Adding the number of exotic bird species to the full model does not alter the final MAM. The estimate is a linear parameter estimate.

Predictor	Estimate	SE	*t* value
Intercept	–4.25	0.67	
Number of introduced predatory mammal species	0.41	0.07	5.75***
Log (area)	–0.70	0.16	–4.40***
Log (maximum elevation)	0.69	0.27	2.48*

*$P < 0.05$. **$P < 0.01$. ***$P < 0.001$.

[1]School of Biosciences, University of Birmingham, Edgbaston, Birmingham B15 2TT, UK. [2]Bioprotection and Ecology Division, Post Office Box 84, Lincoln University, and Landcare Research, Post Office Box 69, Lincoln, New Zealand. [3]Biodiversity and Macroecology Group, Department of Animal and Plant Sciences, University of Sheffield, Sheffield S10 2TN, UK.

*To whom correspondence should be addressed. E-mail: t.blackburn@bham.ac.uk

species. Numbers of exotic bird species and native bird extinctions are also positively correlated across islands ($r = 0.62$, $n = 220$ islands, $P < 0.01$), as are numbers of both exotic bird and mammal species ($r = 0.65$, $n = 220$ islands, $P < 0.01$). However, the proportion of bird species extirpated from an island is independent of the number of exotic bird species in a multiple regression that includes the number of exotic mammalian predator species (Table 1).

Islands with more exotic predatory mammals suffered higher probabilities of bird extinction presumably because more diverse predator assemblages target a wider range of prey species or increase the overall predation rate on each species. However, alternative possibilities are that extinction has been driven by the range of predator types or by the presence of one or two particularly damaging predators, such as rats or cats (*17*, *19*, *20*, *28*), with the probability of these species being present on an island increasing with predator assemblage size [the sampling effect (*29*)]. We assessed these possibilities by comparing the fit to the data of different models in which the assemblage of introduced mammals was characterized in different ways (Table 2). Characterizing an assemblage by the number of predator species clearly provided the best fit to the data (the probability that this model was the best fitting out of the candidate set is 0.77), better than models in which the assemblage is characterized by the number of all mammal species or by the specific presence or absence of rats and/or cats. It was also a better fit than the number of taxonomic orders of predators introduced, which we used as a metric of number of predator types. These results strongly imply that each successive addition of an exotic predator acts to eliminate an additional proportion of an island's avifauna.

The impacts of mammalian predators ought to be greater on bird species endemic to islands, because these are more likely to have evolved in the absence of predators. For a given number of exotic predators, the probability of extinction is higher for island endemics than for species with continental populations (endemism: estimate ± SE = 1.55 ± 0.28, $P < 0.01$). Moreover, although higher extinction probability for species with continental populations is associated with decreasing island area (estimate ± SE = –0.84 ± 0.22, $P < 0.01$), increasing island elevation (estimate ± SE = 0.79 ± 0.32, $P < 0.01$), and the number of predatory mammal species (estimate ± SE = 0.35 ± 0.07, $P < 0.01$), extinction probability for island endemics is solely associated with the number of predatory mammal species (estimate ± SE = 0.16 ± 0.05, $P < 0.01$).

The probability that a species in the extant native avifauna is threatened with extinction also varies substantially across islands in our data (Fig. 1B). Is this variation also explained by the numbers of exotic mammal predator species? Certainly, the probability of threat is positively correlated with the probability that a species has already been extirpated from an island ($r = 0.43$, $n = 220$ islands, $P < 0.01$), and the proportion threatened is positively related to the total number of exotic mammal species (estimate ± SE = 0.04 ± 0.01, $P < 0.01$). However, in contrast to extinctions, there is no significant relationship between the probability of current threat and the number of exotic predators, although there is for the number of exotic herbivores (herbivores: estimate ± SE = 0.08 ± 0.03, $P < 0.05$; predators: estimate ± SE = 0.04 ± 0.05, $P = 0.36$). Moreover, in multiple regression, the probability of threat is significantly related only to biogeographic features of the islands (Table 3), with variation in the probability of threat across islands independent of the number of exotic mammal predator species.

The introduction of mammalian predators has been a major cause of bird extinctions on oceanic islands worldwide. Each successive predator introduction increases the number of species lost (Table 1), and island endemic species have suffered the most. In contrast, the proportion of an island's avifauna currently threatened with extinction is unrelated to the current number of exotic mammal species, even though many individual bird species are at risk from such predators (*30*), and islands with many extinctions in the past are also those with high levels of current threat. However, the current threat to native birds is higher on larger, more elevated, isolated islands that have been colonized more recently, consistent with the well-known filter effect (*21*, *31*). Presumably, most species susceptible to the current assemblages of exotic predators have already been driven extinct, especially on smaller, more easily colonized islands. However, these results do not imply that there is no longer any danger to island birds from exotic predatory mammals, because they relate to the current communities of exotic mammals on these islands. The establishment of each additional predator species is predicted to lead to additional extinctions among the native birds. This implies that exotic predators remain one of the major threats to island avifaunas, given that most islands currently have few predators (and some have none) and are likely to suffer progressively more extinctions if and when additional predators colonize. The likely consequences of future introductions are clearly presaged by the losses of the past.

Table 2. Comparison of models for the probability of historical bird extinction on oceanic islands (response variable) with the assemblage of introduced mammals characterized in different ways. Predictor variables in each model are $\log_{10}$ area, $\log_{10}$ elevation, and the variable in the first column; thus, the first model in this table is identical to that in Table 1, and subsequent models replace the number of predators in that model with the variable in the first column. Akaike's Information Criterion (AIC) values were calculated with PROC NLMIXED in SAS (*32*). ΔAIC is the difference between AIC values for each model and that with the lowest AIC (in this case, number of predators). *W* is the model's Akaike weight, which is the relative probability that the model is the best fit to the data of those tested (*33*).

Predictor	AIC	ΔAIC	*W*
Number of exotic predator species	335.9	0.0	0.77
Number of exotic herbivore species	341.0	5.1	0.06
Number of exotic mammal species	339.7	3.8	0.12
Number of exotic mammal orders	341.9	6.0	0.04
Rats, presence or absence	348.9	13.0	<0.01
Cats, presence or absence	345.3	9.4	0.01
Rats and cats, presence or absence	347.4	11.5	<0.01

Table 3. The MAM for probability of threat in extant island bird species. The MAM was derived by backward deletion of nonsignificant terms from a full model that also included the number of exotic predator species, the number of exotic herbivore species, and the number of exotic bird species. The estimate is a linear parameter estimate.

Predictor	Estimate	SE	*t* value
Intercept	–4.83	1.32	
Log (area)	0.19	0.09	2.21*
Log (maximum elevation)	0.39	0.17	2.24*
Log (years since colonization)	–0.76	0.24	–3.15***
Log (isolation)	1.06	0.31	3.38***

*$P < 0.05$. **$P < 0.01$. ***$P < 0.001$.

References and Notes

1. P. S. Martin, in (*11*), pp. 354–403.
2. T. F. Flannery, *The Future Eaters* (Reed, Melbourne, 1994).
3. D. W. Steadman, *Science* **267**, 1123 (1995).
4. P. S. Martin, D. W. Steadman, in (*12*), pp. 17–56.
5. J. Diamond, *Philos. Trans. R. Soc. London Ser. B* **325**, 469 (1989).
6. R. G. Roberts *et al.*, *Science* **292**, 1888 (2001).
7. R. Cassels, in (*11*), pp. 741–767.
8. P. Milberg, T. Tyrberg, *Ecography* **16**, 229 (1993).
9. E. Biber, *Ecography* **25**, 661 (2002).
10. J. Curnutt, S. L. Pimm, *Stud. Avian Biol.* **22**, 15 (2001).
11. P. S. Martin, R. G. Klein, *Quaternary Extinctions: A Prehistoric Revolution* (Univ. of Arizona Press, Tucson, AZ, 1984).
12. R. D. E. MacPhee, *Extinctions in Near Time: Causes, Contexts, and Consequences* (Kluwer/Plenum, New York, 1999).
13. P. S. Martin, in *Encyclopedia of Biodiversity*, S. A. Levin, Ed. (Academic Press, San Diego, 2001), vol. 3, pp. 825–839.
14. D. K. Grayson, *J. World Prehist.* **15**, 1 (2001).

15. R. N. Holdaway, C. Jacomb, *Science* **287**, 2250 (2000).
16. K. J. Gaston, in *Encyclopedia of Evolution*, M. Pagel, Ed. (Oxford Univ. Press, New York, 2002), vol. 1, pp. 344–349.
17. R. N. Holdaway, in (*12*), pp. 189–238.
18. D. A. Roff, R. J. Roff, *Evol. Ecol. Res.* **5**, 759 (2003).
19. N. P. Ashmole, N. J. Ashmole, K. E. L. Simmons, in *Seabirds on Islands: Threats, Case Studies and Action Plans*, D. N. Nettleship, J. Burger, M. Gochfeld, Eds. (BirdLife International, Cambridge, 1994), pp. 94–121.
20. I. A. E. Atkinson, in *Conservation of Island Birds: Case Studies for the Management of Threatened Island Species*, P. J. Moors, Ed. (Technical Publication No. 3, International Council for Bird Preservation, Cambridge, 1985), pp. 35–81.
21. S. L. Pimm, M. P. Moulton, L. J. Justice, in *Extinction Rates*, J. H. Lawton, R. M. May, Eds. (Oxford Univ. Press, Oxford, 1995), pp. 75–87.
22. J. M. Diamond, in *Extinctions*, M. H. Nitecki, Ed. (Chicago Univ. Press, Chicago, 1984), pp. 191–246.
23. J. M. Diamond, in (*11*), pp. 824–862.
24. T. M. Blackburn, P. Cassey, R. P. Duncan, *Ecography* **27**, 124 (2004).
25. R. H. MacArthur, E. O. Wilson, *The Theory of Island Biogeography* (Princeton Univ. Press, Princeton, 1967).
26. Materials and methods are available as supporting material on *Science* Online.
27. T. J. Case, *Biol. Conserv.* **78**, 69 (1996).
28. I. A. E. Atkinson, T. J. Atkinson, in *Invasive Species in the Pacific: A Technical Review and Draft Regional Strategy*, G. Sherley, Ed. (South Pacific Regional Environment Programme, Apia, Samoa, 2000), pp. 19–84.
29. D. Tilman, C. L. Lehman, K. T. Thomson, *Proc. Natl. Acad. Sci. U.S.A.* **94**, 1857 (1997).
30. BirdLife International, *Threatened Birds of the World* (Lynx Edicions and BirdLife International, Barcelona and Cambridge, 2000).
31. A. Balmford, *Trends Ecol. Evol.* **11**, 193 (1996).
32. R. C. Littell, G. A. Milliken, W. W. Stroup, R. D. Wolfinger, *SAS System for Mixed Models* (SAS Institute Inc., Cary, NC, 1996).
33. K. P. Burnham, D. R. Anderson, *Wildl. Res.* **28**, 111 (2001).
34. We thank D. P. Armstrong, L. Birch, R. L. Boulton, J. G. Ewen, and G. R. and K. B. Cassey. Supported by the Leverhulme Trust (grant no. F/00094/AA), a British Ecological Society small ecological project grant (no. 2264), and Foundation for Research, Science & Technology contract no. C09X0004.

Supporting Online Material
www.sciencemag.org/cgi/content/full/305/5692/1955/DC1
Materials and Methods
Table S1
References and Notes

17 June 2004; accepted 12 August 2004

The Impact of United States Recreational Fisheries on Marine Fish Populations

Felicia C. Coleman,[1]* Will F. Figueira,[2]† Jeffrey S. Ueland,[3]‡ Larry B. Crowder[2]

We evaluated the commercial and recreational fishery landings over the past 22 years, first at the national level, then for populations of concern (those that are overfished or experiencing overfishing), and finally by region. Recreational landings in 2002 account for 4% of total marine fish landed in the United States. With large industrial fisheries excluded (e.g., menhaden and pollock), the recreational component rises to 10%. Among populations of concern, recreational landings in 2002 account for 23% of the total nationwide, rising to 38% in the South Atlantic and 64% in the Gulf of Mexico. Moreover, it affects many of the most-valued overfished species—including red drum, bocaccio, and red snapper—all of which are taken primarily in the recreational fishery.

Many of the ecological and political problems associated with fishing in U.S. waters historically have been attributed to foreign fishers (*1*, *2*). This perspective led to the passage of the Magnuson Act nearly 30 years ago to eliminate foreign competition, which set in motion a wave of expansion for U.S. commercial fishing fleets. By 1996, it was clear that removing the foreign fleets had not resulted in sufficient conservation (*3*), and amendments to the Magnuson Act more strongly emphasized reducing the fishing pressure of domestic fleets.

In the years following the amendment, the public focused on stock depletion, bycatch, and habitat damage caused by commercial fisheries (*4*, *5*) but paid little attention to the recreational sector. The perception that recreational fishing had little influence on stock declines derived from estimates that it contributed only 2% to U.S. landings (*6*). However, marine recreational fishing effort has increased by over 20% in the past 20 years (*7*), rivaling commercial fisheries for many major fish stocks, including summer flounder (*Paralichthys dentatus*), scup (*Stenotomus chrysops*), and red snapper (*Lutjanus campechanus*) (*8*).

We examined data from the National Marine Fisheries Service (NMFS) online databases (*9*), because we assumed that these readily accessible data sets were used to produce the existing estimates of recreational landings. Using these data, we produced a similar estimate. However, substantial inconsistencies in the online databases cloud the relevance of the number, such as the inclusion of commercially caught freshwater species and the exclusion of recreational data sets, such as data from the southeastern headboat sector (table S1).

We developed a comprehensive landings database (*10*) with data provided by the Marine Recreational Fisheries Statistics Survey (MRFSS), NMFS science centers and fishery management councils (FMCs), multistate marine fisheries commissions, and state natural resource agencies (table S2). We included landings data only and did not include fish discarded at sea either as regulatory discards (for commercial and recreational fisheries) or as a result of catch-and-release (exclusively a recreational fishing practice). After standardizing the data to allow for reasonable comparisons of these diverse data sets (tables S1 to S3), we assimilated a 22-year (1981 to 2002) time series of commercial and recreational landings.

We conducted analyses for the continental United States at national and regional levels, the latter based on the management jurisdictions of the following FMCs: Northeast (combining Northeast and Mid-Atlantic FMCs, Maine through Virginia), South Atlantic (*11*) (North Carolina through the east coast of Florida), Gulf of Mexico (the west coast of Florida through Texas), and Pacific (Washington through California, including Alaska only in the nationwide comparisons).

The nationwide analyses included three successively smaller groups of species: all federally managed marine fish; all marine fish, excluding walleye pollock (*Theragra chalcogramma*, used to produce frozen fish products) and menhaden (*Brevoortia tyrannus* and *Brevoortia patronus*, used almost exclusively to produce fish meal); and all "populations of concern" [i.e., those populations listed by NMFS (*12*) as either overfished or experiencing overfishing]. Menhaden and pollock were excluded because they have little or no recreational value and they are not considered overfished (*12*), although they comprise more than half of all U.S. fisheries landings: pollock landings approximate 1.8 million metric tons

[1]Department of Biological Science, Florida State University, Tallahassee, FL 32306–1100, USA. [2]Nicholas School of the Environment and Earth Sciences, Duke University, 135 Duke Marine Lab Road, Beaufort, NC 28516–9721, USA. [3]Department of Geography, Florida State University, Tallahassee, FL 32306–2190, USA.

*To whom correspondence should be addressed. E-mail: coleman@bio.fsu.edu
†Present address: Department of Environmental Sciences, University of Technology Sydney, Westbourne Street, Gore Hill, NSW 2065, Australia.
‡Present address: Department of Geography, Clippinger Lab 122, Ohio University, Athens, OH 45701, USA.

(4 billion pounds) annually, and menhaden landings approximate 0.454 million metric tons (1 billion pounds). The regional analyses focused only on the populations of concern.

Our database indicates that the percentage of all U.S. landings of marine finfish attributable to recreational fishing in 2002 is actually about 4%, averaging 5% over 22 years (Fig. 1A). Excluding pollock and menhaden raises the recreational contribution to 10% of the total landings in 2002 (Fig. 1A), and focusing on the most relevant populations—the populations of concern—raises it to 23% (Fig. 1B). The regional differences in landings of populations of concern are pronounced (Fig. 1, C to F). In the Gulf of Mexico, 64% are taken recreationally (Fig. 1C); in the South Atlantic, 38% (Fig. 1D); along the Pacific Coast, 59% (averaging 14% over 22 years) (Fig. 1E); and in the Northeast, 12% (Fig. 1F) (*13*).

Current management of recreational fisheries focuses on controlling the landings of individual fishermen without restricting the number of individuals allowed to fish. In this open access scenario, control is limited to bag limits and size limits, which increases regulatory discards, thereby increasing fishing mortality (*14–20*) and sublethal effects on growth and reproduction (*21–24*). Increased fishing mortality also occurs with nonregulatory discards caused by high grading (wherein fishermen limited by quotas or bag limits discard small, less-valued fish to replace them with larger, more-valued fish) and catch-and-release in recreational fisheries. Discards are not included in this analysis, so these results underestimate likely impacts. Current regulatory methods have done little to constrain recreational fisheries, and for some major fish populations, recreational landings in the United States outstrip commercial landings, notably for red drum (*Sciaenops ocellatus*) in the South Atlantic (93% recreational), bocaccio (*Sebastes paucispinus*) on the Pacific Coast (87%), and red snapper (*Lutjanus campechanus*) in the Gulf of Mexico (59%).

Commercial and recreational fishing have similar demographic and ecological effects on fished populations. They truncate size and age structures, reduce biomass, and alter community composition (*25–31*). Whereas commercial fisheries fish intensely on both lower levels (e.g., menhaden and anchovies) and upper levels (top-level predators) of the food web, the recreational sector concentrates on the latter. All these fishery removals can cause cascading trophic effects that alter the structure, function, and productivity of marine ecosystems (*1*, *32–37*). Where recreational fishery landings rival those of commercial fisheries for major stocks of concern, sometimes even replacing them, they can have equally serious ecological and economic consequences on fished populations. If the goal of fishery management is to sustain viable populations and ecosystems, then recreational as well as commercial fishing requires effective regulations.

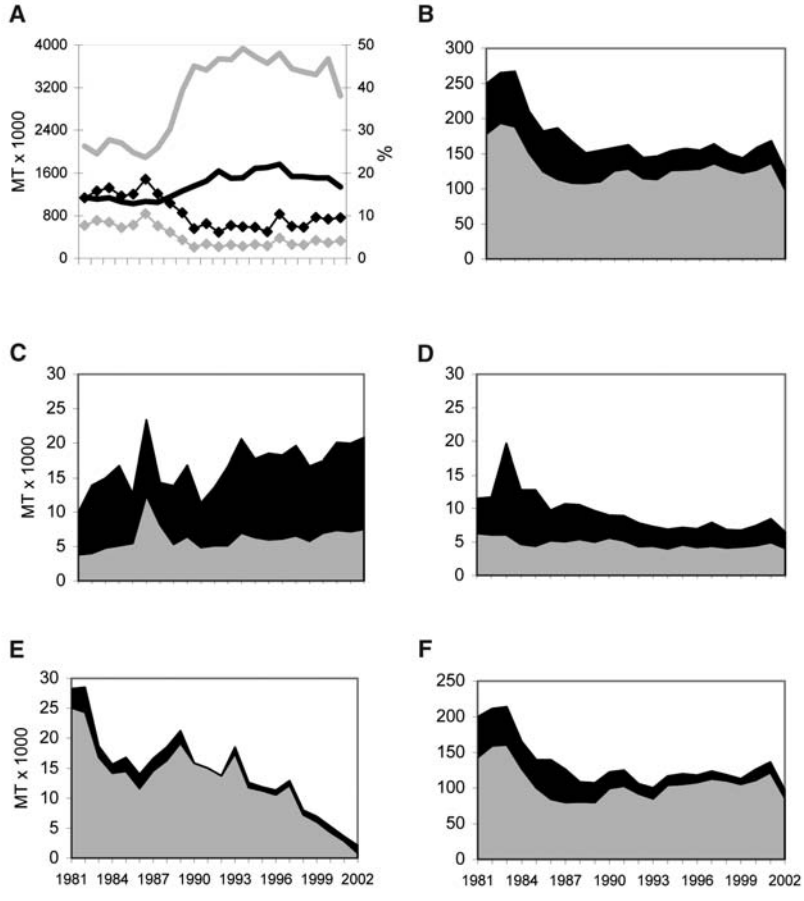

Fig. 1. Time series of marine fisheries landings from the continental United States in metric tons (MT) × 1000. (**A**) Total combined commercial and recreational landings (left *y* axis, solid lines) with recreational percentage of the total (right *y* axis, diamonds). The total, including all species, is shown in gray and the total, excluding menhaden and pollock, is in black. (**B** to **F**) Total (cumulative) landings of populations of concern separated into commercial (gray) and recreational (black) components for (B) all regions combined, (C) Gulf of Mexico, (D) South Atlantic, (E) Pacific Coast (excluding Alaska), and (F) Northeast. On the Pacific Coast, no complete sets of recreational data were collected for the years 1990 to 1992 from any of the federal or state organizations that maintain these databases.

References and Notes

1. R. A. Myers, B. Worm, *Nature* **423**, 280 (2003).
2. D. Pauly, V. Christensen, J. Dalsgaard, R. Froese, F. Torres, *Science* **279**, 860 (1998).
3. NMFS, "Our living oceans" *NOAA Tech. Memorandum NMFS-F/SPO-19* (1996).
4. S. F. Thrush, P. K. Dayton, *Annu. Rev. Ecol. Syst.* **33**, 449 (2002).
5. National Research Council, *Effects of Trawling and Dredging on Seafloor Habitat*, N. R. Council, Ed. (National Academy Press, Washington, DC, 2002).
6. National Research Council, *Sustaining Marine Fisheries*, N. R. Council, Ed. (National Academy Press, Washington, DC, 2002).
7. J. Sutinen, R. J. Johnston, *Mar. Policy* **27**, 471 (2003).
8. NMFS defines major stocks as those having annual landings >200,000 pounds (90,909 kg).
9. The database for commercial landings is available at www.st.nmfs.gov/st1/commercial/; the database for recreational landings is available at www.st.nmfs.gov/st1/recreational/queries/index.html. Note NMFS disclaimers on these sites.
10. Materials and methods are available as supporting material on *Science* Online.
11. The South Atlantic refers to the Atlantic off the southeastern United States.
12. NMFS, "Annual report to Congress on the status of U.S. fisheries, 2003" (U.S. Department of Commerce, NOAA/NMFS, Silver Spring, MD, 2004).
13. Although NMFS listed Pacific hake (*Merluccius productus*) as overfished in 2003 (*12*), they reversed the designation in March 2004. Thus, we excluded this species from the populations of concern. Pacific hake is an industrial fishery comprising 25% of the Pacific Coast landings. It has virtually no recreational value.
14. M. R. Collins, J. C. McGovern, G. R. Sedberry, H. S. Meister, R. Perdieck, *N. Am. J. Fish. Manage.* **19**, 828 (1999).
15. M. I. Muoneke, W. M. Childress, *Rev. Fish. Sci.* **2**, 123 (1994).
16. G. R. Gitschlag, M. L. Renaud, *N. Am. J. Fish. Manage.* **14**, 131 (1994).
17. D. V. Guccione, *Technical Report No. 98-FEG-02* (Fisheries Grant Project, Raleigh, NC, 1999).
18. M. H. Malchoff, *Technical Report No. NA36FD0102* (U.S. Department of Commerce, NOAA/NMFS, Gloucester, MA, 1995).
19. J. C. McGovern, M. R. Collins, O. Pashuk, H. S. Meister, *N. Am. J. Fish. Manage.* **22**, 1151 (2002).
20. R. R. Wilson, K. M. Burns, *Bull. Mar. Sci.* **58**, 234 (1996).
21. N. W. Pankhurst, D. F. Sharples, *Aust. J. Mar. Freshw. Res.* **43**, 345 (1992).
22. S. P. Quinn, *N. Am. J. Fish. Manage.* **9**, 86 (1989).
23. R. G. Taylor, J. A. Whittington, D. E. Haymans, *N. Am. J. Fish. Manage.* **21**, 70 (2001).
24. D. F. Clapp, R. D. Clark, *N. Am. J. Fish. Manage.* **9**, 81 (1989).
25. M. Westera, P. Lavery, G. Hyndes, *J. Exp. Mar. Biol. Ecol.* **294**, 145 (2003).

26. D. M. Schroeder, M. S. Love, *Calif. Coop. Oceanic Fish. Invest. Rep.* **43**, 182 (2002).
27. C. D. Buxton, J. R. Clarke, *S. Afr. J. Mar. Sci.* **10**, 285 (1991).
28. B. A. Bennett, *S. Afr. J. Mar. Sci.* **13**, 1 (1993).
29. R. D. Sluka, K. M. Sullivan, *Fish. Bull.* **96**, 388 (1998).
30. J. Y. Jouvenel, D. A. Pollard, *Aquat. Conserv. Mar. Freshw. Ecosyst.* **11**, 1 (2001).
31. G. C. Young, B. S. Wise, S. G. Ayvazian, *Mar. Freshw. Res.* **50**, 633 (1999).
32. J. B. C. Jackson *et al.*, *Science* **293**, 629 (2001).
33. D. Pauly, *Trends Ecol. Evol.* **10**, 430 (1995).
34. P. M. Vitousek, H. A. Mooney, J. Lubchenco, J. M. Melillo, *Science* **277**, 494 (1997).
35. L. W. Botsford, J. C. Castilla, C. H. Peterson, *Science* **277**, 509 (1997).
36. D. Pauly, J. Maclean, *In a Perfect Ocean* (Island Press, Washington, DC, 2002).
37. A. M. Friedlander, E. E. DeMartini, *Mar. Ecol. Prog. Ser.* **230**, 253 (2002).

38. We thank the following for providing assistance: D. Van Voorhees, L. Donniger-Few (MRFSS, Silver Spring, MD); J. MacClellan (Alaska Fish and Game); T. Kerns (Atlantic States Marine Fisheries Commission); G. Kobyinski, J. Robertson, J. Paulo Serpa (California Department of Fish and Game); S. Atran (Gulf of Mexico FMC); D. Donaldson, R. Lukens (Gulf States Marine Fisheries Commission); C. Evans, B. Dixon, D. Vaughan (NMFS, Beaufort); J. Poffenberger (NMFS, Miami); M. Fogarty, S. Murawski (NMFS, Woods Hole); J. Palmer (NOAA and Northeast Fisheries Science Center); L. Paramore (North Carolina Division of Marine Fisheries); J. O'Leary (New England FMC); J. Seabourne (Oregon Department of Fish and Wildlife); W. Daspit (Pacific Fisheries Information Network); W. Van Buskirk (Recreational Fisheries Information Network); K. Iverson (South Atlantic FMC); J. Bennett, P. Phares (NOAA Southeast Fisheries Science Center); M. Fisher, V. Swan (Texas Parks and Wildlife); D. Gombert, L. Hoines, G. Lippert, M. Stanley (Washington Department of Fish and Wildlife); and J. O'Driscoll and J. McMillon (Florida State University). R. Myers (Dalhousie University), R. Hilborn (University of Washington), and three anonymous reviewers who provided comments on the manuscript. This study was supported by The Pew Charitable Trusts.

Supporting Online Material
www.sciencemag.org/cgi/content/full/1100397/DC1
Materials and Methods
Tables S1 to S3
References and Notes

17 May 2004; accepted 9 August 2004
Published online 26 August 2004;
10.1126/science.1100397
Include this information when citing this paper.

Amazonian Ecology: Tributaries Enhance the Diversity of Electric Fishes

Cristina Cox Fernandes,[1,2]* Jeffrey Podos,[1] John G. Lundberg[3]

Neotropical rivers support a diverse array of endemic taxa, including electric fishes of the order Gymnotiformes. A comprehensive survey of the main channels of the Amazon River and its major tributaries (>2000-kilometer transect) yielded 43 electric fish species. Biogeographical analyses suggest that local mainstem electric fish diversity is enhanced by tributaries. Mainstem species richness tends to increase downstream of tributary confluences, and species composition is most similar between tributaries and adjacent downstream mainstem locations. These findings support a "nodal" or heterogeneous model of riverine community organization across a particularly extensive and diverse geographical region.

Biogeographers since Alfred Russel Wallace (*1*) have observed that the distribution of many terrestrial plant and animal species concords with the geography of major river systems. In the Amazon basin, for example, river and tributary channels appear to limit the ranges of taxa such as primates and lowland-forest birds [(*2*, *3*) but see (*4*)]. Similarly, divides between river basins can circumscribe the distribution of aquatic taxa such as freshwater fishes (*5*). Less clear, especially for large river systems such as the lowland Amazon, is the relationship between the structure of rivers [including channel geometry, network configuration, and geomorphology (*6*, *7*)] and the distribution of aquatic species.

Previous studies of fishes in temperate regions have suggested that local species diversity along main river channels is relatively high at tributary confluences (*8*, *9*). Tributaries might enrich mainstem fish diversity by providing access to the mainstem for migrating fishes, offering refugia for early life stages of mainstem species, or enhancing local ecological heterogeneity and thus augmenting local niche diversity (*6*, *10*). The potential impact of tributaries on fish distribution and diversity, however, has never been tested on as broad a spatial scale as that of the Amazon River basin.

Here, we report on the diversity and distribution of electric fishes (Teleostei, Gymnotiformes) along the Amazon mainstem and its major tributaries. Electric fishes are a distinctive and moderately diverse clade endemic to the freshwaters of South and Central America (*11*–*13*). These fishes are best known for their electroreceptive sense and production of electric fields for near-field orientation and electrocommunication (*14*). Recent taxonomic studies of these fishes have revealed an impressive degree of diversity, with 46 new species described within the past quarter century (*15*). In 1992, two of us (C.C.F. and J.G.L.) initiated the "Calhamazon Project," designed to document the fish fauna of the principal river channels of the Brazilian Amazon. Our field operations produced large samples of fishes trawl-netted in the deep main channels along >2,000 km of the Brazilian Solimões-Amazon mainstem, and in the lower reaches of major tributaries from the Içá River downstream to the Tocantins River (Fig. 1) (*16*). From these collections, we have recently described two new species of a new genus (*17*), identified 11 additional undescribed species, and resolved taxonomic errors caused by pronounced sexual dimorphism (*18*, *19*). These efforts set the stage for the present analysis of species diversity and distribution.

We focus here on three questions: (i) How many species of electric fishes are there in the mainstem channels of the Brazilian Amazon River and its major tributaries? (ii) What is the contribution, if any, of major tributaries to electric fish species diversity in the Amazon mainstem channels? (iii) How do patterns of electric fish diversity vary along the extent of the Amazon River?

Based on morphological criteria, we identify in our collections 43 electric fish species: 29 *Apteronotidae*, 8 *Sternopygidae*, 5 *Rhamphichthyidae*, and 1 *Hypopomidae* (table S1). The cumulative number of species collected, plotted as a function of the number of individuals sampled [in which sample order was randomized with the use of EstimateS (*20*)], yields a curve that is asymptotic (Fig. 2). Thus, our survey of channel species was arguably complete within the limits of our sampling method, and an accurate estimate of species richness was reached after about 16,000 individuals were captured. We do not imply that there are no additional electric fish species in the Amazon; other species are certainly present in microhabitats that were not sampled with our deep-water gear and possibly present in substrate depressions, among the branches of submerged trees, or in shallows near islands or the riverbank.

[1]Department of Biology and Graduate Program in Organismic and Evolutionary Biology, University of Massachusetts, Amherst, MA 01003, USA. [2]Instituto Nacional de Pesquisas da Amazônia, Alameda Cosme Ferreira, 1756 Caixa Postal 478, CEP 69083, Manaus, AM, Brazil. [3]Department of Ichthyology, The Academy of Natural Sciences, Philadelphia, PA 19103, USA.

*To whom correspondence should be addressed. E-mail: cristina@bio.umass.edu

Our estimate of 43 electric fish species in Amazon channels exceeds that from another major Neotropical river, the Orinoco, for which the same deep-water sampling methods were used and in which 28 species were identified (*11*). Twenty-two electric fish species were identified from multiple gear (including trawl) samples from the Amazonian Napo and Aguarico rivers of Eastern Ecuador (*21*); collections in the Negro River also made with multiple gears identified 35 species of electric fishes (*22*); and 31 electric fish species were collected with seine nets in the marginal habitats of Catalão island, at the confluence of the Amazon and Negro rivers (*23*). Twenty-two of the Catalão species were also found in our deep-water collections. We believe that the comparatively high species diversity we identified in the channels of the Amazon and its tributaries reflects both our intensive sampling effort and the unusually high richness of the region. It will be instructive to apply a comparable sampling effort to additional rivers to assess the extent to which the Amazon may be a "hot spot" for electric fish diversity (*24*).

To test whether tributaries enrich local mainstem electric fish diversity, we calculated Coleman rarefaction estimates of species richness on a site-by-site basis (*16*, *20*). This rarefaction procedure allowed us to control for differences among stations in sampling effort and abundance (Table 1). In our calculations, when comparing stations within each site (e.g., upstream of Içá, Içá, and downstream of Içá) we used the lowest observed abundance among the three stations as the basis for estimating and comparing species richness between stations.

We identified a significant positive effect of tributaries on Amazon mainstem species richness, in two respects. First, we found that sample stations downstream of each tributary contained more species than did their respective upstream stations (10 of 12 pairwise comparisons, tie at Juruá excluded, one-tail binomial test, $P = 0.019$; Fig. 3). This pattern occurred in spite of a similar sampling effort at upstream and downstream stations, both in the number of trawl tows (344 at upstream stations compared with 366 at downstream stations) and in the number of individuals captured (7618 at upstream stations compared with 7246 at downstream stations) (Table 1).

Second, we found that species richness within tributaries exceeded that within their adjacent upstream mainstem stations (10 of 13 pairwise comparisons, one-tail binomial test, $P = 0.046$) but was comparable between tributaries and their adjacent downstream mainstem stations ($P > 0.05$). An analysis of species composition across sampling stations further illustrates the contribution of tributaries to the mainstem fish fauna. We found that downstream mainstem stations tend to share more species with their adjacent tributaries than with their corresponding upstream mainstem stations (table S2, compare first and second columns, 10 of 13 pairwise comparisons, one-tail binomial test, $P = 0.046$).

These results agree with our observation that tributaries contained comparatively high abundances of electric fishes. We collected, on average, 48 individuals per trawl in the tributaries, as compared with only 22.1 and 19.8 fishes per trawl in the mainstem (upstream and downstream) stations. The high abundance of fish in tributaries enhances the likelihood that more species move from tributaries into the mainstem, even if relative richness (number of species divided by number of individuals captured) is lower in tributaries than in mainstem stations, as in our samples (calculated from Table 1). We do not imply that electric fishes move only from tributaries to the mainstem downstream of confluences; movements in other directions seem likely. In a study of lateral migration, a small number of electric fishes were captured within large groups of other fishes moving between floodplains and the Amazon mainstem (*25*).

Our sample also allows a large-scale test of the hypothesis that species diversity accumulates in a downstream direction. This pattern has been shown for fishes in numerous rivers, and has been attributed to increases downriver in food availability, habitat heterogeneity, and habitat stability (*7*). For this test, we first combined samples from each pair of upstream and downstream mainstem stations to provide a comprehensive estimate of species richness at each site. We then estimated mainstem species richness at each site, again standardized with the Coleman rarefaction method. Across the Amazon, we did not find support for the species addition hypothesis ($n = 8$ sites; $r^2 = 0.245$; $P = 0.212$).

Our main finding, that tributaries tend to enhance mainstem electric fish diversity, is perhaps surprising given that our sample covered such a large and diverse geographical region (table S3) (*26*). If the patterns exhibited by gymnotiforms prove to be general to fishes or other taxa, they would provide a notable exception to the "river continuum" model of lotic community organization, which posits that rivers, particularly the main channels, are continuous entities that express gradients of biotic and physicochemical change. Yet the organization of

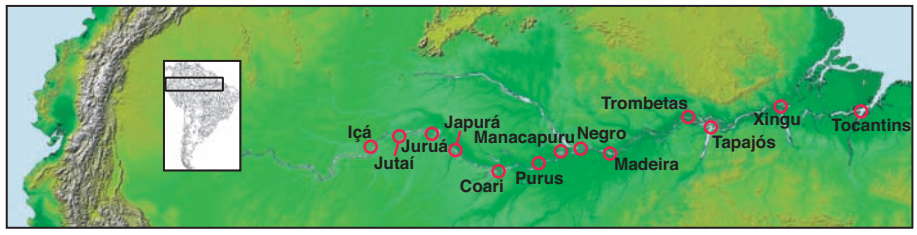

Fig. 1. Map of area sampled, used with permission from the National Aeronautics and Space Administration Jet Propulsion Laboratory. Red circles mark the 13 tributary sites. Samples were taken at three "stations" within each site: (i) within the lower reaches of the tributary, (ii) in the Amazon mainstem, upstream of the tributary confluence, and (iii) in the Amazon mainstem, downstream of the tributary confluence (*16*).

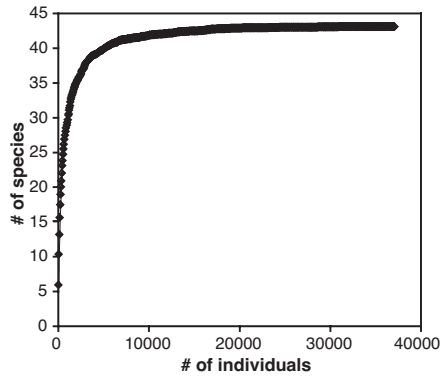

Fig. 2. Estimated species richness, randomized over 50 iterations with EstimateS (*20*), as a function of the number of individuals captured. The asymptote value of 43 species is achieved after about 16,000 individuals.

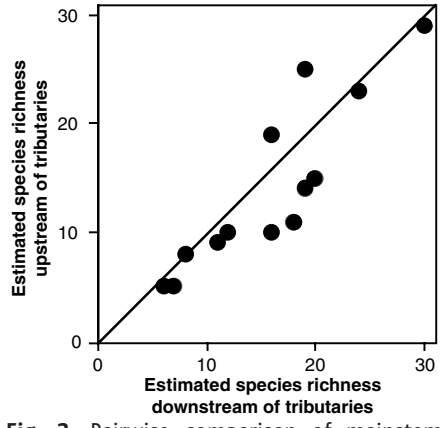

Fig. 3. Pairwise comparison of mainstem electric fish species richness upstream and downstream of 13 tributary confluences. Species richness estimates were calculated with the Coleman rarefaction method (*16*, *20*) (Table 1). Stations downstream of tributaries tended to contain more species than did their respective upstream stations.

Table 1. Sample of electric fishes collected across the 39 collection stations.

Station	*n* trawls	*n* individuals	*n* species	Coleman estimate
Upstream of Içá	49	316	14	14
Içá	49	479	26	23
Downstream of Içá	41	462	21	19
Upstream of Jutaí	34	305	15	11
Jutaí	45	1737	28	15
Downstream of Jutaí	32	103	18	18
Upstream of Juruá	22	17	8	8
Juruá	32	1938	31	13
Downstream of Juruá	25	62	15	8
Upstream of Japurá	9	18	9	9
Japurá	23	1884	25	16
Downstream of Japurá	42	2203	30	11
Upstream of Coari	4	27	5	5
Coari	5	1232	11	7
Downstream of Coari	5	21	7	7
Upstream of Purus	19	231	10	10
Purus	27	2532	31	23
Downstream of Purus	13	808	19	16
Upstream of Manacapuru	5	32	5	5
Manacapuru	5	147	14	8
Downstream of Manacapuru	5	93	9	6
Upstream of Negro	17	746	26	23
Negro	58	3957	34	26
Downstream of Negro	46	497	24	24
Upstream of Madeira	60	1225	29	29
Madeira	63	4806	31	24
Downstream of Madeira	40	1457	31	30
Upstream of Trombetas	34	2761	29	19
Trombetas	67	3937	32	20
Downstream of Trombetas	27	188	16	16
Upstream of Tapajós	37	1087	24	16
Tapajós	38	166	5	5
Downstream of Tapajós	68	919	28	20
Upstream of Xingu	40	669	27	25
Xingu	51	553	25	24
Downstream of Xingu	19	392	21	21
Upstream of Tocantins	14	184	14	10
Tocantins	29	253	13	12
Downstream of Tocantins	3	41	12	12

Amazon River channel fish diversity, at least for electric fishes, shows a large local or "nodal" effect of large tributaries. This pattern is consistent with recent data sets that emphasize river habitat heterogeneity and its influence on species distribution (*6*, *10*, *27*).

One possible explanation for the "tributary effect" we describe here is that tributaries carry nutrients and organic material from terrestrial sources and floodplain lakes into the mainstem (*28*), and may thus provide food and habitat resources for electric fishes. Three major categories of Amazonian tributaries are represented in our sample (*29*): "black water" (Jutaí and Negro), "clear water" (Trombetas, Tapajós, Xingu, and Tocantins), and "white water" (all other tributaries). White waters are comparatively rich in nutrients and invertebrates, such as zooplankton and aquatic insect larvae, on which electric fishes feed (*11*, *28*). The nine westernmost sites (Fig. 1) were uniform in the positive contribution of tributaries to species diversity and composition. All but two of these tributaries, Jutaí and Negro, are white water. In contrast, exceptions to the reported patterns occurred in the four easternmost tributaries, all of which are clear water. Another possible explanation for the tributary effect centers on differences in flow volume and water levels between the Amazon mainstem and its tributaries, which are caused by basinwide seasonal variation in rainfall and flood stages (*30*). Resultant "backwater effects" tend to reduce current speed in the lower reaches of tributaries above their confluences, and might directly increase the density and distribution of food resources.

We found that tributaries enrich the species diversity and composition of Amazon mainstem electric fish communities, particularly in the westernmost white water tributaries. However, at a regional scale along the Amazon, these local increases do not result in an overall accumulation of species from upriver to downriver. Together, these results support the idea that rivers are not homogeneous or graded physical and biological entities (*6*). The generality of the patterns found here for the Amazon remains to be tested with other taxa, including the numerous other fishes collected along with the gymnotiforms.

References and Notes

1. A. R. Wallace, *Proc. Zool. Soc. London* **20**, 107 (1876).
2. J. M. Ayres, T. H. Clutton-Brock, *Am. Nat.* **140**, 531 (1992).
3. A. P. Capparella, *Acta Congr. Int. Ornithol.* **20**, 307 (1991).
4. J. L. Patton, M. N. F. da Silva, J. R. Malcolm, *Bull. Am. Mus. Nat. Hist.* **244**, 1 (2000).
5. J. G. Lundberg *et al.*, in *Phylogeny and Classification of Neotropical Fishes*, L. R. Malabarba, R. E. Reis, R. P. Vari, C. A. S. Lucena, Z. M. S. Lucena, Eds. (Museu de Ciências e Tecnologia, PUCRS, Porto Alegre, Brazil, 1998), pp. 13–48.
6. L. Benda *et al.*, *Bioscience* **54**, 413 (2004).
7. W. J. Matthews, *Patterns in Freshwater Fish Ecology* (Chapman & Hall, New York, 1998).
8. O. T. Gorman, *Am. Nat.* **128**, 611 (1986).
9. L. L. Osborne, M. J. Wiley, *Can. J. Fish. Aquat. Sci.* **49**, 671 (1992).
10. S. P. Rice, M. T. Greenwood, C. B. Joyce, *Can. J. Fish. Aquat. Sci.* **58**, 824 (2001).
11. J. G. Lundberg, W. M. Lewis, J. F. Saunders, F. Mago-Leccia, *Science* **237**, 81 (1987).
12. J. G. Lundberg, M. Kottelat, G. R. Smith, M. L. J. Stiassny, A. C. Gill, *Ann. Missouri Bot. Gard.* **87**, 26 (2000).
13. F. Mago-Leccia, *Electric Fishes of the Continental Waters of America* (Fundacion para el Desarrollo de las Ciencias Fisicas, Caracas, Venezuela, 1994).
14. C. D. Hopkins, *Annu. Rev. Neurosci.* **11**, 497 (1988).
15. S. Kullander, R. Reis, C. Ferraris, *Check List of Freshwater Fishes of South and Central America* (Edipucrs, Porto Alegre, Brazil, 2003).
16. Materials and methods are available as supporting material on *Science* Online.
17. J. G. Lundberg, C. C. Fernandes, J. S. Albert, M. Garcia, *Copeia* **1996**, 657 (1996).
18. C. C. Fernandes, J. G. Lundberg, C. Riginos, *Copeia* **2002**, 52 (2002).
19. C. C. Fernandes, *Copeia* **1998**, 730 (1998).
20. R. Colwell, http://viceroy.eeb.uconn.edu/estimates.
21. D. Stewart, R. E. Barriga-Salazar, M. Ibarra, *Politécnica Ser. Biol.* **1**, 9 (1987).
22. M. Goulding, M. L. Carvalho, E. G. Ferreira, *Rio Negro: Rich Life in Poor Water* (SPB Academic Publishing, The Hague, Netherlands, 1988).
23. L. R. Py-Daniel, C. C. Fernandes, J. A. S. Zuanon, C. P. D. Silva, unpublished data.
24. N. Myers, R. A. Mittermeier, C. G. Mittermeier, G. A. B. da Fonseca, J. Kent, *Nature* **403**, 853 (2000).
25. C. C. Fernandes, *Ecol. Freshw. Fish* **6**, 36 (1997).
26. J. E. Richey, R. L. Victoria, E. Salati, B. R. Forsberg, in *Biogeochemistry of Major World Rivers*, E. T. Degens, S. Kempe, J. E. Richey, Eds. (Wiley, Chichester, UK, 1991), pp. 51–74.
27. M. Ibarra, D. J. Stewart, *Copeia* **1989**, 364 (1989).
28. R. Lowe-McConnell, *Ecological Studies in Tropical Fish Communities* (Cambridge Univ. Press, London, 1987).
29. H. Sioli, in *Coupling of Land and Water Systems*, A. D. Hasler, Ed. (Springer-Verlag, New York, 1975), pp. 199–213.
30. R. H. Meade, J. M. Rayol, S. C. da Conceição, J. R. G. Natividade, *Environ. Geol. Water Sci.* **18**, 105 (1991).

31. We thank R. Colwell for guidance with statistical analyses. Fieldwork ("Calhamazon Project") supported by grants to C.C.F. from the Instituto Nacional de Pesquisas da Amazônia (INPA), Programa RHAE-INPA-CNPq, and a Mellon Foundation Grant to the Duke University–University of North Carolina Latin American Studies Program, and by grants to J.G.L. from NSF and by the Office of Forestry, Environment, and Natural Resources, Bureau of Science and Technology, of the U.S. Agency for the International Development under DEB-9300151, DEB-0089612, and the Charles A. Lindbergh Foundation (INT-9213839). We dedicate this paper to the memory of F. Mago-Leccia and C. A. R. M. Araujo-Lima.

Supporting Online Material

www.sciencemag.org/cgi/content/full/305/5692/1960/DC1
Materials and Methods
Tables S1 to S3
References

8 June 2004; accepted 29 July 2004

Soma–Germ Line Competition for Lipid Phosphate Uptake Regulates Germ Cell Migration and Survival

A. D. Renault,[1] Y. J. Sigal,[2] A. J. Morris,[2] R. Lehmann[1]*

Lipid phosphates can act as signaling molecules to influence cell division, apoptosis, and migration. *wunen* and *wunen2* encode *Drosophila* lipid phosphate phosphohydrolases, integral membrane enzymes that dephosphorylate extracellular lipid phosphates. *wun* and *wun2* act redundantly in somatic tissues to repel migrating germ cells, although the mechanism by which germ cells respond is unclear. Here, we report that *wun2* also functions in germ cells, enabling them to perceive the *wun/wun2*–related signal from the soma. Upon Wun2 expression, cultured insect cells dephosphorylate and internalize exogenously supplied lipid phosphate. We propose that *Drosophila* germ cell migration and survival are controlled by competition for hydrolysis of a lipid phosphate between germ cells and soma.

Extracellular lipid phosphates influence proliferation, programmed cell death, and the migration of various cell types. For example, lysophosphatidic acid (LPA) and sphingosine 1-phosphate (S1P) are secreted by stimulated platelet cells leading to migratory and proliferative effects on smooth muscle cells, endothelial cells, and white blood cells (*1*, *2*). Signaling by means of such lipid phosphates not only is vital to normal development (*3*, *4*) but also contributes to the progression of diseases such as tumorigenesis and atherosclerosis (*5*, *6*).

In *Drosophila*, extracellular lipid phosphates have been implicated in guiding germ cell migration (*7*, *8*). As in most organisms, *Drosophila* germ cells form spatially and temporally separate from the somatic cells of the gonad and must migrate through the embryo to associate with them (*9*). *Drosophila* germ cells form at the syncytial blastoderm stage, and during gastrulation they are carried into the posterior midgut pocket where they actively migrate through the midgut epithelium. Once on the basal side of the midgut, they reorient dorsally, which is important for the subsequent migration into the mesoderm, where they associate with the somatic gonadal precursors (SGPs).

The dorsal reorientation after crossing the gut results from the repellent activity of two redundant genes, *wunen* (*wun*) and *wunen2* (*wun2*), which are zygotically expressed in regions of the midgut that germ cells avoid (fig. S1A) (*7*, *8*). In embryos with no *wun* and *wun2* in somatic tissues, most germ cells fail to reach the SGPs and instead scatter throughout the embryo (*7*, *8*). In contrast, overexpression of either *wun* or *wun2* in somatic tissues results in germ cell death (*7*).

wun and *wun2* encode lipid phosphate phosphohydrolases (LPPs), membrane enzymes that dephosphorylate extracellular lipid phosphates. There are three mammalian LPPs (*10*), and human LPP3 (hLPP3), but not mouse LPP1 (mLPP1), is able to kill *Drosophila* germ cells when it is overexpressed in the soma (*11*). Although in vivo substrates for LPPs are yet to be confirmed, in vitro substrates include the bioactive lipids S1P, LPA, phosphatidic acid (PA), and ceramide 1-phosphate (*10*).

Key to understanding the effects of these lipids is the identification of their receptors and downstream pathways. Mammalian cells respond to S1P and LPA through the G protein–coupled receptors (GPCRs) $S1P_{1\text{-}5}$ and $LPA_{1\text{-}4}$, respectively (*12*). Although LPPs are found in vertebrates, insects, and worms, these GPCRs seem to be restricted to vertebrates (*13*), raising the possibility that additional lipid phosphate signaling pathways exist. While screening for such pathways in *Drosophila* germ cells, we noticed that *wun2* RNA, but not *wun*, is expressed in early germ cells (*14*). This expression is presumably due to selective stabilization of the maternal RNA, because early germ cells are transcriptionally inactive (*15*).

To test whether maternal *wun2* expression is necessary for germ cell formation, migration, or survival, we generated a *wun2*-null allele (*16*) (fig. S1B). We examined embryos laid by *wun2*-null females, which cannot supply *wun2* expression to the germ cells, and used the paternal chromosome to supply zygotic *wun* and *wun2* expression to the soma. Such embryos formed normal numbers of germ cells, but their numbers dropped from more than 30 to 9, on average, by late embryogenesis (Fig. 1, A, C, and F). The death phenotype is nonapoptotic and results specifically from the lack of maternal *wun2* and not *wun* (see SOM Text).

To determine whether the germ cell death caused by lack of maternal *wun2* reflects a requirement for *wun2* in germ cells or soma, we used the *nanos::*GAL4VP16 driver (*17*) to express *wun2* specifically in germ cells. We found that germ cell expression of *wun2* was sufficient to rescue germ cell death in embryos laid by *wun2*-null mothers (Fig. 1J). Overexpression of *wun2* in germ cells using this driver in a wild-type background caused slight migration defects (*7*), explaining the imperfect migration observed in the rescued embryos. In addition, we found that germ cell expression of *wun2* Y225W (*7*) (which contains a control substitution in a nonconserved residue), *wun*, and hLPP3 was able to rescue the death but that expression of *wun2* H326K (a catalytically dead mutant form of *wun2*) or mLPP1 was not. This result indicates that the ability to function in germ cells parallels the ability to act in the soma (Fig. 1, H to M). We conclude that catalytically active *wun2* is required in germ cells for their survival and that *wun* and hLPP3 can substitute for its function.

To test how the requirement of *wun2* in germ cells relates to the function of *wun/wun2* in the soma, we examined the behavior of *wun2*-null germ cells in embryos lacking somatic expression of *wun/wun2*. In such embryos, the germ cells showed only a slight reduction in number, comparable to the normal decrease seen in wild-type embryos (Fig. 1, A, D, and G). Although some germ cells migrated to the gonad, most were scattered, resembling the zygotic *wun/wun2* loss of function phenotype in which germ cells scatter but survive (*8*). Thus, death of *wun2*-null germ cells can be rescued by a reduction in the somatic expression of *wun/wun2* (compare Fig. 1, F and G). To further examine the relationship between somatic and germ cell Wunens, we examined whether we could suppress the germ cell death resulting from somatic overexpression of *wun2*. We found that germ cell expression of *wun*, *wun2*, *wun2* Y225W, and hLPP3, but not *wun2* H326K or mLPP1, could suppress the death from *wun2* overexpression in the soma (Fig. 2).

Our data show that the same molecule has opposite effects on germ cell survival: Wun2 in germ cells protects them from death, whereas Wun/Wun2 in somatic cells repels and kills germ cells. In both germ and somatic cells, the effect of Wun2 on germ

[1]Howard Hughes Medical Institute, Developmental Genetics Program, Skirball Institute and Department of Cell Biology, New York University School of Medicine, 540 First Avenue, New York, NY 10016, USA. [2]Department of Cell and Developmental Biology, Room 522, Taylor Hall, CB#7090, University of North Carolina at Chapel Hill, Chapel Hill, NC 27599–7090, USA.

*To whom correspondence should be addressed. E-mail address: lehmann@saturn.med.nyu.edu

cell survival requires its phosphatase activity. Furthermore, there is a direct and dose-sensitive relationship between somatic and germ cell Wunens: Germ cell death resulting from lack of germ cell *wun2* can be rescued by reducing somatic *wun/wun2* (Fig. 1, A, F, and G), and germ cell death resulting from somatic overexpression of *wun2* can be suppressed by increasing germ cell *wun2* expression (Fig. 2). These data strongly argue that germ cell *wun2* and somatic *wun/wun2* share the same function and are consistent with a model in which the soma and the germ cells compete for a common *wun/wun2* substrate that is required to allow germ cells to survive.

To explore how Wun2 might be acting in germ cells to regulate their survival, we examined Wun2 biochemical activity. We expressed Wun2 in insect Hi5 cells and, using membrane fractions, determined that Wun2 dephosphorylates PA and LPA in vitro, similar to hLPP1 (table S1) and Wun (*11*). The predicted catalytically null Wun2 mutant forms, H274K or H326K, exhibited no phosphatase activity, whereas the non-conserved substitution, Y225W, retained high phosphatase activity (table S1). We then analyzed the fate of such lipids using intact Hi5 cells and a PA analog, 1-Oleoyl-2-[6-[(7-nitro-2-1,3-benzoxadiazol-4-yl)amino]hexanoyl]-sn-Glycerol-3-Phosphate (NBD-PA), that is fluorescently labeled on its lipid moiety (*16*). We found that cell-associated fluorescence increased by a factor of 3 to 4 in Wun2 wild-type or Wun2 Y225W–expressing cells compared with control (Fig. 3). Expression of Wun2

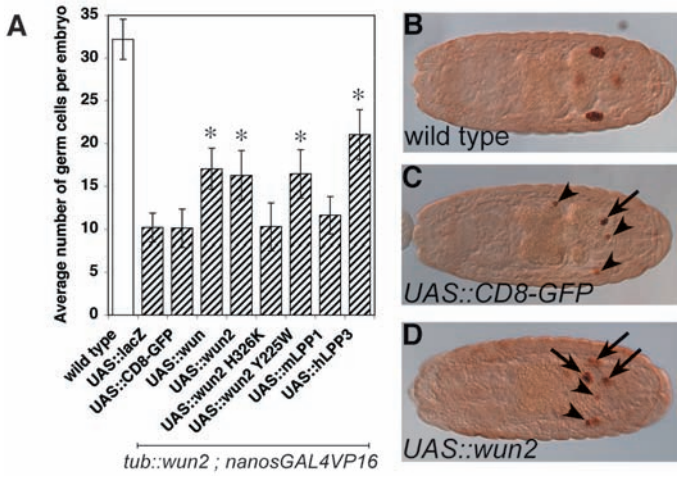

Fig. 2. Suppression of germ cell death due to *wun2* overexpression in soma. Constitutively overexpressed somatic *wun2* (from *tubulin::wun2* transgene) kills germ cells. (**A**) Graph showing average number of germ cells in stage 15 and 16 wild-type (white bar) and *tubulin::wun2* embryos misexpressing various genes (as UAS lines) in germ cells using the *nanos::GAL4VP16* driver (shaded bars). Significant differences relative to the control *UAS::CD8-GFP* [analysis of variance (ANOVA), $P < 0.01$] are indicated with an asterisk. Note the partial rescue of number of germ cells when *wun*, *wun2*, and hLPP3, but not mLPP1 or *wun2* H326K, are misexpressed in germ cells. (**B** to **D**) Stage 16 embryos with germ cells in brown (dorsal view, anterior left). (B) Wild-type embryo. Expression of *wun2* (D) compared with the control CD8-GFP (C) in germ cells partially suppresses the germ cell death in *tubulin::wun2* embryos. Germ cells are found singly (arrowhead) or clumped together (arrow), often associated with the gut. Not all germ cells are in the focal plane shown.

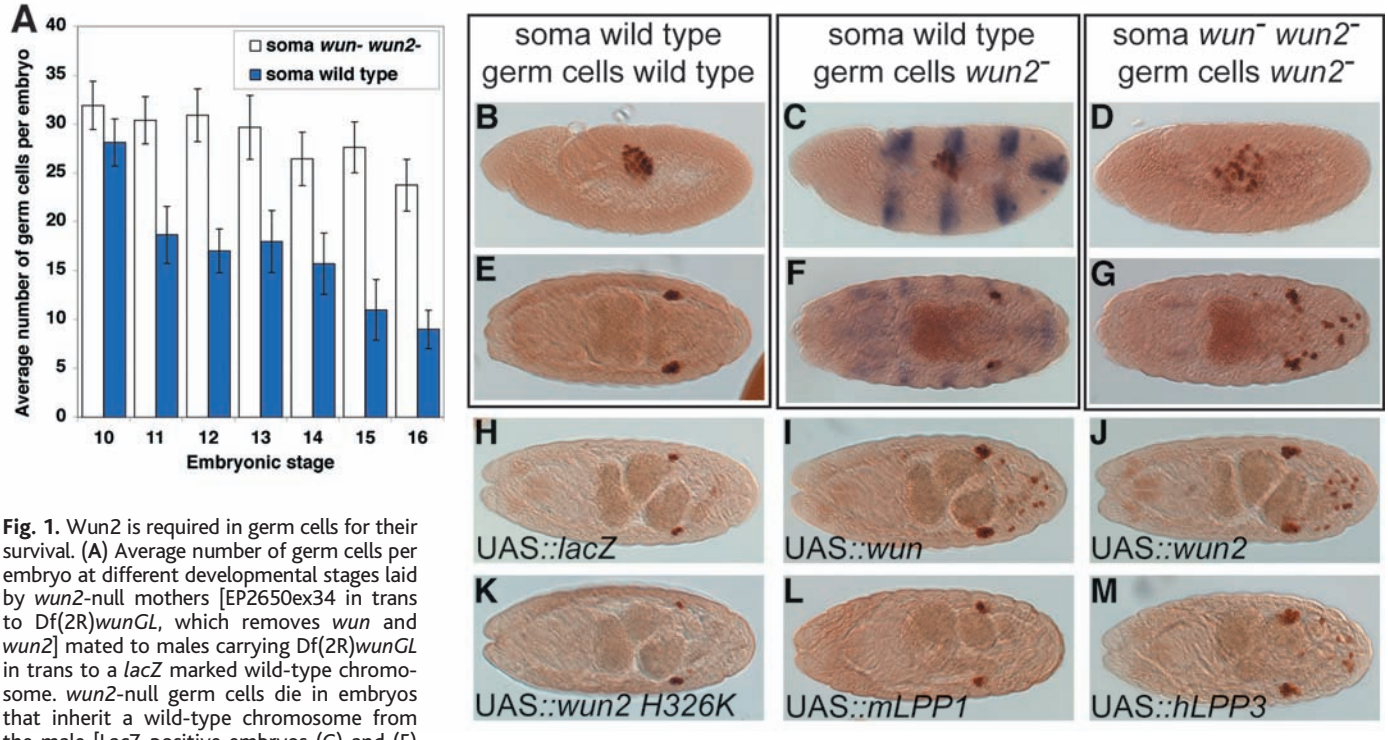

Fig. 1. Wun2 is required in germ cells for their survival. (**A**) Average number of germ cells per embryo at different developmental stages laid by *wun2*-null mothers [EP2650ex34 in trans to Df(2R)*wunGL*, which removes *wun* and *wun2*] mated to males carrying Df(2R)*wunGL* in trans to a *lacZ* marked wild-type chromosome. *wun2*-null germ cells die in embryos that inherit a wild-type chromosome from the male [LacZ-positive embryos (C) and (F) and blue bars in (A)], whose soma expresses *wun/wun2* zygotically. Some germ cells survive and reach the gonad, but this survival does not depend on SGPs (see SOM Text). However, *wun2*-null germ cells survive but mismigrate in embryos that inherit the Df(2R)*wunGL* chromosome from the male [LacZ-negative embryos (D) and (G) and white bars in (A)], whose soma cannot express *wun/wun2* zygotically. (B to M) *Drosophila* embryos (anterior left) with Vasa-stained germ cells (brown). (**B** and **E**) Wild-type embryos. (**C**, **D**, **F**, and **G**) Embryos from cross described for (A), also stained for lacZ (blue). (B to D) Stage 10 lateral view. (E to G) Stage 15 dorsal view. (**H** to **M**) Stage 16 embryos (dorsal view) laid by *wun2*-null mothers also containing the germ cell driver *nanos::GAL4VP16* mated to *UAS::lacZ* (H), *UAS::wun* (I), *UAS::wun2* (J), *UAS::wun2 H326K* (K), *UAS::mLPP1* (L), and *UAS::hLPP3* (M) males.

H274K or H326K did not result in any increase in cell-associated fluorescence compared with the control (Fig. 3). We analyzed the localization of the internalized lipid and found that Wun2 promotes its rapid accumulation in the cytoplasm, similar to hLPP1 (fig. S3, C and E). Wun2 therefore confers the ability of cells to internalize lipid substrates concurrent with dephosphorylation.

We suggest that Wun2 function in germ cells is to uptake a lipid by dephosphorylation and that this lipid, or a metabolite, is responsible for the survival of germ cells by binding an intracellular or membrane-bound target (Fig. 4A). Germ cells are unique in requiring this lipid for their survival, whereas the somatic cells do not (*18*). We further propose that through their restricted expression pattern, the function of somatic *wun/wun2* is to create a gradient of lipid phosphate that provides directional cues to the germ cells. Regions of high *wun/wun2* expression correlate with lowest levels of lipid phosphate and are therefore unfavorable for germ cell survival. Germ cells follow the lipid phosphate gradient and migrate away from *wun/wun2*–expressing somatic cells (Fig. 4A) (*18*). For *wun2*-null germ cells, if the soma expresses *wun/wun2*, the common phospholipid pool is depleted and germ cells die (Fig. 4C). If, on the other hand, the soma lacks *wun/wun2*, lipid phosphate levels remain high throughout the embryo and germ cells survive but mismigrate as a result of the loss of a gradient, which provided the spatial cues needed for correct migration (Fig. 4D). The fact that *wun2*-null germ cells survive in the absence of somatic *wun/wun2* further suggests that at high phospholipid levels alternate mechanisms for lipid uptake may exist.

We propose that germ cell survival is controlled through competition between somatic and germ cell Wunens for an extracellular lipid phosphate. Because the same genes have opposite effects on germ cell survival when expressed in the germ line and soma, our observations represent a novel paradigm for cell survival and migration. It had been assumed that all lipid phosphate signaling occurs through GPCRs, but our data suggest an alternate or parallel pathway through which lipid phosphates can signal, namely by means of internalization through dephosphorylation by LPPs. This pathway may be conserved in vertebrates because the mitogenic responses of some mammalian cells to LPA are inconsistent with GPCR receptor activation (*19*). In *Drosophila*, this pathway shows remarkable specificity for germ cell survival, because somatic cells seem to be insensitive to *wun/wun2* levels (*18*). Although it is clear that *wun* and *wun2* are critical in controlling germ cell migration and survival, their function is likely to be redundant with other pathways such as *Hmgcr* (*20*), as demonstrated by the ability of some germ cells to reach the gonad even in the absence of *wun/wun2* signaling.

Recent studies have revealed striking similarities between the guidance cues regulating germ cell migration in *Drosophila* and vertebrates (*9*). Mouse germ cells also express an LPP (*21*), and analysis of its function may reveal further parallels between early germ cell behavior in flies and mice.

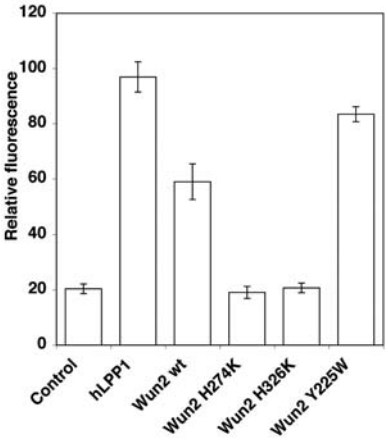

Fig. 3. Catalytically active Wun2 confers lipid uptake ability. Relative fluorescence of Hi5 cells after exposure to the fluorescent PA analog NBD-PA, expressing a control protein, hLPP1, wild-type or mutant forms of Wun2, including H274K and H326K (catalytically dead), or Y225W (catalytically active).

References and Notes

1. T. Eichholtz, K. Jalink, I. Fahrenfort, W. H. Moolenaar, *Biochem. J.* **291**, 677 (1993).
2. Y. Yatomi, F. Ruan, S. Hakomori, Y. Igarashi, *Blood* **86**, 193 (1995).
3. I. Ishii *et al.*, *J. Biol. Chem.* **277**, 25152 (2002).
4. D. Escalante-Alcalde *et al.*, *Development* **130**, 4623 (2003).
5. G. B. Mills, W. H. Moolenaar, *Nature Rev. Cancer* **3**, 582 (2003).
6. W. Siess, *Biochim. Biophys. Acta* **1582**, 204 (2002).
7. M. Starz-Gaiano, N. K. Cho, A. Forbes, R. Lehmann, *Development* **128**, 983 (2001).
8. N. Zhang, J. Zhang, K. J. Purcell, Y. Cheng, K. Howard, *Nature* **385**, 64 (1997).
9. A. C. Santos, R. Lehmann, *Curr. Biol.* **14**, R578 (2004).
10. R. Roberts, V. A. Sciorra, A. J. Morris, *J. Biol. Chem.* **273**, 22059 (1998).
11. C. Burnett, K. Howard, *EMBO Rep.* **4**, 793 (2003).
12. W. H. Moolenaar, *Exp. Cell Res.* **253**, 230 (1999).

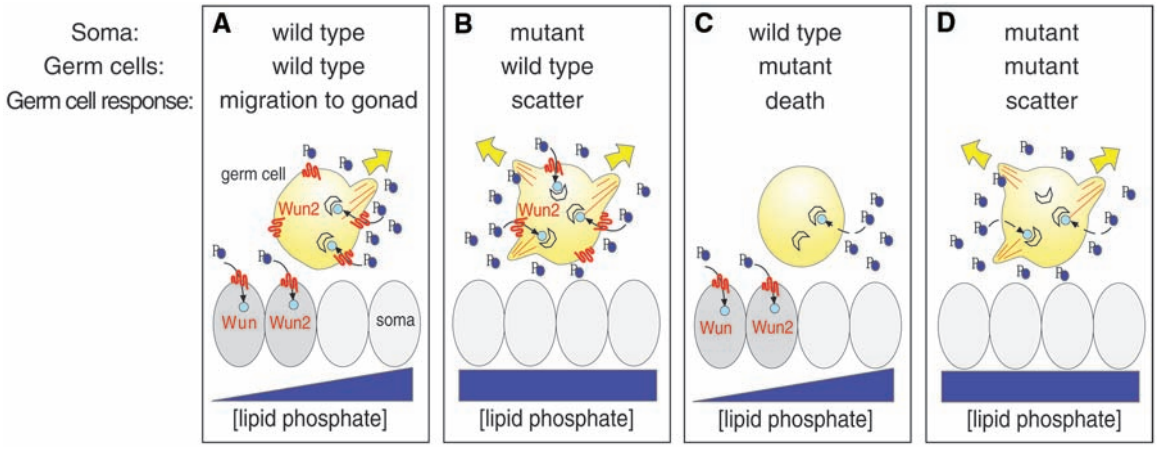

Fig. 4. Germ line–soma competition model for *wun2* function in germ cell migration and survival. In wild-type embryos (**A**), a gradient of a lipid phosphate (blue) attractant is established by restricted expression of somatic Wun/Wun2 through dephosphorylation. Germ cells express Wun2 and compete with the soma for this lipid phosphate. Germ cell Wun2 perceives lipid phosphate levels by dephosphorylation-dependent internalization of the lipid moiety (light blue) activating an intracellular pathway (open half moon). The germ cells migrate toward higher concentrations of lipid phosphate (arrow). In embryos with wild-type germ cells and *wun/wun2* mutant soma (**B**), germ cells mismigrate due to lack of lipid phosphate gradient. In embryos with *wun2*-null germ cells and wild-type soma (**C**), germ cells die because they are unable to compete with the soma, which is depleting lipid phosphate levels. In embryos with *wun2*-null germ cells and *wun/wun2* mutant soma (**D**), germ cells survive because the soma is no longer depleting lipid phosphate levels. The loss of directional cues from the lipid phosphate gradient leads to germ cell scattering. The mechanism by which germ cells perceive lipid phosphate levels independent of *wun2* is not known.

13. J. Chun *et al.*, *Pharmacol. Rev.* **54**, 265 (2002).
14. A. D. Renault, M. Starz-Gaiano, R. Lehmann, *Mech. Dev.* **119**, (Suppl 1), S293 (2002).
15. R. G. Martinho, P. S. Kunwar, J. Casanova, R. Lehmann, *Curr. Biol.* **14**, 159 (2004).
16. Materials and methods are available as supporting material on *Science* Online.
17. M. Van Doren, A. L. Williamson, R. Lehmann, *Curr. Biol.* **8**, 243 (1998).
18. For further discussion of dependence on lipid phosphate in germ cells versus soma and the lipid phosphate attractant model, see SOM Text.
19. S. B. Hooks *et al.*, *J. Biol. Chem.* **276**, 4611 (2001).
20. M. Van Doren, H. T. Broihier, L. A. Moore, R. Lehmann, *Nature* **396**, 466 (1998).
21. C. Wylie, LPP1, personal communication.
22. We thank Lehmann lab members and the fly community for stocks and constructs. This work was supported by NIH grants HD421900 RO1 to R.L. and GM54388 to A.J.M. Y.J.S. is an American Heart Association Predoctoral Fellow. A.D.R. is a Howard Hughes Medical Institute (HHMI) research associate. R.L. is an HHMI investigator.

Supporting Online Material
www.sciencemag.org/cgi/content/full/1102421/DC1
Materials and Methods
SOM Text
Figs. S1 to S4
Table S1
References

7 July 2004; accepted 9 August 2004
Published online 26 August 2004;
10.1126/science.1102421
Include this information when citing this paper.

The Genomic Sequence of the Accidental Pathogen *Legionella pneumophila*

Minchen Chien,[1]* Irina Morozova,[1]* Shundi Shi,[1]* Huitao Sheng,[1] Jing Chen,[1] Shawn M. Gomez,[2] Gifty Asamani,[1] Kendra Hill,[1] John Nuara,[1] Marc Feder,[1] Justin Rineer,[1] Joseph J. Greenberg,[1] Valeria Steshenko,[1] Samantha H. Park,[1] Baohui Zhao,[3] Elita Teplitskaya,[1] John R. Edwards,[1,4] Sergey Pampou,[1] Anthi Georghiou,[1] I.-Chun Chou,[1] William Iannuccilli,[1] Michael E. Ulz,[1] Dae H. Kim,[1] Alex Geringer-Sameth,[1] Curtis Goldsberry,[1] Pavel Morozov,[1] Stuart G. Fischer,[1] Gil Segal,[5] Xiaoyan Qu,[1] Andrey Rzhetsky,[1] Peisen Zhang,[1] Eftihia Cayanis,[1] Pieter J. De Jong,[3]† Jingyue Ju,[1,4] Sergey Kalachikov,[1] Howard A. Shuman,[6] James J. Russo[1]‡

We present the genomic sequence of *Legionella pneumophila*, the bacterial agent of Legionnaires' disease, a potentially fatal pneumonia acquired from aerosolized contaminated fresh water. The genome includes a 45–kilobase pair element that can exist in chromosomal and episomal forms, selective expansions of important gene families, genes for unexpected metabolic pathways, and previously unknown candidate virulence determinants. We highlight the genes that may account for *Legionella*'s ability to survive in protozoa, mammalian macrophages, and inhospitable environmental niches and that may define new therapeutic targets.

Legionella pneumophila was recognized as a human opportunistic pathogen after its isolation from patients in an outbreak of fatal pneumonia (Legionnaires' disease) at an American Legion convention in Philadelphia (*1*). *L. pneumophila* and other members of the genus are found within biofilms and fresh and industrial water systems worldwide, posing a significant public health concern. Inhaled *Legionella* spp. cause sporadic and epidemic cases of Legionnaires' disease and the flu-like Pontiac fever (*2*).

L. pneumophila are aerobic Gram-negative, motile, rod-shaped bacteria of the γ-proteobacterial lineage. These intracellular pathogens use the Icm/Dot type IVB secretion system (*3*, *4*) to deliver effector proteins to the host cells (*5*–*7*) that modulate the fate of the phagocytic vacuole by preventing phagosome-lysosome fusion and vacuole acidification, and recruiting vesicles that confer on it properties of the endoplasmic reticulum (*8*). After proliferating within this compartment, the bacteria destroy the host cell and infect other cells.

The most intriguing aspects of *L. pneumophila* biology are its extraordinary ability to commandeer the organelle trafficking systems of a wide range of host cells and its ability to survive in harsh environments such as plumbing systems treated with potent biocides. *Legionella* species are denizens of soil and water with life-styles ranging from highly virulent (*L. pneumophila*) to non-pathogenic (protozoan symbionts) (*2*). Genomic comparisons permit the development of testable models for the molecular bases of these properties of *Legionella* spp. and their ability to adapt to different niches.

The genome of *L. pneumophila* subsp. *pneumophila* (serogroup 1), Philadelphia 1 strain, derived from the original 1976 isolate, consists of a single circular chromosome of 3,397,754 base pairs (bp) (GenBank accession code AE017354) with 38% G+C content (Fig. 1 and table S1) (*9*, *10*).

As expected for an intracellular pathogen, examination of its genome indicates that *L. pneumophila* has undergone horizontal gene transfer. Several homologs of eukaryotic genes were identified (*11*), including the previously described *ralF* gene, encoding a guanosine triphosphatase (GTPase) modifier required for recruiting the ADP ribosylation factor (ARF) GTPase to the *Legionella*-containing vacuole (*8*). Some phage-derived and insertion sequences, constituting ~2.4% of the genome, are dispersed throughout the genome; others form nine clusters in addition to two loci containing the *icm/dot* genes encoding the type IVB secretion system (*12*, *13*), the *lvh/lvr* cluster encoding a typical type IV secretion system (*14*), and a region containing F plasmid–derived *tra/trb* genes (*15*).

The Philadelphia 1 strain possesses a plasmid-like element of 45 kbp (pLP45) that exists in a circular episomal form or within the chromosome. The *lvh/lvr* gene region, one of the few extensive loci with an elevated G+C content (fig. S5), is found within this element, along with genes potentially involved in DNA recombination. We identified a 100-kb region (fig. S5) containing several genes encoding efflux transporters for heavy metals and other toxic substances. The presence of tRNA, phage-related genes, and transposase genes near the extremities of this region suggest that it was acquired via horizontal transfer. This "efflux island" may contribute to *Legionella*'s ability to flourish in plumbing sys-

[1]Columbia Genome Center, Columbia University College of Physicians and Surgeons, New York, NY 10032, USA. [2]Unite de Biochimie et Biologie Moleculaire des Insectes, Institut Pasteur, Paris 75015 France. [3]BACPAC Resources Laboratory, Roswell Park Cancer Institute, Buffalo, NY 14263, USA. [4]Department of Chemical Engineering, The Fu Foundation School of Engineering and Applied Science, Columbia University, New York, NY 10027, USA. [5]Department of Molecular Microbiology and Biotechnology, Tel Aviv University, Tel Aviv 69978, Israel. [6]Department of Microbiology, Columbia University College of Physicians and Surgeons, New York, NY 10032, USA.

*These authors contributed equally to this work.
†Present address: BACPAC Resources Center, Children's Hospital Oakland Research Institute, Oakland, CA 94609, USA.
‡To whom correspondence should be addressed. E-mail: jjr4@columbia.edu

tems and persist in the presence of toxic biocides.

The fully sequenced species most closely related to *L. pneumophila* is the obligate intracellular pathogen *Coxiella burnettii*, also belonging to the order Legionellales. Its proteome has a high number of basic proteins, which may explain its ability to replicate within phagolysosomes (*16*). *L. pneumophila* replicates in a vacuole resembling the endoplasmic reticulum; its proteome has a lower average isoelectric point (*9*). Altogether, *Legionella* shares ~42% of its genes with *Coxiella* despite differences in genome size (3.4 and 1.9 Mbp, respectively). To date the *icm/dot* genes have been found only in *Legionella* spp. and *C. burnettii*. Out of several identified *L. pneumophila* effectors delivered by the Icm/Dot system, only the recently described *sid* genes (*6*) have counterparts in *C. burnetii*. Very few other genes are shared exclusively by *L. pneumophila* and *C. burnettii* [the only named genes are the "enhanced entry" genes *enhA* and *enhB* (*17*)], implying that specific regulatory circuits or transport capabilities determine the features that distinguish them from other bacteria (table S2).

Of *Legionella*'s gene complement, 60% of the genes have homologs among phylogenetically diverse intracellular bacteria (*Coxiella*, *Salmonella*, *Chlamydia*, *Rickettsia*, *Brucella*, and *Mycobacterium* species), comparable to the 63% found in seven fully sequenced related γ-proteobacteria, suggesting that the species' similar life-styles and common origin may equally affect gene complement similarity.

Paralogous gene family expansions may be associated with adaptation to specific environments, development of novel life strategies, or other species-specific adaptations. In a search for *Legionella* gene family expansions relative to other bacterial genomes (table S3), we identified several examples including β-lactamase, factor for inversion stimulation, and some transporters (*9*), even though overall *Legionella* does not display a high genome redundancy, as judged by its modest average gene family expansion rate. Among intracellular pathogens, *Legionella* groups with *Brucella melitensis* and *Salmonella* species (table S4), whereas reduced genome organisms (e.g., *Rickettsia* and *Coxiella*) exhibit low expansion values, and *M. tuberculosis* contains many expanded gene families including several related to lipid synthesis.

Legionella has multiple family members for genes encoding enhanced entry proteins, peptide methionine sulfoxide reductase, zinc metalloproteases, polyhydroxyalkanoic acid synthase, transposases, and effectors. The Sid effectors, identified on the basis of their ability to be transferred to another cell via the Icm/Dot type IVB system (*6*), form three families in *L. pneumophila*.

Legionella survives and replicates in axenic cultures, fresh water, soil, and in biofilms with other organisms, as well as within intracellular vacuoles of amoebae, ciliates, and human cells. To best utilize the nutrients within these diverse environments, the bacteria would need a broad range of membrane transporters. We identified more than 350 binding proteins and permeases in the *Legionella* genome, representing 62 separate substrate classes.

Among its many multidrug transporters, there is an expanded 11-member major facilitator family in *Legionella*. Nine similar proteins occur in *C. burnetii*, which has an unusually high overall density of multidrug transporters in its genome (*18*), but no clear-cut representatives of this particular family exist in other intracellular pathogens or in the substantially larger genomes of *Escherichia coli*, *Salmonella typhimurium*, and *Pseudomonas aeruginosa*. *L. pneumophila* has more members of not only this particular gene family, but of multidrug transporters as a general class. It has an unusually high number of genes encoding putative effluxers for toxic compounds and heavy metals relative to other γ-proteobacteria, perhaps because the natural protozoan hosts for *Legionella* accumulate heavy metals, including lead and cadmium, from the environment (*19*).

A family of four glutamate/γ-aminobutyrate–specific amino acid antiporters is apparently represented by two members in *Coxiella* and only one member in 10 other species examined (GadC in *E. coli*). This antiporter is involved in bacterial survival within acidic environments (*20*); its possible functional redundancy may account for the suggested ability of *L. pneumophila* to survive in a putative acidic compartment late in its life cycle (*16*).

Because *L. pneumophila* utilizes amino acids as carbon and energy sources and cannot ferment or oxidize carbohydrates (*21*), we were surprised to find an intact glycolytic chain, pyruvate dehydrogenase complex, tricarboxylic acid cycle and respiratory chain, and a glucose-6-phosphate

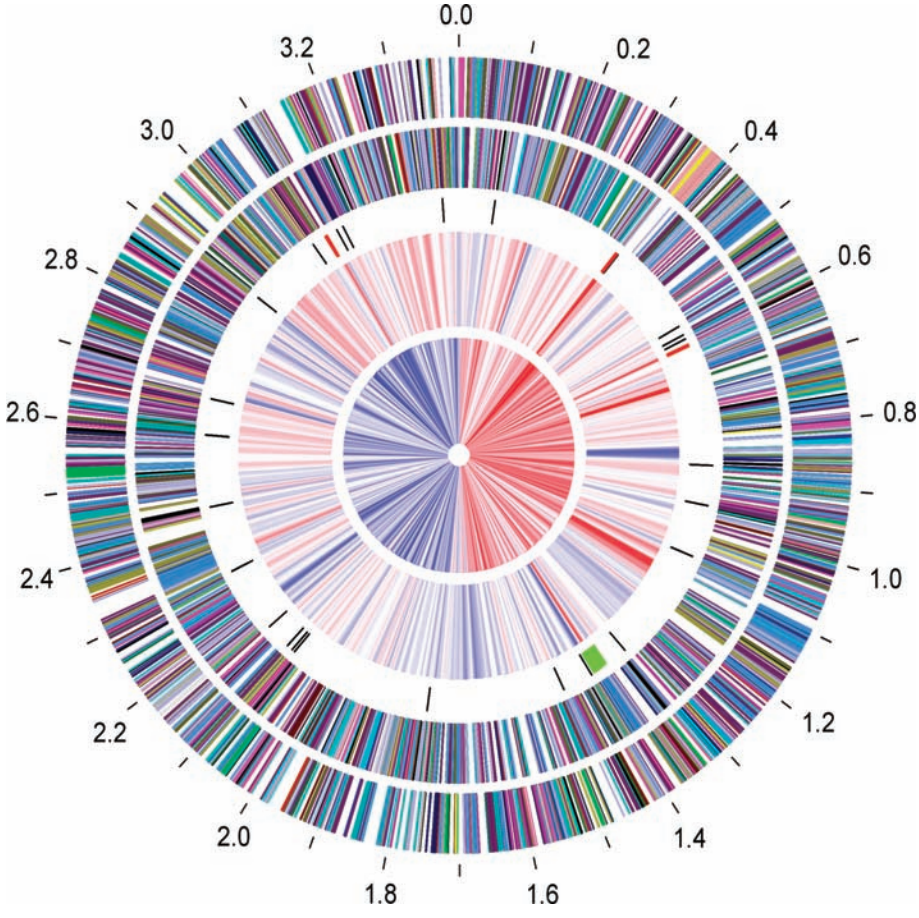

Fig. 1. Circular map of *L. pneumophila* genome. Circles from outside in: gene distribution on the forward (1) and reverse (2) strands (fig. S6), color-coded according to function (fig. S2). (3) tRNA (black) and rRNA (red) genes and the chromosomal plasmid-like pLP45 region (green). (4) G+C content, lower (blue) and higher (red) than genome average. (5) GC-skew. *oriC* was positioned in the *rpmH-dnaA* intergenic region (figs. S3 and S4). Other regions of interest are shown in fig. S5.

transporter. Perhaps these pathways are used when bacteria are exposed to the complex molecular content of intracellular organelles of host cells or potentially nutrient-rich biofilms. *Legionella* is reportedly auxotrophic for several amino acids, so it was surprising to find potential genes for their synthetic pathways: cysteine from pyruvate or serine, methionine from cysteine, and both phenylalanine and tyrosine from phosphoenolpyruvate. Even if some of these genes are not expressed under laboratory growth conditions, their presence presumably relates to the organism's ability to persist in diverse environments.

In addition to previously recognized virulence factors (table S5), we identified new candidates (table S6), including homologs of genes encoding virulence functions in other bacteria. Moreover, ~145 apparent secreted or membrane proteases and other hydrolases, some of which may function as virulence factors, exist in *L. pneumophila*. Among fully sequenced organisms, this is exceeded only by the predatory *Bdellovibrio* (*22*). *L. pneumophila* has been proposed to utilize bacterial-induced apoptotic (early) and/or necrotic pore-forming (late) events to exit infected hosts (*23*); its putative hydrolases may be involved in these processes.

The genome sequence of *L. pneumophila* offers the opportunity to explain its broad host range and extraordinary ability to resist eradication in water supplies. Having lists of genes unique to *Legionella* or shared with unrelated bacteria with similar life-styles, it should now be possible to determine experimentally which of them distinguish *Legionella* species displaying different host preferences or pathogenicity.

References and Notes

1. D. W. Fraser *et al.*, *J. Med.* **297**, 1189 (1977).
2. B. S. Fields, R. F. Benson, R. E. Besser, *Clin. Microbiol. Rev.* **15**, 506 (2002).
3. D. S. Zamboni, S. McGrath, M. Rabinovitch, C. R. Roy, *Mol. Microbiol.* **49**, 965 (2003).
4. T. Zusman, G. Yerushalmi, G. Segal, *Infect. Immun.* **71**, 3714 (2003).
5. H. Nagai, J. C. Kagan, X. Zhu, R. A. Kahn, C. R. Roy, *Science* **295**, 679 (2002).
6. Z.-Q. Luo, R. R. Isberg, *Proc. Natl. Acad. Sci. U.S.A.* **101**, 841 (2004).
7. J. Chen *et al.*, *Science* **303**, 1358 (2004).
8. H. Nagai, C. R. Roy, *Cell. Microbiol.* **5**, 373 (2003).
9. Supporting materials are available on *Science* Online.
10. Additional details are at http://legionella.cu-genome.org/annotation/annotation.html.
11. K. Suwwan de Felipe, S. Pampou, S. Kalachikov, H. A. Shuman, unpublished data.
12. G. Segal, M. Purcell, H. A. Shuman, *Proc. Natl. Acad. Sci. U.S.A.* **95**, 1669 (1998).
13. J. P. Vogel, H. L. Andrews, S. K. Wong, R. R. Isberg, *Science* **279**, 873 (1998).
14. G. Segal, J. J. Russo, H. A. Shuman, *Mol. Microbiol.* **34**, 799 (1999).
15. A. K. Brassinga *et al.*, *J. Bacteriol.* **185**, 4630 (2003).
16. S. Sturgill-Koszycki, M. S. Swanson, *J. Exp. Med.* **192**, 1261 (2000).
17. S. L. Cirillo, J. Lum, J. D. Cirillo, *Microbiology* **146**, 1345 (2000).
18. R. Seshadri *et al.*, *Proc. Natl. Acad. Sci. U.S.A.* **100**, 5455 (2003).
19. G. Fernandez-Leborans, Y. Olalla Herrero, *Ecotoxicol. Environ. Saf.* **47**, 266 (2000).
20. D. De Biase, A. Tramonti, F. Bossa, P. Visca, *Mol. Microbiol.* **32**, 1198 (1999).
21. J. R. George, L. Pine, M. W. Reeves, W. Knox Harrell, *J. Clin. Microbiol.* **11**, 286 (1980).
22. S. Rendulic *et al.*, *Science* **303**, 689 (2004).
23. L. Y. Gao, Y. Abu Kwaik, *Environ. Microbiol.* **2**, 79 (2000).

24. We thank M. Horwitz (UCLA School of Medicine, Los Angeles, CA) for supplying the Philadelphia 1 bacterial stock used in this study. We are especially grateful to I. S. Edelman for his constant encouragement during the course of this project. Large-scale analyses were aided by the availability of software and hardware from the Bioinformatics Core Facility sponsored by the AMDeC Foundation, Inc. This work was supported by NIH grants U01 1 AI 4437 (J.J.R.) and AI 23549 (H.A.S.), a Packard Fellowship for Science and Engineering (J.J.), and funds generously provided by the Columbia Genome Center. S.M.G. is supported by a grant from the Pasteur Foundation of New York.

Supporting Online Material

www.sciencemag.org/cgi/content/full/305/5692/1966/DC1
Materials and Methods
SOM Text
Tables S1 to S6
Figs. S1 to S6

30 April 2004; accepted 9 August 2004

Nitric Oxide Represses the *Arabidopsis* Floral Transition

Yikun He,[1,2]* Ru-Hang Tang,[1]* Yi Hao,[1]* Robert D. Stevens,[3] Charles W. Cook,[1] Sun M. Ahn,[1] Liufang Jing,[1] Zhongguang Yang,[4] Longen Chen,[4] Fangqing Guo,[5] Fabio Fiorani,[1]† Robert B. Jackson,[1] Nigel M. Crawford,[5] Zhen-Ming Pei[1]‡

The correct timing of flowering is essential for plants to maximize reproductive success and is controlled by environmental and endogenous signals. We report that nitric oxide (NO) repressed the floral transition in *Arabidopsis thaliana*. Plants treated with NO, as well as a mutant overproducing NO (*nox1*), flowered late, whereas a mutant producing less NO (*nos1*) flowered early. NO suppressed *CONSTANS* and *GIGANTEA* gene expression and enhanced *FLOWERING LOCUS C* expression, which indicated that NO regulates the photoperiod and autonomous pathways. Because NO is induced by environmental stimuli and constitutively produced, it may integrate both external and internal cues into the floral decision.

The life of flowering plants is divided into two distinct phases, an initial vegetative phase during which meristems produce leaves and a subsequent reproductive phase during which meristems produce flowers. Genetic studies of the timing of flowering in *Arabidopsis* have revealed four major pathways (*1*). The photoperiod and vernalization pathways integrate external signals into the floral decision, whereas the autonomous and gibberellin (GA) pathways act independently of environmental cues (*2*).

NO plays a pivotal role in animals and has emerged as a key growth regulator in plants (*3*, *4*). NO promotes leaf expansion, inhibits maturation and senescence, stimulates light-dependent germination, and promotes deetiolation (*5*, *6*). Excess endogenous NO reduces growth and delays development in tobacco plants (*7*). NO production is induced by biotic and abiotic stimuli, such as drought, salt stress, and pathogen infection (*4*). In addition, substantial NO is emitted from plants into the atmosphere. Conversely, atmospheric NO, a major greenhouse pollutant produced by combustion of fossil fuels, can affect plants. Thus, NO has a central role in coordinating plant growth and development with environmental conditions. However, little is known about the molecular mechanisms underlying the function of NO in plants.

Treatment of *Arabidopsis* seedlings with an NO donor, sodium nitroprusside (SNP), enhanced vegetative growth and delayed flowering (Fig. 1). SNP increased shoot growth by ~65% at low concentrations (≤100 μM), although it inhibited growth at high concentrations (Fig. 1, A and B; fig S1A). The optimal SNP concentration for promoting shoot growth was ~100 μM. A similar promotive effect of

[1]Department of Biology, Duke University, Durham, NC 27708, USA. [2]Department of Biology, Capital Normal University, Beijing 100037, China. [3]Mass Spectrometry Laboratory, Duke University Medical Center, Research Triangle Park, NC 27709, USA. [4]Orthopaedic Research Laboratory, Duke University Medical Center, Durham, NC 27710, USA. [5]Division of Biological Sciences, University of California, San Diego, La Jolla, CA 92093, USA.

*These authors contributed equally to this work.
†Present address: Department of Plant Systems Biology, VIB-Ghent University, B-9052 Ghent, Belgium.
‡To whom correspondence should be addressed. E-mail: zpei@duke.edu

NO on chlorophyll content was also found (*8*). SNP delayed flowering in a dose-dependent manner, as measured by the increase in rosette leaf number and days to bolting—swift upward growth at the transition to flowering (Fig. 1, A, C, and D; fig. S1A). A standard indicator for flowering time is the number of leaves produced on the primary shoot before the first flower is initiated; plants that flower late form more leaves (*9*).

Exogenously applied NO may not replicate the function of endogenous NO and may have side effects in plants. Thus, analysis of genetic mutants with altered endogenous NO levels was conducted to determine the in vivo relevance of NO. An NO-hypersensitive screen for *NO overproducer* (*nox*) mutants in *Arabidopsis* was performed (*10*). NO inhibition of root growth was used as a phenotype for the initial screen (fig. S1B). Subsequently, NO production was measured with an NO-sensitive dye, 4,5-diaminofluorescein diacetate (*11*, *12*). Six *nox1* alleles were isolated (Fig. 2A; fig. S2) that contained high levels of NO in roots (*8*) and leaves (table S1) compared with wild type (WT) (Fig. 2B). The *nox1* mutant, which refers to *nox1-1* unless otherwise specified, showed the most root-growth hypersensitivity to SNP of all the mutants isolated. Mutants with altered NO biosynthesis or signaling have not yet been isolated via genetic screens, so *nox1* could provide a powerful tool for dissecting NO function. Despite recent identification of two types of NO synthase (NOS), pathogen-inducible iNOS and constitutive AtNOS, the sources of NO in plants remain to be fully elucidated (*4*, *11*, *12*).

NOX1 was identified as either very close or identical to *CUE1* by map-based cloning (fig. S3A). The morphological phenotype of *nox1* was almost identical to that described for *chlorophyll a/b binding protein* (*CAB*) *underexpressed 1* mutant (*cue1*), including small plant size and pale green leaves with a reticulate pattern (*13*). *CUE1* encodes a chloroplast phosphoenolpyruvate/phosphate translocator (*14*). Several lines of molecular genetic evidence demonstrated that *NOX1* is *CUE1* (fig. S3). The *cue1* mutants were hypersensitive to SNP and displayed an elevated

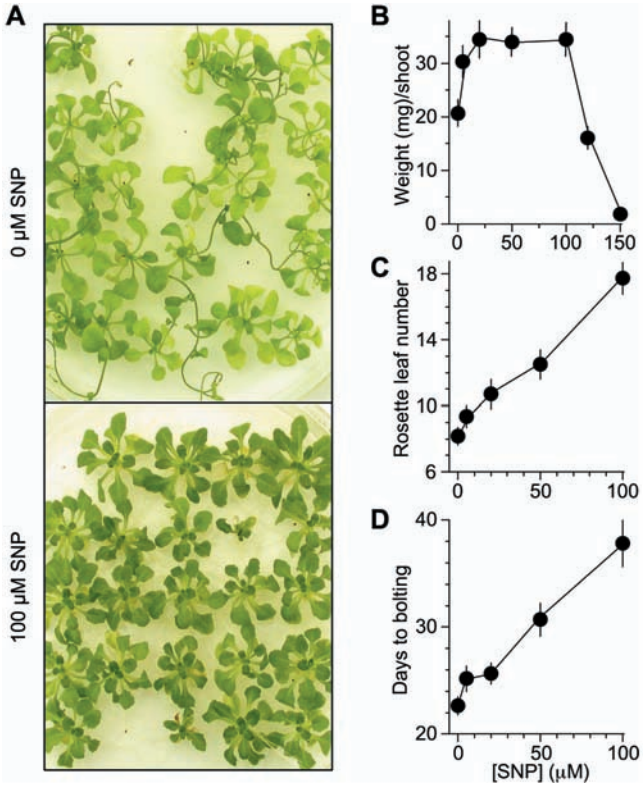

Fig. 1. Exogenous NO promotes vegetative growth but inhibits reproductive development. (**A**) The effects of an NO donor SNP on plant growth and development. *Arabidopsis* seedlings were grown in petri dishes containing SNP during long days (16-hour light/8-hour dark) for 5 weeks (*10*). (**B**) The effect of SNP concentration on shoot growth. (**C** and **D**) The effect of SNP on flowering times. Fresh weight per shoot (B), the rosette leaf number (C), and days to bolting (D) from experiments as in (A) and fig. S1A plotted as a function of the concentrations of SNP that were applied, respectively. Data from four separate experiments are presented (mean ± SD; n = 150 seedlings).

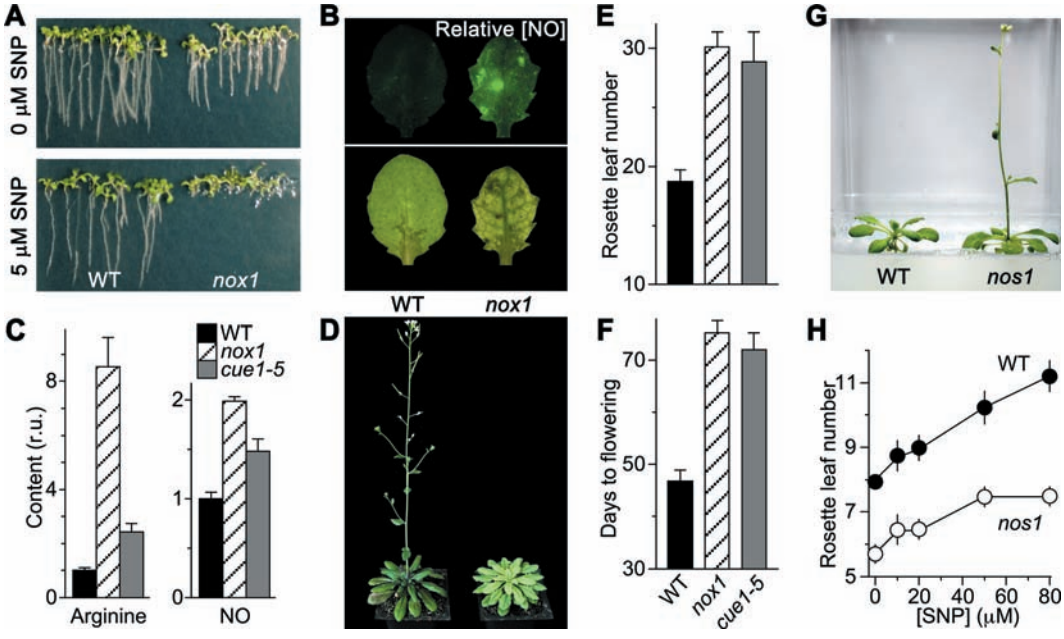

Fig. 2. Endogenous NO represses the floral transition. (**A**) The root growth phenotype in *nox1* mutant. (**B**) The endogenous NO levels in *nox1* and WT. Leaves were stained with DAF-2DA. Fluorescence was analyzed with excitation 490 nm and emission 515 nm (top) with the same exposure times (*10*). White-light images are shown at the bottom. (**C**) The levels of L-Arg and NO in WT, *nox1*, and *cue1-5*. Plants grown under 12-hour light/12-hour dark cycles were harvested 6 hours after dawn (*10*). The absolute levels of L-Arg and NO were 51.8 and 0.45 nmol per gram of fresh rosette leaves in WT, respectively. Values are normalized to those of WT. Each data point represents nine independent measurements (r.u., relative unit). (**D**) The *nox1* mutant flowers late. WT and *nox1* were grown in soil under 12-hour light/12-hour dark cycles and were photographed after 60 days of growth. (**E** and **F**) Flowering times of *nox1* and *cue1-5* mutants. The rosette leaf number (E) and days to flowering (F) from experiments as in (D) were scored (mean ± SD; $n \geq 25$ plants). (**G**) The *NO synthase 1* (*nos1*) mutant that produces fewer NO flowers early under long days. (**H**) The *nos1* mutant flowers earlier than WT under SNP treatments. Experiments similar to that in (G) were analyzed (mean ± SD; n = 20 to 30 plants).

level of endogenous NO. The *cue1* could not complement *nox1* phenotypes. In all six *nox1* alleles, the *CUE1* gene was deleted. Because NO is synthesized from the conversion of L-arginine (L-Arg) to L-citrulline (L-Cit) by NOS (*3*), free L-Arg and L-Cit are several-fold higher in *cue1* mutants than in WT plants (*14*), and *nox1* overproduces NO, we reasoned that disruption of the *CUE1* gene would increase the endogenous L-Arg concentration and thus would promote its conversion to NO. *nox1* and the *cue1-5* mutant harboring a single amino acid mutation (*14*) indeed exhibited larger amounts of L-Arg, L-Cit, and NO than WT (Fig. 2C; fig. S4), indicating that NOS-based NO production occurs in *Arabidopsis*.

Soil-grown *nox1* and *cue1* mutants showed a late-flowering phenotype (Fig. 2, D to F; table S1). This phenotype is not photoperiod-dependent, as *nox1* flowered late under all photoperiods. However, the phenotypic severity was influenced by photoperiods, with 18%, 61%, and 17% increases in the rosette leaf number seen under the light/dark (hours) cycles of 16/8, 12/12, and 8/16, respectively (table S1). This observation is consistent with the light-dependent phenotypes seen in *cue1* mutants (*13*).

In addition, we determined whether down-regulation of endogenous NO promotes the floral transition. The mutant *Atnos1* (*nos1*) that contains a reduced amount of NO (*11*) flowered earlier than WT (Fig. 2G), but still displayed sensitivity to SNP (Fig. 2H). The NO content of *nos1* plants was about 18% that of WT (*8*). The positive correlation between endogenous NO and the number of leaves produced indicates that NO may have a specific role in controlling the floral transition.

To test which components in the floral pathways are affected by NO, we analyzed expression of the floral meristem identity gene *LEAFY* (*LFY*). *LFY* is an important determinant in flower initiation, and its expression increases gradually before flowering commences (*15*). SNP suppressed *LFY* expression in a dose-dependent manner (Fig. 3, A and C). *LFY* expression was low in *nox1*, but was high in *nos1* plants compared with WT (Fig. 3, B and C). The negative correlation between *LFY* expression and endogenous NO suggests that NO repression of the floral transition is mediated, at least in part, by LFY.

Genetic epistasis studies have placed the genes that regulate the floral transition into four major pathways in *Arabidopsis*, all of which converge on the target *LFY* (*2*). The *nox1* mutants flowered late and showed a dwarf phenotype, resembling those of GA-deficient mutants (*16*). GA promoted flowering in *nox1* and WT plants but could not reverse the *nox1* dwarf phenotype (*8*), which suggests that NO may function in parallel with GA. Because *nox1* and mutants of the autonomous pathway flower late on both long and short days (*1*), we reasoned that *nox1* might affect this pathway. The vernalization and autonomous pathways converge on a floral repressor, *FLOWERING LOCUS C* (*FLC*), and late-flowering mutants of the autonomous pathway always have elevated *FLC* expression (*17*). Treatment with low concentrations (≤50 μM) of SNP decreased *FLC* expression, whereas high concentrations (>50 μM) increased *FLC* expression (Fig. 3, D and F). *FLC* expression was high in *nox1* and slightly reduced in *nos1* compared with WT (Fig. 3, E and F). The late-flowering phenotype observed in WT plants treated with high doses of SNP or in *nox1* may result from up-regulation of *FLC* expression. However, the late-flowering phenotype in plants treated with low doses of SNP may be caused by components independent of *FLC*. Nonetheless, the flowering phenotypes observed in *nox1*, WT, and *nos1* are consistent with the expression level of *FLC*, which suggests that endogenous NO may down-regulate the autonomous pathway, which results in late flowering.

Because previous studies have indicated the light-dependent nature of NO effects in plants, and *cue1* mutants show various defects in light perception and photomorphogenesis (*6*, *13*), we investigated whether NO regulates the photoperiod pathway. *Arabidopsis* is a facultative, long-day plant; long days promote flowering (*9*). *CONSTANS* (*CO*) is the most genetically downstream component of this pathway identified so far that promotes floral induction, and it acts as a link between the circadian clock and the control of flowering (*18*, *19*). SNP suppressed *CO* expression in a dose-dependent manner (Fig. 3, G and I). The *CO* expression was high in *nos1* but low in *nox1* plants compared with WT (Fig. 3, H and I). Consistently, *CO* and *FLC* expression were down- and up-regulated, respectively, in *cue1-5* plants (fig. S5). *CO* expression displays a diurnal rhythm (*18*); thus, the repression of *CO* by NO could be due to a reduction of amplitude, a phase shift, or both.

To quantify this effect of NO, we determined *CO* mRNA expression over a 12-hour light/12-hour dark cycle. The overall *CO* mRNA abundance was lower in *nox1* and higher in *nos1* than in WT, although the phase of *CO* mRNA level was not greatly disturbed (Fig. 4, A and B; fig. S6), consistent with previous studies on *gigantea* (*gi*) and *early flowering 3* (*elf3*), mutants of the photoperiod pathway (*20*, *21*). A *gi* lesion

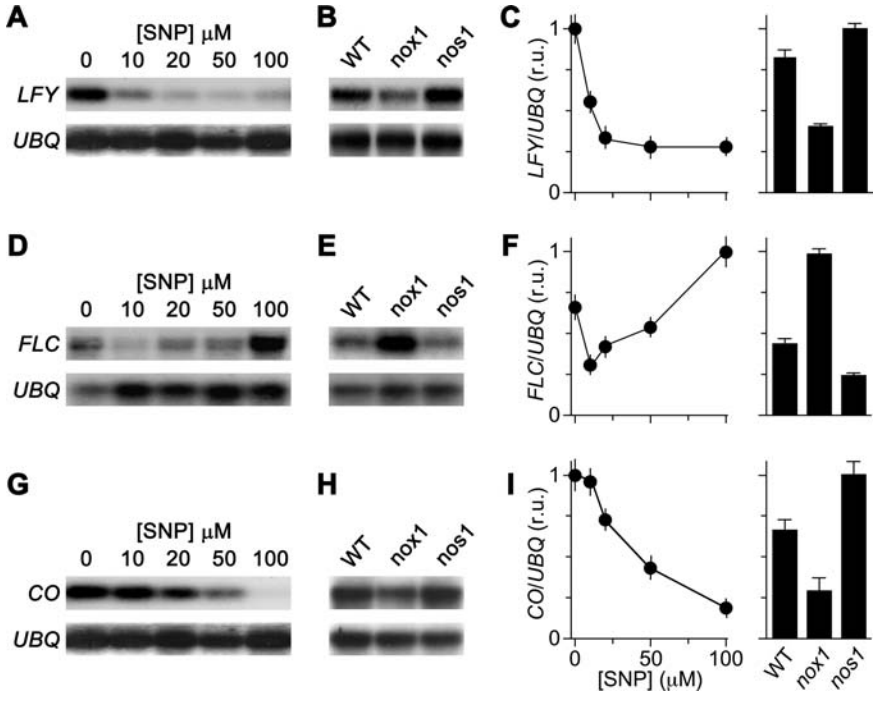

Fig. 3. NO affects the expression of genes that control the floral transition. (**A**, **D** and **G**) The effect of NO on the expression of *LFY*, *FLC*, and *CO*, respectively. Seedlings were grown in media containing SNP under long days. Leaves were collected 8 hours after dawn. The *LFY* and *CO* mRNA abundance was analyzed by using reverse transcription–polymerase chain reaction (PCR) and *FLC* mRNA by Northern blot (*10*). Ubiquitin mRNA (*UBQ*10) was used as a loading control. Similar results were seen for plants grown in 12-hour light/12-hour dark cycles. (**B**, **E**, and **H**) The expression levels of *LFY*, *FLC*, and *CO*, respectively, in WT, *nox1*, and *nos1* plants. Materials were prepared, and mRNA was analyzed as described in (A). (**C**, **F**, and **I**) Analysis of the effects of NO on *LFY*, *FLC*, and *CO* expression, respectively. The relative mRNA abundance was normalized to the *UBQ* levels. The maximum value was arbitrarily set to 1 (mean ± SEM; $n = 3$).

down-regulates *CO* expression, which results in late flowering, whereas an *elf3* lesion up-regulates *CO* expression, which leads to early flowering (*18*). To test whether NO directly affects *CO* expression, we analyzed *GIGANTEA* (*GI*), which is upstream of CO (*21*). The circadian amplitudes of *GI* mRNA abundance, similar to those of *CO*, were lower in *nox1* than WT (Fig. 4, C and D), which suggests that NO acts upstream of CO. Additionally, we analyzed the flowering phenotypes of *elf3* and *CO* overexpressing plants (*35S::CO*) (*22*) in response to NO. NO suppression of flowering was largely abolished in *elf3* mutants and *35S::CO* plants (Fig. 4F), which further supports the role of NO in the photoperiod pathway.

The expression of *CO* is regulated by the circadian clock and photoperiod, and the circadian rhythm of *CAB* expression can represent the circadian output in plants (*2*). The amplitudes of *CAB* mRNA abundance after switching from 12-hour light/12-hour dark cycles to continuous light for 3 days were greatly reduced in *nox1*, as well as in *cue1* mutants (*13*), whereas the circadian phases were not altered (*8*), similar to the expression of *CO* and *GI*. The amplitudes of another circadian output, cotyledon leaf movements, were also reduced by 43.8 ± 4.9% in *nox1* compared with WT, and no alteration of the circadian period was observed (Fig. 4E; fig S7). To analyze whether NO affects the circadian clock itself, we examined components of circadian clock central oscillators, *TIMING OF CAB EXPRESSION* (*TOC1*) and *CIRCADIAN CLOCK ASSOCIATED 1* (*CCA1*) (*23*, *24*). Neither the amplitude nor the circadian period of *TOC1* and *CCA1* expression was altered in *nox1* (*8*). Therefore, it is more likely that NO may affect circadian outputs rather than these central oscillators. Additionally, NO content in leaves in the middle of the night was 70.6% of that in the middle of the day in a 12-hour light/12-hour dark cycle for WT plants and 58.0% for *nox1* (table S2). This result suggests that the endogenous NO levels display a diurnal rhythm, consistent with a previous study (*7*). Although it is unclear whether NO production is dependent on light or the circadian clock, the alteration of NO homeostasis in *nox1* may cause its flowering phenotype.

We have provided pharmacological, physiological, molecular, and genetic data demonstrating that NO represses the photoperiod and autonomous floral pathways. These results are largely consistent with previous observations of delayed development in tobacco where NO is overproduced and of its inhibitory effects on maturation and senescence (*5*, *7*). Given that NO is induced by environmental changes, as well as constitutively produced, external and internal cues may converge on the regulation of endogenous NO status, which then relays these signals to the transcription regulatory network that controls the floral transition, which provides a unique layer of floral regulation. Oscillating NO levels, in addition to *CCA1* and *TOC*, may provide a mechanism to measure day/night switches, acting downstream of light perception to regulate certain circadian outputs and thus to control the floral transition, although the precise action of NO remains to be determined. Because several genes affected by NO (*CAB*, *CO*, and *GI*) are also regulated by light, the primary effect of NO may be on light signaling, and the effect on flowering may be secondary. Thus, identification of the direct target of NO will further our understanding of the molecular function of NO in plants.

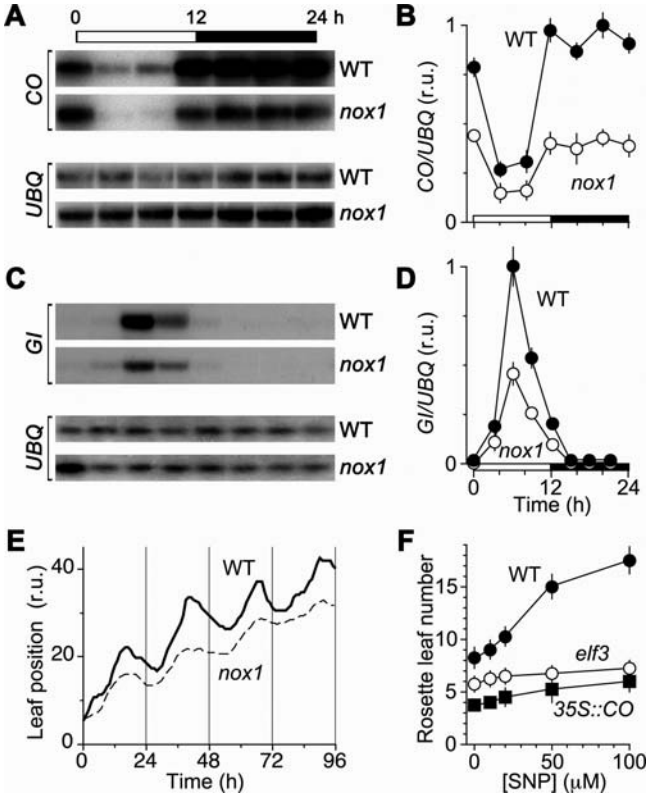

Fig. 4. NO suppresses the photoperiod pathway. (**A** and **C**) The mRNA abundance of *CO* and *GI* over a 24-hour time course. Plants were grown under 12-hour light/12-hour dark cycles for 10 days. Seedlings were collected every 4 hours for *CO* and every 3 hours for *GI* starting at dawn. The black and white bars at the top represent objective lights off and on, respectively. (**B** and **D**) Quantification of *CO* and *GI* mRNA abundance in (A) and (C), respectively (mean ± SEM; $n = 5$). (**E**) Circadian rhythms of cotyledon movements. Seedlings were grown under 12-hour light/12-hour dark cycles for 5 days, and cotyledon movements were recorded under constant dim light (*10*). (**F**) Analysis of the flowering time of *elf3* and *35S::CO* in response to SNP treatments (mean ± SD; $n = 150$ seedlings).

References and Notes

1. G. G. Simpson, C. Dean, *Science* **296**, 285 (2002).
2. A. Mouradov, F. Cremer, G. Coupland, *Plant Cell* **14**, S111 (2002).
3. H. H. Schmidt, U. Walter, *Cell* **78**, 919 (1994).
4. L. Lamattina, C. Garcia-Mata, M. Graziano, G. Pagnussat, *Annu. Rev. Plant Biol.* **54**, 109 (2003).
5. Y. Y. Leshem, E. Haramaty, *J. Plant Physiol.* **148**, 258 (1996).
6. M. V. Beligni, L. Lamattina, *Planta* **210**, 215 (2000).
7. Y. Morot-Gaudry-Talarmain *et al.*, *Planta* **215**, 708 (2002).
8. Y. He, Z.-M. Pei, data not shown.
9. M. Koornneef, C. J. Hanhart, J. H. van der Veen, *Mol. Gen. Genet.* **229**, 57 (1991).
10. Information on materials and methods is available on *Science* Online.
11. F.-Q. Guo, M. Okamoto, N. M. Crawford, *Science* **302**, 100 (2003).
12. M. R. Chandok, A. J. Ytterberg, K. J. van Wijk, D. F. Klessig, *Cell* **113**, 469 (2003).
13. H. Li, K. Culligan, R. A. Dixon, J. Chory, *Plant Cell* **7**, 1599 (1995).
14. S. J. Streatfield *et al.*, *Plant Cell* **11**, 1609 (1999).
15. M. A. Blazquez, L. N. Soowal, I. Lee, D. Weigel, *Development* **124**, 3835 (1997).
16. T.-p. Sun, F. Gubler, *Annu. Rev. Plant Biol.* **55**, 197 (2004).
17. S. D. Michaels, R. M. Amasino, *Plant Cell* **11**, 949 (1999).
18. P. Suarez-Lopez *et al.*, *Nature* **410**, 1116 (2001).
19. M. J. Yanovsky, S. A. Kay, *Nature* **419**, 308 (2002).
20. K. A. Hicks *et al.*, *Science* **274**, 790 (1996).
21. S. Fowler *et al.*, *EMBO J.* **18**, 4679 (1999).
22. H. Onouchi, M. I. Igeno, C. Perilleux, K. Graves, G. Coupland, *Plant Cell* **12**, 885 (2000) .
23. C. Strayer *et al.*, *Science* **289**, 768 (2000).
24. Z.-Y. Wang, E. M. Tobin, *Cell* **93**, 1207 (1998) .

25. We thank S. Han for assistance; Z. Mou and W. Wang for advice concerning map-based cloning; R. Fehon for use of a fluorescence stereomicroscope; R. Amasino for the *FLC* clone; G. Coupland for the *GI* clone and *35S::CO* seeds; *Arabidopsis* Biological Resource Center for *elf3* and *cue1* seeds; J. Chory, G. Coupland, J. Schroeder, X. Dong, and J. Dangl's lab for helpful discussion; and J. Siedow, T. Sun, P. Benfey, R. Fehon, P. Reeves, J. Reed, and R. Amasino for critical comments on the manuscript. Y.H. was supported by an exchange program between Duke University and Capital Normal University, Chinese NSF (30328003), and the Ministry of Science and Technology of China (2002AA2Z1001), and R.-H.T. by a Hargitt Fellowship. This work was supported by NSF (MCB-0132894), start-up funds, and Arts and Sciences Research funds from Duke University to Z.-M.P.

Supporting Online Material

www.sciencemag.org/cgi/content/full/305/5692/1968/DC1
Materials and Methods
Supporting Text
Figs. S1 to S7
Tables S1 and S2
Reference and Notes

6 April 2004; accepted 11 August 2004

Recycling Endosomes Supply AMPA Receptors for LTP

Mikyoung Park,[1]* Esther C. Penick,[3]* Jeffrey G. Edwards,[3] Julie A. Kauer,[3] Michael D. Ehlers[1,2]†

Long-term potentiation (LTP) of synaptic strength, the most established cellular model of information storage in the brain, is expressed by an increase in the number of postsynaptic AMPA receptors. However, the source of AMPA receptors mobilized during LTP is unknown. We report that AMPA receptors are transported from recycling endosomes to the plasma membrane for LTP. Stimuli that triggered LTP promoted not only AMPA receptor insertion but also generalized recycling of cargo and membrane from endocytic compartments. Thus, recycling endosomes supply AMPA receptors for LTP and provide a mechanistic link between synaptic potentiation and membrane remodeling during synapse modification.

Information storage and processing in the brain involve modification of synaptic strength. This process is exemplified by long-term potentiation (LTP) in the hippocampus (*1*, *2*), the dominant cellular model for learning and memory. LTP-inducing stimuli increase the number of functional AMPA-type glutamate receptors at the postsynaptic membrane (*3*–*8*), leading to an increase in AMPA receptor–mediated transmission at excitatory synapses (*9*). However, the source of AMPA receptors mobilized for LTP is unknown.

AMPA receptors inserted during LTP are thought to originate from an intracellular reserve pool (*6*, *10*, *11*). In hippocampal dendrites, AMPA receptors undergo continuous cycling into and out of the postsynaptic membrane (*12*, *13*). Upon internalization, AMPA receptors are sorted in early endosomes either to a specialized recycling endosome compartment for reinsertion to the plasma membrane or to late endosomes and lysosomes for degradation (fig. S1) (*13*, *14*). We hypothesized that dendritic endosomes may contain a reserve pool of AMPA receptors available for modifying synaptic strength.

To test whether transport from recycling endosomes to the plasma membrane was required to maintain the supply of AMPA receptors at the dendritic plasma membrane, we took advantage of a mutant version of the Eps15–homology domain protein EHD1/Rme1 (Rme1-G429R) as well as a constitutively inactive guanosine diphosphate–bound form of the small guanosine triphosphatase (GTPase) Rab11a (Rab11a-S25N). Both of these mutants selectively impair endocytic recycling by preventing trafficking from recycling endosomes to the plasma membrane (fig. S1) (*15*, *16*). To detect AMPA receptors at the cell surface, we performed live-cell immunocytochemistry of hippocampal neurons with the use of antibodies directed against extracellular epitopes of the AMPA receptor subunit GluR1. Upon blockade of endocytic recycling, the surface expression of AMPA receptors was markedly reduced (Fig. 1A). Conversely, expression of wild-type Rme1 to augment recycling caused a corresponding increase in surface AMPA receptors (Fig. 1A).

To determine whether the reduction in surface AMPA receptors in neurons expressing

[1]Department of Neurobiology; [2]Department of Cell Biology, Department of Pharmacology and Cancer Biology, Department of Pathology, and Neuroproteomics Laboratory; Duke University Medical Center, Box 3209, Durham, NC 27710, USA. [3]Department of Molecular Pharmacology, Physiology, and Biotechnology, Brown University, Providence, RI 02912, USA.

*These authors contributed equally to this work.
†To whom correspondence should be addressed. E-mail: ehlers@neuro.duke.edu

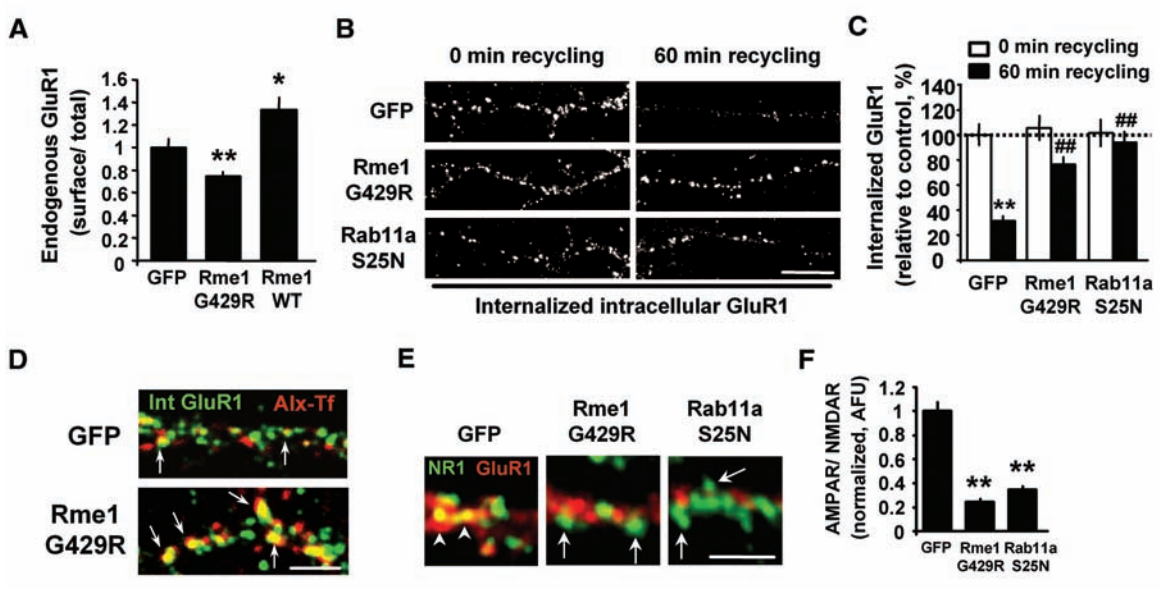

Fig. 1. Transport through recycling endosomes maintains AMPA receptors at synapses. (**A**) The ratio of surface to total endogenous GluR1 on individual hippocampal neurons expressing the indicated constructs (*n* values are 21, 19, and 18 from left to right; $*P < 0.05$ and $**P < 0.01$ relative to GFP control; *t* test). Error bars indicate SEM. (**B**) Inhibitory mutants of Rme1 and Rab11a retard AMPA receptor recycling. Live antibody feeding and receptor recycling assays were performed on neurons cotransfected with HA/T-GluR1 and either GFP, GFP-Rme1-G429R, or GFP-Rab11a-S25N (*17*). Fluorescence signal indicates remaining intracellular HA/T-GluR1 after 0 min and 60 min of recycling. Scale bar indicates 5 μm. (**C**) Means ± SEM of internalized intracellular HA/T-GluR1 on individual neurons from (B) (*n* values are 27, 19, 11, 28, 19, and 17 from left to right; $**P < 0.001$ relative to 0-min recycling of GFP and double pound symbols indicate $P < 0.001$ relative to 60-min recycling of GFP; *t* test). (**D**) Overexpressing Rme1-G429R traps internalized AMPA receptors (Int GluR1, green) in recycling endosomes along with internalized Alx-Tf (red). Arrows indicate colocalization. Scale bar, 2 μm. (**E**) Endogenous NMDA (NMDAR, NR1) and AMPA receptors (AMPAR, GluR1) were visualized by immunocytochemistry on neurons expressing GFP, Rme1-G429R, or Rab11a-S25N. Arrowheads indicate synapses containing both NR1 and GluR1. Arrows indicate synapses containing NR1 without detectable GluR1. Scale bar, 2 μm. (**F**) Average pixel intensity ratios of GluR1 to NR1 on individual synapses were measured. Values of *n* are 79, 48, and 88 synapses on four to six neurons each. $**P < 0.001$ relative to GFP, *t* test. Error bars indicate SEM. AFU, arbitrary fluorescence units.

Rme1-G429R and Rab11a-S25N was due to decreased reinsertion of internalized receptors, we monitored AMPA receptor endocytosis and recycling by using live-cell antibody uptake assays and quantitative fluorescence microscopy (*13*, *17*). In neurons expressing Rme1-G429R or Rab11a-S25N, endocytosis of recombinant AMPA receptors containing an N-terminal hemagglutinin (HA) epitope tag immediately followed by a thrombin protease cleavage site (HA/T-GluR1) was indistinguishable from that in green fluorescent protein (GFP)–expressing control neurons (Fig. 1, B and C). After endocytosis, the majority of internalized AMPA receptors recycled within 1 hour in control neurons (Fig. 1, B and C). In contrast, internalized AMPA receptors were retained intracellularly and failed to cycle back to the plasma membrane in neurons expressing Rme1-G429R or Rab11a-S25N (Fig. 1, B and C). Total AMPA receptor expression levels were unchanged by the expression of Rme1-G429R or Rab11a-S25N (fig. S2). Thus, transport from recycling endosomes maintains surface AMPA receptors by regulating their recycling to the postsynaptic membrane.

Expression of Rme1-G429R caused a notable redistribution of the total pool of AMPA receptors from dendritic spines to endosomal compartments in the dendritic shaft (fig. S3). In further experiments, we simultaneously monitored the endocytic trafficking of endogenous AMPA receptors and transferrin receptors (TfRs) originating from the cell surface (*17*) and found that expression of Rme1-G429R resulted in the trapping of both endocytic cargos in recycling endosomes without affecting their endocytosis (Fig. 1D). To test whether the redistribution from spines to endosomes was selective for AMPA receptors, we double-labeled hippocampal neurons expressing Rme1-G429R or Rab11a-S25N with antibodies against the AMPA receptor subunit GluR1 and the *N*-methyl-D-aspartate (NMDA) receptor subunit NR1. There was a marked decrease in the average AMPA receptor–to–NMDA receptor fluorescence intensity ratio at hippocampal synapses (Fig. 1, E and F), indicating a selective loss of AMPA receptors. Thus, blocking membrane trafficking out of recycling endosomes trapped AMPA receptors in TfR-positive recycling compartments within dendrites, and endocytic recycling was required to maintain AMPA receptors, but not NMDA receptors, at excitatory synapses.

We next tested whether AMPA receptors recruited during LTP use the transport pathway from recycling endosomes to arrive at synapses. We used a cell culture model of LTP employing glycine stimulation to activate synaptic NMDA receptors (*6*, *18*, *19*) together with selective detection of newly inserted AMPA receptors using HA/T-GluR1 (*6*, *11*, *17*, *19*, *20*). As expected, 20 to 25 min after a brief application of glycine (200 μM for 3 min), newly inserted AMPA receptors were significantly increased compared to unstimulated control cells (Fig. 2, A and B). This increase was blocked by coapplication of the NMDA receptor antagonist D-AP5 (Fig. 2, A and B) (*6*, *19*). Hippocampal neurons expressing Rme1-G429R and Rab11a-S25N to prevent transport from recycling endosomes failed to exhibit a detectable increase in AMPA receptor insertion upon glycine stimulation (Fig. 2B). In contrast, neurons expressing wild-type versions of Rme1 and Rab11a exhibited robust glycine-induced AMPA receptor insertion (Fig. 2B). Expression of Rab6a-T27N, a dominant negative version of the Golgi-associated Rab family GTPase Rab6a (*21*–*23*), had no effect on glycine-induced AMPA receptor insertion (Fig. 2B). Expression of a soluble fragment of the recycling endosome SNARE [SNAP (soluble *N*-ethylmaleimide–sensitive factor attachment protein) receptor] protein syntaxin 13 (Syn13ΔTM) (*24*) that forms cognate SNARE complexes but blocks membrane fusion due to its inability to bind membranes (*25*) completely abolished glycine-induced AMPA receptor insertion (Fig. 2B). In contrast, a soluble fragment of the late endosome SNARE protein syntaxin 7 (*25*) had no effect on LTP-induced AMPA receptor insertion (Fig. 2B). Together, these results provide strong evidence that recycling endosomes supply newly inserted AMPA receptors during LTP.

To determine whether AMPA receptors inserted during LTP derive originally from

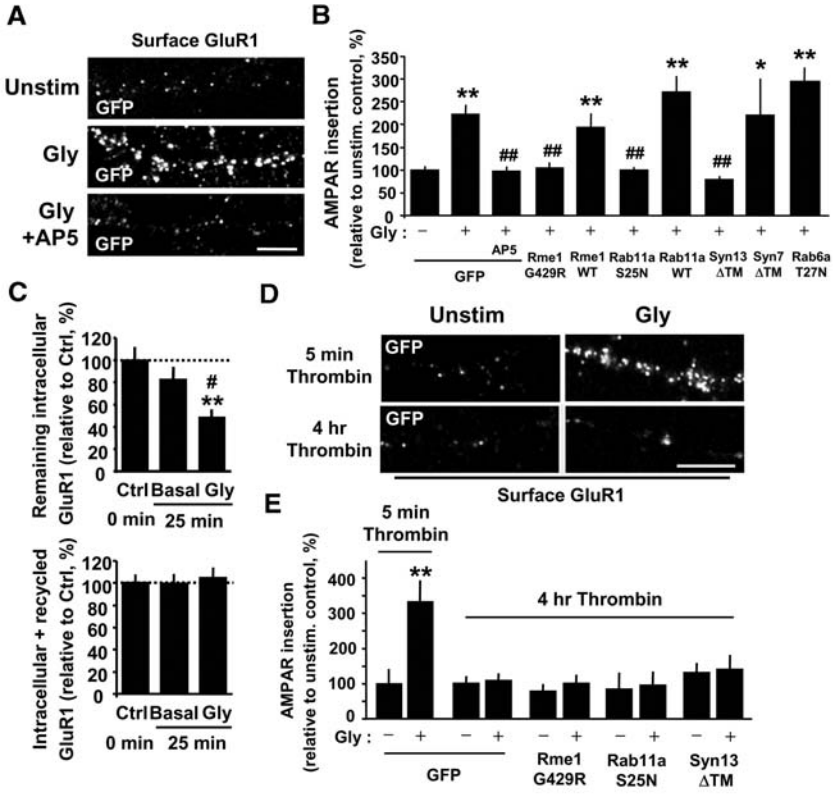

Fig. 2. Recycling endosomes supply newly inserted AMPA receptors during LTP. (**A**) After a 5-min thrombin treatment to remove HA tags from surface HA/T-GluR1, neurons were stimulated with glycine with or without AP5 and incubated to allow new receptor insertion (*6*, *17*, *18*). Newly inserted HA/T-GluR1 was detected by anti-HA surface labeling (*19*). Scale bar, 5 μm. (**B**) Quantitative analysis of AMPAR insertion in neurons expressing the indicated constructs. Values of *n* are 29, 22, 28, 20, 13, 26, 14, 23, 7, and 20 neurons for each condition from left to right; $*P < 0.05$, $**P < 0.005$ relative to unstimulated GFP control, and double pound symbols indicate $P < 0.005$ relative to glycine-stimulated GFP-expressing neurons; *t* test. Error bars indicate SEM. (**C**) Previously endocytosed AMPA receptors are returned to the plasma membrane by LTP-inducing stimuli. Live antibody feeding and AMPA receptor recycling assays were performed on hippocampal neurons under basal or glycine-stimulated conditions. A decrease in the remaining intracellular GluR1 (top) indicates recycling to the plasma membrane (*17*) (top *n* values are 38, 24, and 33 neurons; bottom *n* values are 36, 27, and 24; pound symbol indicates $P < 0.05$ relative to basal and $**P < 0.005$ relative to control; *t* test). Error bars indicate SEM. (**D**) Glycine-induced HA/T-GluR1 insertion after either standard thrombin incubation (5 min) or prolonged thrombin treatment (4 hours) to deplete the cycling pool of HA/T-GluR1 (*17*). (**E**) Means ± SEM of newly inserted HA/T-GluR1 (AMPAR) (*n* values are 33, 48, 62, 77, 14, 14, 17, 17, 22, and 11 neurons for each condition from left to right; $**P < 0.01$ relative to unstimulated GFP control; *t* test). Scale bar, 5 μm.

the plasma membrane or are newly synthesized, we tested the effect of protein synthesis inhibition. Inhibiting protein synthesis in hippocampal neurons (20 μM anisomycin for 4 hours) had no effect on glycine-induced insertion of HA/T-GluR1 (Gly/basal insertion: untreated, 156 ± 16% and n = 37; anisomycin, 144 ± 13% and n = 21; P = 0.63), consistent with the notion that mobilized AMPA receptors were not newly synthesized. Next, we tested whether previously endocytosed AMPA receptors were delivered to the plasma membrane in response to LTP-inducing stimuli. With use of live-cell antibody feeding, we visualized internalized HA/T-GluR1 receptors and followed the loss of intracellular HA/T-GluR1 fluorescence as a direct measure of AMPA receptor recycling back to the plasma membrane (*17*). Under these conditions, internalized AMPA receptors recycled to the plasma membrane, and this recycling was enhanced twofold by glycine stimulation (Fig. 2C, top). The loss of internalized receptors was not due to degradation, because the sum total of intracellular plus recycled AMPA receptors was constant under all conditions (Fig. 2C, bottom). After the standard 5-min thrombin treatment (*19*) (Fig. 2A), glycine stimulation caused a robust insertion of HA/T-GluR1 at the dendritic plasma membrane (Fig. 2, D and E). In contrast, after prolonged thrombin incubation (4 hours at 37°C) to remove HA tags from all HA/T-GluR1 receptors cycling to the plasma membrane during this time period, glycine-induced insertion of HA/T-GluR1 was undetectable (Fig. 2, D and E). Thus, AMPA receptors inserted during LTP derived from a pool that was present at the plasma membrane in the previous 4 hours. Prolonged thrombin treatment had no effect on cell viability (fig. S4), the internalization or recycling of transferrin (Tf) (fig. S4), or ongoing basal insertion of HA/T-GluR1 (Fig. 2, D and E). In neurons expressing Rme1-G429R, Rab11a-S25N, or Syn13ΔTM, depletion of the cycling pool of HA/T-GluR1 had no effect on AMPA receptor insertion (Fig. 2E), establishing the specificity of these reagents for disrupting endocytic recycling but not de novo insertion of newly synthesized receptors. Thus, AMPA receptors mobilized during LTP-inducing stimuli derive from a recycled pool.

To investigate the physiological role of recycling endosome transport in synaptic plasticity, we used whole-cell patch-clamp recordings to measure LTP at the Schaffer collateral-CA1 synapse in hippocampal slices. To interfere with endocytic recycling, we infected CA1 pyramidal neurons with recombinant Sindbis virus to express GFP, GFP-Rme1-G429R, or GFP-Rab11a-S25N before electrophysiological measurements. In control neurons expressing GFP, brief high-frequency afferent stimulation (HFS) elicited robust LTP (Fig. 3A). When transport from recycling endosomes to the plasma membrane was blocked by expressing Rme1-G429R or Rab11a-S25N, LTP was absent (Fig. 3A). This effect was not due to generalized changes in synaptic function because no differences between neurons transfected with different constructs were seen in the sizes of evoked excitatory postsynaptic currents (EPSCs) (for Rme1-G429R, 39.3 ± 10.9 pA and n = 8; P = 0.45; for Rab11a-S25N, 34.1 ± 9.1 pA and n = 7; P = 0.83; for control GFP, 32.4 ± 3.4 pA and n = 17), paired-pulse facilitation (for GFP, 2.24 ± 0.21 and n = 11; for Rme1-G429R, 2.65 ± 0.26 and n = 12; P = 0.26), posttetanic potentiation (PTP) (fig. S5), or the depolarization envelope in response to HFS (for GFP, 0.68 ± 0.07 V·s and n = 4; for Rme1-G429R, 0.70 ± 0.07 V·s and n = 4; P = 0.84). Disruption of endocytic recycling by expressing Rme1-G429R also abolished LTP induced by pairing postsynaptic depolarization with afferent stimulation (fig. S6). Expression of GFP-Rab6a-T27N to disrupt vesicular transport at the level of the Golgi had no effect on LTP (fig. S7). NMDA receptor–mediated synaptic currents in neurons expressing Rme1-G429R did not differ from those in neighboring uninfected neurons within the same slice (for Rme1-G429R, 30.1 ± 4.3 pA and n = 6; for control, 23.6 ± 3.7 pA and n = 6; P = 0.36), indicating that the absence of LTP could not be accounted for by a decrease in functional NMDA receptors and supporting the idea that LTP-inducing stimuli promoted the recycling of AMPA receptors but not NMDA receptors.

To rule out effects of chronic disruption of endocytic recycling, we delivered purified syntaxin13ΔTM or syntaxin7ΔTM fusion proteins intracellularly by inclusion in the pipette solution used to record CA1 cells in acutely prepared hippocampal slices. After brief HFS, CA1 neurons filled with syntaxin7ΔTM exhibited robust LTP (Fig. 3B). In contrast, LTP was blocked in those neurons filled with syntaxin13ΔTM (Fig. 3B). Perfusion of syntaxin13ΔTM in the absence of HFS had no effect on basal EPSC amplitudes over the 30-min course of the experiment (Fig. 3B), and neither syntaxin13ΔTM nor syntaxin7ΔTM infusion altered PTP (fig. S5). The rapidity of action of syntaxin13ΔTM (10 to 13 min) indicated that even a very brief block of endocytic recycling was sufficient to prevent LTP.

Given our finding that AMPA receptors come from recycling endosomes for LTP (Figs. 2 and 3), we hypothesized that LTP is accompanied by an overall increase in membrane trafficking from recycling endosomes to the plasma membrane, providing a potential source of membrane and other proteins for synapse and spine remodeling (*26*, *27*).

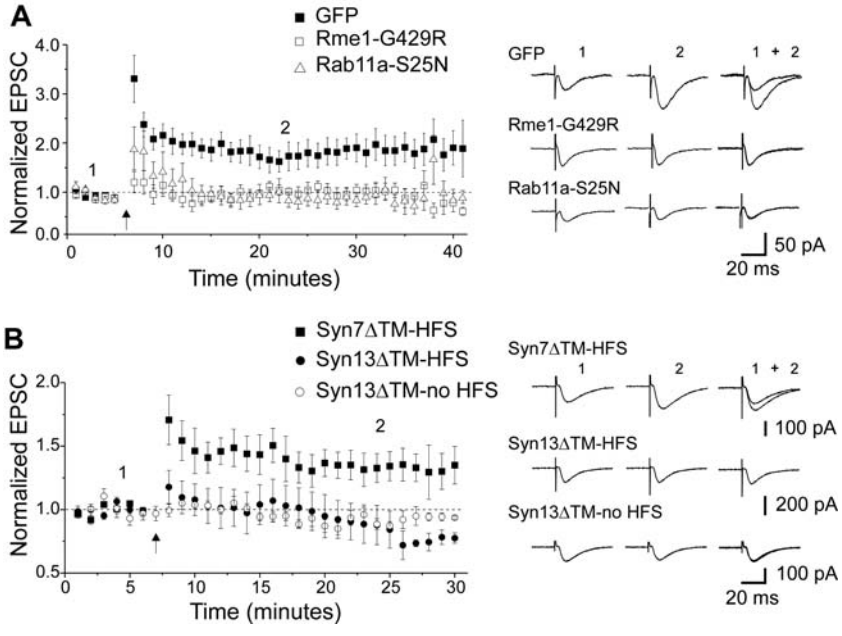

Fig. 3. Blocking transport through recycling endosomes abolishes LTP. (**A**) Hippocampal slices were infected with Sindbis virus expressing GFP (n = 17), GFP-Rme1-G429R (n = 8), or GFP-Rab11a-S25N (n = 7). EPSCs were measured by whole-cell patch-clamp recordings from GFP-positive CA1 pyramidal neurons before and after HFS (arrow) to induce LTP (100 Hz, four 1-s trains). (**B**) EPSCs were recorded from CA1 pyramidal neurons with or without an LTP-inducing HFS (arrow). Purified syntaxin13ΔTM (Syn13ΔTM; n is 8 for HFS and 6 for no HFS) or syntaxin7ΔTM (Syn7ΔTM, n = 7) proteins (2 μg/ml each) were included in the recording pipette solution. In both (A) and (B), error bars indicate SEM. Representative current traces at the times indicated (1 and 2) are shown at right.

To test this hypothesis, we measured the effect of LTP-inducing stimuli on overall endocytic recycling in hippocampal neurons by using the classic constitutive recycling cargo Tf (*15*). Hippocampal neurons exhibited robust uptake of fluorescent Alexa 568–Tf (Alx-Tf; Molecular Probes, Eugene, OR) into recycling endosomes at steady state (Fig. 4, A and B; 60-min saturation). A subsequent 25-min period of further incubation in excess unlabeled Tf revealed a loss of intracellular Alx-Tf, reflecting ongoing basal recycling (Fig. 4, A and B). Brief application of glycine sufficient to induce LTP (*6*, *18*) accelerated the recycling of intracellular Alx-Tf (Fig. 4, A and B). Recycling was enhanced roughly twofold (Fig. 4, A and B), an effect quantitatively similar to observed changes in AMPA receptor insertion (Fig. 2) and AMPA receptor-mediated EPSCs (Fig. 3). The glycine-induced increase in Tf recycling was prevented by coapplication of D-AP5 (Fig. 4, A and B), indicating a requirement for NMDA receptor activation. The enhanced Tf recycling triggered by glycine was absent in neurons expressing Rme1-G429R (Fig. 4B). In addition, astrocytes in the same mixed cultures displayed robust endocytosis and recycling of Alx-Tf, but the recycling was unaffected by glycine stimulation (Fig. 4C). Thus, LTP-inducing stimuli enhance overall transport from recycling endosomes to the neuronal plasma membrane, and membrane trafficking events associated with LTP are not limited to AMPA receptors.

We have demonstrated that transport of AMPA receptors between the plasma membrane and recycling compartments maintains AMPA receptors in a dynamic pool that is subject to rapid mobilization in response to NMDA receptor activation (fig. S8). Such kinetic retention or kinetic mobilization from recycling endosomes provides a powerful mechanism for tightly tuning the abundance of postsynaptic AMPA receptors by shifting the steady-state equilibrium between intracellular compartments and the postsynaptic membrane. Our results suggest that mechanisms linking LTP induction and expression may converge on the recycling endosome, providing a potential framework for clarifying and merging the diverse molecular mechanisms for LTP. Several effectors of endosome fusion and vesicular transport are Ca^{2+}-sensitive (*28*, *29*) or targets of calcium/calmodulin-dependent protein kinase II (*30*), two primary upstream signals for LTP (*2*). Certain endosomal proteins are restricted to or enriched in neurons (*28*, *31*), suggesting specialized functions that remain to be elucidated. It will thus be important for future studies to delineate the protein machinery on endosomes that senses and responds to NMDA receptor–mediated Ca^{2+} influx during LTP as well as the regulatory proteins within endosomes that associate directly or indirectly with AMPA receptors.

Stimulus-dependent recycling of endocytic cargo provides an attractive cellular mechanism linking the insertion of AMPA receptors to morphological changes in synapse structure during LTP. We have shown that, in response to LTP-inducing stimuli, overall transport from recycling endosomes to the neuronal plasma membrane is enhanced. This enhanced recycling provides more AMPA receptors and ensures enhanced synaptic efficacy, but also supplies additional lipid membrane and other yet-unknown proteins that could mediate spine growth, postsynaptic density expansion, and retrograde messenger release and more globally alter postsynaptic composition. By coupling synaptic potentiation with membrane remodeling, LTP-induced transport from recycling endosomes to the plasma membrane provides an appealing unifying mechanism for activity-dependent synapse modification.

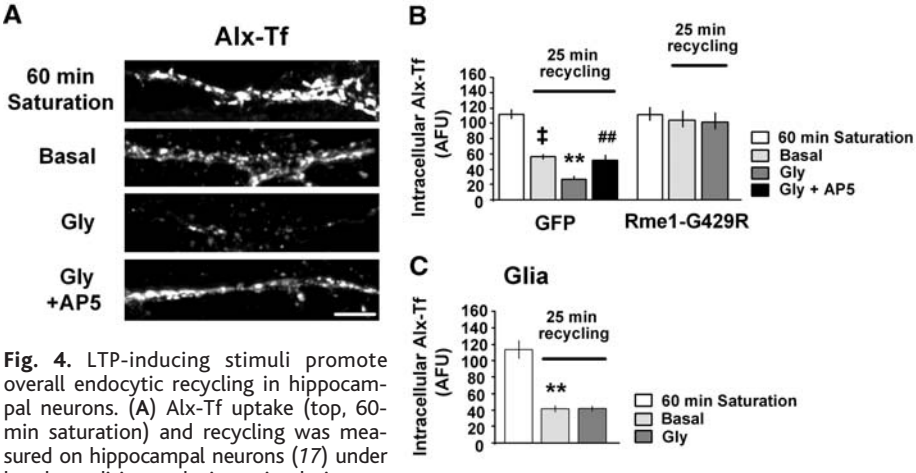

Fig. 4. LTP-inducing stimuli promote overall endocytic recycling in hippocampal neurons. (**A**) Alx-Tf uptake (top, 60-min saturation) and recycling was measured on hippocampal neurons (*17*) under basal conditions, glycine stimulation, or glycine stimulation in the presence of NMDA receptor antagonist. Loss of Alx-Tf fluorescence reflects recycling. Scale bar, 5 μm. (**B**) Remaining intracellular Alx-Tf from neurons expressing GFP or Rme1-G429R (*n* values of 30, 21, 42, 12, 11, 14, and 16 cells for each condition from left to right; double dagger indicates $P < 0.05$ relative to 60-min saturation, $^{**}P < 0.001$ relative to basal recycling, and double pound symbols indicate $P < 0.001$ relative to Gly; *t* test). (**C**) Alx-Tf uptake and recycling experiments on astrocytes (Glia). Values of *n* are 20, 26, and 28; $^{**}P < 0.001$ relative to 60-min saturation; *t* test. In both (B) and (C), error bars indicate SEM.

References and Notes

1. T. V. Bliss, T. Lomo, *J. Physiol.* **232**, 331 (1973).
2. R. C. Malenka, R. A. Nicoll, *Science* **285**, 1870 (1999).
3. D. Liao, N. A. Hessler, R. Malinow, *Nature* **375**, 400 (1995).
4. J. T. Isaac, R. A. Nicoll, R. C. Malenka, *Neuron* **15**, 427 (1995).
5. S. H. Shi *et al.*, *Science* **284**, 1811 (1999).
6. W. Lu *et al.*, *Neuron* **29**, 243 (2001).
7. R. Malinow, R. C. Malenka, *Annu. Rev. Neurosci.* **25**, 103 (2002).
8. D. S. Bredt, R. A. Nicoll, *Neuron* **40**, 361 (2003).
9. J. A. Kauer, R. C. Malenka, R. A. Nicoll, *Neuron* **1**, 911 (1988).
10. M. Passafaro, C. Sala, M. Niethammer, M. Sheng, *Nat. Neurosci.* **2**, 1063 (1999).
11. L. Pickard *et al.*, *Neuropharmacology* **41**, 700 (2001).
12. C. Luscher *et al.*, *Neuron* **24**, 649 (1999).
13. M. D. Ehlers, *Neuron* **28**, 511 (2000).
14. S. H. Lee, A. Simonetta, M. Sheng, *Neuron* **43**, 221 (2004).
15. S. X. Lin, B. Grant, D. Hirsh, F. R. Maxfield, *Nat. Cell Biol.* **3**, 567 (2001).
16. M. Zerial, H. McBride, *Nat. Rev. Mol. Cell Biol.* **2**, 107 (2001).
17. Materials and methods are available as supporting material on *Science* Online.
18. H. Y. Man *et al.*, *Neuron* **38**, 611 (2003).
19. M. Passafaro, V. Piech, M. Sheng, *Nat. Neurosci.* **4**, 917 (2001).
20. M. Rosenberg, J. Meier, A. Triller, C. Vannier, *J. Neurosci.* **21**, 5036 (2001).
21. C. Nizak *et al.*, *Science* **300**, 984 (2003).
22. B. Short, C. Preisinger, J. Schaletzky, R. Kopajtich, F. A. Barr, *Curr. Biol.* **12**, 1792 (2002).
23. J. White *et al.*, *J. Cell Biol.* **147**, 743 (1999).
24. R. Prekeris, J. Klumperman, Y. A. Chen, R. H. Scheller, *J. Cell Biol.* **143**, 957 (1998).
25. W. Sun, Q. Yan, T. A. Vida, A. J. Bean, *J. Cell Biol.* **162**, 125 (2003).
26. R. Yuste, T. Bonhoeffer, *Annu. Rev. Neurosci.* **24**, 1071 (2001).
27. C. Luscher, R. A. Nicoll, R. C. Malenka, D. Muller, *Nat. Neurosci.* **3**, 545 (2000).
28. M. V. Khvotchev, M. Ren, S. Takamori, R. Jahn, T. C. Sudhof, *J. Neurosci.* **23**, 10531 (2003).
29. D. E. Knight, *Traffic* **3**, 298 (2002).
30. R. L. Karcher *et al.*, *Science* **293**, 1317 (2001).
31. P. Steiner *et al.*, *J. Cell Biol.* **157**, 1197 (2002).

32. We thank C. Zhang, H. Zhang, and I. Lebedeva for culturing neurons; M. Sheng for the HA/T-GluR1 construct; F. Maxfield for GFP-Rme1-WT and GFP-Rme1-G429R; M. Zerial for GFP-Rab11a-WT; G.-W. Cho for generating GFP-Rab11a-S25N; J. White for GFP-Rab6a-T27N; Y. Li for generating Sindbis virus constructs; A. Bean for GST-syntaxin13ΔTM and GST-syntaxin7ΔTM; and G. Augustine, T. Blanpied, G. Feng, J. Hernandez, A. Horton, L. Katz, J. Lu, R. Mooney, Y. Mu, I. Perez-Otano, and P. Skene for critical review of the manuscript. This work was supported by the NIH (NS39402 and MH64748), the American Heart Association, the Alzheimer's Association and a Broad Scholar Award (to M.D.E.), and DA11289 to J.A.K.

Supporting Online Material

www.sciencemag.org/cgi/content/full/305/5692/1972/DC1
Materials and Methods
Figs. S1 to S8
References

28 June 2004; accepted 6 August 2004

New Products

Mo Bio Laboratories
For more information
800-606-6246
www.mobio.com
www.scienceproductlink.org

Soil DNA Isolation Kit

PowerSoil is a new kit for DNA isolation from difficult soils. The PowerSoil DNA Isolation Kit features a novel and proprietary method for isolating genomic DNA from environmental samples. The kit is intended for use with environmental samples containing a high humic acid content, including difficult soil types such as compost, sediment, and manure. The isolated DNA has a high level of purity allowing for more successful polymerase chain reaction (PCR) amplification of organisms from the sample. PCR analysis has been performed to detect a variety of organisms, including bacteria, fungi, algae, and actinomycetes.

BD Biosciences
For more information
858-812-8800
www.bdbiosciences.com
www.scienceproductlink.org

Bioanalyzer

The BD FACSArray bioanalyzer is a new platform for fast and sensitive high-content analysis of proteins in cell biology, immunology, and proteomics. Capable of both multiplexed bead and cellular assays, the BD FACSArray bioanalyzer is easy to use, flexible, and sensitive.

Syncroscopy
For more information
800-686-4415
www.syncroscopy.com
www.scienceproductlink.org

Focus and Stage Control System

SyncroScan, a high-speed focus and stage control system, automates sample scanning with many leading optical microscopes to rapidly provide accurate image maps. A SyncroScan system comes with a high-resolution camera, a motorized XY stage, and a Z stepper, all of which can attach to virtually any optical microscope. This hardware is linked to a personal computer running SyncroScan software and a stage controller board, which automates the stage and stepper, and controls the microscope's illumination, condenser, top lens, and objectives. With SyncroScan, the stage moves continuously to scan at up to 25 fields per second. While scanning, the software simultaneously focuses, captures, shade corrects, and stitches each image side by side to produce one large "real-time" image map of image tiles. Both the map and tiles can be saved to ensure users have a secure record of each sample. For microscopists who require accuracy in image-stitching, SyncroScan can be supplied with XY encoders to control the fine adjustment of image capture from the stage.

Olympus
For more information
+49 40 2 37 73-326
www.olympus-europa.com
www.scienceproductlink.org

Laser Scanning Confocal Microscope

The FluoView FV1000 for high-resolution confocal imaging of living cells, offers a unique scanning system with two independent, fully synchronized laser scanners for simultaneous confocal high-resolution imaging and laser stimulation. This advanced microscope allows improved fluorescence imaging of living cells with high sensitivity, high speed, and minimal damage to samples. The FV1000 allows bright, fast, and precise imaging and features technology to capture without a time lag data from the rapid cellular processes that occur during and immediately after laser stimulation. The FV1000 is suitable for advanced techniques such as fluorescence recovery after photobleaching, fluorescence loss in photobleaching, uncaging, photoactivation, and photoconversion. Its optical system features an ultra-high wavelength resolution of 2 nm, allowing fluorescence dyes with almost similar emission spectra to be clearly separated. The FV1000 is fully motorized and designed in an open configuration for easy expansion. With up to five detection channels and a new graphical interface, the laser scanning microscope is simple to use and easy to set up for advanced experiment protocols.

Shimadzu
For more information
800-477-1227
www.shimadzu.com
www.scienceproductlink.org

MALDI Plate Spotter

AccuSpot is a new matrix-assisted laser desorption ionization (MALDI) plate spotter that automates liquid chromatography micro-fractionation, spotting, and preparation for mass spectrometry analysis. Used in tandem with any high performance liquid chromatography system for precise proteome analysis with greater sequence coverage, AccuSpot enables spotting in volumes of 10 nL or more on up to nine microtiter plates in 96- or 384-plate format or 18 2×2 format plates. Spotting can be performed in either continuous or time-specific mode. The AccuSpot features automatic addition of matrix solution, which can be applied as a variable rate between 0.1 μL/min and 10 μL/min, and a standard charge-coupled device camera that continuously monitors the spotting operation. The AccuSpot prevents plate damage and eliminates cross-contamination through the use of a patent-pending "half-contact spotting method" that makes use of plate sensors. Users control spotting conditions, such as the fractionation mode and compensation parameters from a personal computer.

Camo Smart
For more information
732-602-8886
www.camo.com
www.scienceproductlink.org

Statistical Software

The Unscrambler Version 9.0 multivariate statistical software features three-dimensional data analysis with three-way regression modeling to model relationships between three-dimensional X-data and two-dimensional Y-data. New features also include "Automatic Pretreatment in Prediction and Classification" to correct raw data for various types of instrument errors and shifts and "Optimized PC Navigation Tools" for flexibility on personal computer-oriented plots. Other new features include improved compatibility with other software, an increased number importable instrument data formats, and enhanced visualization capabilities.

Newly offered instrumentation, apparatus, and laboratory materials of interest to researchers in all disciplines in academic, industrial, and government organizations are featured in this space. Emphasis is given to purpose, chief characteristics, and availability of products and materials. Endorsement by *Science* or AAAS of any products or materials mentioned is not implied. Additional information may be obtained from the manufacturer or supplier by visiting www.scienceproductlink.org on the Web, where you can request that the information be sent to you by e-mail, fax, mail, or telephone.

Published by AAAS